

DRIVEN QUANTUM SYSTEMS

Josephson junction arrays, Floquet systems and active quantum matter

DISSERTATION

zur Erlangung des Grades eines
Doktors der Naturwissenschaften

AM FACHBEREICH PHYSIK DER FREIEN UNIVERSITÄT BERLIN

vorgelegt von

ALEXANDER-GEORG PENNER

Berlin, 2026

Erstgutachter: Prof. Felix von Oppen, PhD

Zweitgutachter: Prof. Dr. Piet W. Brouwer

Tag der Abgabe: 07.01.2026

Tag der Disputation: 27.02.2026

SELBSTSTÄNDIGKEITSERKLÄRUNG

Name: Alexander-Georg

Vorname: Penner

Ich erkläre gegenüber der Freien Universität Berlin, dass ich die vorliegende Dissertation selbstständig und ohne Benutzung anderer als der angegebenen Quellen und Hilfsmittel angefertigt habe. Die vorliegende Arbeit ist frei von Plagiaten. Alle Ausführungen, die wörtlich oder inhaltlich aus anderen Schriften entnommen sind, habe ich als solche kenntlich gemacht. Diese Dissertation wurde in gleicher oder ähnlicher Form noch in keinem früheren Promotionsverfahren eingereicht.

Mit einer Prüfung meiner Arbeit durch ein Plagiatsprüfungsprogramm erkläre ich mich einverstanden.

Datum: 07.01.2026

Unterschrift:

KURZFASSUNG

Das umfangreiche Forschungsfeld der getriebenen Quantensysteme hat in den letzten Jahren zahlreiche theoretische und experimentelle Fortschritte verzeichnet, mit Arbeiten, welche von Messtechniken über die Erzeugung von Nichtgleichgewichtsphasen der Materie bis hin zu Betrachtungen aktiver Materie auf Quantenebene reichen. In dieser Arbeit untersuchen wir drei aktuelle Richtungen dieses Forschungsbereichs.

Zunächst betrachten wir Gitter von Josephson-Kontakten, die dank jüngster Fortschritte in der Fertigung in Experimenten präzise Kontrolle über die Systemparameter ermöglicht. Numerische Berechnungen deuten darauf hin, dass ein transversales Magnetfeld im Kontaktgitter eine Kaskade unterschiedlicher Vortex-Gitterzustände induziert. Wir zeigen in dieser Arbeit, dass die Messung des vollständigen Widerstandstensors direkten Zugang zu Informationen über diese Vortex-Gitter ermöglicht.

Darüber hinaus untersuchen wir ein Gitter von φ_0 -Kontakten. Wir stellen fest, dass bei Einbeziehung von Kopplungen über nächste Nachbarn hinaus die φ_0 -Verschiebungen zu einem asymmetrischen Pinning-Potential für die Vortizes führen, was wiederum einen Josephson-Diodeneffekt durch das Depinning der Vortizes hervorruft.

Im zweiten Teil wenden wir uns periodisch getriebenen Spin-Ketten zu. Motiviert durch ein aktuelles Experiment auf einem Quantenprozessor untersuchen wir das Floquet-Quanten-Ising-Modell in seiner fermionischen Formulierung. Abhängig von den Parametern kann das Modell Randmoden aufweisen, die entweder mit einer topologischen Gleichgewichtsphase (Majorana-Nullmoden) oder mit einer Nichtgleichgewichtsphase (Majorana- π -Moden) verknüpft sind. Im Gegensatz zur Gleichgewichtsphase stellen wir fest, dass die Randmoden in der Nichtgleichgewichtsphase durch eine bemerkenswerte Resistenz gegenüber paritätsbrechenden Störungen gekennzeichnet sind, was wir mithilfe einer stroboskopischen Störungstheorie erklären.

Daran anschließend untersuchen wir Spinkorrelationsfunktionen eines Floquet-Zeitkristalls. Hier finden wir einen Zusammenhang zwischen Paarbildungen im Spektrum des Floquet-Operators und den charakteristischen Perioden-2-Spinkorrelationen der zeitkristallinen Phase. Insbesondere können wir die Korrelationsfunktionen mit der Fourier-Transformation der Paarungsverteilung verbinden, welche näherungsweise eine lognormale Form aufweist. Wir diskutieren außerdem Implikationen für das Phasendiagramm des Zeitkristalls.

Das dritte und letzte Thema dieser Arbeit ist das aufkommende Feld der aktiven Quantenmaterie. Zunächst diskutieren wir die allgemeinen Bedingungen für ein einzelnes aktives Quantenteilchen. Anschließend betrachten wir das konkrete Beispiel eines Spin-1/2-Teilchens. Wir zeigen, unter welchen Bedingungen das Teilchen aktive Bewegungen ausführt und demonstrieren, dass diese Bewegungen durch quantenmechanische Eigenschaften charakterisiert werden.

ABSTRACT

The extensive field of driven quantum systems has seen numerous theoretical and experimental advances in recent years, with studies ranging from measurement techniques, over engineering of out-of-equilibrium phases of matter to considerations of active matter on the quantum level. In this thesis, we explore three timely directions of this body of research.

First, we consider arrays of Josephson junctions, which have become highly tunable in experiments due to recent fabrication progress. Numerical calculations suggest that transverse magnetic fields induce a cascade of different vortex lattice states on the arrays. We find in this thesis that the measurement of the full resistivity tensor gives direct access to information about the vortex lattices.

Motivated by a recent experiment, we further study an array of φ_0 -junctions. We find that going beyond nearest neighbor coupling, the φ_0 -shifts lead to an asymmetric pinning potential for the vortices which consequently facilitates a Josephson diode effect via vortex depinning.

Second, we turn towards periodically driven spin chains. Motivated by a recent experiment on a quantum processor, we study the Floquet quantum Ising model in its fermionic formulation. Depending on the parameters, the model can host edge modes that are associated with a topological, equilibrium (Majorana zero modes) or out-of-equilibrium (Majorana π modes) phase. In contrast to the equilibrium phase, we find that the edge modes in the out-of-equilibrium phase are characterized by remarkable resistance against parity-breaking perturbations, which we explain in terms of a stroboscopic perturbation theory.

Following this, we study spin correlation functions of a Floquet time crystal. Here we find a connection of pairings in the spectrum of the Floquet operator to the defining period-2 spin correlations of the time-crystalline phase. Specifically, we can express the correlation functions in terms of the Fourier transform of the pairing distribution, which is approximately of log-normal form. We also discuss implications for the phase diagram of the time crystal.

The third and final topic of this thesis is the emerging field of active quantum matter. We first state the general framework for a single active quantum particle, after which we consider the specific example of a spin-1/2 particle. We then show under which conditions the particle carries out active motion and demonstrate that the motion is characterized by genuine quantum features.

LIST OF PUBLICATIONS

This thesis is based on the following five peer-reviewed and published articles.

- Alexander-Georg Penner, Karsten Flensberg, Leonid Glazman, Felix von Oppen
Resistivity tensor of vortex-lattice states in Josephson junction arrays
Phys. Rev. Lett. **131**, 206001 [1]
<https://doi.org/10.1103/PhysRevLett.131.206001>
Chapter 3 is based on this work.
- Simon Reinhardt, Alexander-Georg Penner, Johanna Berger, Christian Baumgartner, Sergei Gronin, Geoffrey C. Gardner, Tyler Lindemann, Michael J. Manfra, Leonid I. Glazman, Felix von Oppen, Nicola Paradiso, Christoph Strunk
Spontaneous supercurrents and vortex depinning in two-dimensional arrays of φ_0 -junctions
Phys. Rev. B **112**, 224503 [2]
<https://doi.org/10.1103/31zv-84hw>
Chapter 4 is based on this work.
- Harald Schmid, Alexander-Georg Penner, Kang Yang, Leonid Glazman, Felix von Oppen
Robust Spectral π Pairing in the Random-Field Floquet Quantum Ising Model
Phys. Rev. Lett. **132**, 210401 [3]
<https://doi.org/10.1103/PhysRevLett.132.210401>
Chapter 6 is based on this work.
- Alexander-Georg Penner, Harald Schmid, Leonid Glazman, Felix von Oppen
Subharmonic spin correlations and spectral pairing in Floquet time crystals
Phys. Rev. B **111**, 184308 [4]
<https://doi.org/10.1103/PhysRevB.111.184308>
Chapter 7 is based on this work.
- Alexander-Georg Penner, Ludmila Viotti, Rosario Fazio, Liliana Arrachea, Felix von Oppen
Heat-to-motion conversion for quantum active matter
Phys. Rev. B **112**, L180303 [5]
<https://doi.org/10.1103/r6tm-nx19>
Chapter 9 is based on this work.

The author has published an additional article that is not part of this thesis:

- Alexander-Georg Penner, Felix von Oppen, Gergely Zarand, Martin R. Zirnbauer
Hilbert-space geometry of random-matrix eigenstates
Phys. Rev. Lett. **126**, 200604 [6]
<https://doi.org/10.1103/PhysRevLett.126.200604>

CONTENTS

1	INTRODUCTION	1
2	INTRODUCTION TO SUPERCONDUCTING NETWORKS	5
2.1	Josephson junctions	5
2.2	Josephson junction arrays	7
2.2.1	Vortices and the BKT transition	8
2.3	Frustrated Josephson junction arrays	10
2.3.1	Villain approximation and duality transformation	11
2.3.2	Effective vortex Hamiltonian and charge neutrality	14
2.4	Vortex motion driven by external currents	16
2.4.1	Vortex motion	17
3	RESISTIVITY TENSOR OF VORTEX-LATTICE STATES IN JOSEPHSON JUNCTION ARRAYS	19
3.1	Introduction	19
3.2	The model	20
3.3	Striped vortex-lattice states	21
3.3.1	Different regions of ground-state structures	22
3.4	Resistivity tensor	24
3.4.1	Vortex transport along diagonals	25
3.4.2	Calculation of the resistivity	26
3.4.3	Resistivity of vortex-lattice liquid crystals	27
3.5	Conclusion	28
4	SUPERCONDUCTING DIODE EFFECT IN φ_0 -JOSEPHSON JUNCTION ARRAYS	31
4.1	Introduction	31
4.2	Andreev bound-states	32
4.3	Anomalous Josephson effect	35
4.3.1	Spin-dependent Andreev levels and anomalous phase shift	38
4.4	Model of the φ_0 -Josephson junction array	39
4.4.1	Calculation of the ground state	41
4.5	Modulated vortex potential	42
4.6	Diode effect due to vortex depinning	43
4.6.1	Langevin equation for vortex motion	43

4.6.2	Relaxation effects and washboard potential	47
4.7	Conclusion	49
5	PERIODICALLY DRIVEN QUANTUM ISING MODELS	51
5.1	Transverse field Ising Model	51
5.2	Jordan-Wigner transformation	52
5.2.1	Open boundary conditions - Edge modes	53
5.2.2	Periodic boundary conditions - Parity sectors	56
5.3	Longitudinal fields	58
5.4	Floquet theory	59
5.4.1	Kicked models	60
6	ROBUST SPECTRAL π PAIRING IN THE RANDOM-FIELD FLOQUET QUANTUM ISING MODEL	63
6.1	Introduction	63
6.2	Clean model	64
6.3	Disorder induced splitting distributions	66
6.3.1	Floquet perturbation theory	67
6.4	Boundary correlation functions	69
6.5	Transverse field disorder	71
6.6	Conclusion	73
7	SUBHARMONIC SPIN CORRELATIONS AND SPECTRAL PAIRING IN FLOQUET TIME CRYSTALS	75
7.1	Introduction	75
7.2	Temporal spin correlations and spectral pairing	77
7.3	Splitting distribution analysis in the fermion model	81
7.3.1	Dual transformation	81
7.3.2	Single-particle splitting distribution	82
7.4	Further analysis in the spin model	85
7.5	Perturbation theory for longitudinal fields	86
7.6	Conclusion	88
8	DYNAMICS OF OPEN QUANTUM SYSTEMS	89
8.1	Lindblad equation	89
8.2	Example: Two-level system coupled to multiple heat baths	93
8.3	Quantum regression theorem	96
9	HEAT-TO-MOTION CONVERSION FOR QUANTUM ACTIVE MATTER	99
9.1	Introduction	99
9.2	Model for an active quantum particle	101

9.3	Heat-to-motion conversion	103
9.4	Momentum relaxation	105
9.5	Quantum signatures of the active particle	107
9.6	Conclusion	109
CONCLUSIONS		111
ACKNOWLEDGMENTS		113
APPENDIX A		115
A.1	Metropolis algorithm for vortex model minimization	115
A.2	Annealing of the phase configurations	116
A.3	Climbing-string method	116
APPENDIX B		119
B.1	Single-particle spectrum and eigenstates of the Floquet quantum Ising model	119
B.2	Stroboscopic perturbation theory	122
B.3	Perturbation theory for splitting distributions	124
	B.3.1 MZM splitting distribution	124
	B.3.2 MPM splitting distribution	125
B.4	Cumulants and correlations of the single-particle splitting distribution	128
B.5	Dual transformation	131
APPENDIX C		133
C.1	Average velocity	133
C.2	Momentum relaxation	135
C.3	Velocity-velocity correlation function	137
C.4	Mean-square displacement	140
C.5	Details of the simulation	140
BIBLIOGRAPHY		143

1 INTRODUCTION

In greatest generality, a driven system is a system whose dynamics are controlled not only by internal forces, but also by external sources of energy. A classic example is the damped harmonic oscillator, driven by a time-periodic force. In the absence of driving, the state of the system oscillates with decaying amplitude and a natural frequency ω_0 . An external force will alter the motion of the oscillator, so that after an initial transient, the system will oscillate at the driving period ω_D . Here, the amplitude does not decay with time as the drive continuously fuels the system with energy. For weak damping, driving the system close to its natural frequency also leads to a large oscillation amplitude. The latter point is especially relevant in construction, as, e.g., multiple bridges collapsed due to mechanical resonance¹. This example demonstrates that understanding the response of a system to external driving may be of vital importance.

Turning to the study of materials, the response to different forms of driving may be used to measure important material properties. An external voltage bias for example drives the charge carriers in a system, resulting in electrical currents that can be measured to determine its resistivity. If the material is anisotropic, one further measures perpendicular currents, which provides conclusions about the lattice structure of the material. There are many other examples, including the measurement of the phonon spectrum via optical driving or the application of a thermal bias to determine the thermal conductivity of a material. These considerations also translate to more complex systems such as superconducting networks, which will be explored over the course of this thesis.

In quantum physics, driving plays a fundamental role. On the one hand, it serves as a tool to extract information from otherwise inaccessible quantum states, e.g. the quantized energy differences in atoms can be measured by driving them with a laser working at resonant frequencies. On the other hand, driving allows for control of quantum states via Rabi oscillations [7]. By applying a periodic drive to the system, its state will oscillate between two eigenstates over time. Using driving pulses, this allows for tuning to particular linear combinations of eigenstates. In the context of quantum computing, this is important both for the preparation of initial states and the implementation of precise gates used to realize quantum algorithms [8–10].

An interesting application of periodic driving and the topic of a multitude of recent studies is Floquet engineering [11–13]. Floquet theory states that a periodically driven Hamiltonian acts as an effective, static Hamiltonian under the condition that the state of the system is only measured at integer values of the driving period. Floquet engineering uses this insight in order to design

¹For example, the Broughton Suspension Bridge collapsed in 1831 due to the synchronous marching of British troops.

effective Hamiltonians that are difficult to realize in a static setting. It also allows for precise control over the parameters of the Hamiltonian via the pulse length of the driving. Furthermore, Floquet engineering enables the creation of exotic, out-of-equilibrium phases of matter like time crystals [14]. Analogously to the breaking of translational symmetry by a (spatial) crystal, a time crystal spontaneously breaks time-translation symmetry, a property impossible to realize in a static setting. Another interesting direction is the engineering of topological, out-of-equilibrium phases. A system in a topological phase hosts edge modes, that in theory can be used as a platform for quantum computations. Analogously, edge modes are also present in an out-of-equilibrium topological phase, albeit with different properties that may be more desirable in applications. The latter point is the subject of a major part of this thesis.

A system can not only be driven from the outside as in the previously discussed examples, but may also have an internal source of energy driving it. Evidently, this description fits to transport vehicles driven by fuel, but also to living beings. The collective behavior of these so-called active agents constitutes an active body of research in the field of statistical mechanics [15]. In very recent studies, considerations about active particles were also extended to the quantum level [16–18]. Active quantum particles might occur naturally in the form of self-propelled molecules or could be created artificially in cold-atom experiments. The extension to the quantum regime naturally raises numerous important questions about the influence of quantum effects on the functionalities of active particles or more fundamentally, the minimal ingredients necessary to facilitate active motion in a quantum system.

This thesis is structured into three blocks: In the first block, we will discuss topics surrounding the current-driven dynamics of vortices in arrays of Josephson junctions (JJAs). After introducing elementary concepts in chapter 2 regarding vortices and JJAs, we consider the full resistivity tensor of a square-grid JJA that is subject to a perpendicular magnetic field in chapter 3. Depending on the fraction of magnetic flux quanta threading the unit cell, different vortex lattices will form, which break rotational and translational symmetries of the underlying array of Josephson junctions. We will show that the resistivity tensor provides a useful, experimental tool in identifying these vortex lattices. In chapter 4, we then consider a JJA of φ_0 -junctions. This is motivated by a recent experiment by the group of Christoph Strunk (Regensburg) [2], where the authors measured a Josephson diode effect on a JJA with strong spin-orbit coupling and an applied in-plane magnetic field. The magnetic and spin-orbit fields induce φ_0 -shifts in the current-phase relation of the junctions, tilting the vortex pinning potential of the array. We will show that as a consequence, the array exhibits a Josephson diode effect due to asymmetric depinning of vortices.

The second block is focused on periodically driven quantum spin chains. In chapter 5, we will introduce the Floquet formalism used to describe periodically driven quantum systems, and further provide an overview of results about the time-independent quantum Ising model. In chapter 6, we then discuss the different topological phases of the periodically-driven quantum Ising model. Depending on the parameters, the chain may host Majorana zero modes (analogously to the time-independent model) or Majorana π -modes, with the latter being associated

with an explicitly out-of-equilibrium phase. Typically, Majorana fermions are quickly destroyed by fermion parity-breaking perturbations. We show that, surprisingly, the π -modes are not only more stable than their equilibrium counterpart, but their stability is even enhanced by such perturbations. To explain this, we develop a stroboscopic perturbation theory, specifically targeted towards periodically kicked quantum systems. Following this, we move towards time crystals in chapter 7. Here, we find an explicit expression describing temporal spin correlation functions, related to statistics of π -pairs in the spectrum of the Floquet operator. In particular, we find that these pairings follow log-normal statistics, a result which we can explain through a connection to single-particle hopping processes along a disordered chain.

In the third and last block of this thesis, we will study a model for a quantum particle that is driven by internal non-equilibrium processes. In chapter 8, we first derive the Lindblad formalism used to describe the time evolution of systems coupled to their environment and further illustrate it via a simple example. Following this, we introduce the general framework for an active quantum particle in chapter 9. We demonstrate via a specific example what conditions facilitate internally driven motion of the particle and also show that the motion is characterized by explicit quantum features.

2 INTRODUCTION TO SUPERCONDUCTING NETWORKS

In this chapter, we will introduce the effects and concepts that are the foundation of the following chapters 3 and 4.

2.1 JOSEPHSON JUNCTIONS

Superconductivity occurs when certain materials are cooled below a critical temperature T_c . At T_c , the system undergoes a quantum phase transition and the electrical resistance falls to zero. First witnessed in 1911, the effect could only be explained around 50 years later by BCS theory [19]. In the BCS ground state, the electrons of the superconductor form a condensate of phase coherent so-called Cooper pairs, which are combinations of two electrons with opposite spin and momentum. These Cooper pairs carry a supercurrent according to the gradient of the phase $\varphi(\mathbf{r})$ of the condensate. This mechanism as well as the fact that the BCS ground state is gapped lead to dissipationless transport in superconductors. Due to the phase coherence, the Cooper pair condensate may be described by a single macroscopic wavefunction $\psi(\mathbf{r}) = |\psi(\mathbf{r})|e^{i\varphi(\mathbf{r})}$, in analogy to Bose-Einstein condensates [20].

Now consider a situation in which two superconductors are placed in close proximity, forming a so-called Josephson junction, see Fig. 2.1. Although the superconductors are separated from each other, Cooper pairs may still tunnel between them. We model the time evolution of this setup via a Schrödinger equation of the following form,

$$i\hbar \frac{d}{dt} \begin{pmatrix} \psi_1 \\ \psi_2 \end{pmatrix} = \begin{pmatrix} E_0 & J \\ J & E_0 \end{pmatrix} \begin{pmatrix} \psi_1 \\ \psi_2 \end{pmatrix}, \quad (2.1)$$

with E_0 being the energy of the superconducting ground states and $J \ll E_0$ a coupling energy. Here we assumed homogeneous wavefunctions ψ_1 and ψ_2 for simplicity. We now want to calculate the current density that is flowing between the superconductors. A current is flowing if the particle number in one of the superconductors changes over time. The current density j is thus given by

$$j = 2e \frac{dn_1}{dt} = 2e \frac{d|\psi_1|^2}{dt} = 2e \left(\psi_1 \frac{d\psi_1^*}{dt} + \psi_1^* \frac{d\psi_1}{dt} \right), \quad (2.2)$$

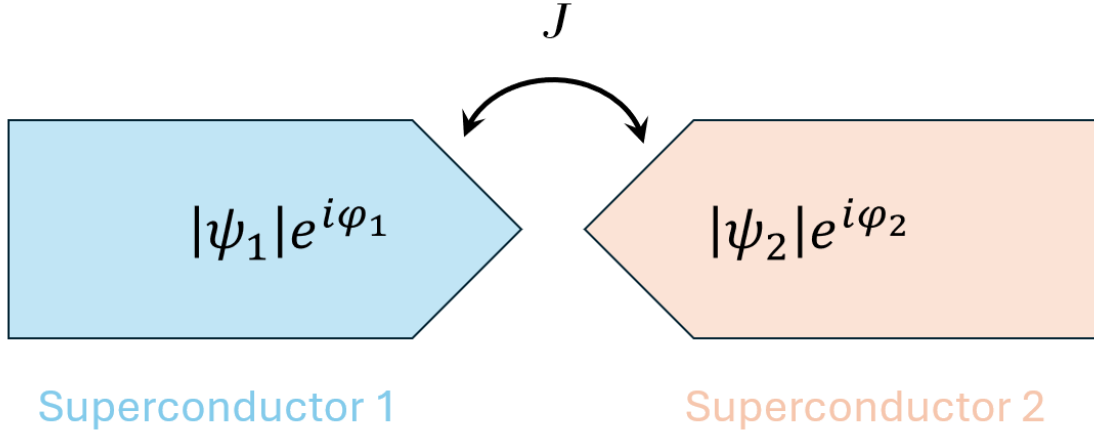


Figure 2.1: Josephson junction sketch. Two superconductors in close proximity, separated by an insulating barrier.

with n_1 being the particle density of the first superconductor and $2e$ the charge of a Cooper pair. Using the Schrödinger equation (2.1), we find for the current density,

$$j = \frac{4eJ}{\hbar} \text{Im}(\psi_1^* \psi_2) = j_c \sin(\varphi_2 - \varphi_1), \quad (2.3)$$

with the critical current density $j_c = 4eJ\sqrt{n_1 n_2}/\hbar$ giving an upper limit for the current density. We thus find that a phase difference between the superconductors induces a current that is purely due to quantum tunneling. This is the dc Josephson effect [20, 21] and was first predicted by Josephson in 1962. The here presented derivation is heuristic however and does not give the correct value for the critical current. A more realistic approach leads to the Ambegakoar-Baratoff formula [22], which relates the critical current to the temperature and the energy gap of the superconductors.

We may also apply a voltage V across the Josephson junction, so that the potential of the Cooper pairs on one side of the junction is increased by $2eV$. The general time-dependent solution of the Schrödinger equation gives $\psi(t) \sim e^{-iEt/\hbar}$ with E being the energy of the state. Thus, adding a potential to the Cooper pairs leads to a relative (with respect to φ_2) linear decrease of the phase with time,

$$\varphi_1 = \varphi_1(t=0) - \frac{2eV}{\hbar}t. \quad (2.4)$$

This may also be written in the following form,

$$\frac{d\varphi}{dt} = \frac{2eV}{\hbar}, \quad (2.5)$$

with $\varphi = \varphi_2 - \varphi_1$ being the phase difference across the junction. We find that applying a voltage leads to a linearly varying phase difference and therefore to an oscillating current, which is known as the ac Josephson effect [20, 21].

Finally, we want to estimate the energy E that is associated with a Josephson junction. To compute it, we note that the power P developing across a Josephson junction is given by

$$P = IV = \frac{dE}{dt}. \quad (2.6)$$

Using the equations for the dc and ac Josephson effects, we find

$$\frac{dE}{dt} = \frac{\hbar I_c}{2e} \frac{d\varphi}{dt} \sin(\varphi) = \frac{\hbar I_c}{2e} \frac{d}{dt}[-\cos(\varphi)], \quad (2.7)$$

with critical current I_c and therefore

$$E = -E_J \cos(\varphi). \quad (2.8)$$

In the last step we defined the Josephson coupling energy $E_J = \hbar I_c / 2e$. In reality, the number of Cooper pairs also contributes to the energy, as a junction also acts as a capacitor. In general, we thus have to write the Hamiltonian of the junction as

$$H = \frac{2e^2 n^2}{C} - E_J \cos(\varphi), \quad (2.9)$$

with C being the capacitance of the Josephson junction and n the excess Cooper pair number across the junction. As the Cooper pair number and the phases of the superconductors are canonically conjugate variables, $[\varphi, n] = i$ [20], the phases of the superconductor are subject to quantum dynamics. Experimentally, the capacitance may be tuned such that the phase term $-E_J \cos(\varphi)$ is the dominant contribution to the Hamiltonian. In that limit, we can treat the phases as classical, well-defined quantities. Going forward in this thesis, we will exclusively consider this classical limit.

2.2 JOSEPHSON JUNCTION ARRAYS

Josephson junctions may be used to construct a plethora of electronic devices, famous examples include the SQUID [23] or the transmon qubit [24]. All of these fall under the category of Josephson junction arrays, which are combinations of multiple Josephson junctions. The subject of this section is a 2D square lattice of superconducting islands, sketched in Fig. 2.2. The islands are coupled to their two neighbors via Josephson junctions in horizontal and vertical direction, thus forming a Josephson junction array. These kinds of systems have been investigated over the years as they provide a platform for studying topological phase transitions [25] and topologically protected qubits [26], among other applications.

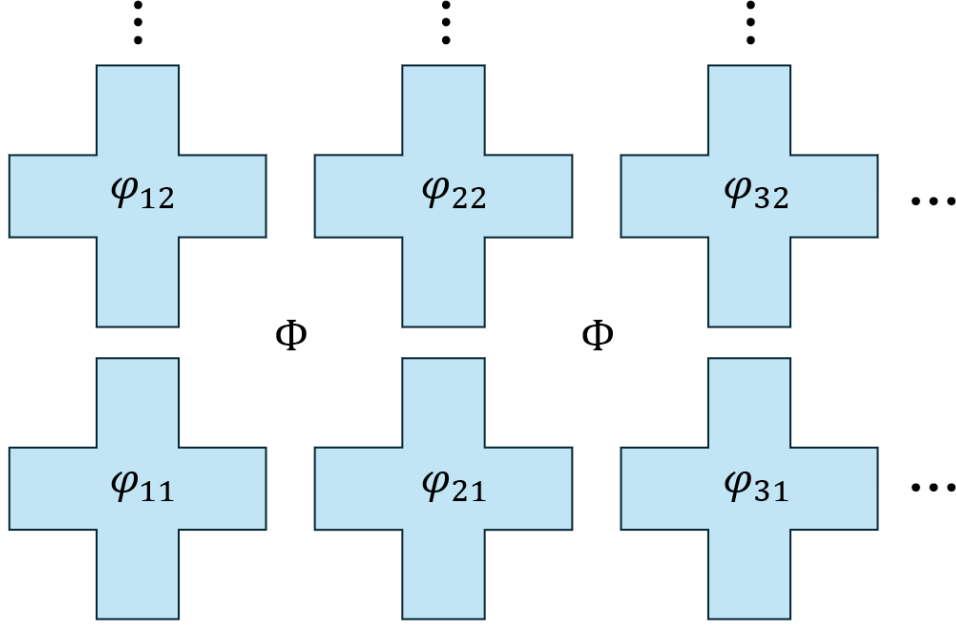


Figure 2.2: Sketch of a 2D Josephson junction array. Superconducting islands in blue are described by the superconductor phase φ_{ij} . The normal region (white) may be penetrated by a magnetic flux Φ , see Sec. 2.3.

Assuming that all junctions are equal and neglecting charging effects, we may write down the (classical) Hamiltonian of the system as

$$H = -E_J \sum_{i,j=1}^N \cos(\varphi_{i+1,j} - \varphi_{i,j}) - E_J \sum_{i,j=1}^N \cos(\varphi_{i,j+1} - \varphi_{i,j}). \quad (2.10)$$

We impose periodic boundary conditions by setting $\varphi_{N+1,j} = \varphi_{1,j}$ and $\varphi_{i,N+1} = \varphi_{i,1}$. The Hamiltonian in Eq. (2.10) is equivalent to the XY model [27], which famously features vortices beyond a critical temperature T_c . The unbinding of vortex-antivortex pairs is known as Berezinskii-Kosterlitz-Thouless (BKT) transition, which we will discuss here briefly.

2.2.1 VORTICES AND THE BKT TRANSITION

In the following, we will provide a heuristic derivation of the BKT transition. First note that the ground state of the model in Eq. (2.10) is given by the state in which all phases are aligned. For small deviations from the ground state, we may approximate the Hamiltonian as

$$H \simeq -E_J \sum_{i,j=1}^N \left[2 - \frac{1}{2}(\varphi_{i+1,j} - \varphi_{i,j})^2 - \frac{1}{2}(\varphi_{i,j+1} - \varphi_{i,j})^2 \right]. \quad (2.11)$$

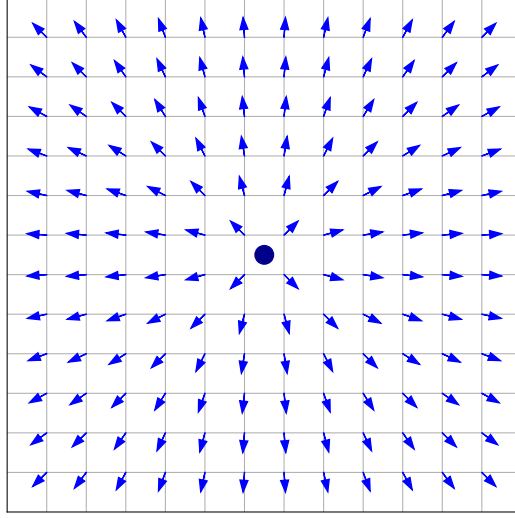


Figure 2.3: Vortex configuration of the XY model. Going around the vortex (blue dot) anti-clockwise, the phases (blue arrows) wind by 2π .

For small lattice spacing a , we may take the continuum limit and find,

$$H \simeq \frac{E_J}{2} \int d\mathbf{r} (\nabla\varphi(\mathbf{r}))^2. \quad (2.12)$$

Next, we want to find the energy associated with a vortex configuration. The defining property of a vortex is that when going in a loop around its center, the phases φ wind by an integer multiple of 2π , see Fig. 2.3. For a stable vortex configuration, it is necessary that it minimizes the energy locally, i.e. the phase configuration satisfies $\nabla \cdot [\nabla\varphi(\mathbf{r})] = 0$. A stable vortex configuration φ_v is given by

$$\varphi_v(r, \phi) = m\phi, \quad (2.13)$$

with m being an integer. Writing the integral in Eq. (2.12) in polar coordinates, we find for the energy E_v of the vortex,

$$\begin{aligned} E_v &= \frac{E_J}{2} \int_0^\infty dr r \int_0^{2\pi} d\phi \left[\left(\hat{e}_r \partial_r + \hat{e}_\phi \frac{1}{r} \partial_\phi \right) m\phi \right]^2 \\ &= \pi E_J m^2 \int_0^\infty \frac{dr}{r}. \end{aligned} \quad (2.14)$$

At first sight, it seems as if the vortex energy diverges logarithmically both at short and large distances. This issue may be fixed on the one hand by noting that the system is finite, which gives an upper bound R for the integral. At small r , the approximation of the continuum limit fails as the phase configuration $m\phi$ becomes ill-defined. To alleviate this, we introduce a constant

so-called core energy E_c and cut off the lower limit of the integral at the lattice scale a . The energy of the vortex is then given by

$$E_v = \pi E_J m^2 \ln\left(\frac{R}{a}\right) + E_c. \quad (2.15)$$

The core energy will be estimated in section 2.3.2. From Eq. (2.15), we see that the lowest energy vortices are associated with a winding of $m = \pm 1$. We will focus on these in the following. We consider the free energy F of the vortex at finite temperature. Noticing that the entropy S of a vortex is given by $k_B \ln(R^2/a^2) = 2k_B \ln(R/a)$, we find

$$F = E_v - TS = E_c + (\pi E_J - 2k_B T) \ln\left(\frac{R}{a}\right). \quad (2.16)$$

For temperatures below $T_c = \pi E_J / 2k_B$, vortices ($m = 1$) and anti-vortices ($m = -1$) appear in bound pairs as their large distance contributions to the energy cancel out, while their entropy reduces the free energy of the system. Above T_c , the vortex-antivortex pairs are able to unbind as each of their respective free energy contributions turns negative. Thus, at the critical temperature T_c , the system undergoes a phase transition which is commonly known as the BKT transition.

2.3 FRUSTRATED JOSEPHSON JUNCTION ARRAYS

In this section, we want to study the effect of a perpendicular magnetic flux Φ piercing the Josephson junction array, as sketched in Fig. 2.2. The phase of a wavefunction is gauge-dependent, since a gauge transformation of the vector potential $\mathcal{A}(\mathbf{r}) \rightarrow \mathcal{A}(\mathbf{r}) + \nabla\Lambda(\mathbf{r})$ leads to a corresponding change in the phase, $\varphi(\mathbf{r}) \rightarrow \varphi(\mathbf{r}) + \frac{q}{\hbar}\Lambda(\mathbf{r})$ with q being the charge of the particle. As the phases φ are connected to the wavefunction of the Cooper pair condensate, the Hamiltonian in Eq. (2.10) is not gauge-invariant. The appropriate Hamiltonian is given by

$$H = -E_J \sum_{i,j=1}^N \cos(\varphi_{i+1,j} - \varphi_{i,j} - A_{i,j}^h) - E_J \sum_{i,j=1}^N \cos(\varphi_{i,j+1} - \varphi_{i,j} - A_{i,j}^v), \quad (2.17)$$

with the horizontal and vertical phase shifts $A_{i,j}^{h;v}$ defined as

$$A_{i,j}^h = \frac{2\pi}{\Phi_0} \int_i^{i+1} dx \mathcal{A}_x(x, j), \quad A_{i,j}^v = \frac{2\pi}{\Phi_0} \int_j^{j+1} dy \mathcal{A}_y(i, y). \quad (2.18)$$

Here, we introduced the components of the vector potential \mathcal{A}_x and \mathcal{A}_y as well as the superconducting flux quantum $\Phi_0 = h/2e$. One readily checks that the Hamiltonian is now invariant under a gauge transformation.

With no magnetic flux applied, we already know that the ground state is the state with all phases aligned. However, adding a magnetic flux significantly complicates the situation, as the phases get frustrated due to the shifts added in the gauge-invariant Hamiltonian. In fact, it is no longer possible to find the global or a local minimum of H analytically. This is due to the cosines in Eq. (2.17). The derivatives $\partial_{\varphi_{i,j}} H$ lead to a non-linear system of equations, which is not solvable for general magnetic flux values. In order to find the ground state with a nonzero magnetic flux, one therefore has to employ numerical methods such as annealing algorithms [28].

2.3.1 VILLAIN APPROXIMATION AND DUALITY TRANSFORMATION

In order to understand the ground states with applied frustration, we want to derive a different description of the Josephson junction array in this section. The goal is to find an effective quadratic Hamiltonian via the so-called Villain approximation [29]. We start by considering the canonical partition function Z of the system,

$$Z = \int \prod_{i,j=1}^N d\varphi_{i,j} \exp\{-\beta H\} \quad (2.19)$$

$$= \int \prod_{i,j=1}^N d\varphi_{i,j} \prod_{i,j=1}^N f_B(\varphi_{i+1,j} - \varphi_{i,j} - A_{i,j}^h) f_B(\varphi_{i,j+1} - \varphi_{i,j} - A_{i,j}^v), \quad (2.20)$$

with $\beta = 1/T$ and the function f_B being the Boltzmann factor of a single bond,

$$f_B(\Delta\varphi) = \exp\{\beta E_J \cos(\Delta\varphi)\}. \quad (2.21)$$

As $f_B(\Delta\varphi)$ is a periodic function of $\Delta\varphi$, we may expand it into a Fourier series,

$$f_B(\Delta\varphi) = \sum_{n=-\infty}^{\infty} e^{in\Delta\varphi} c_n, \quad (2.22)$$

with the coefficients c_n given by

$$c_n = \int_0^{2\pi} \frac{d\Delta\varphi}{2\pi} e^{-in\Delta\varphi} f_B(\Delta\varphi) = \int_0^{2\pi} \frac{d\Delta\varphi}{2\pi} \exp\left\{-\beta \left(\frac{in\Delta\varphi}{\beta} - E_J \cos(\Delta\varphi)\right)\right\}. \quad (2.23)$$

Under the assumption that the temperature is low ($\beta \gg 1$), we may solve the integral in Eq. (2.23) via saddle-point approximation. An elementary calculation gives an extremum of $\Delta\varphi_0 = -in/\beta E_J$ for the exponent. Applying the saddle-point approximation for the integral then yields for the coefficients c_n ,

$$c_n \sim \exp\left\{-\frac{n^2}{2\beta E_J} + \beta E_J\right\}, \quad (2.24)$$

up to a non-exponential prefactor which will not be relevant for the argument. We now return to the partition function. The introduction of the Fourier series introduces a new set of integer variables $n_{i,j}^{h,v}$, each of which is associated with a junction. Since every phase $\varphi_{i,j}$ is connected to two horizontal and two vertical bonds, we find for the partition function,

$$Z \sim \int \prod_{i,j=1}^N d\varphi_{i,j} \prod_{i,j=1}^N \sum_{n_{i,j}^h} \sum_{n_{i,j}^v} \exp \left\{ -\frac{[n_{i,j}^h]^2 + [n_{i,j}^v]^2}{2\beta E_J} - in_{i,j}^h A_{i,j}^h - in_{i,j}^v A_{i,j}^v \right\} \\ \times \exp \left\{ -i\varphi_{i,j} (n_{i,j}^h - n_{i-1,j}^h + n_{i,j}^v - n_{i,j-1}^v) \right\}. \quad (2.25)$$

As the integrals over the phases $\varphi_{i,j}$ go over a period, it is evident now that the integral is zero, unless the bond variables satisfy the condition

$$\gamma(n_{i,j}^{h,v}) \equiv n_{i,j}^h - n_{i-1,j}^h + n_{i,j}^v - n_{i,j-1}^v = 0, \quad (2.26)$$

at all sites. For the terms that do satisfy the condition, the integral over the phases merely yields a prefactor of $(2\pi)^{N^2}$. We thus find for the partition function,

$$Z \sim \prod_{i,j=1}^N \sum_{c(n_{i,j}^{h,v})=0} \exp \left\{ -\frac{[n_{i,j}^h]^2 + [n_{i,j}^v]^2}{2\beta E_J} - in_{i,j}^h A_{i,j}^h - in_{i,j}^v A_{i,j}^v \right\}. \quad (2.27)$$

The sum in Eq. (2.27) now involves all bond variables satisfying the condition $\gamma(n_{i,j}^{h,v}) = 0$. Since there are N^2 conditions and $2N^2$ bond variables, this leaves us with $2N^2 - N^2 = N^2$ degrees of freedom. We may use this condition to introduce yet another set of variables. First we note that the condition in Eq. (2.26) defines the allowed bond variables as a discrete version of a divergence free field,

$$n_{i,j}^h - n_{i-1,j}^h + n_{i,j}^v - n_{i,j-1}^v \sim \partial_x n_{i,j}^h + \partial_y n_{i,j}^v = \nabla \cdot \begin{pmatrix} n_{i,j}^h \\ n_{i,j}^v \end{pmatrix} = 0. \quad (2.28)$$

A two-dimensional divergence free field may generally be written as the curl of a scalar field $p_{i,j}$,

$$\begin{pmatrix} n_{i,j}^h \\ n_{i,j}^v \end{pmatrix} \sim \begin{pmatrix} -\partial_y p_{i,j} \\ \partial_x p_{i,j} \end{pmatrix} \sim \begin{pmatrix} p_{i,j-1} - p_{i,j} \\ p_{i,j} - p_{i-1,j} \end{pmatrix} \quad (2.29)$$

The identification

$$n_{i,j}^h = p_{i,j-1} - p_{i,j}, \quad n_{i,j}^v = p_{i,j} - p_{i-1,j}, \quad (2.30)$$

thus provides us with a new set of N^2 independent integer variables $p_{i,j}$. By construction, the new variables satisfy the condition in Eq. (2.26). Each of the bond variables is connected

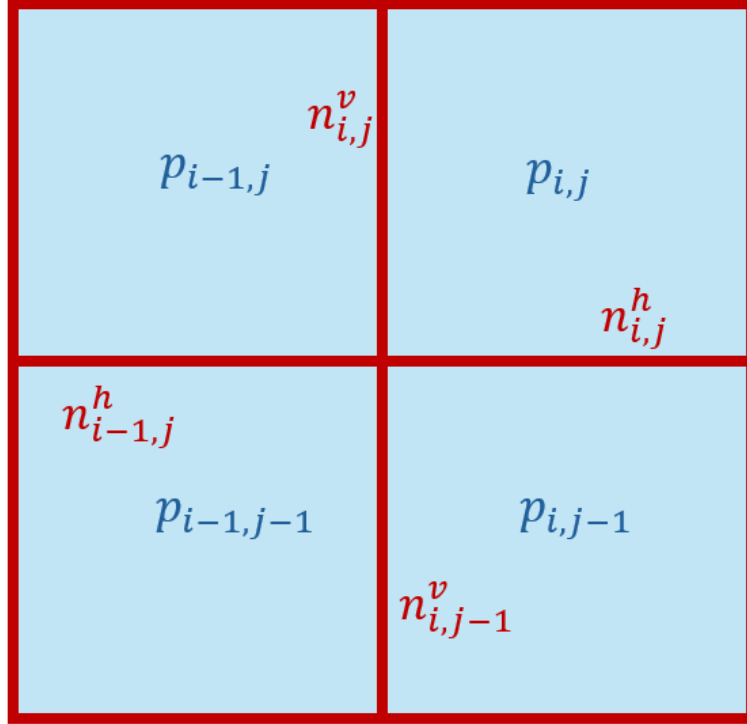


Figure 2.4: Sketch of the variable transformation. The bond variables $n_{i,j}^{h,v}$ (red) are each connected to two of the variables $p_{i,j}$ by Eq. (2.30). The indices suggests a connection of the $p_{i,j}$ to the plaquettes (blue) of the array.

to an orthogonal set of two of the new variables $p_{i,j}$, see Fig. 2.4. This suggests that the $p_{i,j}$ are associated with the plaquettes of the array. We thus performed a duality transformation, changing the description of the array via bonds to a description via the plaquettes.

In the next step, we apply the duality transformation to the partition function. Since the plaquette variables $p_{i,j}$ are connected with a positive sign to the top and left bonds and a negative sign to the bottom and right bonds, we find

$$\begin{aligned}
 Z \sim & \prod_{i,j=1}^N \sum_{p_{i,j}} \exp \left\{ - \frac{(p_{i,j} - p_{i,j-1})^2 + (p_{i,j} - p_{i-1,j})^2}{2\beta E_J} \right\} \\
 & \times \exp \{ -i p_{i,j} (A_{i,j}^v + A_{i,j+1}^h - A_{i+1,j}^v - A_{i,j}^h) \}. \quad (2.31)
 \end{aligned}$$

2 Introduction to superconducting networks

The phase shifts $A_{i,j}^{h,v}$ in Eq. (2.31) are now ordered in such a way that they may be combined into a loop integral around the (i, j) -plaquette. Since a line integral of the vector potential around an area gives the magnetic flux Φ through said area, we find

$$A_{i,j}^v + A_{i,j+1}^h - A_{i+1,j}^v - A_{i,j}^h = \frac{2\pi}{\Phi_0} \oint_{(i,j)} \mathbf{dr} \cdot \mathcal{A}(\mathbf{r}) = \frac{2\pi}{\Phi_0} \Phi = 2\pi f. \quad (2.32)$$

In the last step, we defined the frustration $f = \Phi/\Phi_0$. This insight simplifies the form of the partition function to

$$Z \sim \prod_{i,j=1}^N \sum_{p_{i,j}} \exp \left\{ -\frac{(p_{i,j} - p_{i,j-1})^2 + (p_{i,j} - p_{i-1,j})^2}{2\beta E_J} - i2\pi f p_{i,j} \right\}. \quad (2.33)$$

Again, this highlights that the present description has no knowledge about the bonds (bond phase shifts), but only about the plaquettes (frustration).

2.3.2 EFFECTIVE VORTEX HAMILTONIAN AND CHARGE NEUTRALITY

Before we arrive at the desired effective Hamiltonian, we perform yet another transformation. We use the Poisson summation formula, which states for a general function g and its Fourier transform \tilde{g}

$$\sum_{n=-\infty}^{\infty} g(n) = \sum_{m=-\infty}^m \tilde{g}(m) = \sum_{m=-\infty}^{\infty} \int dx g(x) e^{2\pi i m x}. \quad (2.34)$$

Applying the summation formula to each of the plaquette integers yields for the partition function

$$Z \sim \prod_{i,j=1}^N \sum_{m_{i,j}} \int dx_{i,j} \exp \left\{ -\frac{(x_{i,j} - x_{i,j-1})^2 + (x_{i,j} - x_{i-1,j})^2}{2\beta E_J} + i2\pi(m_{i,j} - f)x_{i,j} \right\}. \quad (2.35)$$

Next, we exchange the order of summation over $m_{i,j}$ and taking the product over i and j . Each summand then becomes a constellation of the $m_{i,j}$, which we will denote via \mathbf{m} . With the product being taken first, we may write the exponent in matrix notation as

$$Z \sim \sum_{\mathbf{m}} \int d\mathbf{x} \exp \left\{ -\frac{1}{2\beta E_J} \mathbf{x}^T \Delta \mathbf{x} + i2\pi(\mathbf{m} - f) \cdot \mathbf{x} \right\}, \quad (2.36)$$

with $\mathbf{x}^T = (x_{1,1}, x_{1,2}, \dots)^T$ and $\mathbf{m}^T = (m_{1,1}, m_{1,2}, \dots)^T$. The matrix Δ is the discrete version of the Laplace operator in two dimensions,

$$\Delta(\mathbf{r}_i, \mathbf{r}_j) = 4\delta_{\mathbf{r}_i, \mathbf{r}_j} - \delta_{\mathbf{r}_i, \mathbf{r}_j \pm \hat{e}_x} - \delta_{\mathbf{r}_i, \mathbf{r}_j \pm \hat{e}_y}. \quad (2.37)$$

Note that we now describe the plaquette position by a vector \mathbf{r}_i instead of two indices. We decouple the continuous and discrete variables in Eq. (2.36), by completing the square in the exponent. Further shifting the integration variables $x_{i,j}$, we find

$$Z \sim \sum_{\{m\}} \int d\mathbf{x} \exp \left\{ -\frac{1}{2\beta E_J} \mathbf{x}^T \Delta \mathbf{x} - 2\pi^2 \beta J (\mathbf{m} - f) \Delta^{-1} (\mathbf{m} - f) \right\}, \quad (2.38)$$

with the inverse of Δ being the Greens function of the 2d lattice Coulomb potential G [30],

$$\Delta^{-1}(\mathbf{r}_i, \mathbf{r}_j) = G(\mathbf{r}_i - \mathbf{r}_j) = \frac{1}{N^2} \sum_{\mathbf{k} \neq 0} \frac{e^{i\mathbf{k} \cdot (\mathbf{r}_i - \mathbf{r}_j)}}{4 - 2 \cos(k_x a) - 2 \cos(k_y a)}. \quad (2.39)$$

This may be readily checked by computing the product of Δ and G . Notice that we exclude the summand $\mathbf{k} = 0$ due to divergence.

The continuous degrees of freedom in Eq. (2.38) are connected to spin waves, which will not play a role in the remainder of this thesis. Thus, we read off the effective Hamiltonian of the frustrated Josephson junction array as

$$H_v = 2\pi^2 E_J \sum_{\mathbf{r}_i, \mathbf{r}_j} (m(\mathbf{r}_i) - f) G(\mathbf{r}_i - \mathbf{r}_j) (m(\mathbf{r}_j) - f). \quad (2.40)$$

We hence switched from a description of the Josephson junction array via the continuous phase variables $\varphi_{i,j}$ connected to the superconducting islands to integer variables $m(\mathbf{r}_i)$ associated with the plaquettes of the array. These integers precisely describe the charges of vortices living on the plaquettes. This is evident due to the fact that the charges m in H_v are associated with an integer number of flux quanta. Furthermore, by approximating the Greens function in the limit of large distances $|\mathbf{r}_i - \mathbf{r}_j|$ and large N ,

$$G(\mathbf{r}_i - \mathbf{r}_j) \simeq -\frac{1}{2\pi} \ln \left(\frac{|\mathbf{r}_i - \mathbf{r}_j|}{a} \right) + \text{const.}, \quad (2.41)$$

we find the interaction energy E of two vortices with opposite charges $\pm m$ at a large distance R as,

$$E = 2\pi E_J m^2 \ln \left(\frac{R}{a} \right). \quad (2.42)$$

The interaction energy is thus twice the energy of adding a single vortex to the array as given in Eq. (2.15), which is clear given that the interaction involves two vortices. The vortex interaction Hamiltonian now also allows us to estimate the core energy E_c of a vortex with charge m as the interaction with itself,

$$E_c = 2\pi^2 E_J m^2 G(0) \approx 0.51 \pi^2 E_J m^2, \quad (2.43)$$

with $G(0)$ numerically estimated via Eq. (2.39).

The frustrated Josephson junction array is effectively described by a 2d Coulomb gas of vortices sitting on a discrete lattice of plaquettes, with the frustration f playing the role of a uniformly charged background. Due to the logarithmic interaction, the energy per plaquette diverges in the thermodynamic limit, unless the charges $m(\mathbf{r}_i)$ exactly cancel out the background. This yields the so-called charge neutrality condition,

$$\sum_{\mathbf{r}_i} (m(\mathbf{r}_i) - f) = 0. \quad (2.44)$$

Applying a constant magnetic field to a Josephson junction array thus induces a finite number of vortices in the array according to charge neutrality, even at zero temperature. These vortices order themselves to minimize their interaction, while respecting the underlying lattice of plaquettes. Depending on the frustration f , the vortices form different vortex lattices which break the rotational symmetry of the system. This will be studied in more detail in Chapter 3 of this thesis.

2.4 VORTEX MOTION DRIVEN BY EXTERNAL CURRENTS

An external current I applied to a Josephson junction adds a washboard potential to the Hamiltonian [20],

$$H = -E_J \cos(\varphi) - \frac{\hbar}{2e} I \varphi. \quad (2.45)$$

Adding the washboard potential tilts the energies of the junction, with the minimum of H being shifted to

$$\sin(\varphi) = \frac{I}{I_c}, \quad (2.46)$$

under the condition that $I < I_c$. Once the external current exceeds the critical current, there is no longer a static solution, and the phase difference φ will keep evolving in time. According to Eq. (2.5), this leads to a voltage drop across the junction and thus to a finite resistance. This transition is commonly modeled via the so-called RCSJ model [31, 32], which also incorporates the capacitive features of the junction,

$$I = I_c \sin(\varphi) + \frac{V}{R_N} + C \frac{dV}{dt} = I_c \sin(\varphi) + \frac{\hbar}{2eR_N} \frac{d\varphi}{dt} + \frac{\hbar C}{2e} \frac{d\varphi^2}{dt^2}, \quad (2.47)$$

with R_N being the normal state resistance of the junction and C its capacity. The junction is hereby modeled as a parallel circuit of a Josephson junction, a resistor and a capacitor.

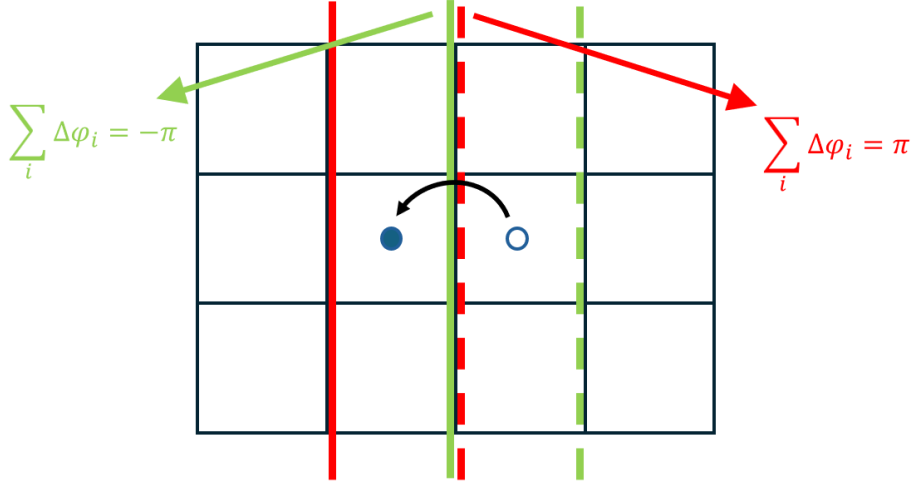


Figure 2.5: Sketch of the phase slip due to vortex hopping. Before crossing through the junction, the phases around the vortex (blue circle) wind by 2π . Consequently, the phase differences along its adjacent vertical lines (red and green dashed lines) have to sum up to $\pm\pi$, if the array is large. After crossing through the junction, the sum of the phase differences along the crossed vertical line (changing from dashed red to green) changes by 2π .

We may extend the washboard potential picture to an array of Josephson junctions in the following way,

$$H = H(I = 0) - \frac{\hbar}{2e} I \sum_{i=1}^N (\varphi_{i,N} - \varphi_{i,1}). \quad (2.48)$$

In this instance, the washboard potential induces a spatially uniform, vertical current per junction I through the array. If this current exceeds the critical currents of the individual junctions, the array will become resistive, analogously to a single junction.

2.4.1 VORTEX MOTION

We now want to consider a situation in which the Josephson junction array hosts a finite number of vortices, either due to thermal fluctuations or via a (weak) magnetic flux. Here, one finds numerically [33] that the array becomes resistive at an applied current of around 10% of the critical current of the individual junctions. This can be explained as follows: A vortex carries a magnetic flux Φ_0 . Correspondingly, it interacts with an applied current via a Lorentz force. Assuming that the array lies in the xy -plane, the force F_L that is exerted by the current on the vortex may be written as

$$F_L = \Phi_0(\mathbf{I} \times \hat{\mathbf{z}})/a, \quad (2.49)$$

with \mathbf{I} the (directed) external current per junction [25]. Moving the vortex core from the center of the plaquette causes an asymmetric current distribution in the array, increasing the energy of

the phase configuration. The vortex is thus sitting in a potential U and is subject to a restoring force $-\nabla U$. Once the Lorentz force exceeds the maximum of the restoring force, the vortex begins to move through the array, causing a phase slip of 2π across the array each time it passes through a junction, see Fig. 2.5. Thus, a voltage develops across the array and the system becomes resistive due to the vortex movement. The barrier energy E_B associated with a vortex moving through a junction has been estimated numerically as $E_B \approx 0.199E_J$ [34]. This explains the greatly reduced critical current of Josephson junction arrays hosting vortices. As the current depins the vortex, it is also called the depinning current.

In the present discussion, we assume that vortices are far away from each other so that interactions can be neglected. Once multiple vortices are involved, they form vortex lattices to reduce their interaction energy. This has a significant influence on the pinning potential U and thus also on the depinning current. In chapter 3, we will study the connection of the resistivity tensor to the density of vortices (or frustration) f in more detail.

3 RESISTIVITY TENSOR OF VORTEX-LATTICE STATES IN JOSEPHSON JUNCTION ARRAYS

The results of this chapter have been published in [1]. The author of this thesis conducted numerical simulations, generated the final numerical data shown in the figures as well as the figures in this thesis. The analytical calculations regarding the resistivity tensor have been performed in collaboration by all authors. The author contributed to the draft. The presented data is available at [35].

3.1 INTRODUCTION

Josephson junction arrays provide a plethora of classical and quantum phases as well as phase transitions [36, 37]. As discussed in Sec. 2.2.1, these systems may undergo a temperature induced BKT transition, changing the phase of the system from superconducting to resistive. As the charging energy increases, the phases of the superconducting islands become disordered due to quantum fluctuations. This induces a superconductor-insulator phase transition, even at zero temperature. Applying a perpendicular magnetic field to the array yields a particularly complex phase structure, even in the classical limit [38–41]. As shown in Sec. 2.3.2, a magnetic field introduces frustration which leads to a cascade of vortex-lattice ground states [42, 43]. While the static properties of these vortex lattices have been studied extensively via numerical methods [30, 42–50], not much is known about their dynamics [51, 52]. Also, their identification in experiments has been lagging.

In this chapter, we show that the resistivity tensor provides an effective tool to identify certain vortex lattices. Our observations can be summarized as follows: On the one hand, the formation of vortex lattices spontaneously breaks the lattice symmetry of the array, which generally leads to an anisotropic resistivity tensor. The anisotropy encodes structural information about the vortex lattices. On the other hand, we find that the temperature dependence of the resistivity tensor signals a phase transition from frozen vortex lattices to liquid-crystalline states [30, 53]. Earlier as well as recent measurements on frustrated Josephson junction arrays revealed a high sensitivity of both the longitudinal and transverse resistance as a function of the applied magnetic field [39, 54, 55]. Importantly, complete information on the vortex-lattice states is only revealed through measurement of the full resistivity tensor, which has not been done yet in experiments.

The motivation for this study are the recent advances in the fabrication of Josephson junction arrays based on semiconductor-superconductor hybrids [56]. These arrays can be constructed in

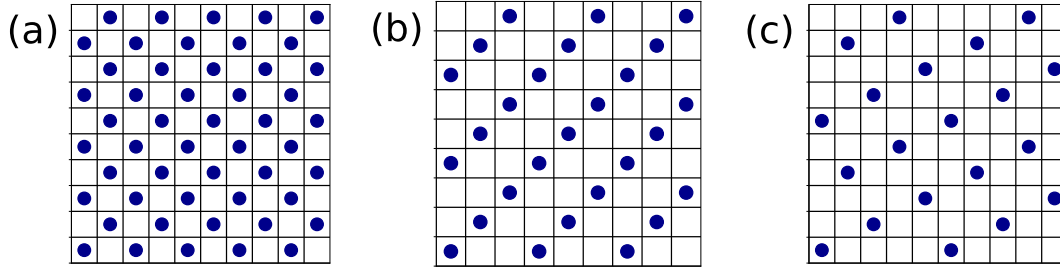


Figure 3.1: Ground-state vortex lattices at different values of frustration f . (a) $f = 1/2$, (b) $f = 1/3$, and (c) $f = 1/5$.

various lattice geometries and provide a remarkable tunability of the properties of the Josephson junctions [57–59]. Until now, work on these has focused on the BKT transition [57, 58] as well as vortex dynamics [59]. These devices should allow for measurements of the complete resistivity tensor, advancing the experimental identification of vortex lattices.

3.2 THE MODEL

In the previous chapter, we introduced the description of a Josephson junction array via a classical XY model. Due to gauge invariance, a perpendicular magnetic field introduces frustration to the phases $\varphi_{i,j}$ of the superconducting islands,

$$H = -E_J \sum_{i,j=1}^N \cos(\varphi_{i+1,j} - \varphi_{i,j} - A_{i,j}^h) - E_J \sum_{i,j=1}^N \cos(\varphi_{i,j+1} - \varphi_{i,j} - A_{i,j}^v). \quad (3.1)$$

The phase shifts $A_{i,j}^{h;v}$ are integrals over the vector potential, defined in Eq. (2.18). We neglect the charging energies of the islands, so that the calculation of the ground state becomes a classical statistical mechanics problem. We consider a spatially uniform magnetic flux configuration, so that the array has homogeneous frustration $f = \Phi/\Phi_0$, with Φ being the magnetic flux in each plaquette.

In Sec. 2.3.2, we found that the magnetic field introduces vortices to the array. These vortices order themselves into configurations that minimize their interaction energy. The resulting vortex lattice is strongly dependent on the applied field, which is due to the competition between the vortices' tendency to order into a triangular lattice (Wigner crystal [60]) and the pinning potential induced by the underlying square lattice. We show a few examples of vortex lattices at simple rational frustrations in Fig. 3.1. At $f = 1/2$, the vortices form a checkerboard pattern, which breaks the discrete translation symmetry of the underlying array, but preserves its C_4 symmetry [Fig. 3.1(a)]. For $f = 1/3$, the vortices form a lattice of diagonal stripes, which only preserves

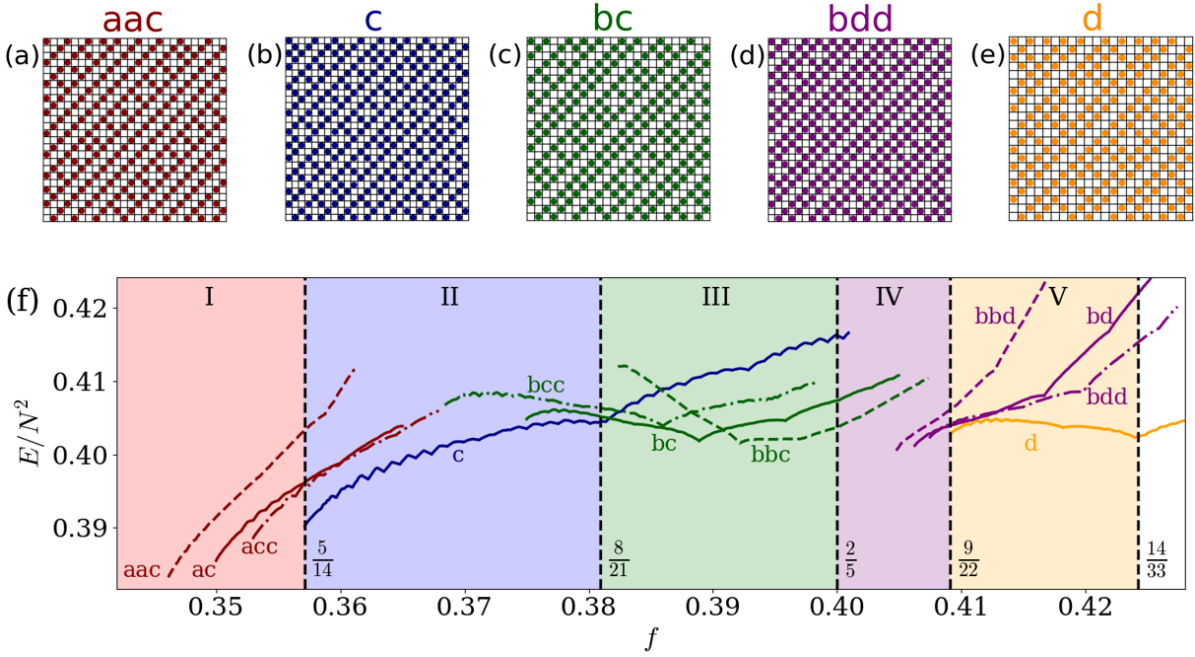


Figure 3.2: (a-e) Vortex-lattice configurations for frustration values $1/3 < f < 1/2$. In this range, vortex lattices consist of combinations of elementary units. a: two empty diagonals enclosing a filled diagonal. b: two filled diagonal enclosing an empty diagonal, with additional empty diagonals on either side. c: channel structure with two a-blocks enclosing a partially filled diagonal. d: thick channel with two b-blocks enclosing a partially filled diagonal. Additional vortices may be accommodated in the partially filled diagonals of the channel structures, increasing the frustration f by $1/N^2$. (f) Energy E per lattice site of different vortex-lattice configurations. Energies are computed by gradually adding vortices to the partially filled diagonals. There are five color-coded regions I-V, separated by dashed lines at particular fractional values of f . The colors indicate the structure of the ground state, see Fig. 3.2(a-e).

C_2 symmetry [Fig. 3.1(b)]. For lower frustrations such as $f = 1/5$, the symmetry axes of the vortex lattice do not align with the diagonals of the square array [Fig. 3.1(c)].

3.3 STRIPED VORTEX-LATTICE STATES

We now consider the vortex-lattice states emerging in the frustration range of $1/3 < f < 1/2$. Here, vortices form striped vortex lattices, which are constructed via a sequence of completely filled, partially filled and empty diagonals as illustrated in Fig. 3.2 (a)-(e) [30, 50]. We will focus on these lattices as they provide a way to analytically access the resistivity tensor of the array via a simple transport mechanism. This will be discussed in the following section 3.4.

The striped vortex lattices shown in Fig. 3.2 are built from elementary units. Two of those units (a and b) consist solely of completely filled and empty diagonals, which correspond to the $f = 1/3$ and $f = 2/5$ vortex lattices. Additionally, there are channel units (c and d) which also contain partially filled diagonals. We characterize the vortex lattices not only by the frustration f ,

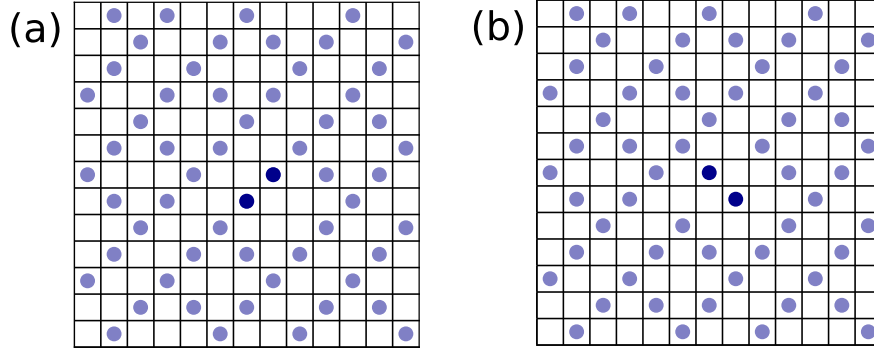


Figure 3.3: Unstable channels for fillings $\nu < 1/2$ of the partially filled diagonals. (a) Metastable configuration with two adjacent vacancies along a partially filled diagonal (light domain wall). Light domain walls necessarily appear for $\nu < 1/2$. (b) Vortex configuration with lower energy, where two vortices (dark blue) have moved out of a full diagonal.

but also by the fraction of partially filled diagonals p as well as their filling ν . For example, in the frustration range of $5/14 < f < 8/21$ [blue region in Fig. 3.2(f)], the fraction of the partially filled diagonals is $p = 1/7$ and $f - p\nu = 2/7$ is the fraction of completely filled diagonals.

In Fig. 3.2(f), we compare the energies of different vortex-lattice structures built from elementary units. The energies have been computed numerically using the vortex representation of the frustrated XY model [61, 62], which was derived in Sec. 2.3.2. Starting from a filling of $\nu = 1/2$, we can increase frustration by adding vortices one at a time to the partially filled diagonals. Given a number of building blocks, we use a Metropolis algorithm in order to minimize the energy of the vortex lattice (see A.1 for a detailed description). We chose large and commensurate system sizes N ($N \approx 100$) for each lattice structure, so that increasing the system size affects the results only weakly. The results of this procedure agree with the findings of Ref. [50], but further show an additional regime originating from a previously unnoticed phase transition at $f = 9/22$.

3.3.1 DIFFERENT REGIONS OF GROUND-STATE STRUCTURES

In the red region of Fig. 3.2(f), the type a building blocks have a natural frustration of $f = 1/3$, while the c channel structures are stable for frustration values beyond $f = 5/14$, which corresponds to half-filled channels. Therefore, an alternation of a and c structures is stable beyond minimal frustrations, growing with the fraction of c building blocks. Each of the displayed structures grows quickly with increasing f , as both the diagonal a structures become less favorable (natural building blocks at $f = 1/3$) and the filling ν of the c structures increases. We point out that Fig. 3.2(a) only features short-period structures. Structures with longer periods are probably ground states in parts of the red region, but are not included in the figure.

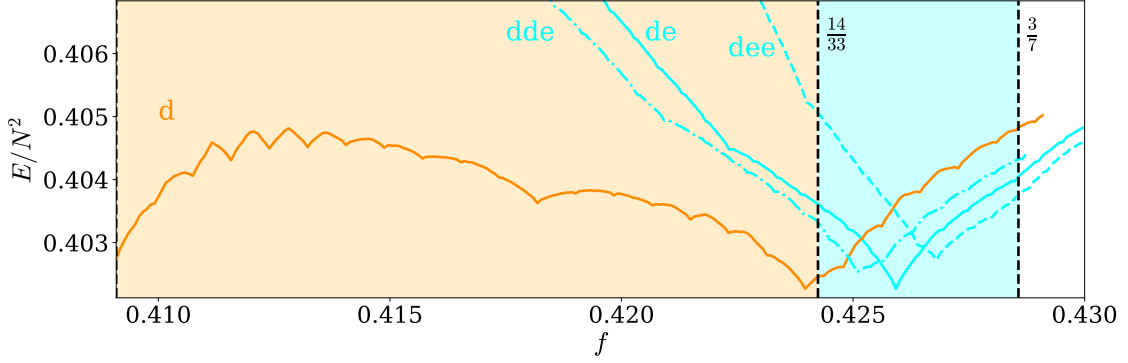


Figure 3.4: Energy per lattice site for different vortex-lattice configurations as a function of f . This figure adds to Fig. 3.2(f) beyond $f = 14/33$, up to $f = 3/7$. Here, the lowest energy striped vortex lattices are combinations of thick d channels and e building blocks (three filled diagonals separated and enclosed by four empty diagonals).

It is possible that in some restricted regions of frustration, the true ground state is not of diagonal, striped structure, but has a more complicated 2d form. For example, partially filled diagonals with filling $\nu < 1/2$ destabilize the walls of the channels, as shown in Fig. 3.3. Thus, it is not unreasonable to assume that before the onset of one of the striped structures, the stripe-like pattern may be destabilized into a more complicated 2d configuration.

The blue region ($5/14 < f < 8/21$) only features c structures as ground states, with the partially filled diagonals filling up from $\nu = 1/2$ at $f = 5/14$, to $\nu = 2/3$ at $f = 8/21$. The energy of the ground state should thus increase with rising frustration f , which is indeed observed. For frustrations beyond $f = 8/21$, the partially filled diagonals of the c structure necessarily host three consecutive occupied sites, leading to a significant cusp in the energy as a function of frustration.

In the green region, $8/21 < f < 2/5$, the ground states consist of combinations of c structures as well as b structures, which are the natural building blocks at $f = 2/5$. Therefore, one expects that the b structures become energetically more favorable with increasing frustration, while the c structures increase the energy due to rising fillings. This is consistent with the relatively weaker f -dependence of the energy of ground-state configurations in the green region, observed in Fig. 3.2(f). We further point out that the bc structure may be competitive with the pure c structure near $f = 8/21$, as the channel filling of the bc structure is much lower than that of the c structure. Likewise, the bcc structure may have a higher energy than the bc structure, as the channel filling in the bcc structure is greater. However, this trend has to reverse eventually, since structures of the form bc...c must be close to the energy of the pure c configuration.

In the purple region, $2/5 < f < 9/22$, the ground states are expected to be combinations of b and d building blocks, with the latter corresponding to a 'thick' channel, see Fig. 3.2(d). At the transition point between the green and purple regions, the ground state should consist of

mainly b building blocks with rare occurrences of d channels. This is masked however due to the short periods of the considered configurations.

In the orange region, where $9/22 < f < 14/33$, the ground states are built exclusively from thick d channels, with fillings varying from $\nu = 1/2$ to $\nu = 2/3$. In comparison to the c channels, we here find that the energy is more weakly dependent on f . We point out, that this region has not been identified in previous works such as Ref. [50].

Lastly, we want to note that in the white region beyond $f = 14/33$, it is conceivable that the ground states consist of combinations $f = 3/7$ (or e) building blocks and thick d channels. We show corresponding energies in Fig. 3.4. At $f = 4/9$, the stripe structure is no longer stable and the ground state is instead formed by a vacancy crystal on top of the $f = 1/2$ state. Therefore, vacancy crystals eventually preclude additional regimes of striped structures.

3.4 RESISTIVITY TENSOR

The resistivity of a square Josephson junction array is isotropic as long as the C_4 symmetry of the lattice is preserved in the ground state. This is the case for frustrations $f = 0$ and $f = \frac{1}{2}$. For general frustrations, the formation of vortex lattices breaks this symmetry, which is indicated by an anisotropic resistivity tensor ρ . The tensor may be split into symmetric and antisymmetric parts as follows,

$$\rho = \begin{pmatrix} \rho_{xx} & \rho_{xy}^s \\ \rho_{xy}^s & \rho_{yy} \end{pmatrix} + \begin{pmatrix} 0 & \rho_H \\ -\rho_H & 0 \end{pmatrix}. \quad (3.2)$$

The symmetric part of ρ describes the dissipative resistivity and may be diagonalized with eigenvalues ρ_1 and ρ_2 . The antisymmetric part on the other hand is invariant under rotations of the coordinate system and encapsulates the Hall resistivity ρ_H of the array.

The two contributions to the transverse resistance ρ_{xy}^s and ρ_H may be separated by their behavior under reversal of the perpendicular magnetic field B . This is a consequence of the Onsager relation, $\rho_{xy}(B) = \rho_{yx}(-B)$. While the Hall resistivity ρ_H is odd under magnetic field reversal, $\rho_H(B) = -\rho_H(-B)$, the transverse resistivity ρ_{xy}^s is even,

$$\rho_{xy}^s(B) = \rho_{xy}^s(-B). \quad (3.3)$$

This is in agreement with the eigenvalues ρ_1 and ρ_2 of the tensor being even functions of the magnetic field.

From this discussion, we conclude that measuring the full resistivity tensor will reveal important information on the vortex lattices. The eigenvalues of the tensor contain information about the density of mobile vortices as well as their mobility. The principal axis along which the tensor is diagonal yields information about the orientation of the lattice. We note in particular that the measurement of a transverse resistance that is symmetric under the reversal of the magnetic field is a direct consequence of ρ being anisotropic and therefore of spontaneous breaking of the C_4

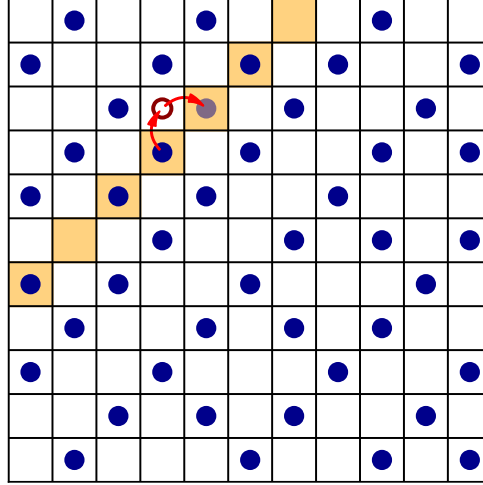


Figure 3.5: Illustration of the hopping process of a heavy domain wall in a c channel structure (blue region in Fig. 3.2). A partially filled diagonal (highlighted in orange) contains a heavy domain wall. At a neighboring saddle-point configuration, a vortex of the heavy domain wall hops into one of the adjacent empty diagonals (red, empty circle). From there, the system reaches a new minimum in which the vortex (gray circle) hops back into the partially filled diagonal, with the heavy domain wall now moved by two sites. The hopping process is indicated by red arrows. No adjacent minima were found, in which a vortex hops into an empty diagonal.

symmetry by the vortex lattice. Remarkably, a transverse resistance that is even in the magnetic field has already been observed in experiments [39, 55].

3.4.1 VORTEX TRANSPORT ALONG DIAGONALS

We now want to show how these considerations may be applied specifically to the striped vortex-lattice states emerging in the frustration range of $1/3 < f < 1/2$. In earlier studies (see e.g. Ref. [30]), it was shown that vortices forming fully occupied diagonals remain stable against low temperatures, while the vortices in the partially filled diagonal become mobile. From this, we deduce that the process which determines the resistivity tensor is vortex motion along the partially filled diagonals, as illustrated in Fig. 3.5.

The partially filled diagonals of a stable vortex-lattice state are at least half filled, $\nu \geq 1/2$. In the limit of low temperature and for $\nu = 1/2$, the vortices inside the partially filled diagonals organize into an alternation of occupied and empty sites along the diagonal. For $\nu > 1/2$, vortex motion becomes possible as there is a finite density of occupied nearest neighbor sites (heavy domain walls). We identify the elementary excitation process numerically as follows: First, we compute the full phase configuration of a low-energy striped vortex-lattice state by using a modified version of a recently proposed annealing algorithm [28] (see A.2 for details). From there, we systematically search for adjacent saddle points via the climbing-string method [63] (see

A.3). Afterwards, we look for new minima that connect to the saddle point, in which the heavy domain wall has moved by two sites. As shown in Fig. 3.5, we find that the elementary excitation process is that the domain wall performs a direct jump along the diagonal. In the saddle-point configuration, one of the two vortices forming the domain wall is located in the neighboring empty diagonal. We have found no minimal energy configuration in which the vortex stays in the empty diagonal. We may estimate the activation barrier of the hopping process via calculating the energy of the saddle-point configuration. For $\nu \simeq 1/2$, we find $E_B \simeq 0.83E_J$. The barrier increases slightly with larger filling ν , e.g., we find an energy barrier of $E_B \simeq 1.01E_J$ for $f = 13/35$ ($\nu = 3/5$). The thermally activated rate at which a heavy domain wall hops along the diagonal is given by $\Gamma \sim \exp\{-E_B/k_B T\}$.

At low temperatures, vortex motion is limited to the partially filled diagonals, leading to a highly anisotropic resistivity tensor. Its principal axes are aligned along and perpendicular to the diagonal vortex lattice. Applying a current perpendicular to the diagonal vortex lattice induces vortex hopping along the partially filled diagonals. Due to the accompanying phase slips, this motion produces a voltage drop along the current direction, yielding a nonzero resistivity eigenvalue ρ_1 . On the other hand, a current along the diagonals will not yield a voltage drop, as the mobile vortices are confined to the partially filled diagonals. Consequently, the eigenvalue ρ_2 of the resistivity tensor for currents along the diagonal of the lattice vanishes, resulting in perfect conductivity in this direction.

3.4.2 CALCULATION OF THE RESISTIVITY

We calculate the eigenvalue ρ_1 of the resistivity tensor by considering an applied uniform current density j perpendicular to the diagonals of the vortex lattice. The current density applies a Lorentz force $F_L = \Phi_0 j$ on the vortices which acts along the partially filled diagonals, as described in Eq. (2.49). This creates a potential energy drop ΔU for vortices on neighboring sites in both the horizontal and vertical direction [64],

$$\Delta U = \Phi_0 a \frac{j}{\sqrt{2}}, \quad (3.4)$$

with $j/\sqrt{2}$ being the current density in horizontal and vertical direction and a the lattice spacing of the Josephson junction array. Equation (3.4) may also be understood on the basis of a single junction with an added washboard potential, $U(\varphi) = -E_J \cos(\varphi) + \frac{\Phi_0}{2\pi} I \varphi$ [see also Eq. (2.45)]. A vortex jumping from one plaquette to a neighboring one induces a phase slip of 2π in the intermediate junction, which changes the potential by $\Phi_0 I$.

Each vortex beyond a filling of $\nu = 1/2$ in the partially filled diagonals creates two heavy domain walls. The areal density of the domain walls is thus given by $2p(\nu - \frac{1}{2})\frac{1}{a^2}$ with p being the fraction of partially filled diagonals. We assume in the following that ν is close to $1/2$, so that the possibility of two adjacent domain walls can be neglected. Due to the potential drop of

$2\Delta U$ ¹ between initial and final state of a vortex hop along the partially filled diagonal, we find an effective hopping rate for a vortex in a heavy domain wall of

$$e^{-(E_B-2\Delta U)/k_B T} - e^{-E_B/k_B T} \approx \Gamma \frac{2\Delta U}{k_B T} \quad (3.5)$$

in linear response. As a consequence, we estimate an areal vortex current density of

$$j_v = 2p \left(\nu - \frac{1}{2} \right) \frac{\sqrt{2}}{a} \Gamma \frac{2\Delta U}{k_B T} \quad (3.6)$$

along the diagonals of the vortex lattice. The vortex current density may be related to the electric field \mathcal{E} in perpendicular direction via Eq. (2.5), which yields

$$\mathcal{E} = \frac{h}{2e} j_v. \quad (3.7)$$

Since $\mathcal{E} = \rho \mathbf{j}$, we find the eigenvalue ρ_1 of the resistivity tensor ρ through a combination of Eqs. (3.4), (3.6) and (3.7),

$$\rho_1 = 4p \left(\nu - \frac{1}{2} \right) \left(\frac{h}{2e} \right)^2 \frac{\Gamma}{k_B T}, \quad (3.8)$$

under the assumption that the number of heavy domain walls is small.

We note that the building block structure of the vortex-lattice ground states remains stable over a wide range of magnetic fields in the regions II (blue) and V (yellow) of Fig. 3.2(f). In comparison, the vortex-lattice structure (and therefore p) depends sensitively on the magnetic field in the regions I (red), III (green) and IV (purple). From Eq. (3.8), we see that this directly translates to a discontinuous resistivity as a function of the applied field in the latter regions.

3.4.3 RESISTIVITY OF VORTEX-LATTICE LIQUID CRYSTALS

For small p and for sufficiently short ranged interactions between vortices (screening), the coupling between different partially filled diagonals is weak. Without coupling, the partially filled diagonals are effectively 1D and melt at any nonzero temperature via the Landau-Peierls argument. As a consequence, weak coupling leads to a melting temperature much smaller than the melting temperature of the entire 2D vortex lattice. In the temperature regime between the two melting temperatures, the vortex lattice is comparable to a smectic liquid crystal.

We may assume that the vortex occupation along the partially filled diagonal become uncorrelated, given that the temperature is far from the melting point. In that case, we may characterize

¹The factor of 2 arises, as the vortex hops twice.

3 Resistivity tensor of vortex-lattice states in Josephson junction arrays

the vortex motion along the partially filled diagonal via a diffusion constant $D = 2a^2/\tau$, with $\frac{1}{\tau}$ being a constant hopping rate. The vortex current j_v then becomes

$$j_v = p\nu(1 - \nu) \frac{1}{a^2} \frac{\sqrt{2}a}{\tau} \frac{2\Delta U}{k_B T}, \quad (3.9)$$

which gives

$$\rho_1 = 2p\nu(1 - \nu) \left(\frac{h}{2e} \right)^2 \frac{1}{k_B T \tau}, \quad (3.10)$$

for the eigenvalue of the resistivity tensor. Note that unlike for ordered partially filled diagonals, the hopping rate here is no longer thermally activated. Thus, the melting transition is accompanied by a significant increase in the resistivity.

Next, we consider the resistivity tensor for currents that are applied either in horizontal or vertical direction. Rotating the tensor we found for diagonally applied currents yields

$$\rho = \begin{pmatrix} \rho_1/2 & \pm\rho_1/2 \\ \pm\rho_1/2 & \rho_1/2 \end{pmatrix}. \quad (3.11)$$

The sign of the transverse resistance is determined by the orientation of the diagonals of the vortex lattice. Also, we neglected ρ_H in the here presented rate equation theory of vortex dynamics. The diagonal structure of the vortex lattice leads to equal values of the diagonal resistivities, $\rho_{xx} = \rho_{yy} = \rho_1/2$. The formation of the vortex lattice is indicated by the nonzero transverse resistance. Due to the constrained vortex motion in the partially filled diagonals, a current along, e.g., the y -direction results in equal voltage drops in both the x - and y -directions. Therefore, the longitudinal and transverse resistivities are equal in magnitude, which is directly related to the diagonal orientation of the vortex lattice.

3.5 CONCLUSION

In this chapter, we showed that a measurement of the entire resistivity tensor reveals both structural as well as dynamical information about the various symmetry-breaking vortex lattices that are induced by external magnetic fields. It also signals the formation of liquid-crystalline vortex states, which have the interesting property of being superconducting in one direction and resistive in the other. The general approach we used here may also be applied to other (nematic) electronic states that break the underlying rotational symmetry, see Ref. [65] for a recent discussion.

Here we solely considered vortex lattices of diagonal structure, as these provide a particularly transparent transport mechanism. The general considerations about the anisotropy of the resistivity tensor should however carry over to other symmetry-breaking vortex lattices, such as,

e.g., the $f = 1/5$ state (see Fig. 3.1(c)). Measurements of the full resistivity tensor might reveal information about the underlying vortex dynamics of these differently oriented vortex-lattice states.

In our discussion, we always assumed that the capacitive effects of the Josephson junction array are negligible. The explicit inclusion of these contributions is an interesting direction for future work, as the introduction of quantum fluctuations may, e.g., lead to a finite Hall resistivity. However, we expect our previous results to persist qualitatively.

We further note that the conducted simulations were performed on uniform lattices with periodic boundary conditions. In experiments, the vortex lattices are subject to boundary effects as well as disorder in the couplings, which may lead to the formation of domains with different orientations. Consequently, the magnitude of the off-diagonal elements of the resistivity tensor ρ_{xy} would be reduced in comparison to ρ_{xx} and ρ_{yy} . This reduction in magnitude could be used as a measure of the degree of domain formation of the vortex lattice.

4 SUPERCONDUCTING DIODE EFFECT IN φ_0 -JOSEPHSON JUNCTION ARRAYS

The results of this chapter are based on Ref. [2]. This project was a collaboration with the experimental group of Christoph Strunk (Regensburg), including his PhD student Simon Reinhardt [66]. The author of this thesis was only involved in developing the theoretical description of the experimental data. He conducted numerical calculations and produced the final data displayed in Fig. 3(e,f). The author computed the ground state of the proposed model, in collaboration with S. Reinhardt. He performed the calculation of the Langevin dynamics of the vortex motion as well as the depinning currents of the relaxed vortex configuration. The author contributed to the draft. The presented data is available at [35].

4.1 INTRODUCTION

Since their development in the early 20th century, diodes have played a fundamental role in virtually all electronic devices. These electronic building blocks are characterized by a current-voltage relation asymmetric under voltage reversal. Ideally, a diode is conductive in one direction of voltage bias, while being insulating in the other one. This behavior is crucial in many applications, for example in the conversion from alternating current (AC) to direct current (DC).

In recent years, the development of superconducting devices has become increasingly important due to their relevance in quantum computing [24]. As diodes are fundamental building blocks of classic electronic devices, it is natural to assume that superconducting diodes will play a similarly important role in superconducting electronics. These diodes pass super currents in one current direction, but become resistive in the other. Single Josephson junctions exhibiting such nonreciprocal critical currents have been studied extensively in recent experiments [67–75]. The underlying mechanism is an asymmetric current-phase relation as a result of broken time-reversal and spatial inversion symmetry of the material. Additionally to the nonreciprocal critical currents, such a junction may also show an anomalous Josephson effect [76, 77], i.e. a supercurrent flowing at zero phase difference between the superconductors. Since the corresponding current-phase relation is of the form $I(\varphi) \sim \sin(\varphi - \varphi_0)$, these junctions are referred to as φ_0 -junctions. Although the necessary symmetries are broken in φ_0 -junctions, they do not necessarily facilitate a diode effect.

As a natural extension of single φ_0 -junctions and motivated by a recent experiment [2], in this chapter we study a 2d array of φ_0 -Josephson junctions. In the experiment, the group of Christoph

Strunk (Regensburg university) performed current measurements on a Josephson junction array, constructed from an epitaxially grown superconductor-semiconductor heterostructure [56]. Currents were measured while applying an in-plane magnetic field to the system at different strengths and angles. The group measured different critical currents in opposing directions, the system thus showed a superconducting diode effect. The measured critical currents were orders of magnitude smaller than the critical currents of the individual junctions, which is an indication of the depinning of vortices. The effect was most pronounced for in-plane fields perpendicular to the applied currents. Our interpretation is that the Josephson junction array becomes an array of φ_0 -junctions due to the applied in-plane field (breaking time-reversal symmetry) and the presence of strong spin-orbit coupling (breaking inversion symmetry) in the material.

As discussed in the previous chapters, Josephson junction arrays host vortices, which are subject to a pinning potential. We will see in this chapter that φ_0 -junctions skew the vortex pinning potential, leading to asymmetric depinning currents. A Josephson junction array consisting of φ_0 -junctions thus exhibits a diode effect due to vortex depinning.

4.2 ANDREEV BOUND-STATES

In chapter 2, we motivated the Josephson effect via a heuristic picture, in which the current across the junction was purely due to quantum tunneling. This is a limiting case however (tunneling limit). In general, the current-phase relation of a Josephson junction can be more complicated. To showcase this, we consider a situation in which two superconducting regions (S) forming a junction are separated by a normal (N) metal region of length L (SNS junction), see Fig. 4.1. The charge carriers in the normal region allow for coherent transport between the superconductors via Andreev reflections [78].

We describe the setup in Fig. 4.1 via the Bogoliubov-de Gennes Hamiltonian

$$H = \begin{pmatrix} h(x) & \Delta(x) \\ \Delta^*(x) & -h(x) \end{pmatrix}, \quad (4.1)$$

with kinetic energy

$$h(x) = -\hbar^2 \partial_x^2 / 2m - E_F \quad (E_F: \text{Fermi energy}) \quad (4.2)$$

and

$$\Delta(x) = |\Delta| [\theta(x - L/2) e^{i\varphi/2} + \theta(-x - L/2) e^{-i\varphi/2}] \quad (4.3)$$

being the gap function in the superconductors. The phases in Eq. (4.3) are chosen such that the phase difference across the junction is φ .

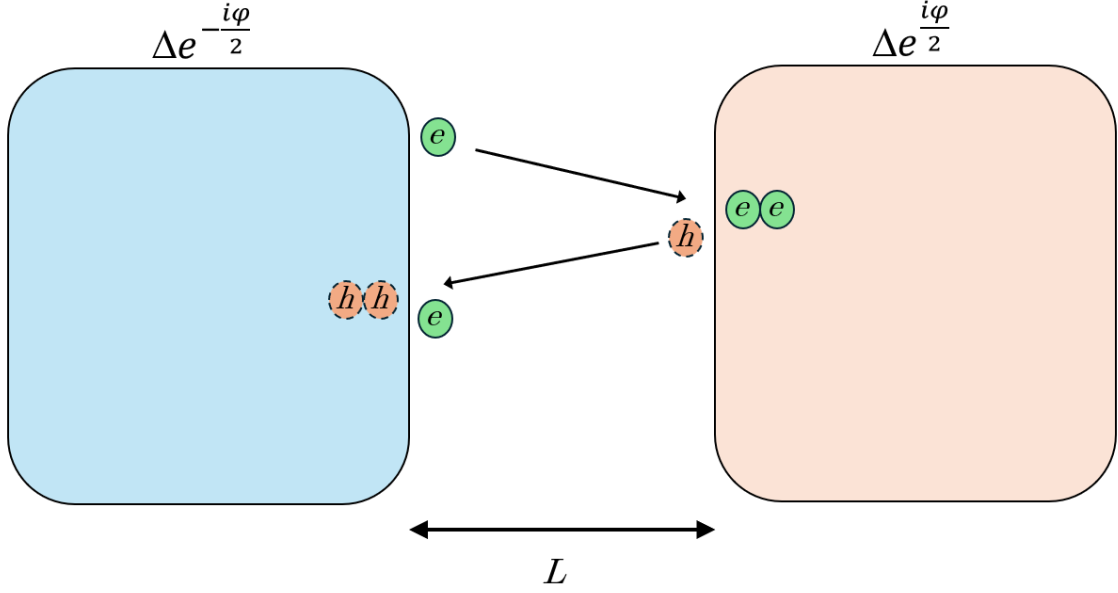


Figure 4.1: Sketch of the Andreev reflection process. An electron (green circle) moves through the normal region of length L . Upon hitting the right SN-interface, it creates a Cooper pair in the right superconductor, while being reflected as a hole (red circle). The hole then travels back to the left superconductor, where it is reflected as an electron, while destroying a Cooper pair. Matching the phases of initial and final electron yields a condition for the Andreev bound-state energy.

In the normal region, $-L/2 < x < L/2$, the spatial component $\psi(x)$ of the eigenstates of H are plane waves, $\psi(x) \sim e^{\pm ikx}$. Thus, the energy of the eigenstates is

$$\pm E = \frac{\hbar^2 k^2}{2m} - E_F, \quad (4.4)$$

with the sign of E indicating particle or hole. From this we obtain

$$k = \frac{1}{\hbar} \sqrt{2m(E_F \pm E)} = k_F \sqrt{1 \pm \frac{E}{E_F}}, \quad (4.5)$$

for the momenta, with $k_F = \sqrt{2mE_F}/\hbar$ being the Fermi momentum.

In the superconducting regions, we first calculate the above-gap eigenstates ($E > |\Delta|$). Here, one finds particle- and hole-like solutions of the form

$$\psi_e(x) \sim \begin{pmatrix} e^{\frac{1}{2} \operatorname{arccosh}(\frac{E}{\Delta})} e^{\pm i\varphi/4} \\ e^{-\frac{1}{2} \operatorname{arccosh}(\frac{E}{\Delta})} e^{\mp i\varphi/4} \end{pmatrix} e^{\pm iq_e x}, \quad \psi_h(x) \sim \begin{pmatrix} e^{-\frac{1}{2} \operatorname{arccosh}(\frac{E}{\Delta})} e^{\pm i\varphi/4} \\ e^{\frac{1}{2} \operatorname{arccosh}(\frac{E}{\Delta})} e^{\mp i\varphi/4} \end{pmatrix} e^{\pm iq_h x}, \quad (4.6)$$

4 Superconducting diode effect in φ_0 -Josephson junction arrays

with

$$q_{e/h} = k_F \sqrt{1 \pm \sqrt{\frac{E^2 - |\Delta|^2}{E_F^2}}} \quad (4.7)$$

being the momentum in the superconducting regions. For a detailed calculation of these eigenstates, see for example Ref. [79]. The sign of the phase factors $e^{\pm i\varphi/4}$ is connected to the left and right superconductors (upper sign: right, lower sign: left). From Eq. (4.6), we may derive the in-gap eigenstates ($E < |\Delta|$) via analytical continuation. In the commonly used Andreev limit ($E, |\Delta| \ll E_F$) [79], we find for the (normalizable) in-gap states,

$$\psi_e(x) \sim \begin{pmatrix} e^{\frac{i}{2}\arccos\left(\frac{E}{|\Delta|}\right)} e^{\pm i\varphi/4} \\ e^{-\frac{i}{2}\arccos\left(\frac{E}{|\Delta|}\right)} e^{\mp i\varphi/4} \end{pmatrix} e^{\pm(ik_F - \kappa)x}, \quad \psi_h(x) \sim \begin{pmatrix} e^{-\frac{i}{2}\arccos\left(\frac{E}{|\Delta|}\right)} e^{\pm i\varphi/4} \\ e^{\frac{i}{2}\arccos\left(\frac{E}{|\Delta|}\right)} e^{\mp i\varphi/4} \end{pmatrix} e^{\pm(ik_F + \kappa)x}. \quad (4.8)$$

Here, the small parameter

$$\kappa = \frac{k_F}{2E_F} \sqrt{|\Delta|^2 - E^2} \quad (4.9)$$

determines which solution is normalizable in each superconducting region.

From the solutions in each individual region, we may calculate the bound-state energies of the Hamiltonian in Eq. (4.1) via a scattering approach. For simplicity, we will assume perfect transparency of the normal region. We consider an electron with energy $E < |\Delta|$, starting from the left SN-interface and moving to the right. After it reaches the right SN-interface, it has gained a phase of $k_e L$, with $k_e = k_F \sqrt{1 + E/E_F}$. Then, the electron is reflected as a left-moving hole at the interface, while creating a Cooper pair in the superconductor. By matching the phases of the reflected hole with the normalizable in-gap state [Eq. (4.8)] in the superconductor, we find that the hole gains an additional phase of $-\arccos(E/|\Delta|) - \varphi/2$. The hole then travels to the left. At the right interface, it has gained a phase of $-k_h L$ (with $k_h = k_F \sqrt{1 - E/E_F}$) and is reflected as an electron, while destroying a Cooper pair in the superconductor. We again match the phases of the outgoing electron with the in-gap state in the superconductor, yielding a phase gain of $-2\arccos(E/|\Delta|) - \varphi$. For a bound state, the overall phase gain of the electron has to be an integer multiple of 2π after returning to its initial position. Using the Andreev limit, we find for the Andreev bound state energies,

$$-2\arccos\left(\frac{E}{|\Delta|}\right) - \varphi + \frac{k_F L}{E_F} E = 2n\pi. \quad (4.10)$$

We can solve for E in the short-junction limit, $L \ll E_F/(k_F E)$, to obtain

$$E = \pm |\Delta| \cos\left(\frac{\varphi}{2}\right). \quad (4.11)$$

This is the result in the limit of a perfectly transparent normal region. However, in order to describe real materials, one also has to take into account backscattering processes. This can be done by, e.g., using the scattering matrix formalism of Beenakker described in Ref. [80]. For finite transparency, one finds for the Andreev bound-state energies,

$$E = \pm |\Delta| \sqrt{1 - \mathcal{T} \sin^2\left(\frac{\varphi}{2}\right)}, \quad (4.12)$$

with \mathcal{T} being the transparency of the normal region. For $\mathcal{T} = 1$, we retrieve the result in Eq. (4.11).

In the limit of zero temperature, the system is in the ground state and negative-energy Andreev bound-states are occupied. The supercurrent flowing between the superconductors is then given by the a derivative of the ground state energy with respect to the phase difference,

$$I(\varphi) = \frac{2e}{\hbar} \frac{\partial E}{\partial \varphi} = \frac{e|\Delta|\mathcal{T}}{2\hbar} \frac{\sin(\varphi)}{\sqrt{1 - \mathcal{T} \sin^2\left(\frac{\varphi}{2}\right)}} \approx I_c \sin(\varphi). \quad (4.13)$$

In the last step, we recovered the usual current-phase relation of a Josephson junction by taking the tunneling limit ($\mathcal{T} \ll 1$).

4.3 ANOMALOUS JOSEPHSON EFFECT

The current-phase relation in Eq. (4.13) satisfies $I(\varphi) = -I(-\varphi)$ as time-reversal symmetry is preserved by the system. Also, the system is symmetric under spatial inversion, provided that $\varphi = 0$, which accordingly yields $I(0) = 0$. These relations do not necessarily hold, when the corresponding symmetries are broken. This would allow for a nonzero current flowing at zero phase difference, an effect known as anomalous Josephson effect [76, 81, 82]. To show this explicitly, we consider the following BdG Hamiltonian,

$$H = \begin{pmatrix} h_s(x) & \Delta(x) \\ \Delta^*(x) & -h_s(x) \end{pmatrix}. \quad (4.14)$$

In contrast to the Hamiltonian in Eq. (4.1), the components of H now involve additional spin structure. The diagonal part of H written in momentum basis is given by

$$h_s(k) = \frac{\hbar^2(k_x^2 + k_y^2)}{2m} - E_F + \alpha \hbar(k_x \sigma_y - k_y \sigma_x) + \mathbf{B} \cdot \boldsymbol{\sigma}. \quad (4.15)$$

Here, α is the strength of the inversion symmetry-breaking (Rashba) spin-orbit coupling and \mathbf{B} the Zeeman field breaking time-reversal symmetry. We again want to calculate the Andreev bound-states of H in order to obtain the current-phase relation of the junction. For simplicity,

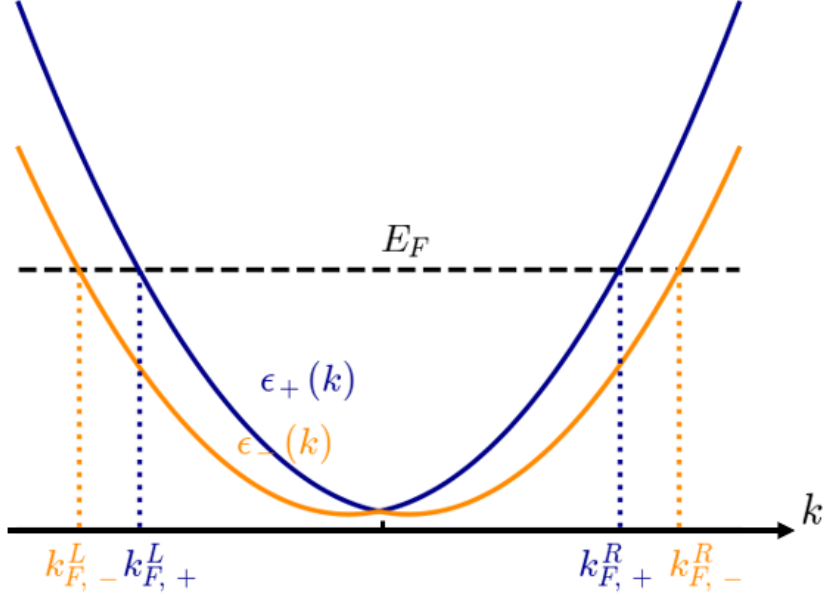


Figure 4.2: Sketch of the dispersion $\epsilon_{\pm}(k)$ given in Eq. (4.17). The different Fermi momenta obtained in Eq. (4.18) are marked by dotted lines.

we assume that the phase gain at the SN-interfaces is the same as in the previous calculation in Sec. 4.2. To calculate the dynamical phase gain, we further need to find the momenta at which the particles travel through the normal region. Previously, these were approximately given by $\pm k_F$, independent of spin polarization. Here, we explicitly want to include spin-dependent contributions that are due to the spin-orbit- and Zeeman fields.

Before we calculate the dispersion of h_s , we make a few assumptions: First, we assume a junction geometry that allows for current flow in the x -direction. Transverse motion is assumed to be confined along a width of W , so that $k_y = \pi/W$ ¹. Also, we initially set the Zeeman field to zero, which simplifies h_s to

$$h_s(k) = \frac{\hbar^2 k^2}{2m} - E_F + \hbar\alpha \left(k\sigma_y - \frac{\pi}{W}\sigma_x \right), \quad (4.16)$$

where we set $k_x = k$. From this, we find the dispersion relation

$$\epsilon_{\pm}(k) = \frac{\hbar^2 k^2}{2m} - E_F \pm \hbar\alpha \sqrt{k^2 + \frac{\pi^2}{W^2}}. \quad (4.17)$$

¹We estimate the transverse momentum using the solution $E_n = \frac{n^2 \hbar^2 \pi^2}{2mW^2}$ of the problem of a particle in a 1d potential well.

In the limit of $E_F \gg \hbar\alpha k_F, B$, we may linearize each dispersion around its Fermi momenta. To calculate the Fermi momenta, we consider the spin-orbit coupling as a perturbation and only keep track of terms linear in α . Setting $\epsilon_{\pm}(k) = 0$ then yields

$$k_{F,\pm}^R = k_F \mp k_{\alpha}, \quad k_{F,\pm}^L = -k_F \pm k_{\alpha}, \quad (4.18)$$

for the Fermi momenta, with

$$k_{\alpha} = \frac{m\alpha}{\hbar} \sqrt{1 + \frac{\pi^2}{k_F^2 W^2}}. \quad (4.19)$$

The different Fermi momenta are illustrated in Fig. 4.2. The R/L superscript of the Fermi momenta is connected to the direction of movement, i.e. R is associated with $+k_F$, L with $-k_F$. To linearize the dispersion relations, we also need to calculate the Fermi velocities, which are given by the derivative of the dispersions around the Fermi momenta,

$$v_{\pm}(k) = \frac{1}{\hbar} \partial_k \epsilon_{\pm}(k) = \frac{\hbar k}{m} \pm \frac{\alpha k}{\sqrt{k^2 + \frac{\pi^2}{W^2}}}. \quad (4.20)$$

Plugging in the Fermi momenta $k_{F,\pm}^R$ and assuming that $k_F^2 W^2 \gg 1$, we find to leading order in α for the Fermi velocities,

$$v_{F,\pm} = v_F \mp \alpha \frac{\pi^2}{k_F^2 W^2}, \quad (4.21)$$

with $v_F = \hbar k_F / m$. The linearized dispersion relations are then given by

$$\epsilon_{\pm}(k) \approx \begin{cases} \hbar v_{F,\pm}(k - k_F \pm k_{\alpha}), & k \simeq k_{F,\pm}^R, \\ -\hbar v_{F,\mp}(k + k_F \pm k_{\alpha}), & k \simeq k_{F,\pm}^L. \end{cases} \quad (4.22)$$

Next, we introduce the Zeeman field to the junction. In the limit $k_F \gg 1/W$, the spin is quantized along the y -direction. A small Zeeman field in the y -direction therefore adds a linear contribution to the dispersion relations as follows,

$$\epsilon_{\pm}(k) \approx \begin{cases} \hbar v_{F,\pm} \left(k - k_F \pm k_{\alpha} \pm \frac{B}{\hbar v_{F,\pm}} \right), & k \simeq k_{F,\pm}^R, \\ -\hbar v_{F,\mp} \left(k + k_F \pm k_{\alpha} \mp \frac{B}{\hbar v_{F,\mp}} \right), & k \simeq k_{F,\pm}^L. \end{cases} \quad (4.23)$$

Here, we neglect the contributions of the Zeeman field to the Fermi velocities. We thus find that, at the Fermi energy, particles travel through the normal region with momenta

$$k_{F,\pm}^R = k_F \mp k_{\alpha} \pm \frac{B}{\hbar v_{F,\pm}}, \quad k_{F,\pm}^L = -k_F \pm k_{\alpha} \pm \frac{B}{\hbar v_{F,\mp}}. \quad (4.24)$$

4.3.1 SPIN-DEPENDENT ANDREEV LEVELS AND ANOMALOUS PHASE SHIFT

In contrast to the Andreev bound-states calculated in the previous Sec. 4.2, we here need to take into account the spin of the particle. We first consider the Andreev scattering process for a spin-up electron, initially located at the left superconductor. Previously, we found that the momentum at which particle and hole travel was depending on the bound-state energy E of the particle, see Eq. (4.10). Here, the energy contribution to the momenta can be neglected in the limit $E_{\pm} \ll B$, $\hbar\alpha k_F \ll E_F$, with E_{\pm} being the spin-dependent bound-state energies.

The electron travels to the right SN-interface, gaining a phase of $k_{F,+}^R L$. Here, it is reflected as a spin-down hole, which then travels back to the left SN-interface, acquiring a phase of $k_{F,-}^L$. Including the phases obtained at the interfaces [see Eq. (4.11)], we find the following condition for the Andreev level,

$$-2 \arccos(E_+/|\Delta|) - \varphi + (k_{F,+}^R + k_{F,-}^L)L = 2n\pi, \quad (4.25)$$

which yields

$$E_+ = \pm|\Delta| \cos \left[\frac{\varphi - (k_{F,+}^R + k_{F,-}^L)L}{2} \right]. \quad (4.26)$$

Analogously, we find for an initial spin-down electron,

$$E_- = \pm|\Delta| \cos \left[\frac{\varphi - (k_{F,-}^R + k_{F,+}^L)L}{2} \right]. \quad (4.27)$$

The Andreev levels now allow us to calculate the current-phase relation of the junction at zero temperature. In the ground state, both negative-valued Andreev levels are occupied. Taking the derivative of the ground state with respect to φ then yields for the current,

$$\begin{aligned} I(\varphi) &= \frac{2e|\Delta|}{\hbar} \left\{ \sin \left[\frac{\varphi - (k_{F,+}^R + k_{F,-}^L)L}{2} \right] + \sin \left[\frac{\varphi - (k_{F,-}^R + k_{F,+}^L)L}{2} \right] \right\} \\ &= \frac{2e|\Delta|}{\hbar} \cos \left(\frac{\theta_B}{2} \right) \sin \left(\frac{\varphi - \varphi_0}{2} \right), \end{aligned} \quad (4.28)$$

with

$$\theta_B = \frac{L}{2}(k_{F,+}^R + k_{F,-}^L - k_{F,-}^R - k_{F,+}^L), \quad \varphi_0 = \frac{L}{2}(k_{F,+}^R + k_{F,-}^L + k_{F,-}^R + k_{F,+}^L). \quad (4.29)$$

The critical current is reduced by the cosine of the angle $\theta_B/2 \approx BL/(\hbar v_F)$. Also, the current-phase relation exhibits an anomalous phase shift. Using Eqs. (4.24) and (4.21), we find

$$\varphi_0 = \frac{LB}{\hbar} \left(\frac{1}{v_{F,-}} - \frac{1}{v_{F,+}} \right) \approx \frac{2\pi^2}{k_F^2 W^2} \frac{B\alpha L}{\hbar v_F^2}. \quad (4.30)$$

This shows that the presence of both Rashba spin-orbit coupling and a Zeeman field perpendicular to the current indeed lead to an anomalous Josephson effect [82]. A Zeeman field parallel to the current would contribute quadratically to the Fermi momenta. As the phase shift has to satisfy $\varphi_0 \rightarrow -\varphi_0$ under time-reversal symmetry, we conclude that only the in-plane component of the Zeeman field perpendicular to the current may contribute to φ_0 . We further note that the scaling of φ_0 in Eq. (4.30) is equivalent to the result of the Ginzburg-Landau calculation by Buzdin in Ref. [76].

In the calculation presented here, we assumed perfect transparency \mathcal{T} of the normal region. In the tunneling limit, $\mathcal{T} \ll 1$, one finds a current-phase relation of the form [82]

$$I(\varphi) \approx I_c \sin(\varphi - \varphi_0), \quad (4.31)$$

analogously to Eq. (4.13). This implies that the energy of the φ_0 -junction is given by

$$H(\varphi) = -E_J \cos(\varphi - \varphi_0). \quad (4.32)$$

In the following, we will use this relation in order to model an array of φ_0 -junctions.

4.4 MODEL OF THE φ_0 -JOSEPHSON JUNCTION ARRAY

We model a $N \times N$ square array of φ_0 -Josephson junctions, see Fig. 4.3. The φ_0 -shift is induced in the horizontal junctions via an applied in-plane magnetic field in vertical direction and Rashba spin-orbit coupling in the normal region. In addition to the coupling along the horizontal and vertical directions parametrized by the Josephson energy E_J , we transcend the description of the previous chapters by including couplings along the diagonals with coupling strength E_D . The ratio of E_J and E_D is determined by the lattice geometry of the Josephson junction array. For example, the square islands of the array considered here are in much closer proximity to their diagonal neighbors in comparison to the array shown in Fig. 2.2. This suggests that diagonal currents play a relevant role in the description of the model. The lattice geometry shown in Fig. 2.2 is analogous to the experiment conducted by the Strunk group [2].

The in-plane magnetic field encloses different angles with the horizontal and diagonal junctions. Therefore, it induces different phase biases in these junctions, which we will dub φ_0^x

4 Superconducting diode effect in φ_0 -Josephson junction arrays

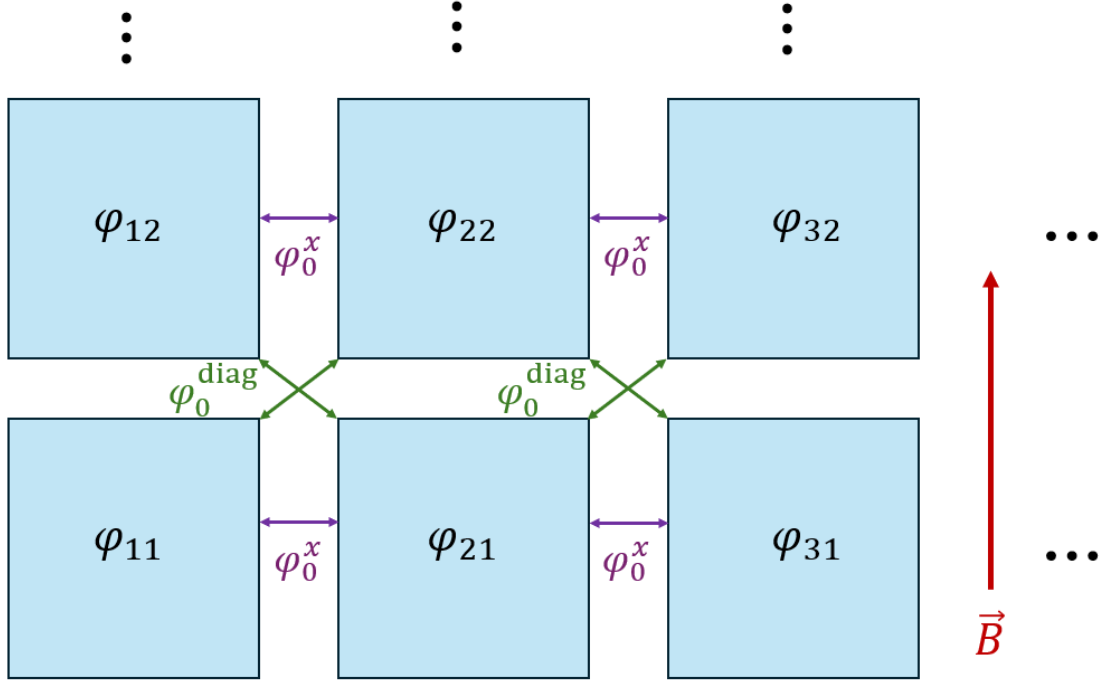


Figure 4.3: Sketch of the square Josephson junction array. Superconducting islands (light blue) are parametrized by phases $\varphi_{i,j}$. An in-plane magnetic field (red) induces φ_0 -junctions in the horizontal (purple) and diagonal (green) directions.

for the horizontal and φ_0^{diag} for the diagonal junctions. As in the previous chapters, we neglect charging effects. The Hamiltonian H may then be written as

$$H = H_0 + H_D, \quad (4.33)$$

$$H_0 = -E_J \sum_{i=1}^{N-1} \sum_{j=1}^N \cos(\varphi_{i+1,j} - \varphi_{i,j} - \varphi_0^x) - E_J \sum_{i=1}^N \sum_{j=1}^{N-1} \cos(\varphi_{i,j+1} - \varphi_{i,j}), \quad (4.34)$$

$$H_D = -E_D \sum_{i,j=1}^{N-1} \left[\cos(\varphi_{i+1,j+1} - \varphi_{i,j} - \varphi_0^{\text{diag}}) + \cos(\varphi_{i+1,j} - \varphi_{i,j+1} - \varphi_0^{\text{diag}}) \right], \quad (4.35)$$

with H_0 describing the vertical and horizontal and H_D the diagonal junctions. Note that in contrast to the previous chapters, we now impose open boundary conditions. This will later allow us to apply an external current.

4.4.1 CALCULATION OF THE GROUND STATE

In the absence of diagonal couplings, the horizontal φ_0 -shift has no physical influence on the ground-state configuration of the array. This is because the shifts do not affect the sums of gauge-invariant phase differences around the plaquettes and may thus be eliminated from the description via a gauge transformation. In the case of finite diagonal couplings, each plaquette is split into smaller triangular plaquettes. The sum of gauge-invariant phase differences around these plaquettes yields $\pm(\varphi_0^x - \varphi_0^{\text{diag}})$ as shown in Fig. 4.4(a). This allows us to eliminate one parameter from our description, as an array with horizontal φ_0 -shift of $\Delta\varphi_0 = \varphi_0^x - \varphi_0^{\text{diag}}$ and zero diagonal shift is gauge equivalent to our current model².

We calculate how the phase shift $\Delta\varphi_0$ influences the ground-state configuration $\varphi_{i,j}^{\text{GS}}$ of the array. In the limit of large N and $E_D < E_J$, we may assume that the phases along each column are equivalent to each other, as there is no relative phase bias. This allows us to write the ground state as $\varphi_{i,j}^{\text{GS}} = i\varphi_x$ with φ_x being the phase difference between adjacent columns. Each site is coupled to the right neighboring column via three junctions, see Fig. 4.4(b). As these couplings are invariant under translation, the ground-state configuration minimizes

$$h(\varphi_x) = -E_J \cos(\varphi_x - \Delta\varphi_0) - 2E_D \cos \varphi_x, \quad (4.36)$$

with $h(\varphi_x)$ being the energy of the couplings described in Fig. 4.4(b). For the minimum, we find

$$\varphi_x = \arctan\left(\frac{E_J \sin \Delta\varphi_0}{E_J \cos \Delta\varphi_0 + 2E_D}\right), \quad (4.37)$$

which translates to the ground-state configuration,

$$\varphi_{i,j}^{\text{GS}} = i \arctan\left(\frac{E_J \sin \Delta\varphi_0}{E_J \cos \Delta\varphi_0 + 2E_D}\right). \quad (4.38)$$

This result is consistent with numerical minimization results of the full model for various parameters for E_D and φ_0 .

The phase bias in combination with the diagonal couplings thus leads to supercurrents flowing in the ground state. Specifically, we find $I_h = (2eE_J/\hbar) \sin(\varphi_x - \Delta\varphi_0)$ for the horizontal and $I_d = (2eE_D/\hbar) \sin \varphi_x$ for the diagonal currents, see Fig. 4.4(c) for an illustration. These currents break the vertical mirror symmetry of the array as well as time-reversal symmetry, which facilitates the possibility of a diode effect.

²Uniform horizontal phase shifts now have physical consequences, due to the finite diagonal coupling.

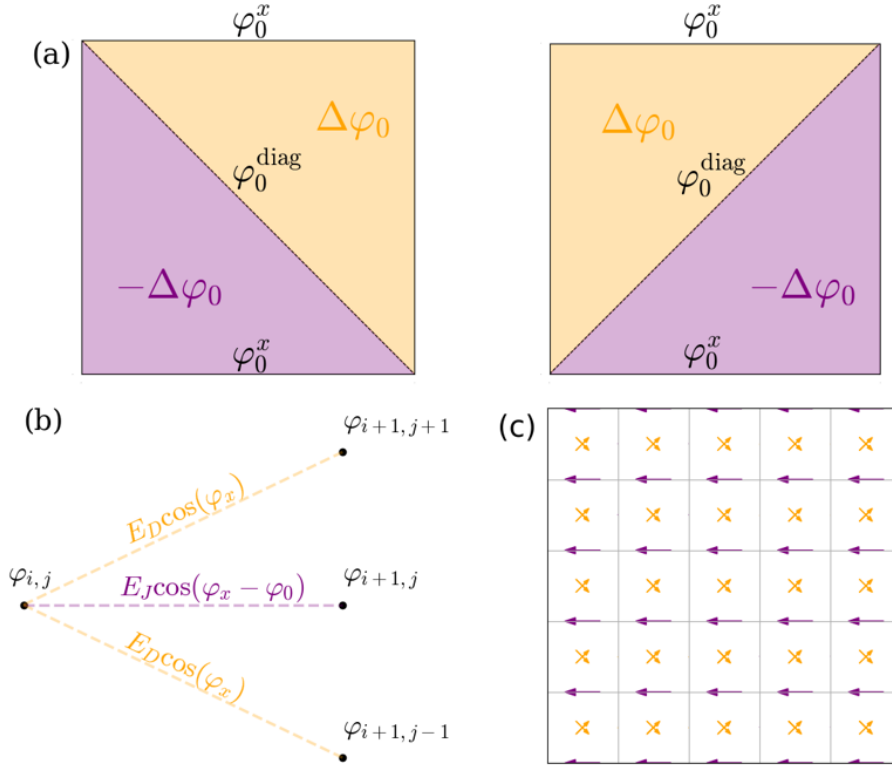


Figure 4.4: Model Hamiltonian with φ_0 -junctions and diagonal couplings. (a) Phase configuration inside of a plaquette. Due to the combination of diagonal couplings and phase offsets of the junctions, the system is effectively threaded by a transverse magnetic flux $\Delta\varphi_0 = \varphi_0^x - \varphi_0^{\text{diag}}$ in the orange region and $-\Delta\varphi_0$ in the purple region. (b) Illustration of the ground state calculation. We only need to consider an elementary cell involving four superconducting islands due to translational symmetry in the x - and y -directions. (c) Ground-state current configuration. The arrows indicate the currents flowing between the superconducting islands. The length of the arrows corresponds to the magnitude of the current, with the critical current corresponding to an arrow connecting two islands. Parameters: $E_D = 0.3E_J$, $\Delta\varphi_0 = \pi/2$.

4.5 MODULATED VORTEX POTENTIAL

The broken mirror symmetry of the ground-state configuration $\varphi_{i,j}^{\text{GS}}$ also affects the vortex pinning potential in the array. In Eq. (2.13), we introduced a vortex configuration $\varphi_{i,j}^v$ in terms of the polar angle. The analogous definition in cartesian coordinates is given by

$$\varphi_{i,j}^v(x, y) = \varphi_{i,j}^{\text{GS}} + \arctan 2 \left(\frac{j-y}{i-x} \right), \quad (4.39)$$

with (x, y) being the spatial coordinates of the vortex core and $\arctan 2(y/x)$ the polar angle in the xy -plane. Here we also take into account the modulated ground-state configuration. However,

we neglect possible relaxation processes due to an interplay of the ground-state currents and the circular currents that are induced by the vortex. This will be addressed in the next section.

The configuration given in Eq. (4.39) allows us to calculate the pinning potential U of the vortex explicitly via

$$U(x, y) = H(\{\varphi_{i,j}^v(x, y)\}), \quad (4.40)$$

with H being the Hamiltonian in Eq. (4.35). For $E_D = \Delta\varphi_0 = 0$, we reproduce the results of Ref. [83]. The minima of the pinning potential are located in the centers of the plaquettes while the maxima sit at the superconducting sites. An illustration of the potential is shown in Fig. 4.5(a). Once we account for the diagonal coupling terms and the φ_0 -shifts, the potential changes substantially, as shown in Fig. 4.5(b). Due to the ground-state currents, the minima of the potential are shifted away from the plaquette centers along the y -direction. We further find a deformation of the potential, breaking the mirror symmetry along the y -direction. We highlight these changes in the potential via line cuts along the y -direction, presented in Fig. 4.5(c,d). One clearly sees the shift of the potential minima in Fig. 4.5(c). In the case of E_D and $\Delta\varphi_0 \neq 0$, we further find a linear modulation of the height of the potential minima, which is due to the finite size of the array. On top of that, the maximal positive and negative derivatives of the potential along the y -direction are different in magnitude for E_D and $\Delta\varphi_0 \neq 0$ as demonstrated in Fig. 4.5(d). As these are directly related to the horizontal depinning currents of the vortex, this implies diode behaviour of the Josephson array due to vortex depinning.

4.6 DIODE EFFECT DUE TO VORTEX DEPINNING

4.6.1 LANGEVIN EQUATION FOR VORTEX MOTION

Here, we want to make the previously described diode effect explicit by modeling the vortex motion via a Langevin equation, in analogy to Ref. [83]. Interestingly, this will allow us to relate the array diode effect due to vortex depinning to the diode effect of a single junction [84].

We describe vortex motion along the y -direction. The application of an external current leads to a Lorentz force F_L acting on the vortex, as discussed in section 2.4. In the present case, the Lorentz force takes the form,

$$\mathbf{F}_L = \gamma\Phi_0(\mathbf{I} \times \hat{\mathbf{z}})/a, \quad (4.41)$$

with $\mathbf{I} = I\hat{x}$ being the applied external current per junction in x -direction. The additional geometric factor γ arises due to the presence of diagonal junctions. This can be seen as follows: We estimate the current distribution in the limit of small phase offsets $\Delta\varphi_0$ by adding a washboard potential to the Hamiltonian. As for the previous calculation of the ground state, we assume a uniform phase difference φ_x between adjacent columns. Minimizing the energy at the boundary with respect to φ_x then yields for the phase configuration

$$\sin(\varphi_x) = \frac{I}{E_J + 2E_D}. \quad (4.42)$$

Thus we find that the applied current splits between the junctions,

$$I_h = I \frac{E_J}{E_J + 2E_D}, \quad I_d = I \frac{E_D}{E_J + 2E_D}, \quad (4.43)$$

with I_h being the current along the horizontal junctions and I_d along the diagonal junctions. The effective Lorentz force applied by the diagonal currents is $2\Phi_0 I_d / (\sqrt{2}a)$, with the factor of $1/\sqrt{2}$ coming from the enclosed angle of the vortex motion and the diagonal currents. Adding all Lorentz force contributions, we find that the geometric factor γ in Eq. (4.41) is given by

$$\gamma = \frac{E_J + \sqrt{2}E_D}{E_J + 2E_D}. \quad (4.44)$$

Note that this calculation is valid only under the assumption that $\Delta\varphi_0$ is small. In general, the calculations of current distribution and geometric factor become more involved.

Once the external current exceeds the depinning current, the vortex starts moving, leading to phase slips as well as normal currents flowing through the array. The dissipative currents damp the motion of the vortex, giving rise to a friction force $-\alpha\dot{y}(t)$ (α : friction coefficient) as well as an associated Langevin force \mathbf{f} . These random forces are zero on average and are related to temperature via $\langle f_y(t)f_y(t') \rangle = 2\alpha k_B T \delta(t-t')$. Including the restoring force imposed by the pinning potential U , we can describe the vortex motion via the Langevin equation

$$-\partial_y U(y) - \alpha\dot{y}(t) - \gamma\Phi_0 I/a = f_y(t). \quad (4.45)$$

We may further relate the Langevin equation to the description of a single Josephson junction. We first replace the position variable y of the vortex by a phase $\theta = 2\pi y/a$. Using the identifications $\gamma I \rightarrow I_{\text{bias}}$ for an effective bias current I_{bias} and $\Phi_0^2/a^2\alpha \rightarrow R$ for an effective resistance R , the Langevin equation becomes

$$-\frac{2e}{\hbar}\partial_\theta U(\theta) - \frac{\hbar}{2eR}\dot{\theta}(t) - I_{\text{bias}} = \delta i(t), \quad (4.46)$$

with the correlator of the random currents δi given by $\langle \delta i(t)\delta i(t') \rangle = (2k_B T/R)\delta(t-t')$. Since the vortex potential $U(\theta)$ is a periodic function of θ for large arrays, we may readily identify it with the Josephson energy of the phase parameter θ and thus find a description of the vortex motion that is analogous to the phase dynamics of a single junction [84]. Thus, for both single junctions and arrays, the possibility of a diode effect is encoded in the pinning potential (Josephson energy for single junction) U .

To show the diode effect explicitly, we calculate the I - V characteristics of the Josephson array. For that, we relate the vortex motion to the voltage V developing across the array. We assume a finite (but small) number of depinned vortices \mathcal{N} moving at an average velocity of \bar{v} . A vortex

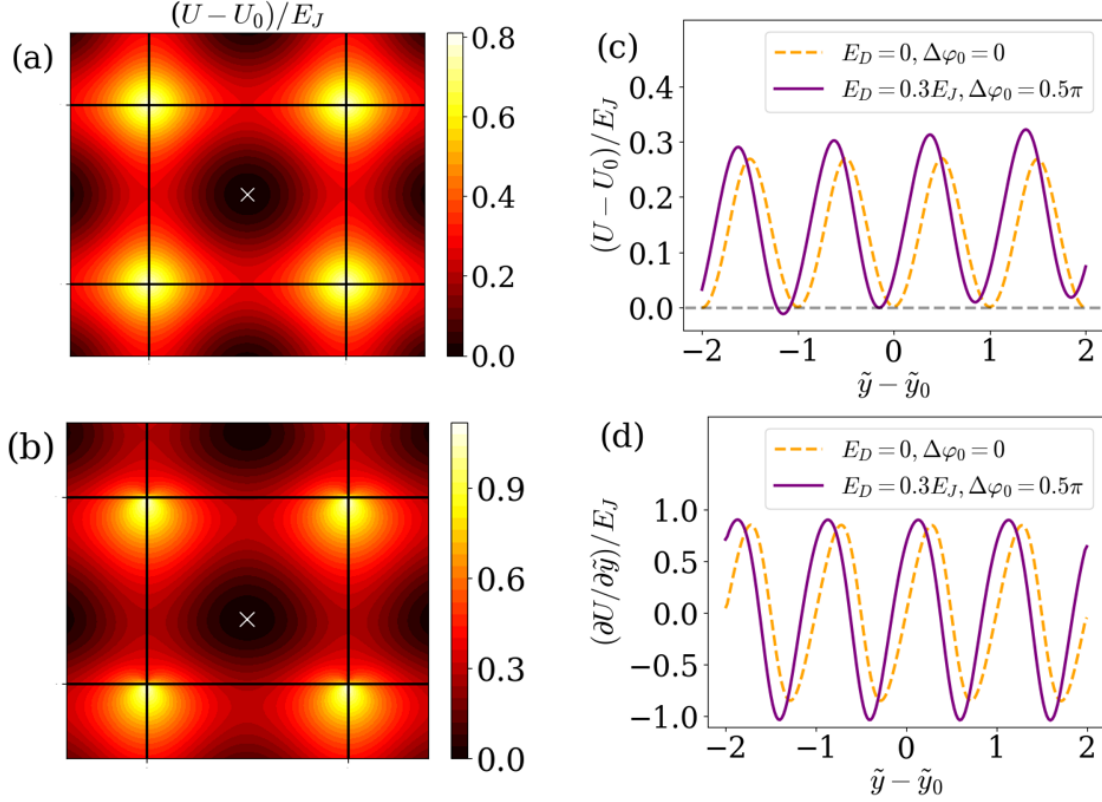


Figure 4.5: Vortex in a Josephson junction array with φ_0 -junctions and diagonal couplings. (a) Contour plot of the vortex potential $U(x, y)$ with $E_D = 0$ and $\Delta\varphi_0 = 0$. The black lines indicate the Josephson junction array, the white cross shows the minimum of the potential. (b) Same plot as (a) with $E_D = E_J/2$ and $\Delta\varphi_0 = \pi/2$. (c) Plot of the vortex potential $U(x_0, y - y_0)$ as a function of y , with (x_0, y_0) denoting coordinates of the array center. Parameters corresponding to both (a) and (b). For easier comparison, we subtract a constant U_0 corresponding to the potential at the minimum closest to the array center. (d) y -derivatives of the potential as a function of y corresponding to (c).

moving through a junction leads to a 2π phase slip across the vertical section of the array it passes. According to Eq. (2.5), we find for the total voltage V developing in the array,

$$V = \mathcal{N} \frac{\hbar}{2e} \frac{2\pi}{\frac{Na}{\bar{v}}} = \frac{\mathcal{N}}{Na} \Phi_0 \bar{v}, \quad (4.47)$$

and thus for the voltage per junction V/N ,

$$\frac{V}{N} = na\Phi_0\bar{v} = na\Phi_0 \overline{\frac{dy}{dt}}, \quad (4.48)$$

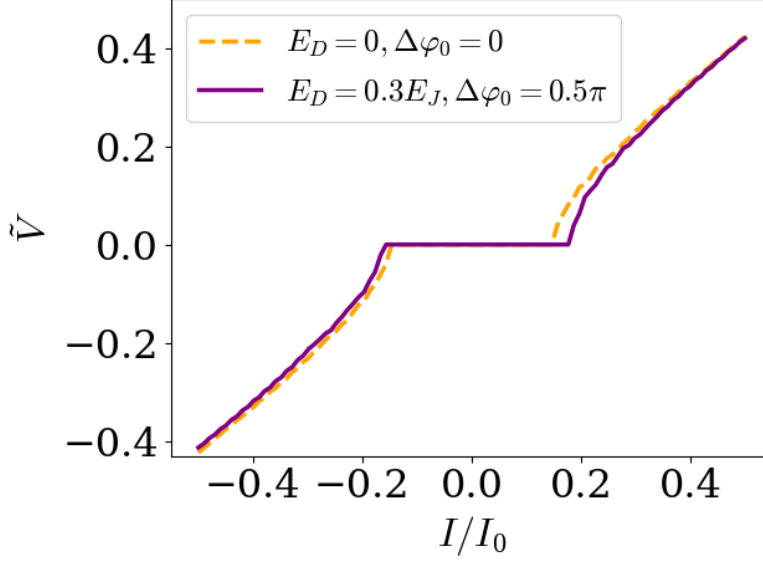


Figure 4.6: $I - V$ curves for both parameter sets computed via the Langevin equation in Eq. 4.45. The depinning currents correspond to the extreme values in Fig. 4.5(d), weighted by the reduction parameter γ . We calculated the voltage for 200 current values between $-I_0/2$ and $I_0/2$. Further parameters: $\tau = 0.05$, $n_{\max} = 2000$.

with $n = \mathcal{N}/(a^2 N^2)$ being the area density of the vortices. For the purpose of numerics, we use dimensionless units in Eq. (4.45) and Eq. (4.48). At zero temperature, the Langevin equation may be written in the following form,

$$-\frac{1}{2\pi} \frac{d\tilde{U}}{d\tilde{y}} - \frac{d\tilde{y}}{d\tilde{t}} - \gamma \tilde{I} = 0. \quad (4.49)$$

Here we introduced dimensionless variables (indicated by a tilde) via $U = E_J \tilde{U}$, $y = a\tilde{y}$, $t = (\alpha a^2 / 2\pi E_J) \tilde{t}$ and $I = I_0 \tilde{I}$, with $I_0 = 2\pi E_J / \Phi_0$ being the critical current per junction. Accordingly, we find for the dimensionless voltage per junction \tilde{V} ,

$$\tilde{V} = \frac{\alpha}{2\pi E_J n \Phi_0} \frac{V}{N} = \frac{d\tilde{y}}{d\tilde{t}}. \quad (4.50)$$

We calculate the time averaged vortex velocity $\overline{dy/dt}$ via Eq. (4.49) as a function of the dimensionless external current I/I_0 as well as the ratio E_J/E_D and the applied phase bias $\Delta\varphi_0$. Our results are displayed in Fig. 4.6. For $E_D = 0$ and $\Delta\varphi_0 = 0$, we find an I - V characteristic that is analogous to a single Josephson junction, with no observable diode effect. However, for $E_D = 0.3E_J$ and $\Delta\varphi_0 = \pi/2$, one clearly sees that the depinning currents increase asymmetrically and that the array shows diode behavior. As discussed earlier, this asymmetry is related to the different negative and positive maximal derivative values of the vortex pinning potential U .

4.6.2 RELAXATION EFFECTS AND WASHBOARD POTENTIAL

In the previous section, we assumed that the vortex phase configuration is given by a linear combination of the modulated ground state and an arctan term, see Eq. (4.39). This assumption did not allow for possible relaxation processes between the two configurations. Here, we consider a vortex configuration that explicitly includes relaxation effects. Starting from Eq. (4.39), we find the relaxed vortex configuration via gradually evolving towards a local minimum of H by the means of a simple gradient descent scheme (see appendix). This procedure however precludes the possibility of calculating the vortex potential, due to the fixed vortex core position of the relaxed configuration. Instead, we calculate the critical currents of the array via the application of a washboard potential,

$$H_I = H + \frac{\hbar}{2e} I \sum_{j=1}^N (\varphi_{1,j} - \varphi_{N,j}). \quad (4.51)$$

Starting from a local minimum containing a single vortex in the center of the array, we apply small external currents I to the system via Eq. (4.51). If the current is below the depinning current I_c , the system will monotonically converge towards a stable configuration, with the vortex staying at its initial position. Above the depinning current, the vortex will move between plaquettes along the y -direction, eventually leaving the array. The numerical procedure is as follows: We apply an initial current I_{\min} to the array and evolve the system over n_{\max} time steps of length τ . If the vortex remains stable, the current is smaller than the depinning current. We then increase the external current gradually in k small increments, up to a maximum current I_{\max} . For each increase, we repeat the time evolution step. The depinning current is then identified by the current value, at which the vortex has moved from its initial position. We perform this scheme for both positive and negative currents.

We present the results in Fig. 4.7. In Fig. 4.7(a), we show the current distribution related to the relaxed vortex configuration in the presence of diagonal couplings and phase offsets. We observe diagonal currents flowing through the plaquette containing the vortex. The currents circulate only around the lower triangular plaquettes, as highlighted in the figure. This suggests, that the vortex core is shifted along the negative y -direction, which is in agreement with the previously calculated pinning potential minimum shown in Fig. 4.5(b). Figure 4.7(b) shows the depinning currents I_c^+ and I_c^- as a function of the phase offset $\Delta\varphi_0$ and diagonal coupling strength E_D . The direction of the current is indicated by the color (compare to the arrow colors in Fig. 4.7(a)). Our results suggest that both depinning currents decrease with the phase offset, while the difference between the currents increases. We quantify the asymmetry between the currents via the diode efficiency η , defined as

$$\eta = 2 \frac{I_c^+ - I_c^-}{I_c^+ + I_c^-}. \quad (4.52)$$

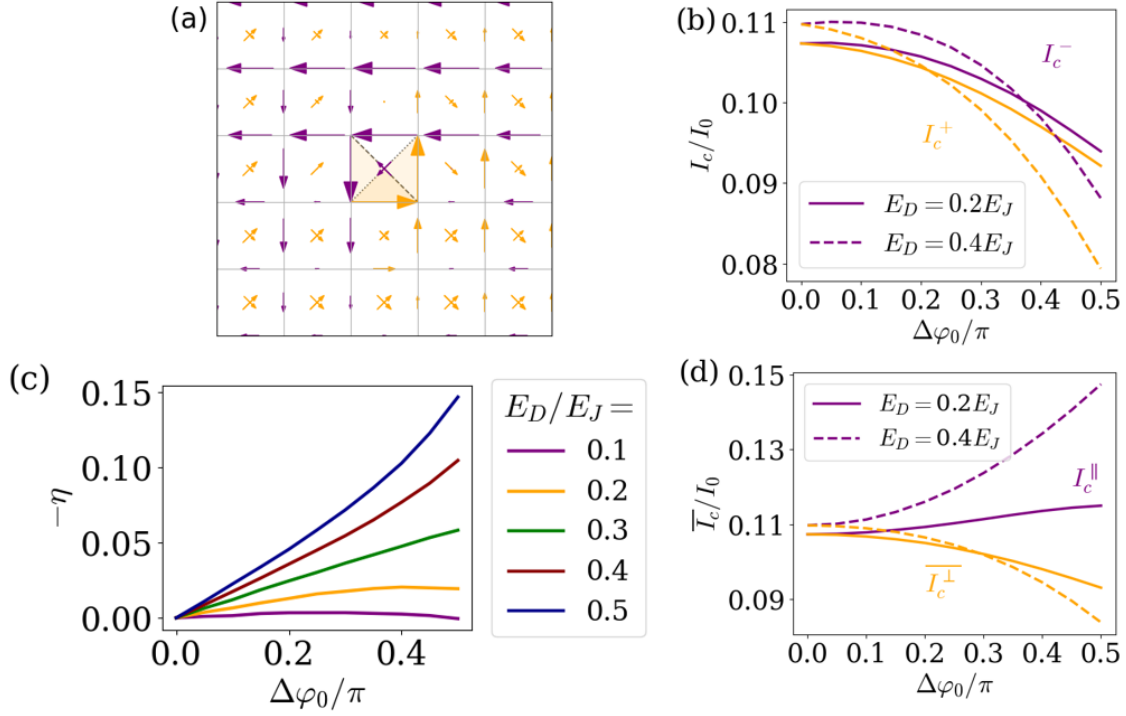


Figure 4.7: Depinning currents with phase relaxation. (a) Current distribution for a relaxed vortex configuration. The length of arrows indicates the magnitude of the currents. Notice that in the central plaquette, the currents circulate around the highlighted triangles, reflecting the shift of the vortex minimum into the lower half of the plaquette. (b) Positive and negative depinning currents as a function of $\Delta\varphi_0$ for two values of E_D . (c) Diode efficiency defined in Eq. 4.52 as a function of $\Delta\varphi_0$ for various values of E_D . (d) Comparison of depinning current parallel (in blue) and perpendicular (in red; averaged over current directions) to the applied in-plane magnetic field as a function of E_D and $\Delta\varphi_0$. Parameters: $n_{max} = 10^5, \tau = 0.2, k = 1200$. For horizontal currents: $I_{min} = 0.06I_0, I_{max} = 0.12I_0$. For vertical currents: $I_{min} = 0.09I_0, I_{max} = 0.15I_0$.

We compute the diode efficiency for multiple values of E_D and $\Delta\varphi_0$, as shown in Fig. 4.7(c). Here we see that both the diagonal coupling strength and the phase offset increase the efficiency of the diode.

Finally, we also computed the critical currents in the vertical direction. We apply vertical currents through the washboard potential given in Eq. (2.48). We find that the vertical depinning currents³ I_c^\parallel do not show a diode effect, which matches our expectation, given the absence of symmetry breaking along the direction of vortex motion. We also notice that the vertical depinning currents increase with increasing phase offset $\Delta\varphi_0$, in contrast to the decreasing horizontal depinning currents I_c^\perp (averaged over both directions).

³The vertical current is parallel to the in-plane magnetic field.

4.7 CONCLUSION

In this chapter, we provided a model facilitating a Josephson diode effect in an array of φ_0 -junctions via the depinning of vortices. We point out that there are other methods of tilting the vortex pinning potential, e.g., by using an intrinsically asymmetric Josephson array as described in Ref. [85, 86]. Our approach however leads to qualitatively different behaviour. As the asymmetric pinning potential is due to the ground-state currents of the model, the depinning currents are the same for both vortices and antivortices. This is in contrast to Ref. [85, 86], where the depinning currents of vortices and antivortices are switched.

The natural next step of the model provided here is the inclusion of frustration effects. In the previous chapter, we saw that frustration leads to fascinating ground-state configurations connected to periodic vortex lattices. The addition of diagonal couplings yields a different underlying plaquette lattice for the vortices, which consequently leads to different vortex lattice structures. The depinning currents of the vortices are highly dependent on the frustration value. Including φ_0 -junctions should therefore lead to a frustration-dependent diode efficiency, with some frustration values yielding particularly high efficiencies. Furthermore, the diode efficiency might also be useful in identifying the formation of vortex lattices.

5 PERIODICALLY DRIVEN QUANTUM ISING MODELS

In this chapter, we introduce important concepts that are the foundation of the following chapters 6 and 7.

5.1 TRANSVERSE FIELD ISING MODEL

The quantum Ising model [87] in its various incarnations plays an essential role in modern condensed matter physics and in quantum information theory. It is paradigmatic for symmetry breaking quantum phase transitions in its spin formulation [88] as well as for topological quantum phase transitions in its fermionic version [89]. Even more interestingly, applications of driven quantum Ising models can be used to realize non-equilibrium phases such as Floquet time crystals [90, 91], which will be the subject of the following two chapters. Before that, we want to briefly go over essential results regarding the quantum Ising model.

The transverse field quantum Ising model in one dimension is described by the Hamiltonian

$$H = -g \sum_{i=1}^N X_i - J \sum_{i=1}^{N-1} Z_i Z_{i+1}. \quad (5.1)$$

The model in Eq. (5.1) describes a spin chain of length N with nearest-neighbor Ising coupling J and a transverse field g . For $g = 0$, the eigenstates of the Hamiltonian are eigenstates of the spin operators Z_i . The ground state is two-fold degenerate, with the degenerate subspace being spanned by the states

$$|\uparrow_N\rangle = |\uparrow, \uparrow, \dots, \uparrow\rangle, \quad |\downarrow_N\rangle = |\downarrow, \downarrow, \dots, \downarrow\rangle. \quad (5.2)$$

If we flip a spin of the ground state to the opposite orientation either at the boundary or in the bulk of the chain, the state of the system has one or two domain walls, respectively. These (static) domain walls are associated with an energy of $2J$ and are the elementary excitations underlying the excitation spectrum of the Ising model.

For small but nonzero g , the degeneracy of the ground state is lifted. However, the energy difference Δ between the two previously degenerate states remains exponentially small in the system size N . This can be understood by perturbation theory. First, an arbitrarily small trans-

verse field g fixes symmetric and antisymmetric combinations of the basis vectors in Eq. (5.2) as eigenvectors of the Hamiltonian,

$$|+\rangle = \frac{1}{\sqrt{2}}(|\uparrow_N\rangle + |\downarrow_N\rangle), \quad |-\rangle = \frac{1}{\sqrt{2}}(|\uparrow_N\rangle - |\downarrow_N\rangle). \quad (5.3)$$

This follows because the Hamiltonian commutes with the spin-flip symmetry operator P ,

$$P = \prod_{i=1}^N X_i. \quad (5.4)$$

This constrains the non-degenerate eigenstates of H to also be eigenstates of P . In order for the degeneracy to be lifted, the transverse field operator $\sum_{i=1}^N X_i$ needs to induce a nonzero matrix element between the two states $|+\rangle$ and $|-\rangle$. However, it may only flip one spin at a time. In order for the two states to be connected, we thus need to apply the operator N times. The two ground-state energies then differ only in N th order perturbation theory by a small splitting,

$$\Delta \sim \frac{g^N}{J^{N-1}} \quad (5.5)$$

with the energy denominator arising from the intermediate virtual states¹. For $g \ll J$, we thus find that the ground state of the system remains degenerate in the thermodynamic limit, $N \rightarrow \infty$. In this limit, the system is infinitely sensitive to perturbations which break the spin-flip symmetry, e.g., $V = \sum h_i Z_i$. For any arbitrarily small h_i , either $|\uparrow_N\rangle$ or $|\downarrow_N\rangle$ becomes the ground state. The ground state thus breaks the \mathbb{Z}_2 or spin flip symmetry of the Hamiltonian spontaneously. This spontaneous symmetry breaking defines the ferromagnetic phase. In contrast, the non-degenerate and gapped ground state of the system in the extreme case of finite g and $J = 0$ is given by

$$|-\rightarrow_N\rangle = |\rightarrow, \rightarrow, \dots, \rightarrow\rangle. \quad (5.6)$$

As it is non-degenerate, a small perturbation V has no significant effect on the ground state. Thus, the \mathbb{Z}_2 symmetry remains unbroken by the ground state and the system is in the paramagnetic phase. In the next section, we will argue that the transition between ferromagnetic and paramagnetic phases occurs precisely at $g = J$.

5.2 JORDAN-WIGNER TRANSFORMATION

Spin and fermionic operators both anticommute with each other when acting on the same site. However there is a difference when permuting operators on different sites. The spin operators

¹The splitting actually involves a sum over all possible elementary spin flip sequences, giving rise to a numerical prefactor.

commute while the fermionic ones anticommute. We want to construct operators c_j from spin operators which satisfy the fermion commutation relations,

$$\{c_i, c_j\} = 0, \quad \{c_i^\dagger, c_j^\dagger\} = 0, \quad \{c_i, c_j^\dagger\} = \delta_{i,j}. \quad (5.7)$$

This is achieved by spin operators acting on a site j with a multiplicative string operator acting on all sites $i < j$. This accounts for the commutation relation on different sites. We construct the fermionic operators as follows,

$$c_j = \frac{1}{2} \prod_{i=1}^{j-1} X_i (Z_j - iY_j), \quad c_j^\dagger = \frac{1}{2} \prod_{i=1}^{j-1} X_i (Z_j + iY_j). \quad (5.8)$$

One confirms straightforwardly that the operators in Eq. (5.8) satisfy (5.7). The inverse transformation is given by

$$X_j = 1 - 2c_j^\dagger c_j, \quad Y_j = i \prod_{i=1}^{j-1} e^{i\pi c_i^\dagger c_i} (c_j - c_j^\dagger), \quad Z_j = \prod_{i=1}^{j-1} e^{i\pi c_i^\dagger c_i} (c_j^\dagger + c_j). \quad (5.9)$$

This mapping between spin and fermion operators is referred to as Jordan-Wigner transformation [92].

By applying the transformation in Eq. (5.9) to Eq. (5.1), we find the following fermionic version of the quantum Ising model,

$$H = -g \sum_{j=1}^N (1 - 2c_j^\dagger c_j) - J \sum_{j=1}^{N-1} [c_j^\dagger c_{j+1} + c_j^\dagger c_{j+1}^\dagger + h.c.]. \quad (5.10)$$

If we compare this to the Kitaev chain model [93], we see that the Ising model in its fermionic formulation just becomes a special case of the Kitaev chain with chemical potential $-2g$ and equal hopping amplitude and pairing potential J . In the following, we will solve the fermionic model for both open and periodic boundary conditions and compare the solutions to the results obtained for the spin model.

5.2.1 OPEN BOUNDARY CONDITIONS - EDGE MODES

We solve the fermionic version of the transverse field Ising model with open boundary conditions, which is done through the introduction of Majorana fermions [93]. These operators are constructed as hermitian linear combinations of fermionic particles and holes,

$$\gamma_{2j-1} = c_j + c_j^\dagger, \quad \gamma_{2j} = i(c_j - c_j^\dagger), \quad (5.11)$$

5 Periodically driven quantum Ising models

so that $\gamma_i = \gamma_i^\dagger$. From the fermionic commutation relations, we find that the Majoranas satisfy

$$\{\gamma_i, \gamma_j\} = 2\delta_{i,j}, \quad (5.12)$$

which means that $\gamma_i^2 = 1$. Thus, creating or destroying two Majoranas is identical to doing nothing.

We will now formulate the quantum Ising model in terms of Majoranas. First, we note that from Eq. (5.11), we may write the fermionic operators as

$$c_j = \frac{1}{2}(\gamma_{2j-1} - i\gamma_{2j}), \quad c_j^\dagger = \frac{1}{2}(\gamma_{2j-1} + i\gamma_{2j}). \quad (5.13)$$

This represents the Majoranas as real and imaginary parts of the Jordan-Wigner fermions. Introducing them now to the Hamiltonian in Eq. (5.10) and simplifying yields

$$H = g \sum_{j=1}^N (1 - i\gamma_{2j-1}\gamma_{2j}) - iJ \sum_{j=1}^{N-1} \gamma_{2j}\gamma_{2j+1}. \quad (5.14)$$

First, we focus on the case $g = 0$. The Hamiltonian does not involve all the Majorana operators, since the edge operators γ_1 and γ_{2N} are missing. We may diagonalize the Hamiltonian by introducing quasiparticle operators $d_j = (\gamma_{2j} - i\gamma_{2j+1})/2$,

$$H = 2J \sum_{j=1}^{N-1} \left(d_j^\dagger d_j - \frac{1}{2} \right). \quad (5.15)$$

All quasiparticles come with an energy of $2J$. The edge mode $d_N = (\gamma_{2N} - i\gamma_1)/2$ however does not appear in the Hamiltonian and therefore has zero energy. Here we may draw a connection to the spin version of the model: The zero energy mode corresponds to the degenerate ground state of the transverse field Ising model. Switching between the two ground states is analogous to adding or subtracting an edge mode in the fermionic model. This is a highly non-local operation, as in the spin picture, every spin must be flipped. Similarly, the edge mode is created (non-locally) at both edges of the chain. The quasiparticles d_i correspond to domain walls in the spin picture which is apparent from their energy of $2J$. Each level E_i in the excitation spectrum of the spin model may be decomposed into $N - 1$ elementary excitations given by the quasiparticle spectrum,

$$E_i = \sum_{j=1}^{N-1} \epsilon_j \left(n_j - \frac{1}{2} \right). \quad (5.16)$$

In the present case, the quasiparticle spectrum is $\epsilon_j = 2J$ and the occupation numbers given by the eigenmodes of $\hat{n}_j = d_j^\dagger d_j$. Analogously to domain walls, the quasiparticles sit "in between" sites, as they consist of Majorana operators associated with neighboring sites.

For finite values of g , we employ a transfer-matrix approach, see e.g., Ref. [94]. We assume a semi-infinite chain. We start by considering the action of the Hamiltonian onto the eigenstate

$$|\psi\rangle = \sum_{j=1} (\psi_{2j-1}\gamma_{2j-1} + \psi_{2j}\gamma_{2j})|\Omega\rangle. \quad (5.17)$$

Here, ψ_{2j-1} and ψ_{2j} are the wavefunctions of the respective Majoranas and $|\Omega\rangle$ the quasiparticle vacuum of the Kitaev chain. Then, applying the Hamiltonian in Eq. (5.14) to the state yields

$$H|\psi\rangle = E|\psi\rangle = \sum_{j=1} (-2ig\psi_{2j} + 2iJ\psi_{2j-2})\gamma_{2j-1} + (2ig\psi_{2j-1} - 2iJ\psi_{2j+1})\gamma_{2j}. \quad (5.18)$$

Note that the energy E is measured relative to the ground-state energy. By comparing the coefficients of the Majorana operators on both sides, we obtain a system of equations for the wave functions, which may be brought into the form

$$\begin{pmatrix} \psi_{2j} \\ \psi_{2j+1} \end{pmatrix} = \begin{pmatrix} \frac{J}{g} & -\frac{E}{2ig} \\ -\frac{E}{2ig} & -\frac{E^2}{4gJ} + \frac{g}{J} \end{pmatrix} \begin{pmatrix} \psi_{2j-2} \\ \psi_{2j-1} \end{pmatrix}. \quad (5.19)$$

From this, we may extract the zero energy eigenstate. Since $\psi_0 = 0$, only the wavefunction components with odd site labels are non-zero. For these, we find that

$$\psi_{2j+1} = \frac{g}{J}\psi_{2j-1} = e^{-\log(\frac{J}{g})j}\psi_1. \quad (5.20)$$

Thus, the system hosts a localized edge mode at $E = 0$ with localization length ξ , given by

$$\xi = \frac{1}{\log\left(\frac{J}{g}\right)}. \quad (5.21)$$

This is true only for the semi-infinite chain. If we reintroduce the other edge of the chain, there is a second Majorana localized there. Both Majoranas hybridize, forming a fermion. Its energy ΔE is given by the wavefunction overlap of the Majoranas,

$$\Delta E \sim e^{-N/\xi}. \quad (5.22)$$

Clearly, this argument for nonzero values of g is consistent with the $g = 0$ case, as ξ goes to zero for $g \rightarrow 0$, leading to perfect localization at the boundaries of the chain. It also reveals that there is a topological phase transition at $g = J$. At that point, ξ diverges and the system no longer hosts edge modes. Due to the relationship of the spin model with the Kitaev chain, this also implies that the phase transition between paramagnet and ferromagnet occurs at the same point.

5.2.2 PERIODIC BOUNDARY CONDITIONS - PARITY SECTORS

We consider how the phase transition occurs in the case of periodic boundary conditions. We impose periodic boundary conditions by adding a term $-JZ_NZ_1$ into the Hamiltonian in Eq. (5.1),

$$H = -g \sum_{i=1}^N X_i - J \sum_{i=1}^N Z_i Z_{i+1}, \quad (5.23)$$

with $Z_{N+1} = Z_1$. The main difference compared to the open chain is that the lowest energy excitations now involve two domain walls and thus come with energy $4J$. However, the ground state degeneracy persists. We want to study how this is reflected in the fermion model. First we note a subtlety arising from the term $Z_N Z_1$. Previously, transforming the operators $Z_i Z_{i+1}$ yielded a simple quadratic Hamiltonian, as the string operators canceled. This does not happen for the boundary term, as we find

$$Z_N Z_1 = \prod_{i=1}^{N-1} e^{i\pi c_i^\dagger c_i} (c_N^\dagger + c_N)(c_1^\dagger + c_1) = -P(c_N^\dagger c_1 + c_N^\dagger c_1^\dagger + h.c.), \quad (5.24)$$

with P being the fermion parity operator or the total spin flip operator in Eq. (5.4) after applying the Jordan-Wigner transformation. Due to the appearance of P , the Hamiltonian no longer has a simple quadratic form. However, as the Hamiltonian is parity conserving, we may consider the Hamiltonian in each parity sector separately. Then, the Hamiltonians H_\pm become quadratic for each sector,

$$\begin{aligned} H_\pm = & -g \sum_{j=1}^N (1 - 2c_j^\dagger c_j) - J \sum_{j=1}^{N-1} (c_j^\dagger c_{j+1} + c_j^\dagger c_{j+1}^\dagger \\ & \mp c_N^\dagger c_1 \mp c_N^\dagger c_1^\dagger + h.c.), \quad P = \pm 1. \end{aligned} \quad (5.25)$$

Both Hamiltonians are solved by passing to momentum space,

$$c_j = \frac{1}{\sqrt{N}} \sum_k e^{ikj} \tilde{c}_k. \quad (5.26)$$

The difference lies in the values of k . In order for the Hamiltonians to be solved by Eq. (5.26), the values of k have to satisfy $e^{ikN} = 1$ for the odd parity sector ($P = -1$) and $e^{ikN} = -1$ for

the even sector ($P = 1$). Without loss of generality, we focus on the case of N being even. The momenta are then restricted to,

$$k = \frac{2\pi n}{N}, \quad n = -\frac{N}{2} + 1, \dots, -1, 0, 1, \dots, \frac{N}{2} \quad (P = -1), \quad (5.27)$$

$$k = \frac{2\pi}{N} \left(n - \frac{1}{2} \right), \quad n = -\frac{N}{2}, \dots, -1, 1, \dots, \frac{N}{2} \quad (P = 1). \quad (5.28)$$

The allowed values of k reflect the fact that the fermions effectively see periodic boundary conditions (PBC) in the odd parity sector and antiperiodic boundary conditions (ABC) in the even sector. After transforming to momentum space, the Hamiltonian becomes

$$\begin{aligned} H_- = & -g \sum_k^{\text{PBC}} (1 - 2\tilde{c}_k^\dagger \tilde{c}_k) - J \sum_k^{\text{PBC}} (2 \cos(k) \tilde{c}_k^\dagger \tilde{c}_k + e^{-ik} \tilde{c}_k^\dagger \tilde{c}_{-k} + h.c.) \\ & + 2(g - J) \left(\tilde{c}_0^\dagger \tilde{c}_0 - \frac{1}{2} \right) + 2(g + J) \left(\tilde{c}_\pi^\dagger \tilde{c}_\pi - \frac{1}{2} \right), \end{aligned} \quad (5.29)$$

$$H_+ = -g \sum_k^{\text{ABC}} (1 - 2\tilde{c}_k^\dagger \tilde{c}_k) - J \sum_k^{\text{ABC}} (2 \cos(k) \tilde{c}_k^\dagger \tilde{c}_k + e^{-ik} \tilde{c}_k^\dagger \tilde{c}_{-k}^\dagger + h.c.). \quad (5.30)$$

Notice that we made the 0- and π -momentum terms explicit in H_- , as the corresponding pairing terms vanish. They will play a special role in the following. First, we solve for the bulk modes. In both cases, the Hamiltonian may be written as

$$H_\pm = 2 \sum_{k>0} \Psi_k^\dagger \begin{pmatrix} g - J \cos(k) & iJ \sin(k) \\ -iJ \sin(k) & -g + J \cos(k) \end{pmatrix} \Psi_k, \quad (5.31)$$

with Nambu spinor $\Psi_k = (\tilde{c}_k, \tilde{c}_{-k}^\dagger)$. This yields the spectrum

$$\pm \epsilon_k = \pm 2 \sqrt{(g - J \cos(k))^2 + J^2 \sin^2(k)} \quad (5.32)$$

for the quasiparticles. We perform a basis transformation to new spinors $\tilde{\Psi}_k = (\tilde{d}_k, \tilde{d}_{-k}^\dagger)$ so that the Hamiltonian becomes diagonal,

$$H_\pm = \sum_{k>0} \tilde{\Psi}_k^\dagger \begin{pmatrix} \epsilon_k & 0 \\ 0 & -\epsilon_k \end{pmatrix} \tilde{\Psi}_k = \sum_{k \neq 0} \epsilon_k \left(\tilde{d}_k^\dagger \tilde{d}_k - \frac{1}{2} \right). \quad (5.33)$$

Now let us consider the ground state in each of the parity sectors. In the odd sector, it is necessary that at least one quasiparticle is occupied. In Eq. (5.29), we see that the mode at $k = 0$ comes with energy $\epsilon_0 = 2(g - J)$. If $J > g$, its energy ϵ_0 is negative while any other mode is

associated with a positive energy ϵ_k . Thus, the $k = 0$ mode is occupied in the ground state. In comparison, the even sector allows only for an even number of occupied single-particle states. Since all energies ϵ_k are positive, no mode is occupied in the ground state. If we now compare the ground state energies of both sectors, we see that for $J > g$, both are given by summing the quasiparticle energies ϵ_k over the Brillouin zone. The difference ΔE in the ground state energies arises as one evaluates the sum at integer values n for the odd sector and at half-integer values for the even sector. However, as both sums tend to the same integral, ΔE rapidly vanishes with increasing N ,

$$\Delta E = \frac{1}{2} \sum_k^{\text{PBC}} \epsilon_k - \frac{1}{2} \sum_k^{\text{ABC}} \epsilon_k \rightarrow 0 \quad \text{for } N \rightarrow \infty. \quad (5.34)$$

From the argument of the ground-state splitting in the spin model and the Kitaev chain, it is clear that ΔE vanishes exponentially with N .

We note the phase transition occurring at $g = J$. Once g exceeds J , the energy ϵ_0 becomes positive which leads to a finite ΔE for any N . Also, we see that due to the parity sector structure of the problem, excitations always appear in pairs. This is reminiscent of the fact, that domain walls in the spin chain also always appear pairwise due to the periodic boundary conditions.

5.3 LONGITUDINAL FIELDS

Lastly, we consider the effect of adding a random longitudinal field $h_i \in [-h, h]$. The Hamiltonian is then given by

$$H = -g \sum_{i=1}^N X_i - J \sum_{i=1}^{N-1} Z_i Z_{i+1} - \sum_{i=1}^N h_i Z_i. \quad (5.35)$$

Without longitudinal fields, the excitation spectrum in the ferromagnetic phase is primarily determined by the number of domain walls. This changes when adding a longitudinal field, as now the spins are trying to align themselves along the field. A description of the excitations solely via domain walls can thus no longer be sufficient. Let us see what happens in the fermionic picture. Applying the Jordan-Wigner transformation as before now yields

$$\begin{aligned} H = & -g \sum_{j=1}^N (1 - 2c_j^\dagger c_j) - J \sum_{j=1}^{N-1} [c_j^\dagger c_{j+1} + c_j^\dagger c_{j+1}^\dagger + h.c.] \\ & - \sum_{i=1}^N h_i \prod_{j=1}^{i-1} (1 - 2c_j^\dagger c_j) (c_i + c_i^\dagger) \end{aligned} \quad (5.36)$$

First, the longitudinal field introduces odd powers of fermionic operators into the Hamiltonian. We may however recover an even number of fermionic operators by introducing an ancilla Majorana $a + a^\dagger$ via a unitary transformation as follows [95],

$$c_i \rightarrow e^{i\frac{\pi}{4}(a+a^\dagger)} c_i e^{-i\frac{\pi}{4}(a+a^\dagger)} = i(a + a^\dagger) c_i. \quad (5.37)$$

The more striking issue that is introduced by the longitudinal field is the appearance of quartic and higher order terms in the Hamiltonian, giving rise to interactions between the fermions. The system can thus not be described by N quasiparticle excitations. This connects to the fact that the excitation spectrum is no longer determined by domain walls in the spin model.

The disorder-free quantum Ising model in its fermionic formulation may feature Majorana zero modes at its boundaries. As a consequence, not only the ground state is degenerate, but each excited state is as well. While the quasiparticle description fades under the longitudinal field, it is still possible for the system to have a (nearly) degenerate spectrum. It is thus an interesting question to ask to which degree the phase of the system is stable against parity-breaking perturbations such as longitudinal disorder. In the following two chapters, we will explore this question for a driven version of the transverse field Ising model. Before that, we introduce basic concepts of Floquet theory.

5.4 FLOQUET THEORY

We consider a general, time-periodic Hamiltonian $H(t)$ with period T ,

$$H(t) = H(t + T). \quad (5.38)$$

The time evolution of a quantum state $|\psi(t)\rangle$ is dictated by the Schrödinger equation,

$$i\hbar \frac{d}{dt} |\psi(t)\rangle = H(t) |\psi(t)\rangle. \quad (5.39)$$

The solution to Eq. (5.39) may be written in terms of the state at an initial time t_0 and the time evolution operator $U(t, t_0)$,

$$|\psi(t)\rangle = U(t, t_0) |\psi(t_0)\rangle, \quad U(t, t_0) = \mathcal{T} \exp \left\{ -\frac{i}{\hbar} \int_{t_0}^t dt' H(t') \right\}, \quad (5.40)$$

with \mathcal{T} being the time-ordering operator [96]. We may separate the time t into an integer number of periods mT as well as a micromotion time $t_1 < T$. Using the composition property of the time evolution operator, we write U as

$$U(t, t_0) = U(t_1 + mT + t_0, t_0) = U(t_1 + mT + t_0, mT + t_0) U(mT + t_0, t_0). \quad (5.41)$$

5 Periodically driven quantum Ising models

This decomposes the time evolution into two separate parts. The first part $U(mT + t_0, t_0)$ describes how the system evolves over long times (slow dynamics), while the second part governs the micromotion happening in between periods (fast dynamics) [97]. Here, we will be focusing exclusively on the slow dynamics. We will also be setting $t_0 = 0$ and $\hbar = 1$ from now on.

Since the Hamiltonian is time-periodic, we may decompose the time evolution operator further,

$$U(mT, 0) = [U(T, 0)]^m = U_F^m. \quad (5.42)$$

Here, we defined the Floquet operator $U_F = U(T, 0)$. As it is a unitary operator, the Floquet operator can always be written as

$$U_F = e^{-iH_F T}, \quad (5.43)$$

with H_F being the Floquet Hamiltonian [97]. This description is analogous to the time evolution induced by a time-independent Hamiltonian H_F over a time T . Thus, by focusing only on the time evolution over integer periods mT , the problem becomes effectively time-independent.

We further introduce the eigenvalues and eigenstates of the Floquet operator. The eigenvalues of any unitary matrix are complex numbers with modulus 1. Applying the Floquet operator to its eigenstate $|\psi_n\rangle$ thus gives the eigenvalue equation

$$U_F |\psi_n\rangle = e^{-i\epsilon_n T} |\psi_n\rangle. \quad (5.44)$$

As the eigenphases ϵ_n are only determined modulo $2\pi/T$, they are referred to as quasienergies (analogously to the quasimomenta in Bloch theory). The eigenstates $|\psi_n\rangle$ are called Floquet states [97].

5.4.1 KICKED MODELS

The periodically driven systems we consider in this thesis are described by so-called kicked models. The Floquet operator U_F of a kicked model is of the following structure,

$$U_F = e^{-iH_0 T} e^{-iH_1 T} e^{-iH_2 T} \dots, \quad (5.45)$$

with the H_i being time-independent hermitian operators. In general, the H_i do not commute. Thus, the dynamics is not captured by a trivial Floquet Hamiltonian $\sum_i H_i$, but will show non-trivial features specific to driven systems. One way of realizing such a time-evolution operator is via a time-dependent Hamiltonian $H(t)$ of the form

$$H(t) = T \sum_{j=0}^{\infty} \left[H_0 \delta(t - jT) + H_1 \delta\left(t - \left(j + \frac{1}{2}\right)T\right) \right]. \quad (5.46)$$

This drive applies time-independent Hamiltonians H_0 and H_1 at integer and half-integer multiples of the period T . By using Eq. (5.40), we find that $H(t)$ yields a Floquet operator of the structure given in Eq. (5.45). The generalization to more than two kicks is straightforward.

6 ROBUST SPECTRAL π PAIRING IN THE RANDOM-FIELD FLOQUET QUANTUM ISING MODEL

The results of this chapter have been published in Ref. [3]. This project was a collaboration with other co-authors, including another PhD student, Harald Schmid [98]. The author of this thesis conducted numerical calculations in parallel to H. Schmid. The final numerical data and figures in [3] were generated by H. Schmid. The author here reproduces these independently. The author developed the perturbation theory used in [3] for the general case. The application to the splitting distribution was conducted by H. Schmid. The author contributed to the draft. The presented data is available at [35].

6.1 INTRODUCTION

In the previous chapter, we discussed the properties of the transverse field quantum Ising model in its spin version as well as its fermionic formulation for both open and periodic boundary conditions. Here we present a study on the Floquet quantum Ising model, defined via the Floquet operator¹

$$U_F = \exp\left\{\frac{i\pi}{2} \sum_{i=1}^N h_i Z_i\right\} \exp\left\{\frac{i\pi g}{2} \sum_{i=1}^N X_i\right\} \exp\left\{\frac{i\pi J}{2} \sum_{i=1}^{N-1} Z_i Z_{i+1}\right\}. \quad (6.1)$$

The operator is generated by successive and time-periodic application of the transverse field- and the coupling part of the transverse field Ising model, as well as a disordered longitudinal field.

Our study is motivated by a recent experiment [99], in which the Floquet operator in Eq. (6.1) was implemented on a quantum processor consisting of 47 superconducting qubits. In the experiment, an initially prepared random product-state of Pauli- z eigenstates evolves stroboscopically over many cycles and correlation functions of the form $\overline{\langle Z_j(0) Z_j(t) \rangle}$ are measured, with $\langle \dots \rangle$ indicating the expectation value in the initial state and $\overline{(\dots)}$ the average over disorder. For all qubits, oscillations at half the driving frequency were observed. While the bulk correlation functions rapidly decayed, the boundary correlation functions showed a surprising longevity limited only by the finite lifetime of the qubits. The authors associate the long-lived boundary

¹The period T is set to 1 for simplicity.

correlations with stable π -Majorana edge modes. As Majorana modes are typically protected by fermion parity, the stability is surprising, given that the drive includes a fermion parity-breaking longitudinal field.

In this chapter, we will first go over the clean version of the Floquet quantum Ising model and explain its phase diagram. We will further calculate boundary correlation functions of the kind measured in Ref. [99], and explain the longevity via an analysis of the distribution function of the spectral pairings of the Floquet operator.

6.2 CLEAN MODEL

We define the Floquet operator of the clean model $U_{F,0}$ via the Floquet operator in Eq. (6.1) in the absence of disordered longitudinal fields,

$$U_{F,0} = U_F(h = 0) = \exp\left\{\frac{i\pi g}{2} \sum_{i=1}^N X_i\right\} \exp\left\{\frac{i\pi J}{2} \sum_{i=1}^{N-1} Z_i Z_{i+1}\right\}. \quad (6.2)$$

In this limit, the Floquet quantum Ising model becomes integrable, as it maps to a Floquet Kitaev chain via a Jordan-Wigner transformation [94, 100, 101]. This is discussed in detail in B.1. Here we focus on the results. After applying the Jordan-Wigner transformation, the single-particle spectrum is calculated via a diagonalization of the Bogoliubov-de Gennes Hamiltonian. For the bulk modes, this may be done in momentum representation, analogously to the calculation in Sec. 5.2.2. The corresponding quasiparticle operators γ_k satisfy

$$U_{F,0}^\dagger \gamma_k U_{F,0} = e^{-i\epsilon_k} \gamma_k, \quad (6.3)$$

with the quasienergies ϵ_k given by

$$\cos(\epsilon_k) = \cos(\pi J) \cos(\pi g) + \sin(\pi J) \sin(\pi g) \cos(k). \quad (6.4)$$

We illustrate the bulk spectrum in Fig. 6.1(a) for various parameters. Here we see that the spectrum is gapped, both around quasienergies 0 and $\pm\pi$. Depending on the parameters, these gaps may be either trivial or topological. This constitutes the phase diagram of the model, shown in Fig. 6.1(b). We note that the phase diagram is periodic under $g \rightarrow g+2$ and $J \rightarrow J+2$ and symmetric under $g \rightarrow -g$ and $J \rightarrow -J$, which justifies the considered limited parameter range in Fig. 6.1(b). In the following discussion, we will thus limit the values of g and J to the interval $[0, 1]$. The topological phases are signaled by a pair of levels inside either gap, associated with quasiparticle edge modes. For $g < J$, we find Majorana zero modes (MZM) localized at the boundaries of the open chain. This can be understood by noting that the Floquet model approaches the time-independent Kitaev chain model in the limit of $g, J \ll 1$, which was discussed in Sec. 5.2.1. If $1 - g < J$, the chain hosts Majorana π modes (MPM) with corresponding levels in the

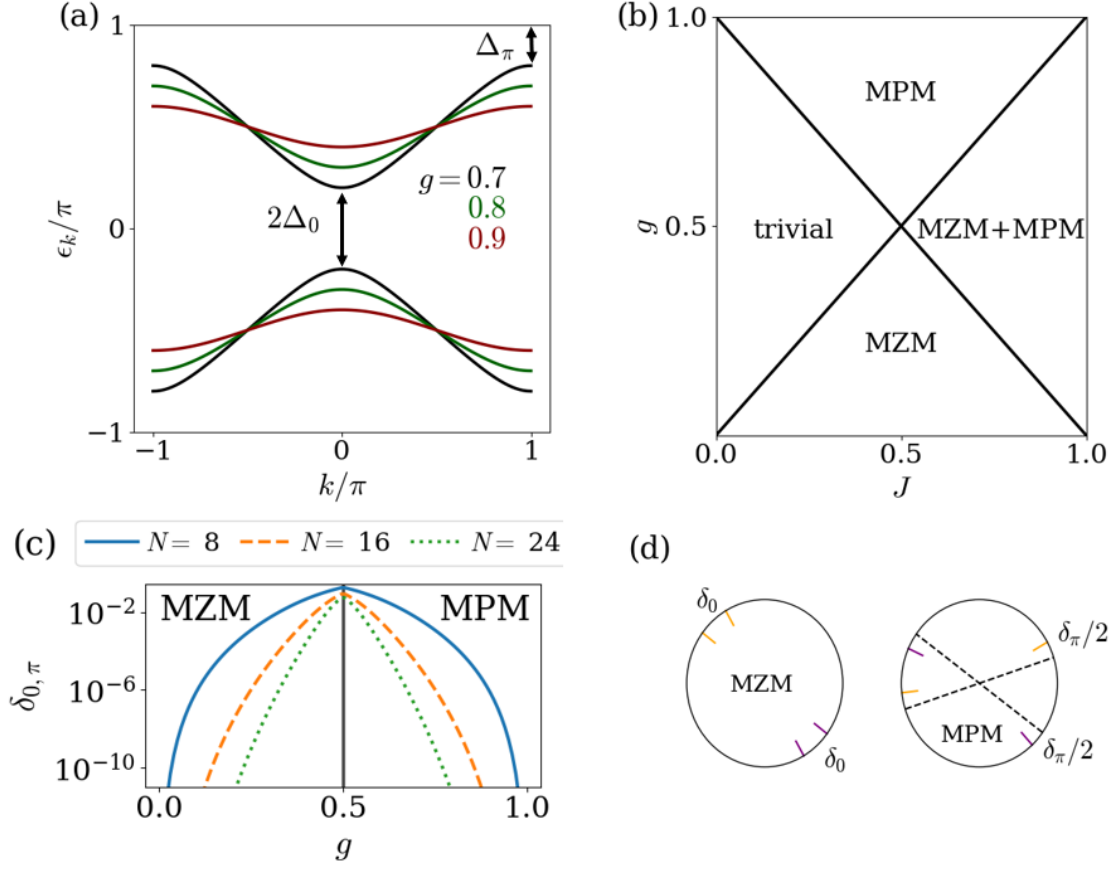


Figure 6.1: Clean Floquet quantum Ising model. (a) Single-particle spectrum ϵ_k of the bulk modes. (b) Phase diagram of the Floquet model. (c) Hybridization splittings δ_0 ($g < 0.5$) and δ_π ($g > 0.5$) plotted for different system sizes N and transverse fields g . (d) Sketch of the many-body pairing in both the MZM and MPM phase. Parameters: (a,c) $J = 0.5$.

gap around $\pm\pi$ [102]. These excitations are exclusively found in the periodically driven version of the transverse field Ising model. In the MZM+MPM phase, both conditions are satisfied and the chain hosts both MZMs and MPMs, whereas no edge modes are present in the trivial phase.

As we discussed in Sec. 5.2.1, the quasienergy of the MZMs is zero, up to a hybridization splitting $\delta_0 \sim e^{-N/\xi_0}$. Likewise, we find a hybridization splitting $\delta_\pi \sim e^{-N/\xi_\pi}$ for the MPMs, shifting their energy away from $\pm\pi$. We present the splittings in Fig. 6.1(c) for various parameters. The symmetry between δ_0 and δ_π is due to the localization lengths ξ_0 and ξ_π mapping into each other under $g \leftrightarrow 1 - g$. If the system is in one of the Majorana mode hosting phases, the quasienergies E_n of the many-body eigenstates of the Floquet operator $U_{F,0}$ come in pairs. Up to the hybridization splittings $\delta_{0,\pi}$, the energies are either degenerate (MZM) or shifted by π (MPM), as illustrated in Fig. 6.1(d). This is a particular example within the wider framework of strong modes in interacting, kicked spin models [103–107].

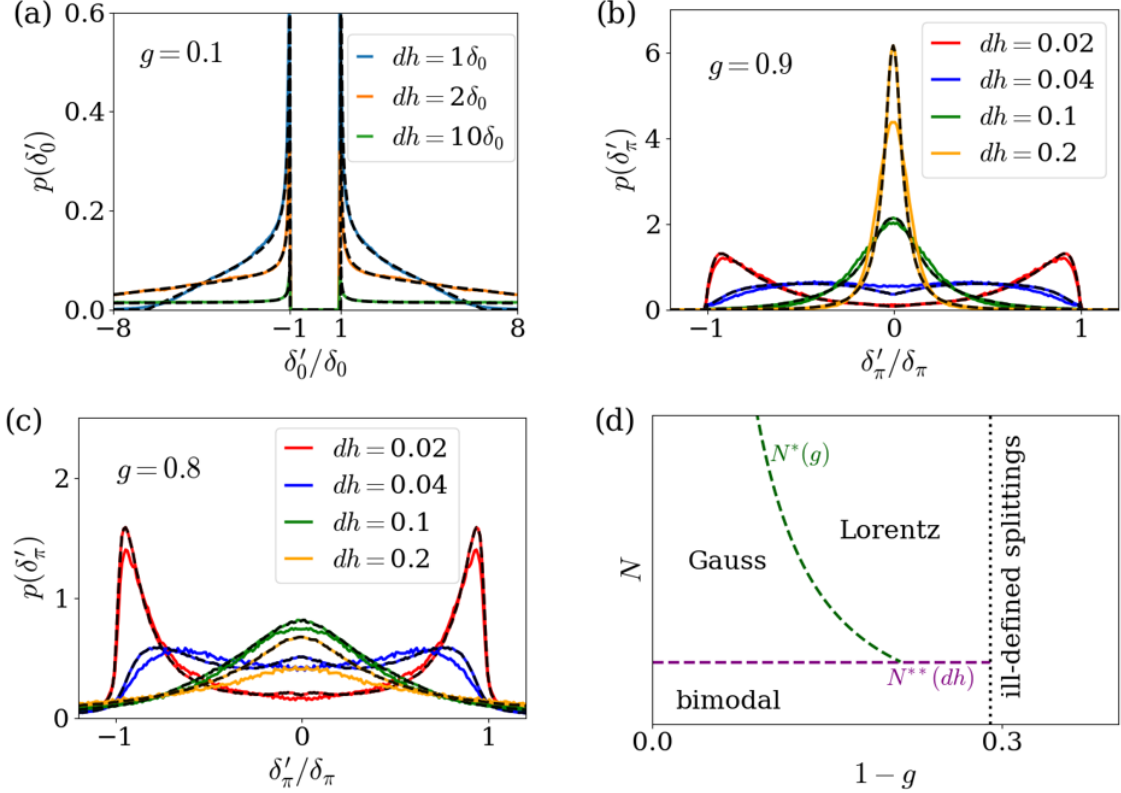


Figure 6.2: Splitting distributions in the MZM and MPM phase with random longitudinal fields. (a) MZM splitting distribution $p(\delta'_0)$ for different longitudinal field strengths of the order of the nominal splitting $\delta_0 \simeq 5 \cdot 10^{-10}$ (full lines), with corresponding analytical distributions as given in Eq. (6.6) (black dashed lines). (b,c) MPM splitting distributions for different longitudinal field strengths of the order of unity (full lines), as well as corresponding distribution functions obtained via self-consistent perturbation theory (dashed lines). (d) "Phase diagram" for the MPM splitting distributions as a function of N and g , with fixed dh . Parameters: $N = 12$, $J = 0.5$, $\mathcal{N} = 10^3$ (number of disorder realizations), (b) $\delta_\pi \simeq 5 \cdot 10^{-10}$ (c) $\delta_\pi \simeq 2 \cdot 10^{-6}$.

6.3 DISORDER INDUCED SPLITTING DISTRIBUTIONS

Motivated by the experiment conducted in Ref. [99], we study the effects of a disordered longitudinal field on the spectral pairings. This is of particular interest for two reasons. On the one hand, inaccurate implementation of gate operations commonly lead to the presence of disorder, making robustness against it an important issue in applications and experiments. Second, the introduction of disorder raises theoretical questions in the context of strong modes, particularly since random longitudinal fields break the fermion parity protecting the boundary modes of the clean model as well as its integrability.

We now consider the full Floquet operator U_F given in Eq. (6.1), with the longitudinal fields h_j drawn independently from a box distribution, $h_j \in [-dh, dh]$. As we discussed in Sec. 5.3, longitudinal fields give rise to interactions in the fermion model, making the hybridization

splittings inaccessible in the single-particle picture. However, we find that the many-body level pairings in the MZM and MPM phases approximately persist. Our numerical results are presented in Fig. 6.2. Here we find fundamental differences in the distribution functions of the MZM and MPM splittings $\delta'_{0,\pi}$. In the MZM phase, small longitudinal fields of the order of δ_0 substantially (and strictly) enhance the splittings of the level pairings, see Fig. 6.2(a). In contrast, longitudinal disorder of order δ_π has essentially no effect on the splitting distribution in the MPM phase as can be seen in Fig. 6.2(b),(c). Even for longitudinal fields of order unity, the splittings are hardly increased. Instead, we find that the bulk of the distribution $p(\delta'_\pi)$ lies within the range of $[-\delta_\pi, \delta_\pi]$. If g is close enough to 1, we find that the splittings are strictly reduced, as shown in Fig. 6.2(b).

6.3.1 FLOQUET PERTURBATION THEORY

We may understand the sensitivity of the MZM splittings as well as the robustness of the MPM splittings through a low order stroboscopic Floquet perturbation theory. We consider $U_F = e^{iV}U_{F,0}$ with V being the disordered longitudinal field. By expanding the quasienergies E_n to quadratic order in V , we find $E_n = E_n^{(0)} + E_n^{(1)} + E_n^{(2)} + \dots$ with

$$E_n^{(1)} = \langle n^{(0)} | V | n^{(0)} \rangle, \quad E_n^{(2)} = \sum_{m \neq n} \frac{|\langle n^{(0)} | V | m^{(0)} \rangle|^2}{2 \tan \frac{E_n^{(0)} - E_m^{(0)}}{2}}, \quad (6.5)$$

with $|n^{(0)}\rangle$ being the unperturbed eigenstates of the Floquet operator. We derive these expressions explicitly in B.2. Importantly, we assume that the quasienergies are non-degenerate. Otherwise one first diagonalizes the perturbation V in the degenerate subspace. Evidently, coupling two nearby levels with energy difference δ_0 leads to a small denominator in $E_n^{(2)}$, whereas one finds a large denominator $\tan \frac{\pi - \delta_\pi}{2} \simeq \frac{2}{\delta_\pi}$ for levels with quasienergy difference $\pi - \delta_\pi$. In fact, π partnered states repel both ways around the unit circle, reducing the second-order correction $E_n^{(2)}$ and sending the splittings closer to π .

In the following, we will denote the many-body eigenstates of $U_{F,0}$ as $|n^e\rangle$ and $|n^o\rangle$. These states share the same quasiparticle occupations $\gamma_\alpha^\dagger \gamma_\alpha$, apart from the edge mode $n_{0,\pi} = \gamma_{0,\pi}^\dagger \gamma_{0,\pi}$, with $n_{0,\pi} = 0$ for $|n^e\rangle$ and $n_{0,\pi} = 1$ for $|n^o\rangle$. As the Z_j spin operators flip the parity of the many-body states, the diagonal matrix elements² $\langle n^e | V | n^e \rangle$ vanish, while we generally find nonzero matrix elements $\langle n^e | V | n^o \rangle$ coupling the partner states.

For the MZM phase, the discussion reduces to that of a two-level system, given that the splitting δ_0 and disorder strength dh are small compared to the many-body level spacing. Diagonalizing the effective Hamiltonian in the degenerate subspace spanned by $|n^e\rangle$ and $|n^o\rangle$ yields the perturbed splittings $\delta'_0 = \sqrt{\delta_0^2 + 4|\langle n_0^e | V | n_0^o \rangle|^2}$. With increasing disorder V , this interpolates between first- and second-order perturbation theory. Once the perturbation exceeds δ_0 , the eigenstates

²Analogously for $|n^o\rangle$.

of $U_{F,0}$ evolve into perturbed eigenstates $|n_{\pm}\rangle \simeq \frac{1}{\sqrt{2}}(|n^e\rangle + |n^o\rangle)$. Considering this, we may derive the distribution function of the perturbed splittings analytically,

$$p(\delta'_0) = \frac{|\delta'_0|}{2v_0} \left(\frac{1}{\sqrt{\delta_0'^2 - \delta_0^2}} - \frac{1}{2v_0} \right) \theta(|\delta'_0| - \delta_0) \theta\left(\sqrt{\delta_0^2 + 4v_0^2} - |\delta'_0|\right), \quad (6.6)$$

with $v_0 \simeq \langle n_0^e | V | n_0^o \rangle$. The detailed derivation is shown in B.3.1. We find that, while the bulk of the distribution is sensitive to the particular choice of the disorder distribution, the square-root singularity at $\delta'_0 = \delta_0$ is generic. In Fig. 6.2(a), we find that the expression in Eq. (6.6) is in excellent agreement with numerical data.

Turning to the MPM phase, we notice that the coupling between π partner states is negligible. We thus also need to consider couplings between states belonging to different π pairs. Calculating the splittings $\delta_n = E_n^e - E_n^o + \pi$ in second-order perturbation theory then yields,

$$\begin{aligned} \delta_n \simeq & \delta_\pi + \sum_m \left\{ \frac{|\langle n^e | V | m^o \rangle|^2}{2 \tan \frac{E_n^e - E_m^o}{2}} - \frac{|\langle n^o | V | m^e \rangle|^2}{2 \tan \frac{E_n^o - E_m^e}{2}} \right\} \\ & + \sum_{m \neq n} \left\{ \frac{|\langle n^e | V | m^e \rangle|^2}{2 \tan \frac{E_n^e - E_m^e}{2}} - \frac{|\langle n^o | V | m^o \rangle|^2}{2 \tan \frac{E_n^o - E_m^o}{2}} \right\}. \end{aligned} \quad (6.7)$$

Here we made the perturbation theory self-consistent by inserting the exact quasienergies $E_n^{e,o}$ into the energy denominators. We justify this by observing that there are many relevant couplings between different pairs of the same order, which may thus be reasonably accounted for in a self-consistent scheme. We may readily solve Eq. (6.7) numerically after linearizing in the small splittings δ_n . The results are displayed in Fig. 6.2(b),(c). We find that the self-consistent perturbation theory reproduces the data of the exact diagonalization notably well for a wide range of disorder strengths. Particularly, it replicates the transition from a bi-modal distribution peaked at $\delta'_\pi = \pm\delta_\pi$ to the narrower distribution with a single peak at $\delta'_\pi = 0$ with increasing disorder.

We find that the distribution peaked at $\delta'_\pi = 0$ is approximately Gaussian, provided that g is close enough to 1. For larger values of $1 - g$, it becomes Lorentzian. We present a 'phase diagram' in Fig. 6.2(d), which we explain via Eq. (6.7). If g is close to 1, the second sum in Eq. (6.7) is negligible. We may then linearize the equation to

$$\delta_n = \delta_\pi - \sum_m (\delta_n + \delta_m) \Sigma_{nm}, \quad (6.8)$$

with the strictly positive-valued matrix Σ ,

$$\Sigma_{nm} = \frac{|\langle n^e | V | m^o \rangle|^2}{4 \cos^2 \frac{E_n^e - E_m^o}{2}}. \quad (6.9)$$

Replacing the splittings with their typical value, i.e. $\delta_n \approx \delta_{\text{typ}}$ and $\delta_m \approx \pm\delta_{\text{typ}}$, we find for the typical splittings,

$$\delta_{\text{typ}} \approx \frac{\delta_\pi}{1 + \langle \sum_m \Sigma_{n,m} \rangle_n}, \quad (6.10)$$

with $\langle \dots \rangle_n$ denoting an average over n . Typically, the splittings are thus reduced by the longitudinal fields. The transition from bi- to unimodal distribution occurs for $\Sigma \sim 1$. We find numerically, that this happens for system sizes $N^{**} \sim 1/\ln(h)$, approximately independent of the transverse field g .

The single-particle bulk spectrum becomes wider, the further g deviates from 1, as illustrated in Fig. 6.1(a). Consequently, the many-body quasienergies E_n cover the entire range of $[-\pi, \pi]$ if $N > N^* \sim 1/(1-g)^2$. In this case, the second sum in Eq. (6.7) becomes significant due to occurrences of small energy denominators. The emerging Lorentzian distribution may then be interpreted as a stable Levy distribution [108]. We point out that the Majorana splittings are well-defined under the condition that they are much smaller than the many-body level spacing, $e^{-N/\xi_\pi} < 2^{-N}$. For $J = 0.5$ this is satisfied when $g > 0.71$.

6.4 BOUNDARY CORRELATION FUNCTIONS

Next, we consider correlation functions of the boundary spin operator,

$$G(t) = \langle Z_1(t)Z_1(0) \rangle. \quad (6.11)$$

Taking the average over all initial states³, the correlation function may be expressed as,

$$G(t) = \frac{1}{2^N} \sum_{n,m} |\langle n|Z_1|m \rangle|^2 e^{-i(E_n - E_m)t}. \quad (6.12)$$

Here the sums are over all 2^N eigenstates of the Floquet operator. We first calculate the correlation function $G(t)$ for the clean model, shown in Fig. 6.3(a),(b). For short times, we find a near constant correlation function in the MZM phase, while period-2 oscillations are observed in the MPM phase. We further find that at large times and in both regimes, the correlation functions oscillate at a frequency corresponding to the inverse hybridization splittings $1/\delta_{0,\pi}$.

In the experiment conducted in Ref. [99], the correlation function $G(t)$ persists for times of the order of the qubit lifetime ($\ll 1/\delta_{0,\pi}$) in the presence of longitudinal fields, independent of the phase. This is a surprising result, considering the dramatic differences in the response of MZM and MPM splittings to longitudinal disorder. Indeed, the mechanisms underlying the stability of $G(t)$ are very different, leading to notably distinct long time behavior in the two phases.

³Or we calculate the correlation function in the infinite temperature state.

6 Robust spectral π pairing in the random-field Floquet quantum Ising model

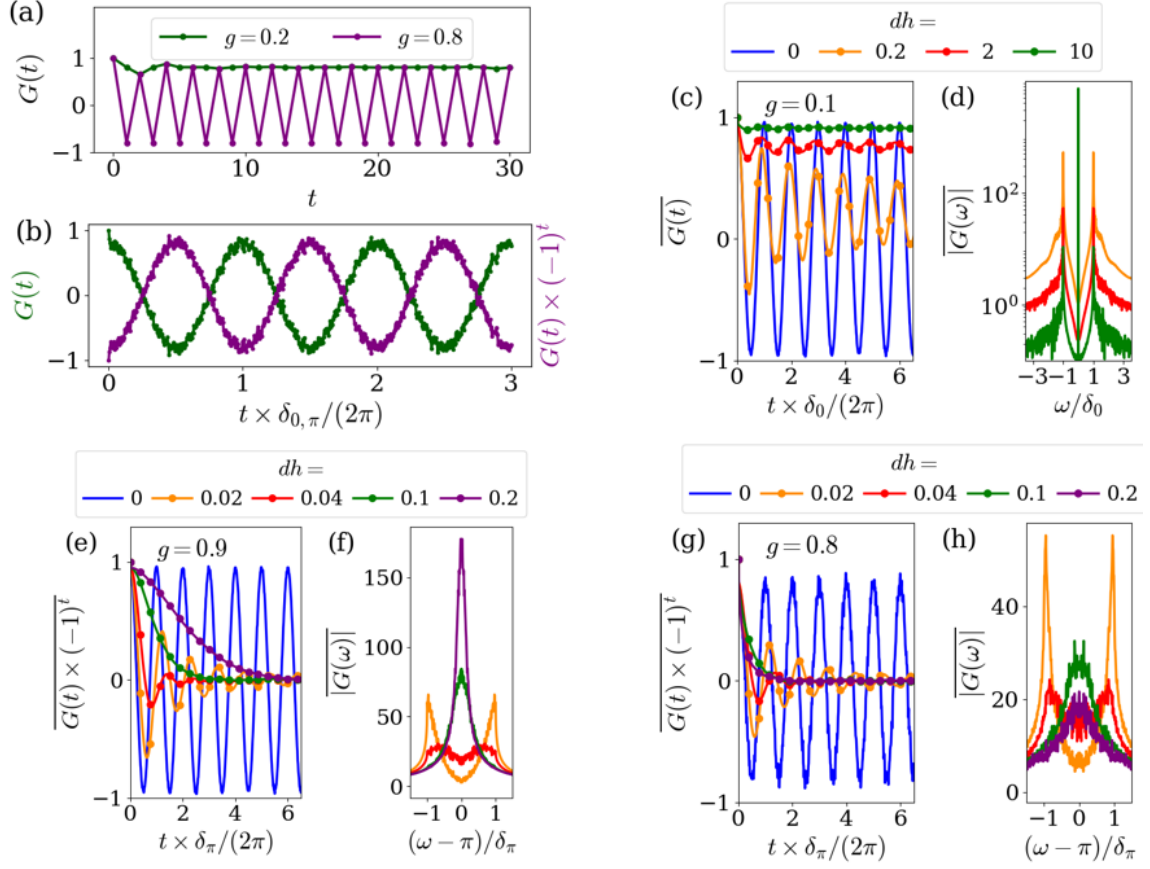


Figure 6.3: Boundary spin-spin correlation functions. (a),(b) Correlation function $G(t)$ of the clean model in the MZM (green) and MPM (purple) regime, for short and long times. (c),(d) Disorder-averaged correlation functions $\overline{G}(t)$ in the MZM regime with different longitudinal field strengths dh , with corresponding Fourier transforms $\overline{G}(\omega)$. (e)-(h) Disorder-averaged correlation functions $\overline{G}(t) \times (-1)^t$ for different longitudinal field strengths dh , with corresponding Fourier transforms $\overline{G}(\omega)$. Parameters: (a),(b) $N = 10$, $J = 0.5$, (c)-(h) $N = 12$, $J = 0.5$, $\mathcal{N} = 10$.

Starting with the MZM phase, we find that a longitudinal field effectively polarizes the boundary spins. The spins in the bulk of the chain on the other hand remain unpolarized due to the existence of mobile domain walls in generic states. In connection to this, first-order perturbation theory yields perturbed eigenstates $|n_{\pm}\rangle$ with nonzero diagonal matrix elements of the boundary spin operators. Consequently, the diagonal terms in Eq. (6.12) add time-independent contributions to the correlation function, given that the longitudinal field is large compared to the hybridization splitting of the clean chain. We present results for $G(t)$ in the MZM phase in Fig. 6.3(c),(d). Corresponding to the polarization of the boundary spins, we find that the Fourier transform of $G(t)$ develops a dominant peak at $\omega = 0$. On the other hand, the longitudinal fields significantly decrease the amplitude of the oscillations connected to the spectral pairings.

In the MPM phase, we find that the subharmonic period-two oscillations remain stable against longitudinal disorder, while the enveloping slow oscillations decay, as shown in Fig. 6.3(e)-(h). The reason for this is that the correlation function in Eq. (6.12) is dominated by terms in which $|n\rangle$ and $|m\rangle$ are MPM partner states. Correspondingly, the envelope of $G(t)$ is just the Fourier transform of the splitting distribution, which is evident by a comparison of the Fourier transform $G(\omega)$ in Fig. 6.3(f),(h) and 6.2(b),(c). For bimodal distributions, we find that damped Majorana oscillations persist with a power-law tail, due to the cutoff of the splitting distribution at $\delta'_\pi = \delta_\pi$. On the other hand, we find a non-oscillatory Gaussian (exponential) decay for parameters in which the splitting distribution becomes a unimodal Gaussian (Lorentzian) distribution. We conclude that in the MPM phase, the correlation function $G(t)$ directly reflects the robustness of the spectral pairings to longitudinal disorder.

6.5 TRANSVERSE FIELD DISORDER

In the previous sections, we discussed how the spectral pairing in the MPM phase is dramatically more stable against a disordered longitudinal field than its MZM counterpart. Here, we want to show that this is not true for any perturbation. For this, we consider the Floquet operator of the clean chain now perturbed by an additional disordered transverse field, $U_F = U_{\delta g} U_{F,0}$ with $U_{dg} = \exp\left\{-\frac{i\pi}{2} \sum_{i=1}^N g_i X_i\right\}$. The random transverse fields g_i are drawn independently from a box distribution $[-dg, dg]$.

Transverse fields fundamentally differ from longitudinal fields in two ways. First, they conserve the spin-flip symmetry of the clean chain and hence the fermion parity of the fermionic model. Second, they do not introduce interactions to the fermionic model, so that the spectral pairing may be extracted from a single-particle framework. Consequently, we find the same splitting $\delta_{0,\pi}$ throughout the entire many-body spectrum in both the MZM and MPM phase.

We present numerically generated splitting distributions across the disorder ensemble in the MZM and MPM phases under transverse disorder in Fig. 6.4(a). We find a broad distribution for the splittings in both phases, which we identify as log-normal distributions. Analogously to the clean chain, the distribution functions of MZM and MPM splittings become identical under $g \rightarrow 1 - g$. We illustrate this further in Fig. 6.4(b), where we show the average and variance of $\ln \delta_{0,\pi}$ as a function of N for corresponding parameter values in the MZM and MPM phases. We find that the cumulants of the log-normal splitting distributions are (up to a constant) well approximated by

$$\overline{\ln \delta_{0,\pi}} = -\frac{N}{\xi_{0,\pi}}, \quad \text{var} \ln \delta_{0,\pi} = \frac{N}{\ell}, \quad (6.13)$$

with $\xi_{0,\pi}$ being the Majorana localization length given in Eq. (B.16). The mean-free path ℓ is accurately described by

$$\ell = \frac{3}{\pi^2 (dg)^2} \sin^2(\pi g). \quad (6.14)$$

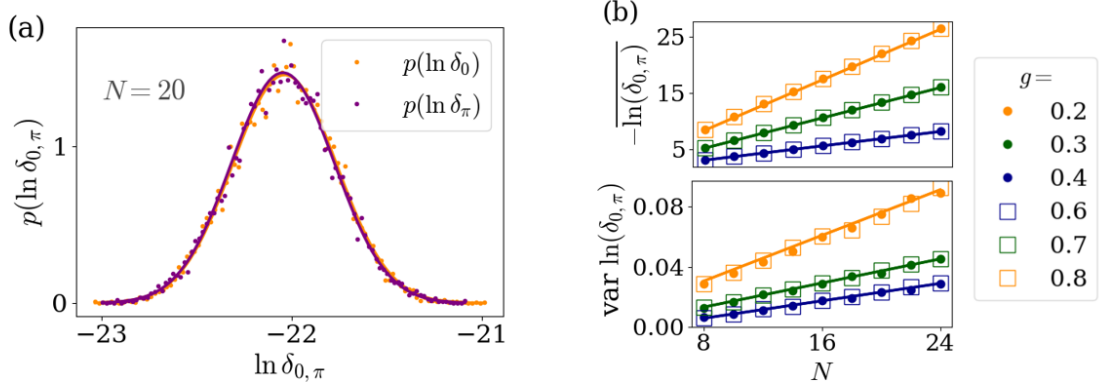


Figure 6.4: MZM and MPM splitting distributions under random transverse field. (a) Splitting distributions in the MZM (orange) and MPM (purple) regimes (dots) with corresponding log-normal fits (full lines). (b) Mean and variance of $\ln \delta_{0,\pi}$. Parameters: (a) $g = 0.2$ (MZM), $g = 0.8$ (MPM). (a),(b) $J = 0.5$, $\delta g = 0.02$, $N = 10^4$.

These findings are closely related to analogous results of the corresponding non-driven Hamiltonian problem [109].

Our results suggest that Majorana zero and π modes react in the same way to perturbations that conserve fermion-parity, but behave differently under parity-breaking perturbations. We can show this explicitly by decomposing the transverse field into $g = 1 + \delta g$, with δg being small. The kick operator U_g applying the transverse field can then be written as

$$U_g = \exp \left\{ -\frac{i\pi(1 + \delta g)}{2} \sum_{i=1}^N X_i \right\} = P U_{\delta g}, \quad (6.15)$$

with $P = \prod_{i=1}^N X_i$ being the fermion-parity operator and $U_{\delta g}$ applying a transverse field corresponding to the MZM phase. Now consider kick perturbations e^{-iV_e} and e^{-iV_o} that are either even or odd under fermion-parity, i.e. $V_e P = P V_e$ and $V_o P = -P V_o$. Using Eq. (6.15), we calculate the time-evolution operator over two periods for the different perturbations as follows,

$$V_e : U_F^2 = e^{-iV_e} U_g U_J e^{-iV_e} U_g U_J = e^{-iV_e} U_{\delta g} U_J e^{-iV_e} U_{\delta g} U_J, \quad (6.16)$$

$$V_o : U_F^2 = e^{-iV_o} U_g U_J e^{-iV_o} U_g U_J = e^{-iV_o} U_{\delta g} U_J e^{iV_o} U_{\delta g} U_J, \quad (6.17)$$

with $U_J = \exp \left\{ -\frac{i\pi J}{2} \sum_{i=1}^{N-1} Z_i Z_{i+1} \right\}$ commuting with P . For even perturbations V_e , we find that the time evolution over two cycles in the MPM phase is equivalent to the corresponding evolution in the MZM phase. This implies equal splittings $\delta_{0,\pi}$ under even perturbations, which is consistent with the equal splitting distributions under transverse disorder. On the other hand, for odd perturbations V_o , we find that one of the perturbation terms in U_F^2 enters with a different sign, compared to the time evolution in the MZM phase. Thus, in the MZM phase,

the perturbations V_o add up over the course of the time evolution, while in the MPM phase, consecutive perturbation terms act with opposite polarity, effectively reducing perturbation effects. This is in agreement with our findings for the splitting distributions under longitudinal disorder.

6.6 CONCLUSION

In this chapter, we showed that the π -pairing in the MPM phase remains exponentially accurate in the system size N , even in the presence of disordered longitudinal fields far exceeding the nominal MPM splitting δ_π . This robustness, which is in stark contrast to the sensitivity of the MZM splittings, is explained in terms of the level repulsion of the many-body quasienergies on the unit circle, without using the notion of prethermalization [99, 104, 110].

The zero pairing in the quantum Ising model has been proposed as a platform for qubit realization, notably through implementations using chains of Josephson junctions [111–113]. However, unlike Majorana-based qubits [114–116], such systems lack protection against symmetry-breaking longitudinal fields. This highlights the potential of the robust π -pairing of the Floquet model for applications in quantum information processing.

7

SUBHARMONIC SPIN CORRELATIONS AND SPECTRAL PAIRING IN FLOQUET TIME CRYSTALS

Parts of this chapter have been previously published in Ref. [4]. This project was a collaboration with other co-authors. H. Schmid and A.-G. Penner both developed independent code for the numerical calculations of spectra and correlation functions in parallel and in close discussions. H. Schmid produced the final data and Figs. 1, 3(b)-(d). A.-G. Penner produced the final data and Figs. 2, 3(a), 4. H. Schmid performed the analytical calculations in the non-interacting case and derived the analytical result for the correlation functions, in close discussion with A.-G. Penner. A.-G. Penner performed the analytical calculations in the interacting case, in close discussion with H. Schmid. Both H. Schmid and A.-G. Penner closely discussed the results of the splitting distribution and the correlation functions with the other authors. H. Schmid and A.-G. Penner wrote a first draft. All authors contributed to the final manuscript. The results of this chapter appear in the doctoral thesis of H. Schmid [3]. Codes and data for the figures are available in [35].

7.1 INTRODUCTION

The possibility of spontaneous breaking of time translation symmetry has been the subject of numerous recent studies [14, 117–125]. Whereas spatial translation symmetry is broken in equilibrium crystalline phases, temporal translation symmetry could only be established for systems driven out of equilibrium. In analogy to (spatial) crystals, this led to the concept of Floquet time crystals, which can be modeled by the Floquet quantum Ising model [90, 91]. In contrast to the model studied in the previous chapter, we here consider periodic boundary conditions and random Ising couplings. The couplings in combination with disordered longitudinal fields lead to localization, which prevents drive-induced thermalization of the system. As before, the Floquet drive induces stable subharmonic spin correlations. Contrary to the edge oscillations of the previous chapter however, the (averaged) correlation functions now appear spatially homogeneous.

The subharmonic correlations are directly linked to the spectral properties of the Floquet operator. Its eigenstates come in pairs, with quasienergies that differ by approximately π . As discussed in [126, 127], the typical splittings from π are exponentially small in the system size, with an exact π pairing in the thermodynamic limit. In the study presented in this chapter, we show that

the splitting distribution follows a log-normal form. Furthermore, we show that the averaged spin correlation functions of the time crystal are directly related to the Fourier transform of the splitting distribution, giving access to an analytical description of the subharmonic spin correlations and their evolution with system size N .

Previous studies of spectral diagnostics of Floquet time crystals have focused on measures of entanglement as well as the statistics of adjacent energy levels [90, 128–133]. While these more generic measures of spectral correlations are useful in identifying the presence of thermalization, the π pairing distribution is directly related to the time crystal defining property of subharmonic spin correlations. The splittings Δ_n from π give rise to decay in the temporal spin correlation functions, at times exponentially long in system size. The time-crystalline state is thus established in the thermodynamic limit. We further find that for finite chains, spin correlation functions are mainly determined by only two parameters: the average and the variance of $\ln \Delta_n$.

The results of this chapter are obtained through a combination of numerical simulations as well as analytical considerations of a Floquet quantum Ising chain with disordered couplings, both with and without longitudinal disorder. We related the emergent log-normal distribution for the π splittings to tunneling processes through the entire chain. In contrast to the pairing via the presence or absence of Majorana modes discussed in the previous chapter, in this instance, partner states are even and odd eigenstates of the spin-flip symmetry of the Ising chain. For weak transverse fields, their splittings Δ_n reflect tunneling between two oppositely polarized states. In essence, this process involves the propagation of a domain wall through the entire chain, with the associated amplitude given by a product of many random factors.

The fermionic formulation of the model offers an alternative description [134, 135]. Analogously to the discussion in Sec. 5.2.2, the model is separated into two sectors of different fermion parity. In these sectors (also known as Neveu-Schwarz and Ramond sectors), the Jordan-Wigner fermions are subject to periodic and anti-periodic boundary conditions respectively. As partner states are connected to different sectors, their splittings reflect the sensitivity to these boundary conditions. In the presence of localization, sensitivity to boundary conditions is commonly characterized by a log-normal distribution. Examples include the conductance [136], level curvatures [137], as well as splittings of Majorana edge modes [109].

The structure of this chapter is as follows: First, we present numerical results in Sec. 7.2, drawing a connection between spin correlations and the π -pair splitting distribution. We then support our findings with analytical considerations, obtained from both the fermionic (Sec. 7.3) as well as the spin formulation (Sec. 7.4) of the Floquet quantum Ising model. Lastly, in Sec. 7.5 we analyze the effects of longitudinal disorder within stroboscopic perturbation theory.

7.2 TEMPORAL SPIN CORRELATIONS AND SPECTRAL PAIRING

We consider the Floquet quantum Ising model with periodic boundary conditions and disordered couplings. The corresponding Floquet operator is given by

$$U_F = \exp\left\{\frac{i\pi}{2} \sum_{i=1}^N h_i Z_i\right\} \exp\left\{\frac{i\pi g}{2} \sum_{i=1}^N X_i\right\} \exp\left\{\frac{i\pi}{2} \sum_{i=1}^N J_i Z_i Z_{i+1}\right\}. \quad (7.1)$$

Here we impose periodic boundary conditions by demanding that $Z_{N+1} = Z_1$. The Ising couplings J_i and longitudinal fields h_i are each drawn from independent box distributions, $J_i \in [J - dJ, J + dJ]$ and $h_i \in [-dh, dh]$.

Time-crystalline behavior of the Ising chain may be observed for transverse fields g close to one [90, 91]. To characterize this behavior, we again consider the temporal spin correlation function,

$$G_j(t) = \langle Z_j(t) Z_j(0) \rangle, \quad (7.2)$$

with the average $\langle \dots \rangle = 2^{-N} \text{tr}[\dots]$ corresponding to the infinite-temperature state. Notice that in contrast to Eq. (6.11), we do not only consider boundary correlation functions, but allow for general spin operators Z_j .

Numerically, we focus on the function $\overline{(-1)^t G_j(t)}$, with the overline indicating an average over disorder. On average, the model is spatially homogeneous due to the imposed boundary conditions, resulting in equivalent results for the correlation function at all sites j . We will therefore drop the label j from now on, so that $G_j(t) = G(t)$. At $g = 1$ and $dh = 0$, the transverse field flips all spins periodically, resulting in perfect period-2 oscillations, $G(t) = (-1)^t$. Slight deviations from $g = 1$ lead to a decaying correlation function at very late times. Before we find that, after an initial transient, the correlation function $\overline{(-1)^t G(t)}$ plateaus over a large number of cycles. This behavior qualitatively persists in the presence of longitudinal fields. We show this in Fig. 7.1(a), where we present our numerical results for the correlation function with and without longitudinal disorder.

The period-2 oscillations featured in the discrete time crystal are connected to spectral π pairings across the spectrum of the Floquet operator. We illustrate this in Fig. 7.1(b). In the absence of longitudinal fields, partner states $|n, \pm\rangle$ are even (+) or odd (−) under application of the total spin-flip operator P . The difference of their quasienergies $E_{n,\pm}$ deviates from π only by a splitting, which is exponentially suppressed in the size of the time crystal. As the operators Z_j are odd under spin-flip, they couple the partner states and consequently lead to the period-2 oscillations. This can be seen explicitly by writing the trace in Eq. (7.2) in terms of eigenstates of the Floquet operator,

$$G_j(t) = \frac{1}{2^N} \sum_{nm} |\langle n | Z_j | m \rangle|^2 e^{i(E_n - E_m)t}, \quad (7.3)$$

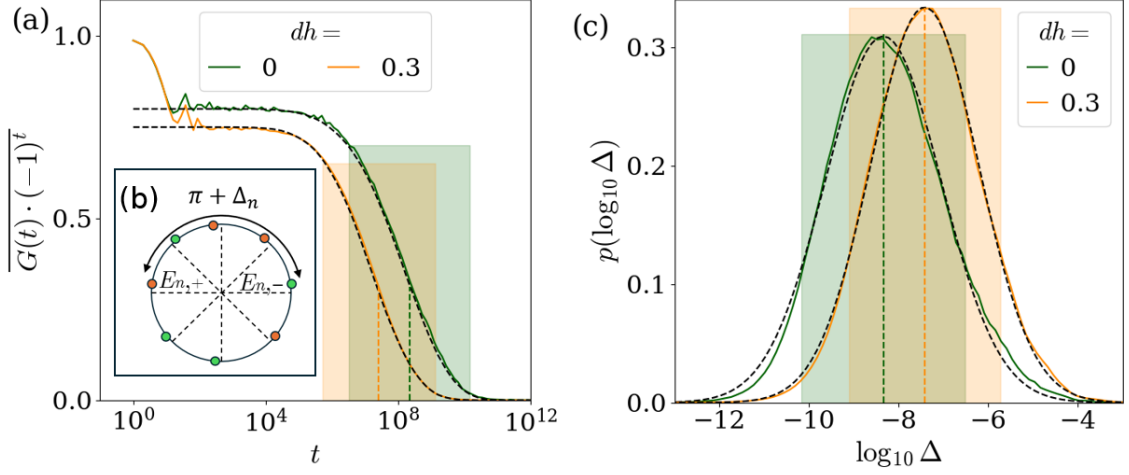


Figure 7.1: (a) Temporal (bulk) spin correlation function $G(t)$ averaged over disorder, with (orange lines) and without (green lines) longitudinal fields. The dashed lines are Fourier transforms $p(t)$ of log-normal distributions $p(\Delta)$. The functions $p(t)$ are further multiplied by a prefactor in order to match the plateaus of the correlation functions. The range of decay (shaded boxes) as well as decay locations (vertical dashed lines) are estimated using $p(\log_{10} \Delta)$ in (c), with corresponding labels and colors. (b) Sketch of the many-body Floquet spectrum. States that are even or odd under a global spin-flip are indicated by orange or green circles. The energy difference between even and odd partner states is $\pi + \Delta_n$, with Δ_n being exponentially small in the system size. (c) Splitting distributions with (orange) and without (green) longitudinal fields and corresponding log-normal fits (dashed lines). The splitting distributions are sampled over the many-body spectrum and different disorder realizations. Shaded boxes determine characteristic time scales of spin correlation functions, see (a). Parameters: $N = 14$, $g = 0.95$, $J = 0.5$, $dJ = 0.25$, (a) $\mathcal{N} = 10^3$, (b) $\mathcal{N} = 2 \cdot 10^4$ ($dh = 0$), $\mathcal{N} = 2 \cdot 10^3$ ($dh = 0.3$).

analogously to Eq. (6.12).

To make the connection between spin correlations and spectral pairing explicit, we calculate the 2^{N-1} splittings $\Delta_n = E_{n,-} - E_{n,+} + \pi$ from π for the entire Floquet spectrum and average over \mathcal{N} disorder realizations. The splittings may be readily identified by sorting the Floquet spectrum and using the close to π energy difference of paired levels, so that $\Delta_n = E_n - E_{n+2^{N-1}} + \pi$, with sorted quasienergies E_n . However, this is true only if the splittings are small compared to the many-body level spacing 2^{-N} . By averaging the splittings across the Floquet spectrum over multiple disorder configurations, we determine the distribution function underlying the splittings Δ_n , both with and without random longitudinal fields. In each case, we find that the distribution function is well approximated by a log-normal distribution,

$$p(\ln \Delta) d \ln \Delta = \frac{1}{\sqrt{2\pi\sigma}} e^{-\frac{1}{2\sigma^2}(\ln \Delta - \mu)^2} d \ln \Delta, \quad (7.4)$$

as presented in Fig. 7.1(c). Slight deviations from the log-normal form are found in the tail sections of the distribution, further discussed in Sec. 7.5.

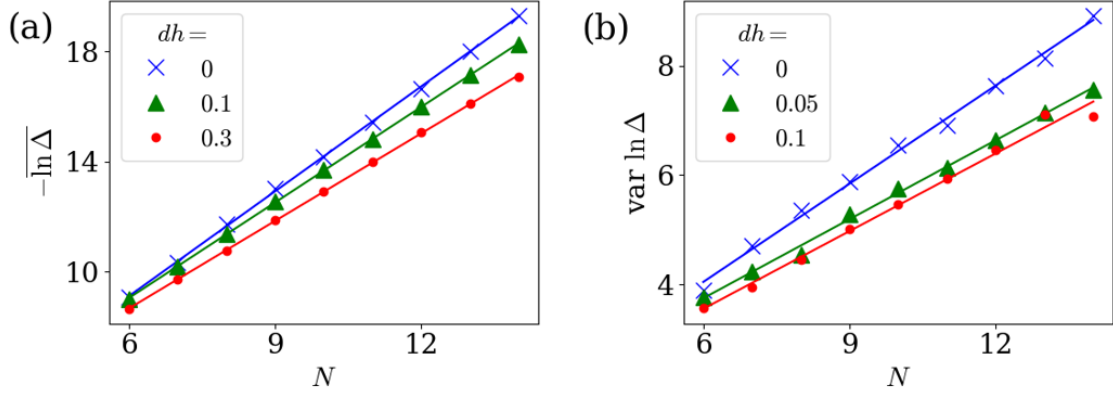


Figure 7.2: Mean (a) and variance (b) of the many-body splitting distribution $p(\ln \Delta)$ as a function of system size and longitudinal disorder strength. Averages and variances have been computed via a log-normal fit to the entire splitting distribution. We find that the data (dots) can be fit by a linear function (solid lines). Parameters: $J = 0.5$, $dJ = 0.25$, $g = 0.95$. Disorder averages over $\mathcal{N} = 5 \cdot 10^3$ realizations ($dh > 0$, $N = 6, \dots, 13$), $\mathcal{N} = 2 \cdot 10^3$ ($dh > 0$, $N = 14$), $\mathcal{N} = 2 \cdot 10^4$ ($dh = 0$, all N).

Analogously to normal distributions, the first two cumulants of $\ln \Delta$ fully determine the log-normal distribution. In Fig. 7.2, we show how these parameters scale with the system size N . Our results suggest a linear relationship,

$$\mu = \overline{\ln \Delta} = -\frac{N}{\zeta}, \quad \sigma^2 = \text{var} \ln \Delta = \frac{N}{\lambda}, \quad (7.5)$$

with characteristic length scales ζ and λ . We thus find that the mean value μ of the distribution, characterizing typical values of Δ , decreases with the size of the time crystal, while the variance σ^2 increases. We further find that an increasing longitudinal field has the opposite effect, the mean value increases whereas the variance decreases. This is evident from Fig. 7.2 and 7.1(c) (peak shifted to the right and peak height increased).

The central result of this chapter is that the correlation function $\overline{(-1)^t G(t)}$ is closely followed by the Fourier transform of the splitting distribution,

$$p(t) = \int d\Delta p(\Delta) e^{i\Delta t}, \quad (7.6)$$

beyond an initial transient. In Fig. 7.1(a), we show that the correlation functions (full lines) are well matched by the scaled Fourier transform of the corresponding splitting distribution (dashed lines). This can be explained via Eq. (7.3). The period-2 oscillations are connected to contributions from partner states, whereas the other contributions are found to primarily affect

the correlation function for short times, giving rise to the initial transient. Neglecting the latter, we find that the correlation function may be approximated as

$$\overline{(-1)^t G(t)} \simeq \frac{A}{2^{N-1}} \operatorname{Re} \overline{\sum_n e^{i(\pi - E_{n,+} + E_{n,-})t}}, \quad (7.7)$$

which relates $\overline{(-1)^t G(t)}$ to $p(t)$. Here we also used that the fluctuations of the matrix element prefactors $|\langle n, + | Z_j | n, - \rangle|^2$ over different states and disorder configurations are small. We account for the matrix elements by the prefactor A ,

$$A \simeq \frac{1}{2^{N-1}} \sum_n \overline{|\langle n, + | Z_j | n, - \rangle|^2}, \quad (7.8)$$

which is the scaling factor necessary to match the correlation function with the Fourier transform of the splitting distribution in Fig. 7.1(a).

The connection between the correlation function and the splitting distribution suggests that the former is determined by the two cumulants μ and σ^2 of $p(\ln \Delta)$. Indeed, we find that two characteristic time scales of the correlation function may be expressed via these cumulants. The bulk of the splitting distribution lies within the range of $[\mu - \sqrt{2}\sigma, \mu + \sqrt{2}\sigma]$. Inverting this range yields the two time scales $t^* = \exp\{-\mu - \sqrt{2}\sigma\}$ and $t^{**} = \exp\{-\mu + \sqrt{2}\sigma\}$. We find that the correlation function $\overline{(-1)^t G(t)}$ remains constant for times prior to t^* , and decays over the interval $[t^*, t^{**}]$, as highlighted by the boxes in Fig. 7.1(a). By using the relation between the cumulants and the system size in Eq. (7.5), we find that $\overline{(-1)^t G(t)}$ remains nonzero for all times, if the thermodynamic limit is taken prior to $t \rightarrow \infty$. Here we have to ensure that the splitting distribution is well-defined, i.e. that the 'maximum' splitting $\exp\{\mu + \sqrt{2}\sigma\}$ is well below the many-body level spacing 2^{-N} . As $\sigma \sim \sqrt{N}$, this yields the condition,

$$\zeta < 1/\ln(2), \quad (7.9)$$

which, as previously mentioned, is satisfied as long as g is sufficiently close to 1.

We may calculate an approximate analytical expression for the Fourier transform $p(t)$ within a saddle-point approximation. Using a log-normal distribution for $p(\Delta)$ in Eq. (7.6) and only keeping quadratic deviations from the saddle, one finds [138]

$$p(t) \simeq \operatorname{Re} \frac{\exp\left\{-\frac{1}{2\sigma^2} [W^2(-i\sigma^2 e^{\mu t}) + 2W(-i\sigma^2 e^{\mu t})]\right\}}{\sqrt{1 + W(-i\sigma^2 e^{\mu t})}}, \quad (7.10)$$

with $W(x)$ being the Lambert-W function, defined by $W(x)e^{W(x)} = x$. The expression in Eq. (7.10) is valid for small σ , but qualitatively matches $p(t)$ even for σ of order unity. From Eq. (7.10), one may also extract the asymptotic behavior $p(t) \simeq e^{-(1/(2\sigma^2)) \ln^2(\sigma^2 e^{\mu t})}$ at large times t .

7.3 SPLITTING DISTRIBUTION ANALYSIS IN THE FERMION MODEL

In the following two sections, we investigate the splitting distribution $p(\Delta)$ by initially considering the integrable limit ($dh = 0$) of the Floquet quantum Ising model. The many-body spectrum of the Floquet operator is then composed of single-particle levels. As we are interested in transverse fields close to 1, it is helpful to write the Floquet operator $U_{F,0} = U_F(dh = 0)$ as

$$U_{F,0} = P \exp \left\{ \frac{i\pi\delta g}{2} \sum_{i=1}^N X_i \right\} \exp \left\{ \frac{i\pi}{2} \sum_{i=1}^N J_i Z_i Z_{i+1} \right\}, \quad (7.11)$$

with $\delta g \ll 1$. Here, we decomposed the transverse field into $g = 1 + \delta g$ and used that a unit transverse field yields the total spin-flip operator $P = \prod_{i=1}^N X_i$.

To make the single-particle description explicit, we map the Floquet operator to a fermionic model via a Jordan-Wigner transformation. Using the formulation given in Sec. 5.2, the Floquet operator transforms to

$$U_{F,0} = P \exp \left\{ \frac{i\pi\delta g}{2} \sum_{j=1}^N (1 - 2c_j^\dagger c_j) \right\} \exp \left\{ \frac{i\pi}{2} \sum_{j=1}^N J_j (c_j^\dagger c_{j+1} + c_j^\dagger c_{j+1}^\dagger) + \text{h.c.} \right\}. \quad (7.12)$$

Here we make the identification $c_{N+1} = -Pc_1$, with P now being the parity operator in the fermionic model. As we discussed in Sec. 5.2.2, the origin of the parity operator lies in the Jordan-Wigner string attached to the operator $Z_N Z_1$. The fermion model is thus split into two sectors, the Neveu-Schwarz sector ($P = 1$) with anti-periodic boundary conditions and the Ramond sector ($P = -1$) with periodic boundary conditions.

7.3.1 DUAL TRANSFORMATION

In the limit of small δg , it is useful to transform to dual fermions living on the bonds of the chain instead [134, 135] (see B.5). The corresponding fermion operators

$$d_j^\dagger = \frac{1}{2}(c_j + c_j^\dagger + c_{j+1} - c_{j+1}^\dagger) \quad (7.13)$$

are then associated with domain walls rather than spin flips of the Ising chain. Writing the Floquet operator in Eq. (7.12) in terms of these operators yields

$$U_{F,0} = P \exp \left\{ \frac{i\pi\delta g}{2} \sum_{j=1}^N (d_j + d_j^\dagger)(d_{j-1} - d_{j-1}^\dagger) \right\} \exp \left\{ \frac{i\pi}{2} \sum_{j=1}^N J_j (1 - 2d_j^\dagger d_j) \right\}. \quad (7.14)$$

As in the previous formulation, the fermion operator at the boundary satisfies $d_0 = -Pd_N$. As the Floquet operator does not involve any interaction terms, we may write the quasienergy of any many-body state as

$$E(\{n_\alpha\}) = \sum_{\alpha} n_{\alpha} \epsilon_{\alpha}, \quad (7.15)$$

with ϵ_{α} with being single-particle quasienergies and n_{α} the corresponding fermion occupation numbers.

We now want to consider the limit of intermediate disorder strength, given by¹

$$\delta g \ll dJ \ll J \ll 1. \quad (7.16)$$

In this limit, we may pull together the exponents, so that the Floquet operator effectively describes the time evolution induced by

$$H = \frac{\pi \delta g}{2} \sum_{j=1}^N (d_j + d_j^{\dagger})(d_{j-1}^{\dagger} - d_{j-1}) + \pi \sum_{j=1}^N J_j d_j^{\dagger} d_j, \quad (7.17)$$

$$H = \frac{\pi(1-g)}{2} \sum_{j=1}^N (d_j + d_j^{\dagger})(d_{j-1}^{\dagger} - d_{j-1}) + \pi \sum_{j=1}^N J_j d_j^{\dagger} d_j, \quad (7.18)$$

apart from the parity operator P . In the following discussion, we will neglect the pairing terms $d_i^{\dagger} d_{i+1}^{\dagger}$, as they are parametrically suppressed in a perturbative expansion of δg . Thus, the Hamiltonian H reduces to a standard Anderson model with random on-site potential J_j . We will see in the next section that the ground state difference between the $P = \pm 1$ sectors is negligible compared to the excitation energy differences. Thus, the many-body splittings Δ_n arise primarily from the latter.

7.3.2 SINGLE-PARTICLE SPLITTING DISTRIBUTION

The Anderson models in each sector differ solely² in their boundary conditions, which may be equivalently formulated via a present or absent π flux threading the ring. The sensitivity of the single-particle levels to the boundary conditions is a measure of conductance, as discussed by Thouless in Ref. [139]. Furthermore, the conductance of a disordered one-dimensional wire follows a log-normal distribution [136], due to Oseledec's theorem [140]. We thus conclude that the single-particle splittings, defined by

$$\delta_j = \epsilon_j(P = 1) - \epsilon_j(P = -1), \quad (7.19)$$

¹All energy scales are much smaller than $\hbar/T = 1$.

²Apart from an overall π difference due to the $g = 1$ parity operator.

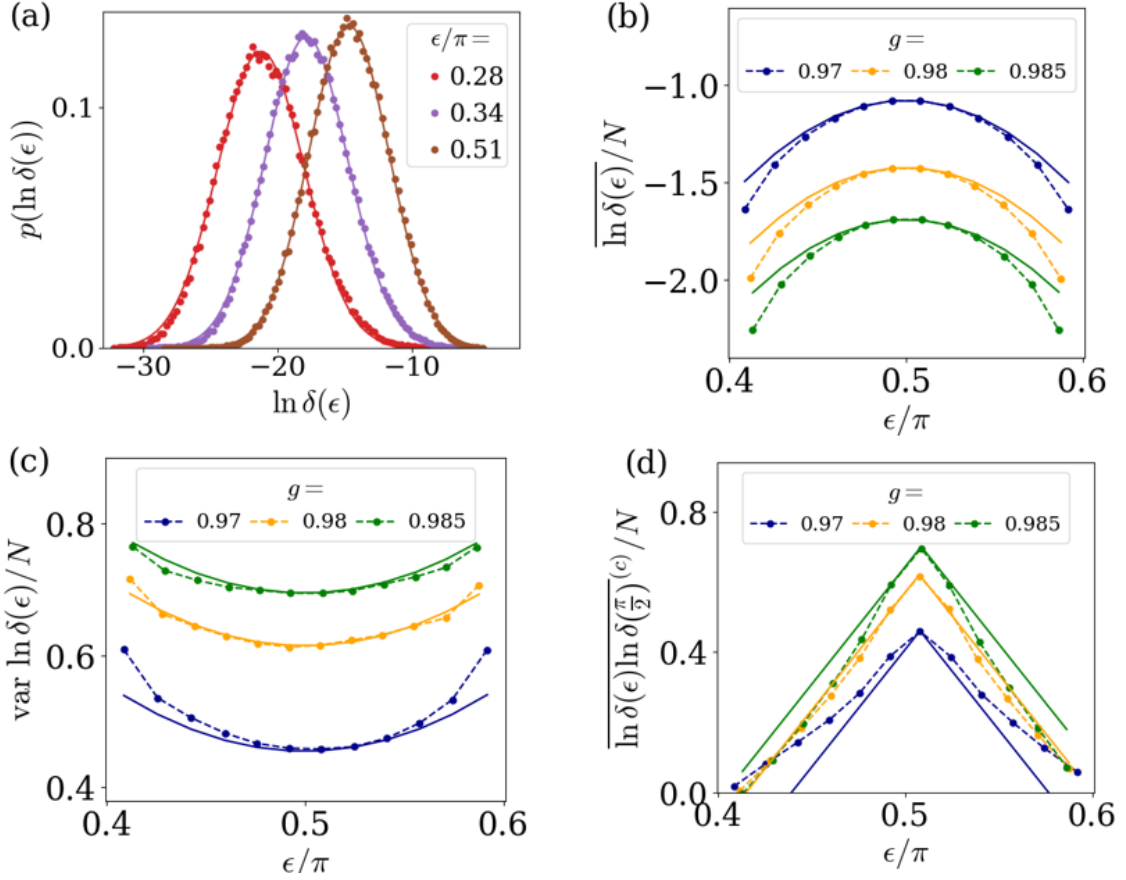


Figure 7.3: Single-particle splittings $\delta(\epsilon)$ between different parity sectors of the Jordan-Wigner fermions. (a) Splitting distribution at different levels ϵ . Data (dots) is well approximated by log-normal fits (solid lines). (b) Mean, (c) variance and (d) Correlations of $\ln \delta(\epsilon)$ (dots). Solid lines: Perturbation theory. Parameters: $J = 0.5, \mathcal{N} = 10^5$, (a) $dJ = 0.25, N = 18, g = 0.9$, (b)-(d) $dJ = 0.1, N = 12$.

also have to obey a log-normal distribution. In Fig. 7.3(a), we present numerical results supporting this conclusion. We may understand this as follows. As a quasiparticle mode with energy ϵ_j is Anderson localized with localization length $\xi(\epsilon_j)$, the corresponding energy difference δ_j between the sectors is exponentially small in $N/\xi(\epsilon_j)$. In zeroth order in the transverse field δg , the spectrum consists of perfectly localized modes at sites with energy πJ_j , so that the energies lie in the interval $\epsilon/\pi \in [J - dJ, J + dJ]$. Introducing a nonzero transverse field then leads to hopping between nearest neighbors. The difference in the $P = \pm 1$ sectors is due to hopping around the entire chain, a process arising in N th order perturbation theory. The splitting at energy ϵ_j can thus be written in terms of the associated hopping amplitude,

$$\delta_j \simeq 2\pi\delta g \prod_{l(\neq j)} \frac{\pi\delta g/2}{\epsilon - \pi J_l}. \quad (7.20)$$

This expression is a limiting case of an exact relation of a similar form [141]. As the product in Eq. (7.20) only involves statistically independent terms, the splittings δ_j are log-normally distributed as a consequence of the central limit theorem. We may further characterize them analogously to the many-body splittings via

$$\overline{\ln \delta(\epsilon)} = -\frac{N}{\xi(\epsilon)}, \quad \text{var} \ln \delta(\epsilon) = \frac{N}{\ell(\epsilon)}, \quad (7.21)$$

with the localization length $\xi(\epsilon)$ and the elastic mean free path $\ell(\epsilon)$ of the Anderson model [142]. We can use Eq. (7.20) in the limit of $N \gg 1$ to obtain the following estimates for the cumulants of $p(\ln \delta)$,

$$\overline{\ln |\delta(\epsilon)|} \simeq -N \left[\ln \frac{2dJ}{e\delta g} + \frac{(\epsilon - \pi J)^2}{2(\pi dJ)^2} \right], \quad \text{var} \ln |\delta(\epsilon)| \simeq N \left[1 + \frac{(\epsilon - \pi J)^2}{(\pi dJ)^2} \right]. \quad (7.22)$$

For details, see B.4. From these expressions, we see that the states near the band edges are localized the strongest, and correspondingly exhibit the largest fluctuations in $\ln \delta$. In Fig. 7.3(b) and (c), we show that the dependencies on ϵ of the estimates in Eq. (7.22) are in good agreement with numerical results. We point out however, that the analytical expressions are subject to a constant shift, compared to numerical results. The most likely explanation for this is that the numerically challenging limit given in Eq. (7.16) is not sufficiently satisfied. In support of this statement, we find that the deviations from Eq. (7.22) decrease when approaching the limit.

The many-body splittings Δ consist of a combination of many log-normally distributed single-particle splittings δ . The first two cumulants of the log-normal distribution are finite. One may think that the distribution of Δ should follow a normal distribution according to the central limit theorem, in contrast to the observed log-normal distribution. The issue is resolved by noticing that the single-particle splittings are not statistically independent, which is a crucial assumption underlying the central limit theorem. Indeed, the splittings are strongly correlated even between distant levels. The connected correlations of splittings at different energies may be estimated from Eq. (7.20). In leading order of $|\epsilon - \epsilon'|$, we find

$$\overline{\ln |\delta(\epsilon)| \ln |\delta(\epsilon')|}^{(c)} \simeq N \left[1 - \frac{|\epsilon - \epsilon'| \ln^2(\pi dJ)}{2\pi dJ} \right], \quad (7.23)$$

which is in good agreement with numerical results as shown in Fig. 7.3(d). As the correlations decay on the scale

$$\epsilon_c = \frac{2\pi dJ}{\ln^2(\pi dJ)}, \quad (7.24)$$

we find that the single-particle splittings are correlated over a broad range of energies.

7.4 FURTHER ANALYSIS IN THE SPIN MODEL

We complement the discussion of the previous section by also considering the limit given in Eq. (7.16) for the spin model (7.11). For $\delta g \rightarrow 0$, the eigenstates of the Floquet operator appear as symmetric and antisymmetric combinations of oppositely polarized bit strings, e.g.,

$$\frac{1}{\sqrt{2}}(|\uparrow\downarrow\downarrow\dots\downarrow\rangle \pm |\downarrow\uparrow\uparrow\dots\uparrow\rangle), \quad (7.25)$$

with antipodal quasienergies E and $E + \pi$. In the considered limit (7.16), we may again pull the exponents together, so that the Floquet operator effectively describes time evolution according to the Hamiltonian H ,

$$H = -\frac{\pi\delta g}{2} \sum_{i=1}^N X_i - \frac{\pi}{2} \sum_{i=1}^N J_i Z_i Z_{i+1}, \quad (7.26)$$

up to an overall shift by π , depending on the spin-flip symmetry P . For small δg , this approximation allows us to obtain the many-body splittings Δ via ordinary Schrödinger perturbation theory. The splittings between the oppositely polarized states in Eq. (7.25) emerge from tunneling processes of amplitude δg . As J is the largest energy scale, all Ising couplings are positive and to leading order, the number of domain walls stays constant in the virtual intermediate states. For definiteness, we consider a state with two domain walls, which is the smallest possible number due to the periodic boundary conditions. The tunneling connecting the states in Eq. (7.25) is then a process, in which the domain walls switch places by hopping once around the chain, involving N individual hopping steps. The associated splitting is given in N th order perturbation theory as

$$\Delta_{I,K} \simeq \frac{\pi\delta g}{2} \sum_{\gamma} \prod_{(i,j) \in \gamma} \frac{\delta g}{J_I + J_K - J_i - J_j}, \quad (7.27)$$

with I and K being the positions of the domain walls of the π paired states. The sum involves all trajectories γ , where (i, j) runs through the $N - 1$ intermediate states with domain walls at i and j .

In contrast to the perturbative expansion for the single-particle splittings in Eq. (7.20), the expansion for the many-body splittings Δ yields a sum over multiple terms. The central limit theorem however still applies approximately, given that the sum is dominated by sufficiently few terms and that the factors are statistically independent. The small deviations seen in Fig. 7.3(c) from the log-normal form demonstrate the degree to which these assumptions are valid. Especially for large values of Δ , we expect that the sum in Eq. (7.27) is dominated by a single rare event yielding a large contribution. Contrary to this, the sum involves many significant terms for smaller values of Δ , giving rise to deviations from the log-normal form in the small- Δ tail

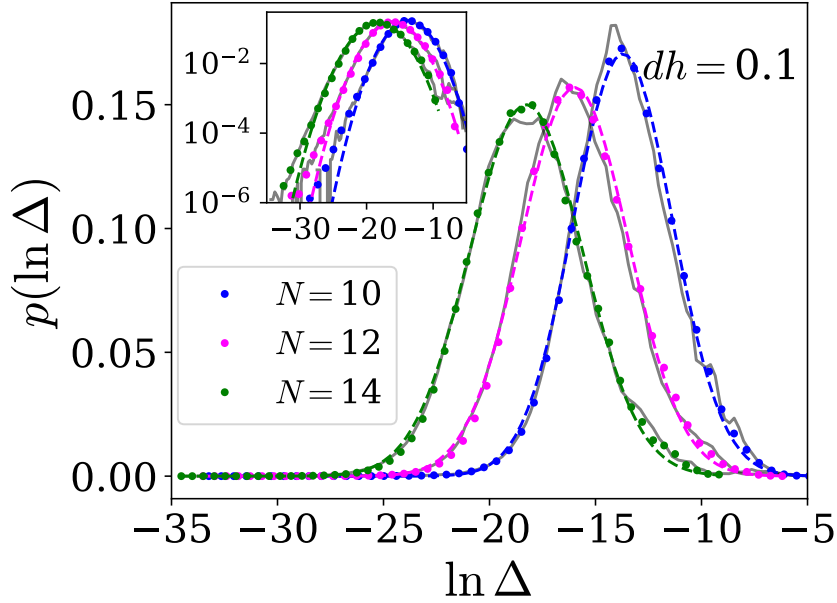


Figure 7.4: Many-body splitting distributions $p(\ln \Delta)$ for different system sizes. Data (dots) are compared to self-consistent perturbation theory (solid gray lines). We further fit the data to log-normal distributions (dashed lines). The inset shows the main plot with a logarithmic y -axis. Parameters: $J = 0.5$, $dJ = 0.25$, $g = 0.95$, $\mathcal{N} = 10^4$ (for $N = 10, 12$) and $\mathcal{N} = 2 \cdot 10^3$ ($N = 14$).

of the distribution. Furthermore, the splittings Δ are subject to an upper cutoff given by the many-body level spacing, leading to deviations in the large- Δ tail.

The two degenerate ground states of the Ising model contain no domain walls in the limit of $\delta g \rightarrow 0$. Since the scattering process connecting the two involves intermediate states with two domain walls, the energy denominator of each step is $\sim J$. Consequently, the ground state splitting is much smaller than the splittings of the excited states in the considered limit of Eq. (7.16).

7.5 PERTURBATION THEORY FOR LONGITUDINAL FIELDS

Lastly, we want to consider the splitting distribution $p(\ln \Delta)$ in the presence of random longitudinal fields. As seen in Fig. 7.1(c), the distribution retains a log-normal form for nonzero dh . The mean of $p(\ln \Delta)$ is increased by the longitudinal disorder while the variance decreases. This is also highlighted in Fig. 7.2, where we further demonstrate that the linear relationship between the first two cumulants and the system size persists.

We want to understand the effects of longitudinal disorder within the stroboscopic perturbation theory we derived in the previous chapter. We again take the longitudinal disorder as a perturbation $V = \frac{\pi}{2} \sum_{i=1}^N h_i Z_i$. The quasienergies of the Floquet operator $U_{F,0}$ then receive

corrections according to Eq. (6.5). In the following, we denote the unperturbed eigenstates of $U_{F,0}$ as $|n_0, \pm\rangle$ and the unperturbed many-body splittings as

$$\Delta_{n,0} = \pi - E_{n,0}^+ + E_{n,0}^-. \quad (7.28)$$

The perturbation V is odd under spin-flip symmetry. Consequently, the first order correction to the quasienergies vanishes and we find in second order,

$$\Delta_n \simeq \Delta_{n,0} - \sum_m \left[\frac{|v_{nm}^{+-}|^2}{2 \tan \frac{E_n^+ - E_m^-}{2}} - \frac{|v_{nm}^{-+}|^2}{2 \tan \frac{E_n^- - E_m^+}{2}} \right], \quad (7.29)$$

with $v_{nm}^\pm = \langle n_0, +|V|m_0, -\rangle$. Analogously to the perturbation theory calculation performed in the previous chapter, we made the perturbation theory here self-consistent by inserting the perturbed quasienergies E_n^\pm into the energy denominators. The justification for this is again that, while the contributions of π pairs $m = n$ are suppressed by the divergent denominator, the sum in Eq. (7.29) contains many significant terms $m \neq n$ of similar magnitude. This may be plausibly captured within a self-consistent approximation.

We proceed by inserting the perturbed splittings Δ_n in the energy denominators via $\Delta_n = \pi - E_n^+ + E_n^-$ and expand in them, as they are small compared to the quasienergy differences. In linear order, this yields an analogous expression to Eq. (6.8) for the splittings,

$$\Delta_n \simeq \Delta_{n,0} + \Lambda_n - \Sigma_n \Delta_n, \quad (7.30)$$

with

$$\Lambda_n \simeq \sum_m \left[\frac{|v_{nm}^{-+}|^2}{2 \tan \frac{E_{n,0}^+ - E_{m,0}^+ + \pi}{2}} - \frac{|v_{nm}^{+-}|^2}{2 \tan \frac{E_{n,0}^- - E_{m,0}^- + \pi}{2}} \right], \quad (7.31)$$

$$\Sigma_n \simeq \sum_m \left[\frac{|v_{nm}^{+-}|^2}{4 \cos^2 \frac{E_{n,0}^- - E_{m,0}^-}{2}} + \frac{|v_{nm}^{-+}|^2}{4 \cos^2 \frac{E_{n,0}^+ - E_{m,0}^+}{2}} \right]. \quad (7.32)$$

Note that we reinserted the unperturbed quasienergies in the definitions of Λ_n and Σ_n . We finally solve for Δ_n to obtain

$$\Delta_n \simeq \frac{\Delta_{n,0} + \Lambda_n}{1 + \Sigma_n}, \quad (7.33)$$

analogously to Eq. (B.45). We point out however that in this instance, the expansion was chosen in such a way that the solution for Δ_n is a scalar equation in contrast to the matrix equation in Eq.(B.45).

In Fig. 7.4, we demonstrate that the self-consistent approximation accurately reproduced the splitting distribution $p(\ln \Delta)$. In the inset, we show the deviations in the small Δ -tail section from the log-normal form, as discussed in the previous section.

7.6 CONCLUSION

It is known that period-2 Floquet time crystals show π pairing within their quasienergy spectrum [126, 127]. These pairings deviate from π in finite-size systems by an exponentially small amount. In this chapter, we demonstrated that the distribution function underlying these splittings across the spectrum and different disorder realizations is accurately captured by a log-normal distribution. Furthermore, we showed that the Fourier transform of the splitting distribution is directly related to the spin correlation function of finite-size time crystals. This connects the defining characteristic of Floquet time crystals to the spectral statistics of the Floquet operator.

The study presented in this chapter provides multiple directions for further research. First, it is interesting to see whether one can relate more spin correlation functions to the spectral π pairing. Particularly, a recent study has pointed out the role of out-of-time correlators in Floquet time crystals [143]. Second, it is important to understand if the time-crystalline order of Floquet time crystals of different oscillation period [127, 144–146], disorder-free models of time crystals [147–149] or time-crystalline behavior in open quantum systems [150–155] may be related to spectral statistics. Third, it would be interesting to see if the log-normal form of the splitting distribution as well as its relation to temporal spin correlation may be derived rigorously.

The results of this chapter may further have ramifications for the phase diagram of Floquet time crystals. It is a natural assumption that the relationship between temporal spin correlations and the pairing distribution is a fundamental property of time-crystalline order. Consequently, the time crystal phase would rely upon a well-defined splitting against the mean-level spacing 2^{-N} . Assuming that these speculations are justified, the condition in Eq. (7.9) defines the phase boundary of the time-crystal phase. The relationship of the characteristic length ζ to the system parameters would thus be interesting to understand. We note that these arguments may also have implications for the existence of higher-dimensional time crystals.

8 DYNAMICS OF OPEN QUANTUM SYSTEMS

In this chapter, we introduce the theoretical framework that is used to describe an active quantum particle in chapter 9.

8.1 LINDBLAD EQUATION

Here we present a derivation of the Lindblad equation that closely follows the book by Breuer and Petruccione [156]. We consider a system that is coupled to one or multiple bosonic baths. The total system is described by a system Hamiltonian H_S , a bath Hamiltonian H_B , and a coupling Hamiltonian H_I mediating the energy exchange between the two,

$$H = H_S + H_B + H_I. \quad (8.1)$$

We will leave the system part of the Hamiltonian unspecified for now. The bath Hamiltonian is given by

$$H_B = \sum_{n,\alpha} \omega_{n,\alpha} b_{n,\alpha}^\dagger b_{n,\alpha}, \quad (8.2)$$

with $\omega_{n,\alpha}$ being the energy of the bosonic mode created by $b_{n,\alpha}^\dagger$. The index set n labels the oscillator modes of the baths, while α labels the coupling channels between system and the environment. The coupling Hamiltonian is assumed to be of the form

$$H_I = \sum_{\alpha} A_{\alpha} \otimes B_{\alpha}, \quad (8.3)$$

where A_{α} and B_{α} are operators acting on the system and the thermal reservoirs respectively. Interactions between system and bath are usually accompanied by creation or annihilation of bosons in the reservoirs. We therefore assume that the bath part of H_I is linear in the bosonic operators. We also allow A_{α} and B_{α} to be non-hermitian. However, this requires that the sum also involves their hermitian conjugates.

Our goal now is to find an equation of motion for the density matrix of the system $\rho_S(t)$. For this, we initially consider the density matrix $\chi(t)$ describing the total system. The derivation is best performed in the interaction picture [156], so that $\chi(t)$ evolves according to the von Neumann equation,

$$\frac{d\chi(t)}{dt} = -i[H_I(t), \chi(t)]. \quad (8.4)$$

Integrating this equation between an initial time t_0 and t , and reinserting into the von Neumann equation yields,

$$\frac{d\chi(t)}{dt} = -i[H_I(t), \chi(t_0)] - \int_{t_0}^t dt' [H_I(t), [H_I(t'), \chi(t')]]. \quad (8.5)$$

In order to explicitly obtain an equation of motion for ρ_S , we now make two assumptions: First, we assume that the coupling between system and bath H_I is weak. Furthermore, we take the baths to be large and to stay in thermal equilibrium at all times. Thus, the bath density of states ρ_B is essentially time-independent. This allows us to use the so-called Born-approximation [156] which states that the time evolution leaves the system and bath uncorrelated,

$$\chi(t) \approx \rho_S(t) \otimes \rho_B. \quad (8.6)$$

Using the approximation, we may eliminate the baths from the left hand side via tracing over the bath part of the Hilbert space. Also, this eliminates the commutator $[H_I(t), \chi(t_0)]$ as the bath part of H_I is linear in the bosonic operators,

$$\frac{d\rho_S(t)}{dt} = -\text{tr}_B \int_{t_0}^t dt' [H_I(t), [H_I(t'), \rho_S(t') \otimes \rho_B]]. \quad (8.7)$$

Here, tr_B indicates the trace over the bath. Assuming that correlations within the bath decay on a much faster scale than the time evolution of the system, we may perform the Markov approximation [156]. This means that the time evolution of $\rho_S(t)$ is independent of the state of the system at any earlier time t' . Replacing $\rho_S(t')$ with $\rho_S(t)$, we obtain an evolution equation that is local in time,

$$\frac{d\rho_S(t)}{dt} = -\text{tr}_B \int_{t_0}^t dt' [H_I(t), [H_I(t'), \rho_S(t) \otimes \rho_B]]. \quad (8.8)$$

This is known as Redfield equation [157]. At this point, the evolution equation still depends on the initial configuration $\rho_S(t_0)$ of the system. To eliminate it, we replace the integration variable t' by $s = t - t'$ and further extend the integration to infinity. This is again allowed under the assumption that the bath correlation time scale is small,

$$\frac{d\rho_S(t)}{dt} = -\text{tr}_B \int_0^\infty ds [H_I(t), [H_I(t-s), \rho_S(t) \otimes \rho_B]]. \quad (8.9)$$

We end up with a Markovian quantum Master equation [156]. The approximations we have performed until this point are summarized in the literature as Born-Markov approximation [156]. The master equation is problematic at this stage. While it is trace preserving, it is not a positive definite map, i.e. eigenvalues of the density matrix may turn negative during time evolution. To

alleviate this, one introduces yet another approximation, known as the secular approximation (or rotating wave approximation) [156].

We start by writing the system part of H_I in terms of eigenoperators $A_\alpha(\omega)$ of the system Hamiltonian,

$$A_\alpha(\omega) = \sum_{\omega=\epsilon-\epsilon'} \Pi_{\epsilon'} A_\alpha \Pi_\epsilon, \quad (8.10)$$

with Π_ϵ being projectors onto the eigenstates of H_S at energy ϵ . The sum here involves all ϵ and ϵ' that satisfy $\omega = \epsilon - \epsilon'$. As summing over all frequencies ω is equivalent to summing over all ϵ and ϵ' , we find the following relation,

$$A_\alpha = \sum_{\omega} A_\alpha(\omega). \quad (8.11)$$

Using this as well as the fact that the $A_\alpha(\omega)$ are eigenoperators of H_S , we find

$$A_\alpha(t) = \sum_{\omega} e^{iH_S t} A_\alpha(\omega) e^{-iH_S t} = \sum_{\omega} e^{-i\omega t} A_\alpha(\omega). \quad (8.12)$$

We return to the master equation. First, we make the commutators explicit,

$$\begin{aligned} \frac{d\rho_S(t)}{dt} = & \int_0^\infty ds \operatorname{tr}_B \{ H_I(t-s) (\rho_S(t) \otimes \rho_B) H_I(t) \\ & - H_I(t) H_I(t-s) (\rho_S(t) \otimes \rho_B) \} + \text{h.c.} \end{aligned} \quad (8.13)$$

We now plug in the explicit expression for H_I and commute the bath operators under the trace to the left. This yields,

$$\begin{aligned} \frac{d\rho_S(t)}{dt} = & \sum_{\alpha,\beta} \sum_{\omega,\omega'} e^{-i(\omega'+\omega)t} \int_0^\infty ds e^{i\omega s} \langle B_\alpha(t) B_\beta(t-s) \rangle \\ & \times \{ A_\beta(\omega) \rho_S(t) A_\alpha(\omega') - A_\alpha(\omega') A_\beta(\omega) \rho_S(t) \} + \text{h.c.}, \end{aligned} \quad (8.14)$$

where we introduced the bath average $\langle \dots \rangle = \operatorname{tr}_B(\dots \rho_B)$. Here we make use of the secular approximation, meaning that we neglect all the oscillating terms in Eq. (8.14) and only keep terms with $\omega = -\omega'$ [156]. We simplify the notation by summarizing the bath average and the integral into

$$\tilde{\Gamma}_{\alpha,\beta}(\omega) = \int_0^\infty ds e^{i\omega s} \langle B_\alpha(t) B_\beta(t-s) \rangle. \quad (8.15)$$

We intentionally neglect the time argument t in $\tilde{\Gamma}$ as the average in Eq. (8.15) depends only on the time difference between the operators (since ρ_B is time-independent). The evolution equation for the density matrix can thus be written as

$$\frac{d\rho_S(t)}{dt} = \sum_{\alpha,\beta} \sum_{\omega} \tilde{\Gamma}_{\alpha,\beta}(\omega) \{A_{\beta}(\omega)\rho_S(t)A_{\alpha}(-\omega) - A_{\alpha}(-\omega)A_{\beta}(\omega)\rho_S(t)\} + \text{h.c.} \quad (8.16)$$

We point out that the standard derivation as given in [156] assumes hermitian operators A_{α} and B_{α} . We may reproduce the standard result for the Lindblad equation in the following way: We know that for every operator A_1 there is an operator A_2 with $A_2^{\dagger} = A_1$ due to H_I necessarily being hermitian. The corresponding bath operators B_1 and B_2 satisfy the analogous condition $B_2^{\dagger} = B_1$. Using Eq. (8.12), we see that this implies $A_1(-\omega) = A_2^{\dagger}(\omega)$. Changing the negative argument $-\omega$ into a conjugated operator thus leads to a reshuffling of the index set α . This change may be compensated by a hermitian conjugation of the respective bath operator. The simultaneous transformation $B_{\alpha} \rightarrow B_{\alpha}^{\dagger}$, $A_{\alpha}(-\omega) \rightarrow A_{\alpha}^{\dagger}(\omega)$ therefore leaves the equation of motion for the density matrix invariant and we find,

$$\frac{d\rho_S(t)}{dt} = \sum_{\alpha,\beta} \sum_{\omega} \Gamma_{\alpha,\beta}(\omega) \{A_{\beta}(\omega)\rho_S(t)A_{\alpha}^{\dagger}(\omega) - A_{\alpha}^{\dagger}(\omega)A_{\beta}(\omega)\rho_S(t)\} + \text{h.c.}, \quad (8.17)$$

with

$$\Gamma_{\alpha,\beta}(\omega) = \int_0^{\infty} ds e^{i\omega s} \langle B_{\alpha}^{\dagger}(t)B_{\beta}(t-s) \rangle. \quad (8.18)$$

Thus we obtain the same result for the Lindblad equation as for the case of A_{α} and B_{α} being hermitian [156]. Next, we want to combine Eq. (8.17) with its hermitian conjugate. For this, we introduce the hermitian and antihermitian parts of $\Gamma_{\alpha,\beta}$ as follows,

$$\gamma_{\alpha,\beta}(\omega) = \Gamma_{\alpha,\beta}(\omega) + \Gamma_{\beta,\alpha}^*(\omega) = \int_{-\infty}^{\infty} ds e^{i\omega s} \langle B_{\alpha}^{\dagger}(t)B_{\beta}(t-s) \rangle, \quad (8.19)$$

$$S_{\alpha,\beta}(\omega) = \frac{1}{2i} [\Gamma_{\alpha,\beta}(\omega) - \Gamma_{\beta,\alpha}^*(\omega)]. \quad (8.20)$$

We did not state the integral form for the antihermitian $S_{\alpha,\beta}(\omega)$ as we will never calculate it explicitly. Substituting $\Gamma_{\alpha,\beta}$ with $\gamma_{\alpha,\beta}$ and $S_{\alpha,\beta}$, we find the following form of the Lindblad equation,

$$\frac{d\rho_S(t)}{dt} = -i[H_{LS}, \rho_S(t)] + \mathcal{D}[\rho_S(t)], \quad (8.21)$$

with

$$\mathcal{D}[\rho_S(t)] = \sum_{\alpha,\beta} \sum_{\omega} \gamma_{\alpha,\beta}(\omega) \left[A_{\beta}(\omega)\rho_S(t)A_{\alpha}^{\dagger}(\omega) - \frac{1}{2} \{A_{\alpha}^{\dagger}(\omega)A_{\beta}(\omega), \rho_S(t)\} \right] \quad (8.22)$$

being the dissipator and

$$H_{LS} = \sum_{\alpha,\beta} \sum_{\omega} S_{\alpha,\beta}(\omega) A_{\alpha}^{\dagger}(\omega) A_{\beta}(\omega) \quad (8.23)$$

the Lamb-shift Hamiltonian [156]. Lastly, we want to return to the Schrödinger picture, which yields the following final evolution equation for ρ_S ,

$$\frac{d\rho_S(t)}{dt} = -i[H_{LS} + H_S, \rho_S(t)] + \mathcal{D}[\rho_S(t)]. \quad (8.24)$$

We note that since the Lamb-shift Hamiltonian only involves eigenoperators of H_S , it commutes with the system Hamiltonian and is thus solely leading to a renormalization of the energy levels. Since we consider weak coupling to the reservoirs, this effect is small however and we will thus neglect H_{LS} for the remainder of this thesis.

8.2 EXAMPLE: TWO-LEVEL SYSTEM COUPLED TO MULTIPLE HEAT BATHS

In this section, we apply the Lindblad equation to a simple example. We consider a two-level system that is coupled to two bosonic, thermal reservoirs. A Hamiltonian H describing this situation is given by

$$H = \frac{\epsilon}{2} \sigma_z + \sum_n \sum_{\alpha=1}^2 \omega_{n,\alpha} b_{n,\alpha}^{\dagger} b_{n,\alpha} + \sum_n \sum_{\alpha=1}^2 O_{\alpha} (b_{n,\alpha} + b_{n,\alpha}^{\dagger}). \quad (8.25)$$

The level spacing of the system is given by ϵ while the bath modes have energy $\omega_{n,\alpha}$. In this instance, the index α labels the baths and n the mode frequencies within each bath. An energy exchange between system and reservoir is associated with a hermitian operator O_{α} acting on the spin of the system, while a boson is absorbed or emitted. If both of the reservoirs have the same temperature T , it is clear that the system will reach thermal equilibrium (i.e. the levels follow a Boltzmann distribution) eventually. A more interesting situation arises in the case of two different temperatures $T_{\alpha} = T \pm \Delta T/2$. Here, the steady state of the system will be a non-equilibrium state. To find it, we make use of the Lindblad formalism derived in the previous section. We first calculate the rates $\gamma_{\alpha,\beta}$ via Eq. (8.19),

$$\begin{aligned} \gamma_{\alpha,\beta}(\omega) &= \int_{-\infty}^{\infty} ds e^{i\omega s} \langle B_{\alpha}^{\dagger}(t) B_{\beta}(t-s) \rangle, \\ &= \sum_{n,n'} \int_{-\infty}^{\infty} ds e^{i\omega s} \text{tr}_B \left[(b_{n,\alpha} + b_{n,\alpha}^{\dagger}) e^{-iH_B s} (b_{n',\beta} + b_{n',\beta}^{\dagger}) e^{iH_B s} \rho_B \right], \end{aligned} \quad (8.26)$$

with H_B being the Hamiltonian of the reservoirs and ρ_B the thermal state. We may simplify the expression for $\gamma_{\alpha,\beta}$ by using that

$$e^{-iH_B s}(b_{n',\beta} + b_{n',\beta}^\dagger)e^{iH_B s} = e^{i\omega_{n',\beta}s}b_{n',\beta} + e^{-i\omega_{n',\beta}s}b_{n',\beta}^\dagger. \quad (8.27)$$

Also, since the density matrix ρ_B is diagonal in the boson occupation basis, the only surviving terms under the trace necessarily involve the same indices and both a creation and annihilation operator. We thus find for the rates,

$$\begin{aligned} \gamma_{\alpha,\beta}(\omega) &= \delta_{\alpha,\beta} \sum_n \int_{-\infty}^{\infty} ds [e^{i(\omega+\omega_{n,\alpha})s} \text{tr}_B(b_{n,\alpha}^\dagger b_{n,\alpha} \rho_B) + e^{i(\omega-\omega_{n,\alpha})s} \text{tr}_B(b_{n,\alpha} b_{n,\alpha}^\dagger \rho_B)] \\ &= 2\pi\delta_{\alpha,\beta} \sum_n \{\delta(\omega + \omega_{n,\alpha})n(\omega_{n,\alpha}, T_\alpha) + \delta(\omega - \omega_{n,\alpha})[n(\omega_{n,\alpha}, T_\alpha) + 1]\}, \end{aligned} \quad (8.28)$$

with $n(\omega, T)$ being the Bose-Einstein distribution¹,

$$n(\omega, T) = \frac{1}{e^{\omega/T} - 1}. \quad (8.29)$$

In order to apply the δ -functions, we write the sum over n as $\sum_n \rightarrow \int_0^\infty d\omega_\alpha \nu_\alpha(\omega_\alpha)$ with ν_α being the density of states in the respective reservoir. For simplicity, we will assume a constant density of states $\nu_\alpha(\omega_\alpha) = \nu_0$ for frequencies close to the level spacing ϵ . In summary, we find for the rates

$$\gamma_{\alpha,\beta}(\omega) = 2\pi\delta_{\alpha,\beta}\nu_0\{\theta(-\omega)n(-\omega, T_\alpha) + \theta(\omega)[n(\omega, T_\alpha) + 1]\}. \quad (8.30)$$

In order to calculate the evolution equation for $\rho_S(t)$, we also need to find the eigenoperators $A_\alpha(\omega)$ as given in Eq. (8.10). Since the system involves only two levels, we solely need to consider $\omega = \pm\epsilon$,

$$A_\alpha(\epsilon) = |0\rangle\langle 0|O_\alpha|1\rangle\langle 1| = \langle 0|O_\alpha|1\rangle\sigma_-, \quad A_\alpha(-\epsilon) = A_\alpha^\dagger(\epsilon) = \langle 1|O_\alpha|0\rangle\sigma_+, \quad (8.31)$$

with $|0\rangle$ and $|1\rangle$ being the ground- and excited states of the system Hamiltonian and σ_\pm the ladder operators switching between the two states. With these, we may write down the Lindblad equation for $\rho_S(t)$. Using shorthand notation for $o_\alpha = 2\pi\nu_0|\langle 0|O_\alpha|1\rangle|^2$, we find

$$\begin{aligned} \frac{d\rho_S(t)}{dt} &= -i[H_S, \rho_S(t)] + \sum_{\alpha=1}^2 o_\alpha [n(\epsilon, T_\alpha) + 1] \left[\sigma_- \rho_S(t) \sigma_+ - \frac{1}{2} \{ \sigma_+ \sigma_-, \rho_S(t) \} \right] \\ &\quad + o_\alpha n(\epsilon, T_\alpha) \left[\sigma_+ \rho_S(t) \sigma_- - \frac{1}{2} \{ \sigma_- \sigma_+, \rho_S(t) \} \right]. \end{aligned} \quad (8.32)$$

¹With vanishing chemical potential.

In order to proceed, we choose a convenient parametrization for the density matrix as follows,

$$\rho_S = \begin{pmatrix} n_0 & \rho_x - i\rho_y \\ \rho_x + i\rho_y & n_1 \end{pmatrix}. \quad (8.33)$$

By projecting the Lindblad equation onto the states $|0\rangle$ and $|1\rangle$, we find the following evolution equations for the level occupations n_0 and n_1 ,

$$\frac{dn_0(t)}{dt} = \left(\sum_{\alpha=1}^2 o_\alpha [n(\epsilon, T_\alpha) + 1] \right) n_1(t) - \left(\sum_{\alpha=1}^2 o_\alpha n(\epsilon, T_\alpha) \right) n_0(t), \quad (8.34)$$

$$\frac{dn_1(t)}{dt} = - \left(\sum_{\alpha=1}^2 o_\alpha [n(\epsilon, T_\alpha) + 1] \right) n_1(t) + \left(\sum_{\alpha=1}^2 o_\alpha n(\epsilon, T_\alpha) \right) n_0(t). \quad (8.35)$$

The evolution equation for the coherences ρ_x and ρ_y may be extracted by multiplying the Lindblad equation with the respective Pauli matrix and taking the trace. One finds,

$$\frac{d\rho_x(t)}{dt} = -\epsilon\rho_y(t) - \frac{1}{2} \sum_{\alpha=1}^2 [2n(\epsilon, T_\alpha) + 1]\rho_x(t), \quad (8.36)$$

$$\frac{d\rho_y(t)}{dt} = \epsilon\rho_x(t) - \frac{1}{2} \sum_{\alpha=1}^2 [2n(\epsilon, T_\alpha) + 1]\rho_y(t). \quad (8.37)$$

The Lindblad equation thus yields independent relaxation processes for the occupation numbers and the coherences. The latter follow an oscillatory decay to zero (dephasing), while for the occupations, we find a classical rate equation. The steady state ρ_∞ may be estimated by setting the derivatives in Eq. (8.34) and (8.35) to zero. We find

$$n_1(\infty) = \frac{\sum_{\alpha} o_\alpha n(\epsilon, T_\alpha)}{\sum_{\alpha} o_\alpha [n(\epsilon, T_\alpha) + 1]} n_0(\infty). \quad (8.38)$$

As a sanity check, we want to know whether this result reproduces the Boltzmann distribution in the case of $\Delta T = 0$. Indeed, for $T_\alpha = T$, the matrix elements o_α in Eq. (8.38) cancel out and one finds

$$n_1(\infty) = e^{-\beta\epsilon} n_0(\infty), \quad (8.39)$$

with $\beta = T^{-1}$.

This calculation serves as an introductory example to the following chapter. There, we also study a spin-1/2 particle coupled to two reservoirs, albeit with an additional degree of freedom being the momentum of the particle.

8.3 QUANTUM REGRESSION THEOREM

In the previous section, we found that the Lindblad equation produced independent processes for the dephasing and the occupation relaxation. This essentially lead to classical dynamics for the occupation numbers and to a classical steady state. It is therefore an interesting question to ask in what sense the system still exhibits quantum behaviour. For the purpose of answering this, it is adequate to calculate temporal correlation functions of the form $\langle A(t + \tau)B(t) \rangle$ with A and B being observables. While these functions decay steadily with τ in classical systems, a typical signature of the system being quantum is an oscillating correlation function [158]. In closed (time-independent) quantum systems, correlation functions are easily estimated in the Heisenberg picture,

$$\begin{aligned} \langle A(t + \tau)B(t) \rangle &= \text{tr}(e^{iH(t+\tau)} A e^{-iH(t+\tau)} e^{iHt} B e^{-iHt} \rho) \\ &= \text{tr}(A e^{-iH\tau} [B \rho(t)] e^{iH\tau}), \end{aligned} \quad (8.40)$$

with H the Hamiltonian and ρ the state of the system. In the last step, we switched to the Schrödinger picture and introduced $\rho(t) = e^{-iHt} \rho e^{iHt}$. We transformed the correlation function to a simple expectation value $\langle A(\tau) \rangle$, albeit the "density matrix" of the system in this case is $B\rho(t)$, which in general does neither satisfy positive semi-definiteness nor the normalization condition. This reasoning however will help us understand how to calculate correlation functions in open systems.

Alternatively to Eq. (8.24), we may also formulate the Lindblad equation in terms of the Liouvillian superoperator \mathcal{L} ,

$$\frac{d\rho_S(t)}{dt} = \mathcal{L}\rho_S(t). \quad (8.41)$$

The Liouvillian incorporates both the coherent time evolution within the system as well as the incoherent relaxation processes that are due to the coupling to the environment. This formulation has the advantage that a formal solution for $\rho_S(t)$ may be simply read off as

$$\rho_S(t) = e^{\mathcal{L}t} \rho_S(0). \quad (8.42)$$

Let us now consider the (unitary) time evolution of the total system generated by the time evolution operator U . The Born approximation allows us to write $\chi(t) = \rho_S(t) \otimes \rho_B$, which provides us with the identity

$$\text{tr}_B(\chi(t)) = \text{tr}_B(U(t)\chi U^\dagger(t)) = \rho_S(t) = e^{\mathcal{L}t} \rho_S(0). \quad (8.43)$$

With this, we may calculate a general correlation function of observables acting on the system as

$$\begin{aligned} \langle A(t + \tau)B(t) \rangle &= \text{tr}(U^\dagger(t + \tau) A U(t + \tau) U^\dagger(t) B U(t) \chi) \\ &= \text{tr}_S [A \text{tr}_B (U(\tau) B \chi(t) U^\dagger(\tau))]. \end{aligned} \quad (8.44)$$

Applying the identity in Eq. (8.43) then yields the quantum regression theorem [156, 159],

$$\langle A(t + \tau)B(t) \rangle = \text{tr}_S(Ae^{\mathcal{L}\tau}[B\rho_S(t)]). \quad (8.45)$$

We did not show yet that the identity in (8.43) holds for other matrices than density matrices. This is trivial however for the reason that any matrix may be written as a linear combination of density matrices (with complex coefficients) and that the action of $e^{\mathcal{L}t}$ is linear.

9 HEAT-TO-MOTION CONVERSION FOR QUANTUM ACTIVE MATTER

The results of this chapter have been published in Ref. [5]. This project was a collaboration with other co-authors. The author of this thesis conducted numerical calculations in parallel to Ludmila Viotti. The final numerical data and figures in [5] were generated by L. Viotti. The author here produces similar figures independently. The author performed the calculations discussed in this thesis in close discussion with all co-authors. The author contributed to the draft. The presented data is available at [35].

9.1 INTRODUCTION

The active matter field constitutes a highly interdisciplinary body of research, bridging between physics, chemistry and biology [160–164]. Here, the main role is played by active particles. These either naturally occurring or artificially fabricated particles use environmental energy via non-equilibrium processes in order to propel themselves. Studies on active matter have provided significant advancements in recent years, leading to fascinating findings both on the single- and many-particle level. Until now, research efforts have been almost exclusively targeted towards classical particles. It is however a natural question to ask, if active motion can also be realized on the quantum level. For this, it is important to understand the minimal ingredients necessary to model active quantum particles as well as to find suitable systems to realize them in experiments. It is interesting to investigate how quantum effects influence or enhance the properties of active particles and to find entirely new functionalities that are genuinely quantum. These questions further extend to the active matter case, where many-body quantum effects open additional directions to research.

In very recent works, some of these questions have begun to be addressed. In Ref. [16], active quantum particles were described via a non-hermitian quantum walk, whereas in [17], the motion was generated through classical noise. Multiple active quantum agents may be synchronized as discussed in [18]. Collective effects induced by activity were discussed in [165–168], using Lindblad [166] as well as non-hermitian dynamics [165, 168]. Finally, there are also important links to earlier studies on directed motion and motors on the nanoscale [169–176].

Here we want to discuss a class of single-particle models facilitating active quantum motion which are suitable for realization in synthetic systems. Specifically, these models are realizable in systems of cold atoms moving in optical lattices. By coupling its internal and translational degrees

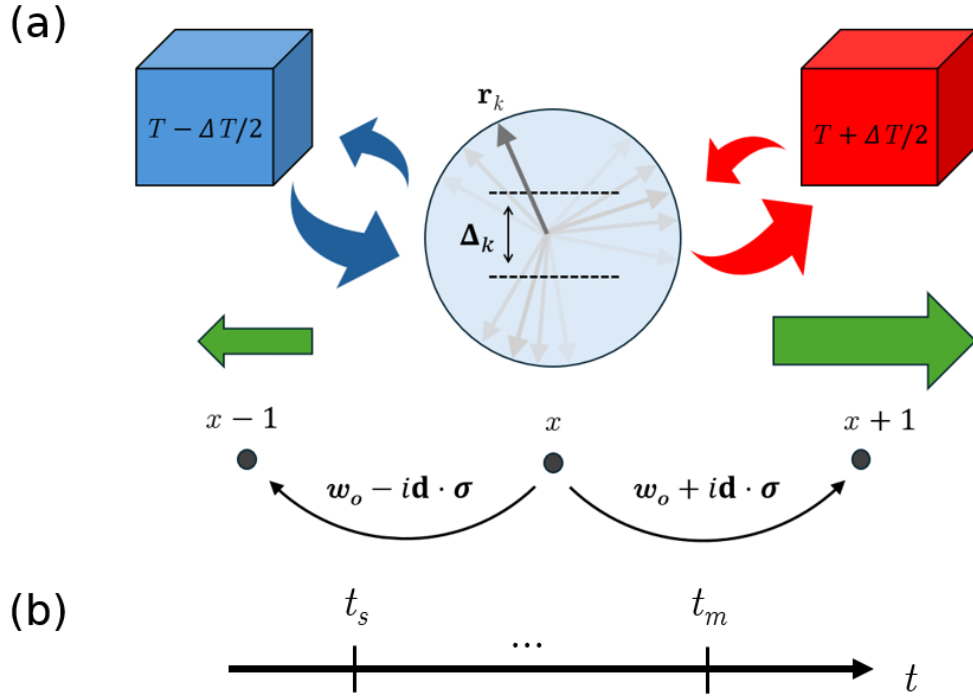


Figure 9.1: Sketch of the model of the active quantum particle. (a) The particle hops along a 1d chain of sites (black dots) with spin-dependent amplitudes (black arrows). The spin of the particle $\boldsymbol{\sigma}$ is coupled to its motion via the spin-orbit field \mathbf{d} and is further aligned by a Zeeman field, leading to a momentum-dependent spin orientation (gray arrows) and internal level spacing Δ_k . The internal state of the particle is coupled to a hot (red) and a cold (blue) heat reservoir and it is further subject to momentum relaxation processes due to scattering events with the environment (not illustrated here). (b) Hierarchy of characteristic time scales, $t_s \ll t_m$. We assume that the momentum relaxation time scale t_m is much larger than the time scale t_s associated with spin relaxation due to the coupling to the heat reservoirs.

of freedom, the quantum particle translates heat transfer in the engine into motion, drawing a connection to quantum heat engines [177–180]. The motion of the particle is characterized by quantum features, which play a significant role in the heat-to-motion transfer. Moreover, the stochastic nature of the heat exchange facilitating the motion becomes important, as the microscopic nature of the quantum heat engine gives rise to relevant fluctuations. This provides a natural connection to the field of quantum thermodynamics [181, 182].

In this chapter, we will first discuss rather general ideas, after which we provide a detailed analysis of a specific case closely related to the example discussed in 8.2: A spin-1/2 particle coupled to two different heat reservoirs. For this, we present explicit calculations characterizing its motion, quantum signatures and stochastic nature.

9.2 MODEL FOR AN ACTIVE QUANTUM PARTICLE

Our active quantum particle possesses a combination of internal and translational degrees of freedom, with the (discrete) internal degrees of freedom being coupled to external reservoirs inducing transitions, as illustrated in Fig. 9.1(a). If the translational degrees of freedom are coupled to the internal ones by e.g., spin-orbit coupling, heat transfer-induced transitions between the internal levels give kicks to the particle, generating motion (see Ref. [183] for a recent discussion on classical active particles originating from spin-orbit coupling). We account for momentum relaxation by further introducing a noisy environment (modeled by a phonon bath) for the active quantum particle. We will show that the motion of the particle does not only persist, but can also be enhanced by the damping of its translational degrees of freedom.

The active particle is only able to perform directed motion in a non-equilibrium setting. This can be achieved by keeping the heat reservoirs at different (hot and cold) temperatures $T_{h,c} = T \pm \Delta T/2$. As the baths only couple to the internal degrees of freedom, this alone does not constitute directed motion. Still, non-equilibrium prevents the absorption and excitation processes from the different baths to balance, which in principle allows for self-propulsion.

The Hamiltonian describing the active quantum particle and its coupling to the environment is of the form of Eq. (8.1), $H = H_p + H_B + H_I$. The model of the particle is as follows,

$$H_p = \sum_{s,s'} B_{s,s'} |s\rangle\langle s'| + \sum_{x,s,s'} w_{s,s'} |x, s\rangle\langle x+1, s'| + \text{h.c.}, \quad (9.1)$$

with the index s labeling the internal state of the particle. The $B_{s,s'}$ capture the internal energy structure of the quantum particle. The hopping on a 1d lattice (with sites labeled by x) is described through $w_{s,s'}$, allowing for hopping processes which change the internal state of the particle (analogously to spin-orbit coupling). While we limit ourselves here to motion on a lattice in one dimension, the extension of the model to higher dimensions or the continuum limit is straightforward. The bath Hamiltonian H_B is a combination of different sets of harmonic oscillators, each in thermal equilibrium, given in Eq. (8.2). The coupling H_I is specified further below.

The Hamiltonian H captures the general essence of heat-to-motion conversion. For the remainder of this chapter, we illustrate the properties of the active quantum particle via focusing on a specific case, namely the minimal model of a spin-1/2 particle. We may then identify the terms in Eq. (9.1) as follows: The spin-1/2 particle is subject to a Zeeman field $B_{s,s'} = [\mathbf{B} \cdot \boldsymbol{\sigma}]_{s,s'}$ and hopping amplitudes $w_{s,s'} = [w_o \mathbb{1}_s + i\mathbf{d} \cdot \boldsymbol{\sigma}]_{s,s'}$. We will assume a real-valued spin-orbit field \mathbf{d} , so that the spin-orbit coupling preserves time-reversal symmetry. The Hamiltonian in Eq. (9.1) for the spin-1/2 particle can then be diagonalized by passing to momentum space and

further applying a k -dependent rotation R_k to the spin. By defining the rotated spin operators $\boldsymbol{\tau}_k = R_k^\dagger \boldsymbol{\sigma} R_k$, we may write the particle Hamiltonian in its eigenbasis as

$$H_p = \sum_k (\epsilon_k \mathbb{1}_s + \Delta_k \tau_{z,k}) |k\rangle\langle k|, \quad (9.2)$$

with $\epsilon_k = -2w_o \cos k$, $\Delta_k = |\boldsymbol{\Delta}_k|$, $\boldsymbol{\Delta}_k = \mathbf{B} - 2\mathbf{d}_k$ and $\mathbf{d}_k = \mathbf{d} \sin k$.

Before we apply a non-zero temperature bias ΔT , we assume that the system is relaxed to thermal equilibrium with temperature T . We parametrize each 2×2 k -block ρ_k on the diagonal of the density matrix via

$$\rho_k = \frac{r_{o,k}}{2} (\mathbb{1}_s + \mathbf{r}_k \cdot \boldsymbol{\tau}_k). \quad (9.3)$$

By applying the Lindblad equation (8.24) derived in section 8.1, we find that each k -block evolves according to

$$\dot{\rho}_k = -i[\Delta_k \tau_{z,k}, \rho_k] + \mathcal{D}_s[\rho_k] + \mathcal{D}_m[\{\rho_{k'}\}], \quad (9.4)$$

with the dissipator

$$\mathcal{D}_s[\rho_k] = \sum_{\ell=\pm} \sum_{\alpha=h,c} \Gamma_{\alpha,k}^{(\ell)} \left[\tau_{\ell,k} \rho_k \tau_{\ell,k}^\dagger - \frac{1}{2} \{ \tau_{\ell,k}^\dagger \tau_{\ell,k}, \rho_k \} \right] \quad (9.5)$$

originating from the coupling to the baths,

$$H_I = H_r + \sum_{k,n} \sum_{\alpha=h,c} |k\rangle\langle k| \otimes \tau_{\alpha,k} \otimes (b_{\alpha,n} + b_{\alpha,n}^\dagger). \quad (9.6)$$

We define the momentum relaxation inducing term H_r in Eq. (9.11) and discuss the associated dissipator \mathcal{D}_m further below. The dissipation rates in Eq. (9.5) are given by

$$\Gamma_{\alpha,k}^{(\ell)} = \xi_{\alpha,k} [n(2\Delta_k, T_\alpha) + \delta_{\ell,-}], \quad (9.7)$$

with the factors $\xi_{\alpha,k} = \gamma_{\alpha,k} |\langle \uparrow | \tau_{\alpha,k} | \downarrow \rangle|^2$ allowing for different coupling strengths γ_α and operators $\tau_{\alpha,k}$ to the two reservoirs. We further introduced the transition operators $\tau_{\pm,k} = (\tau_{x,k} \pm i\tau_{y,k})/2$. The two dissipators \mathcal{D}_s and \mathcal{D}_m give rise to different relaxation time scales t_s and t_m respectively. As sketched in Fig. 9.1(b), we assume that momentum relaxation processes are much slower compared to their spin counterpart, $t_s \ll t_m$. Since the dissipator \mathcal{D}_s does not couple different momenta (see also C.1), the momentum distribution $r_{o,k}$ will stay constant for times $t \ll t_m$ after applying the temperature bias. On the other hand, the spin distribution \mathbf{r}_k will evolve towards a non-equilibrium steady state. Due to the k -dependent quantization axis (defined via the rotation R_k), the corresponding dynamics of the active particle are genuinely quantum.

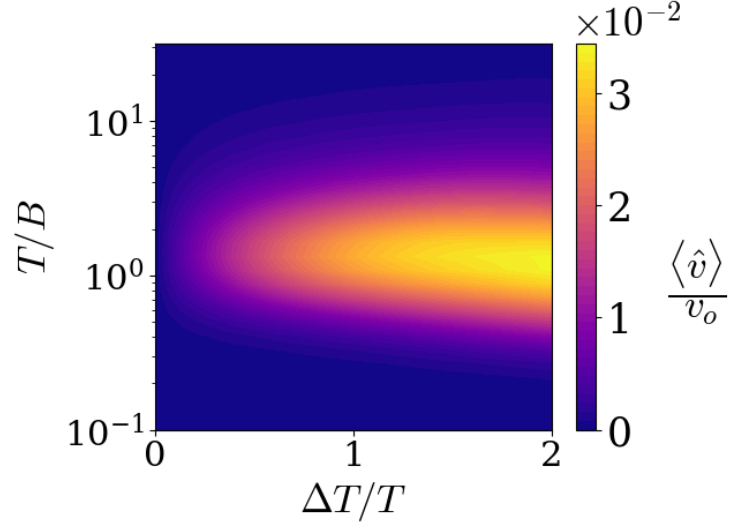


Figure 9.2: Average velocity $\langle \hat{v} \rangle$ in the steady state ($t_s \ll t \ll t_m$) as a function of equilibrium temperature T and relative temperature bias $\Delta T/T$. Velocity scale: $v_o = Ba$ with a the lattice spacing. Parameters: Zeeman field $\mathbf{B} = B(\hat{x} \cos \theta + \hat{z} \sin \theta)$ with $\theta = 3\pi/4 - 0.01$, hopping energy $w_o = 1.5B$, spin-orbit field $\mathbf{d} = B(\hat{x} + \hat{z})/2$ and system size $N = 100$. Coupling to the baths via $\tau_{h,k} = \tau_{y,k}$, $\tau_{c,k} = \tau_{z,k}$ and $\gamma = 0.4B$.

9.3 HEAT-TO-MOTION CONVERSION

We want to characterize the dynamics of the active quantum particle by calculating its average velocity, given by¹

$$\langle \hat{v}(t) \rangle = \sum_k \text{Tr}_s(\hat{v}_k \rho_k(t)). \quad (9.8)$$

Here, the velocity operators v_k are given by the momentum derivative of the Hamiltonian, $\hat{v}_k = \partial_k \epsilon_k \mathbb{1} + (\partial_k \mathbf{\Delta}_k) \cdot \boldsymbol{\sigma}$. By inserting the Boltzmann distribution for $\rho_k(t)$ in Eq. (9.8), it becomes clear that the average velocity vanishes in thermal equilibrium. For a small temperature bias, we calculate the steady state of the density matrix for times $t_s \ll t \ll t_m$. The average velocity of the particle is then given in linear response as

$$\langle \hat{v} \rangle = \frac{\Delta T}{T^2} \sum_k r_{o,k} \frac{\xi_{h,k} - \xi_{c,k}}{\xi_{h,k} + \xi_{c,k}} \frac{\mathbf{\Delta}_k \cdot \partial_k \mathbf{d}_k}{\cosh^2(\beta \Delta_k)}. \quad (9.9)$$

¹We indicate the operator nature of the velocity by a hat in order to distinguish them from the velocity unit v_o used in the figures.

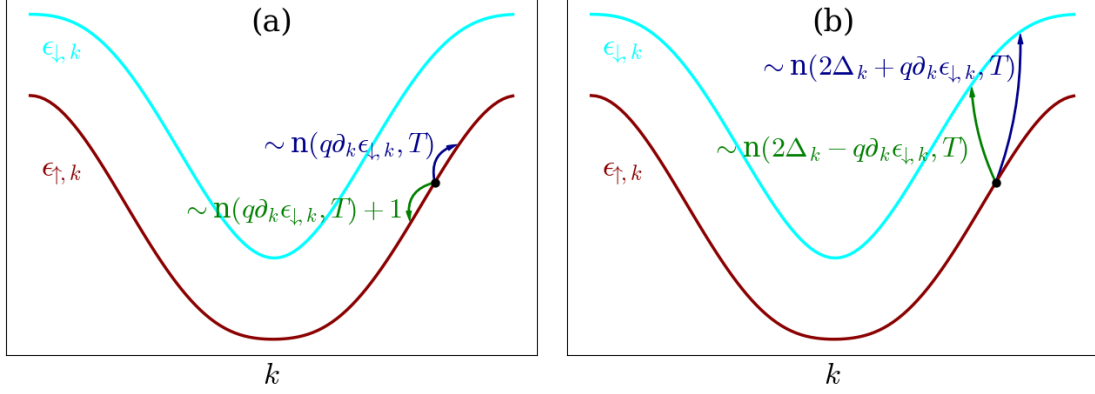


Figure 9.3: Momentum relaxation processes. (a) Spin-conserving relaxation processes between momenta k and $k \pm q$ with $q \simeq q_0$ being small. (b) Scattering processes between k and $k \pm q$ flipping the spin of the particle. The dispersions $\epsilon_{\sigma,k}$ are calculated with the parameters stated in the caption of Fig. 9.2.

For a detailed derivation, see C.1. As we consider times much smaller than t_m , the momentum distribution in Eq. (9.9) is given by the thermal state,

$$r_{o,k}^{\text{th}} = \frac{1}{\mathcal{Z}} e^{-\beta \epsilon_k} \cosh(\beta \Delta_k), \quad (9.10)$$

with $\mathcal{Z} = \text{Tr}(e^{-\beta H_p})$ being the normalizing partition function. Equation (9.9) reveals that the particle moves at a finite velocity only if $\xi_{h,k} \neq \xi_{c,k}$, meaning that different couplings to the baths are necessary to drive the particle. In simulations, we use different coupling operators $\tau_{\alpha,k}$ at equal coupling strengths, $\gamma_h = \gamma_c = \gamma$. Furthermore, Eq. (9.9) implies that the parameters \mathbf{B} , \mathbf{d} and w_o all have to be non-zero in order to generate motion, see C.1.

In Fig. 9.4, we present evaluations of the active particle's average velocity in the steady-state (without momentum relaxation) as a function of temperature T and temperature bias $\Delta T/T$, beyond the linear response regime. Curiously, we find that the velocity vanishes both in the low and high temperature limit, with an intermediate optimal temperature T_{opt} . At low temperatures, the velocity vanishes exponentially with $\langle \hat{v} \rangle \sim e^{-2\beta B}$, $B = |\mathbf{B}|$, as transitions of the internal state become suppressed. Consequently, the heat reservoirs are unable to create the necessary imbalance to drive the particle into motion. On the other hand, the velocity decreases with $\langle \hat{v} \rangle \sim 1/T^3$ at high temperatures. As the mode occupation differences between the reservoirs become less pronounced with increasing temperature, the deviations from equilibrium decrease, leading to weaker driving. We estimate that the velocity is maximized at a temperature $T_{\text{opt}} \simeq 0.83B$, given that $w_o \gg B, d$. We discuss the temperature dependence of the average velocity in detail in C.1.

9.4 MOMENTUM RELAXATION

In a realistic environment, the active particle will be subject to processes that add randomness to its momentum. We can model this by adding a phonon bath at temperature T , which couples to the particle via

$$H_r = \sum_{k,q,n} \sqrt{\frac{\lambda_q}{N}} |k\rangle\langle k+q| \otimes \mathbb{1}_s \otimes (b_{-q,n} + b_{q,n}^\dagger), \quad (9.11)$$

with N denoting the length of the chain. The bosonic operators in Eq. (9.11) create or destroy phonons in transverse mode n with longitudinal momentum q . For the coupling, we choose

$$\lambda_q = \lambda_0 \exp\left\{-\frac{|q|}{q_0}\right\}, \quad (9.12)$$

with small q_0 , so that scattering only occurs between nearby momentum states. As the coupling to the phonon bath in Eq. (9.11) only induces local momentum transitions and the overall probability is conserved, the momentum distribution $r_{o,k}$ evolves according to a drift-diffusion equation,

$$\partial_t r_{o,k} = \partial_k [v_D(k) r_{o,k} + D(k) \partial_k r_{o,k}], \quad (9.13)$$

with $v_D(k)$ being the drift velocity and $D(k)$ the diffusion constant. In C.2, we calculate Eq. (9.13) explicitly using the dissipator \mathcal{D}_m derived from H_r . Here we provide a qualitative analysis, capturing the essence of the dynamics of the momentum distribution: The scattering processes leading to momentum relaxation may conserve or flip the spin of the particle, as the effective Zeeman-field Δ_k is k -dependent. Given that the phonon density of states $\nu(\omega)$ does not increase too fast at small energies ω , we find however that the spin-conserving processes are dominating the momentum relaxation. This can be understood from estimating the q_0 dependence of the drift velocity and the diffusion constants of the respective processes. We illustrate the different momentum transitions in Fig. 9.3. In Fig. 9.3(a), we show spin-conserving momentum transitions. The corresponding scattering processes are associated with phonons of energy ω , with the scattering rates being determined by the phonon density of states $\nu(\omega)$ and the Bose distribution $n(\omega, T)$ with $\omega = \epsilon_{\sigma,k\pm q} - \epsilon_{\sigma,k} \simeq \pm q \partial_k \epsilon_{\sigma,k}$ and q of order q_0 . Fig. 9.3(b) shows momentum transitions where the spin of the particle is flipped. Contrary to the spin-conserving scattering, the phonon energies here approach a non-zero value for $q \rightarrow 0$ due to the finite spin-splitting, $\omega \simeq 2\Delta_k \pm q \partial_k \epsilon_{\sigma,k}$. Assuming a phonon density of $\nu(\omega) = |\omega|^p$, we can estimate the drift velocity $v_D(k)$ (diffusion constant $D(k)$) through the difference (average)

of the scattering rates to the left and right², multiplied by q (q^2). The contributions of the spin-conserving processes then yield

$$\begin{aligned} v_D^{(a)}(k) &\sim q \frac{\nu(\omega)}{|\omega|} \frac{n(\omega, T) + 1 - n(\omega, T)}{2} \sim \frac{1}{2} q^p |\partial_k \epsilon_{\sigma, k}|^{p-1}, \\ D^{(a)}(k) &\sim q^2 \frac{\nu(\omega)}{|\omega|} \frac{2n(\omega, T) + 1}{2} \sim q^p T |\partial_k \epsilon_{\sigma, k}|^{p-2}, \end{aligned} \quad (9.14)$$

where we assumed that $T \gg \omega \sim q$. Additional factors of $1/|\omega|$ arise in Eq. (9.14) as a consequence of momentum conservation along the chain. The contributions of the spin-flip scattering processes are different from Eq. (9.14), as the phonon energy stays finite in the limit of $q \rightarrow 0$. This suggests that we can approximate the Bose distribution as well as the phonon density of states by a q -independent constant. Also, the matrix element associated with a spin-flip process is proportional to q . Overall, the contributions of the spin-flip scattering can be estimated as

$$v_D^{(b)}(k) \sim q^4, \quad D^{(b)}(k) \sim q^4. \quad (9.15)$$

Comparing the contributions of the spin-conserving and spin-flip processes, we find that only the contributions of the spin-conserving scattering processes are relevant to the evolution equation of $r_{o,k}$, under the condition that $p < 4$. We point out that $\nu(\omega) \sim |\omega|^{n-1}$ for a n -dimensional bath of acoustic phonons. In the full calculation given in C.2, we find that the heuristically derived drift velocity and diffusion constant in Eq. (9.14) are remarkably close to the exact expressions. However, contributions from different spin levels are weighed by the spin distribution \mathbf{r}_k . In C.2, we find that to lowest order in t_s/t_m , the spin distribution evolves independently from the momentum distribution $r_{o,k}$, resulting in a time-independent drift velocity and diffusion constant in Eq. (9.13) for times $t \gg t_s$. From the drift-diffusion equation, we can then calculate the steady state momentum distribution $r_{o,k}^\infty$ of the system in the presence of momentum relaxation. For $p = 2$, we find

$$r_{o,k}^\infty = \frac{1}{\mathcal{Z}} \exp \left\{ -\frac{\beta}{2} \int_0^k dk' \text{Tr}_s(\hat{v}_{k'} [\mathbb{1}_s + \mathbf{r}_{k'} \cdot \boldsymbol{\sigma}]) \right\}. \quad (9.16)$$

Results for other values of p are given in C.2. The average velocity in the momentum-relaxed steady state is still given by Eq. (9.9), only that the thermal momentum distribution $r_{o,k}$ is replaced by $r_{o,k}^\infty$.

We numerically simulate the Lindblad dynamics in Eq. (9.4) to illustrate the time evolution of the average velocity over the different time scales, shown in Fig. 9.4 for different phonon bath densities of states. We find that for times much smaller than the momentum relaxation time t_m , the evolution of the velocity is independent of the phonon bath. After an initial transient

²Since the rates are k -dependent, there are additional contributions. These however do not change the here presented conclusions.

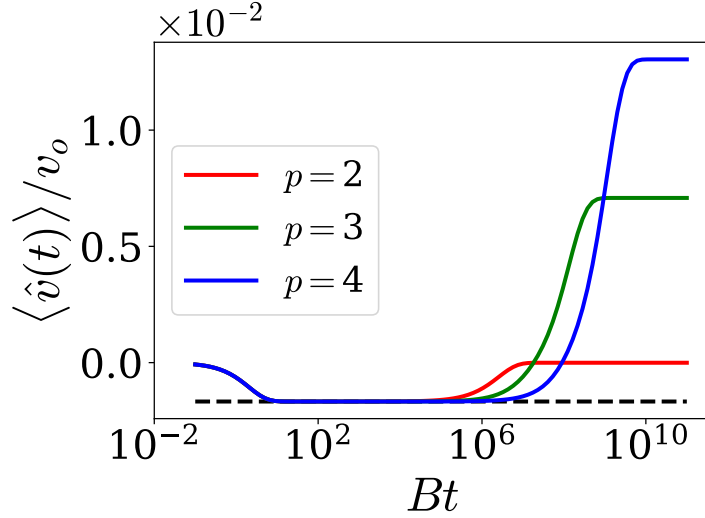


Figure 9.4: Average velocity as a function of time for different phonon bath density of states $\nu(\omega) \sim \omega^p$. Black dashed line: Steady state velocity as given in Eq. (9.9). Parameters: same as in the caption of Fig. 9.2 and $T = B$, $\Delta T = 0.05T$. Coupling to the phonon bath with coupling range $q_0 = 0.02B$. Time scale hierarchy $t_s \ll t_m$ established by choosing $\lambda_0/N = 0.001B \ll \gamma$.

($t \ll t_s$), the active particle reaches an intermediate steady state and moves at the velocity given in Eq. (9.9), driven by the heat exchange with the thermal reservoirs. At much later times ($t \gg t_m$), momentum relaxation sets in and the particle reaches its steady state with a different average velocity. Surprisingly, we find that momentum relaxation may lead to an increase in magnitude of the velocity, as shown in Fig. 9.4. Furthermore, we find that the average velocities in the steady states with and without momentum relaxation not only differ in magnitude, but can also differ in sign. We note that at late times, the time evolution depends sensitively on the phonon bath density of states. The time dependence of the velocity however stays the same qualitatively, even when spin-flip scattering processes become relevant ($p = 4$).

9.5 QUANTUM SIGNATURES OF THE ACTIVE PARTICLE

We reveal the quantum nature of the active particle by a calculation of the velocity-velocity correlation function,

$$g(t, \bar{t}) = \langle \delta \hat{v}(t) \delta \hat{v}(t + \bar{t}) \rangle, \quad (9.17)$$

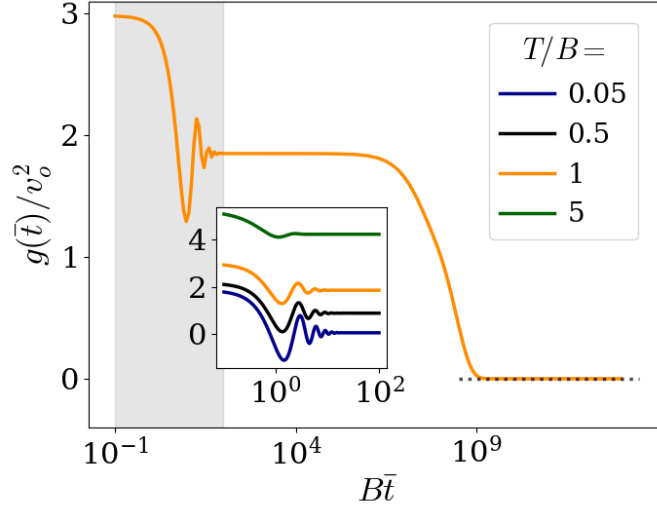


Figure 9.5: Velocity correlation function $g(\bar{t})$ for times $t \gg t_m$ against relative time \bar{t} . Inset-Plot: Behavior at relative times $\bar{t} < t_s$ (gray bar) for various temperatures. Black dotted line: $g(\bar{t}) = 0$.

with $\delta\hat{v}(t) = \hat{v}(t) - \langle\hat{v}(t)\rangle$. We compute the function in the steady state of the system by employing the quantum regression theorem derived in Sec. 8.3. The result is given by

$$g(\bar{t}) = \sum_k r_{o,k} \left(e^{-\Gamma_k \bar{t}/2} \cos(2\Delta_k \bar{t}) (\hat{\Delta}_k \times \partial_k \mathbf{d}_k)^2 \right) + 4 e^{-\Gamma_k \bar{t}} \sum_{\alpha, \alpha'} \frac{\Gamma_{\alpha,k}^+ \Gamma_{\alpha',k}^-}{\Gamma_k^2} (\hat{\Delta}_k \cdot \partial_k \mathbf{d}_k)^2 + g_o, \quad (9.18)$$

where $\Gamma_k = \sum_{\ell, \alpha} \Gamma_{\alpha,k}^{(\ell)}$ and $\bar{t} \ll t_m$. The detailed calculation is shown in C.3. By using the appropriate momentum distribution for $r_{o,k}$, the expression in Eq. (9.18) applies to the steady state with and without momentum relaxation. The correlation function decays to a nonzero constant g_o , which reflects the fact that for times $t_s \ll \bar{t} \ll t_m$, residual correlations remain due to memory of the initial momentum distribution. In the long-time limit $t, \bar{t} \gg t_m$, these decay with the onset of momentum relaxation, so that $g(t, \bar{t}) \rightarrow 0$. We find that the average velocity is orders of magnitude smaller than the fluctuations of the velocity, which highlights the importance of stochasticity. One can also extract the mean-square displacement of the active particle from the velocity-velocity correlation function via integration, see C.4.

We present a typical time trace of the velocity correlations in Fig. 9.5. The oscillations in the correlation function are directly related to the Rabi oscillations of the spin during the motion of the particle. Rabi oscillations are present in thermal equilibrium, and persist clearly for non-zero temperature bias ΔT , where the quantum particle becomes active. The period of the oscillations as well as the temperature scale are determined by the Zeeman field B , whereas the oscillations decay on the spin relaxation time scale t_s . The oscillations in the correlation function are a

clear quantum signature. As can be seen in Eq. (9.18), their appearance is linked to the relative orientation of the vectors \mathbf{d} and Δ_k . For parallel fields, $\mathbf{d} \parallel \Delta_k$, energy between the baths and particle is exchanged through incoherent transitions between the spin states, leading to the absence of oscillations (classical limit).

9.6 CONCLUSION

In this chapter, we provided a scheme of engineering an active particle on the quantum level. The crucial elements of the model consist of a 'spin-orbit coupling' between the translational and internal degrees of freedom of the particle, a 'magnetic field' breaking time-reversal symmetry as well as an asymmetric coupling to the heat reservoirs driving the system out of equilibrium. All of these components are readily available in cold-atom systems [184–188].

This work focused on the deep quantum limit of a particle with two internal levels. We studied the necessary ingredients leading to heat-to-motion conversion, the quantum features of the active motion as well as the effects of a noisy environment, ultimately leading to momentum relaxation. More generally, we expect that our qualitative findings are not restricted to the two-level case, giving higher flexibility in a possible experimental realization of the proposed scheme.

The present discussion was limited to considerations of single-particle properties in one dimension. It is however straightforward to generalize the model to higher dimensions as well as to include interactions between multiple particles. These extensions give rise to interesting effects such as collective behavior and topological phenomena. In a broader sense, the dynamics of active quantum particles are similar to quantum random walks [184–186] and are deeply linked to quantum thermodynamics [181, 182], which connects them to an even wider range of phenomena.

CONCLUSIONS

In this thesis, we explored how driving, whether externally applied or internally generated, may be used to reveal fascinating quantum many-body phenomena as well as to produce quantum effects that are exclusive to driven systems. We demonstrated the richness of this field by considering three distinct physical platforms.

For frustrated Josephson junction arrays, we have shown how current measurements yield information about the ordering of vortices. We further demonstrated how the combination of spin-orbit- and in-plane magnetic field lead to Josephson junction arrays exhibiting a superconducting diode effect. In periodically driven spin chains, we established the resilience of Floquet edge modes against disorder as well as connected the stability of the time-crystalline phase to spectral pairing. Finally, we studied a generic model for quantum particles driven by internal non-equilibrium processes and showed under what conditions directed motion takes place and explicit quantum behavior emerges.

Our results will hopefully impact the ongoing development of quantum technologies. Networks of superconducting qubits provide a platform for quantum computation with steadily improving noise-resilience. These systems are essentially highly engineered arrays of Josephson junctions. The results we obtained in chapters 3 and 4 are valid for two-dimensional square arrays. However, the underlying assumptions were rather generic. Hence, we expect that they can be applied to a wider range of systems, including networks of superconducting qubits. The zero pairing of the quantum Ising model has been proposed as another platform of qubit realization, via implementations of Josephson junction arrays [111–113]. However, these systems lack protection against symmetry-breaking longitudinal fields. We established in chapter 6 that the π pairing of the Floquet quantum Ising model is resistant against longitudinal fields, highlighting its potential for applications in quantum information processing. On the other hand, time crystals may be used as a robust quantum memory [121], meaning they may be used to store quantum information over extended periods of time. In chapter 7, we extend the theoretical understanding of time crystals, possibly leading to new directions of research. Lastly, we contributed to the theoretical groundwork of active quantum matter in chapter 9. Considering the impact of active matter studies on technological developments [15], it is not unlikely that applications of active quantum matter in quantum technologies may emerge in the future.

We also want to point out that new projects build on the results presented in this thesis. In Ref. [189], a quasi-periodic version of the Floquet quantum Ising model is discussed. Their findings are closely related to our results regarding the Floquet quantum Ising model. Furthermore, unpublished experiments on Josephson junction arrays with Kagome lattice geometry and in-

Conclusions

volving in-plane magnetic fields are being conducted in the laboratory of Javad Shabani. The associated current measurements show peculiar behavior, which are reminiscent of our results for the φ_0 -junction array. Lastly, our active quantum particle model is being used and extended to study many-body effects of active quantum particles, as well as active motion in lattices with topological band structure.

ACKNOWLEDGMENTS

First, I want to thank the Einstein Research Unit and the CRC183 for funding this research, as well as giving me the opportunity to partake in numerous events and connect to other aspiring scientists. I also want to thank the HPC service of ZEDAT, Freie Universität Berlin, for computing time [190].

I am especially grateful to my supervisor Felix von Oppen for his guidance and support during this work. At times when I was about to give up, he would always find a way to motivate me to keep going. Also, his excellent lectures on quantum mechanics (2016) and field theory (2018) influenced my interests greatly and ultimately lead me here.

I am thankful to my collaborators Harald Schmid, Simon Reinhardt, Ludmilla Viotti, Kang Yang, Leonid Glazman, Karsten Flensburg, Rosario Fazio and Liliana Arrachea. Without them, this work would not have been possible.

I thank my colleagues from Trakt 4, Krystof Kolar, Harald Schmid, Kang Yang and Larissa Melischek for making my time at the FU a pleasant one.

I thank my friends and my family for their love and support.

APPENDIX A

A.1 METROPOLIS ALGORITHM FOR VORTEX MODEL MINIMIZATION

In Fig. 3.2(f), we show the ground-state energy of striped vortex-lattice configurations over different values of frustration f . The energies are computed as follows: First, we choose a pattern of stripes, for example the ac pattern, and create a vortex lattice on an array with large N , commensurate with the pattern. Each of the partially filled diagonals is initiated with a filling of $\nu = 1/2$, as below that filling, the channels are not stable anymore, see Fig. 3.3. The chosen pattern with filling $\nu = 1/2$ corresponds to an initial frustration value f_0 . The interaction energy of the vortices is computed via the vortex Hamiltonian derived in 2.3.2,

$$H_v = \frac{\pi^2 E_J}{2} \sum_{\mathbf{r}_i, \mathbf{r}_j} [m(\mathbf{r}_i) - f] G(\mathbf{r}_i - \mathbf{r}_j) [m(\mathbf{r}_j) - f], \quad (\text{A.1})$$

with

$$G(\mathbf{r}) = \sum_{k_x, k_y \neq 0} \frac{e^{i\mathbf{k}\cdot\mathbf{r}} - 1}{2 - \cos(k_x) - \cos(k_y)}. \quad (\text{A.2})$$

Here, the interaction energy at zero distance has been set to zero, to exclude the core energies from the calculation. Also, a factor of $1/2$ has been added to avoid overcounting of the interactions in Eq. (A.1). In the next step, the frustration is increased by $1/N^2$ and a vortex is added to a vacant plaquette in one the partially filled diagonals. As we keep the striped structure of the lattice fixed, we first minimize the interaction energy inside each of the partially filled diagonals separately. This is done via a zero-temperature metropolis algorithm: We let each of the partially filled diagonals evolve for a number of time steps $n = 100 \cdot N$. At each time step, a vortex with an adjacent vacant plaquette is chosen at random. The vortex is then moved to the vacant plaquette and the energy of the new diagonal configuration is calculated via Eq. (A.1). The new lattice is accepted if its energy is lower than the energy of the previous lattice. Otherwise, the lattice is returned to the previous state.

After minimizing the interaction energy in each of the partially filled diagonals, the interaction between the diagonals is minimized. We assume that the number of vortices between the partially filled diagonals at most differs by one. The distribution of the diagonals with higher vortex number is then determined via the metropolis algorithm. We minimize the interaction of a one-dimensional chain, where the diagonals with higher filling correspond to vortices, the diagonals with lower filling to vacancies. Finally, the partially filled diagonals are shifted against each other

to further lower the energy of the array. This yields the ground state energy of the initially chosen pattern at filling $f_0 + i/N^2$, with i being the number of added vortices. We perform this procedure for frustrations until f_{\max} , which roughly corresponds to a channel filling of $\nu = 2/3$. Beyond this filling, the interaction energy will rapidly increase. The algorithm is showcased in [35] for a simple example.

A.2 ANNEALING OF THE PHASE CONFIGURATIONS

We use Eq. (3.1) in order to search for minima and saddle points of the energy manifold. We can find the ground-state configuration for a given frustration by using the algorithm proposed in Ref. [44]. The algorithm is based on a description of the Josephson junction array via the RCSJ model and solving the corresponding Kirchhoff's rules at each lattice site of the array, resulting in N^2 coupled linear differential equations. Temperature enters via Langevin currents due to Johnson-Nyquist noise. Starting with an initial random configuration of phases, we compute the time evolution of the system while gradually decreasing the temperature to zero. We also use periodic boundary conditions, which makes it necessary for N to be a multiple of q for a rational frustration $f = p/q$.

For frustrations in the region $1/3 < f < 1/2$, the application of the algorithm of Ref. [44] tends to (local) minimum configurations involving domain walls. This may be avoided by applying a larger magnetic field on diagonals of the array, where the expected vortex lattice has nonzero vortex occupation, and compensate with a decreased magnetic field on the neighboring diagonal to keep the overall magnetic flux fixed. After the annealing process, we gradually revert the flux configuration to a uniform one and let the system evolve according to steepest-descent dynamics. During this process, we find that the vortex configuration remains fixed.

In the simulations, we use the following parameters: Josephson coupling $E_J = 1$, resistance $R = 1$, $n = 10^5$ time steps, step size $\Delta\tau = 0.5$, initial temperature $T_0 = 0.2$. The temperature remains constant for the first $2 \cdot 10^4$ time steps, after which it linearly decays to zero. For striped vortex configurations, we increase the frustration on the expected fully occupied diagonals by $\Delta f = 0.1$ and decrease it on the neighboring diagonal by the same amount. The algorithm is showcased in [35] for a simple example.

A.3 CLIMBING-STRING METHOD

We can estimate the energy barrier between two minima of the vortex lattice as well as the vortex configuration at the barrier by using the climbing-string method described in Ref. [191]. The general idea behind the method is to start with a configuration close to an energy minimum and reversing the force that pushes the phases towards the minimum. This will push the phase configuration towards an adjacent saddle-point in a controlled manner. We here outline each of the important steps as well as specify the parameters used in our simulation.

Step 1: First, we denote the minimum configuration as $\mathbf{V}_0 = (\varphi_{1,1}, \varphi_{2,1}, \dots, \varphi_{N,N})$. The starting point of the procedure is a random configuration \mathbf{V}_M close to \mathbf{V}_0 . We then interpolate linearly between \mathbf{V}_M and \mathbf{V}_0 to obtain $M - 1$ images \mathbf{V}_i with $i = 1, \dots, M - 1$, which form a 'string' between \mathbf{V}_0 and \mathbf{V}_M . Now, we keep the end of the string \mathbf{V}_0 fixed, and evolve the rest of the string according to the following equations of motion,

$$\dot{\mathbf{V}}_i = -\nabla H, \quad 0 < i < M \quad (\text{A.3})$$

$$\dot{\mathbf{V}}_M = -\nabla H + \theta(\nabla H \cdot \boldsymbol{\tau})\boldsymbol{\tau}. \quad (\text{A.4})$$

with $\theta > 1$ and the approximate tangent vector $\boldsymbol{\tau}$ given by

$$\boldsymbol{\tau} = \frac{\mathbf{V}_M - \mathbf{V}_{M-1}}{|\mathbf{V}_M - \mathbf{V}_{M-1}|}. \quad (\text{A.5})$$

Thus, the endpoint \mathbf{V}_M is climbing the basin of the minimum \mathbf{V}_0 along the tangent direction of the string, whereas it follows steepest descent dynamics in the perpendicular direction. All the other images along the string evolve towards the minimum configuration.

Step 2: In order to ensure that the endpoint converges towards to an adjacent saddle-point configuration, we calculate the energy of each image after k time steps and check whether the energy rises monotonically along the string. If there is an image with $H(\mathbf{V}_{j+1}) < H(\mathbf{V}_j)$, the string is truncated at \mathbf{V}_j . Also, we rebalance the images along the string so that they remain evenly distributed. This is done as follows. We parametrize the images in terms of the arclength s_i ,

$$s_0 = 0, \quad s_{i+1} = s_i + |\mathbf{V}_{i+1} - \mathbf{V}_i|. \quad (\text{A.6})$$

The parameters of the images are then given by

$$\alpha_i^* = s_i / s_j. \quad (\text{A.7})$$

We use the images as well as their associated parameters in order to calculate an analytic function describing the string via, e.g., cubic interpolation. The curve $\gamma = \{\mathbf{V}(\alpha), \alpha \in [0, 1]\}$ is then evaluated at $\alpha_i = i/M$ with $0 \leq i \leq M$ to generate $M + 1$ evenly distributed images along the string.

Step 3: We conclude the endpoint of the string converged to an adjacent saddle-point by checking the condition

$$\max\{|\partial_{\varphi_{i,j}} H(\mathbf{V}_M)|, 1 \leq i, j \leq N\} < \delta, \quad (\text{A.8})$$

with δ being a tolerance. If not, we repeat steps 1-3 until convergence.

Appendix A

We specify the parameters used for the simulations in chapter 3. For a striped vortex configuration $\mathbf{V}_0 = (\varphi_{1,1}, \dots, \varphi_{N,N})$ featuring a domain wall at site (i, j) , we use an initial image $\mathbf{V}_M = (\varphi'_{1,1}, \dots, \varphi'_{N,N})$ with

$$\varphi'_{i+1,j+1} = \varphi_{i+1,j+1} + 2, \quad (\text{A.9})$$

and all other phases identical to \mathbf{V}_0 . This ensures that the adjacent saddle-point the string evolves towards is associated with a hopping domain wall. We use $M = 20$ images, an evolution time interval $\Delta t = 0.01$, a force parameter $\theta = 1.2$, and a tolerance $\delta = 10^{-4}$. The images are rebalanced after 500 time steps. The Josephson energy E_J is set to unity. The algorithm is showcased in [35].

APPENDIX B

B.1 SINGLE-PARTICLE SPECTRUM AND EIGENSTATES OF THE FLOQUET QUANTUM ISING MODEL

In this section, we want to calculate the single-particle spectrum of the Floquet quantum Ising model $U_F = U_g U_J$ defined in Eq. (6.1) and show that in certain parameter regimes, the model hosts edge modes. The here given derivation is based on an analogous calculation in Ref. [94]. Since we will make use of the transfer matrix technique, we assume a semi-infinite chain, i.e. the chain has an open boundary on one side and is infinitely long on the other. We start the derivation by switching to the fermionic model via the Jordan-Wigner transformation (Eq. (5.9)) and further introduce Majorana fermions γ_i as defined in Eq. (5.11),

$$U_g = \exp\left\{\frac{i\pi g}{2} \sum_{i=1}^N X_i\right\} = \exp\left\{\frac{i\pi g}{2} \sum_{i=1}^N (1 - 2c_i^\dagger c_i)\right\} = \exp\left\{-\frac{\pi g}{2} \sum_{i=1}^N \gamma_{2i-1} \gamma_{2i}\right\}, \quad (\text{B.1})$$

$$U_J = \exp\left\{\frac{i\pi J}{2} \sum_{i=1}^{N-1} Z_i Z_{i+1}\right\} = \exp\left\{-\frac{\pi J}{2} \sum_{i=1}^{N-1} \gamma_{2i} \gamma_{2i+1}\right\}. \quad (\text{B.2})$$

A quasiparticle operator d_α satisfies the condition

$$U_F^\dagger d_\alpha U_F = e^{-i\epsilon_\alpha} d_\alpha, \quad (\text{B.3})$$

with ϵ_α being the associated quasienergy of the particle. For $g = 0$, it is obvious that $d_\alpha = (\gamma_1 + i\gamma_{2N})/2$ is a quasiparticle operator with quasienergy energy $\epsilon_\alpha = 0$, as the edge Majoranas vanish from the Floquet operator. This is unsurprising, given that the Floquet model coincides with the time-independent Kitaev chain at this point in parameter space. The novelty arises at $g = 1$. Here, U_g becomes the parity operator P . Consequently, we find for d_α ,

$$U_F^\dagger d_\alpha U_F = P d_\alpha P = -d_\alpha = e^{-i\pi} d_\alpha. \quad (\text{B.4})$$

As for the $g = 0$ case we find a localized Majorana edge state, but now with a quasienergy of $\epsilon_\alpha = \pi$. Hence, we name the associated edge particles Majorana π -modes.

In the following, we want to study the bulk spectrum, localization lengths of edge modes and phase transition points of the Floquet quantum Ising model in the parameter range of

Appendix B

$g, J \in [0, 1]$. For this, we make use of the transfer-matrix technique. We define a quasiparticle operator d_α as follows,

$$d_\alpha = \sum_{j=1} (\psi_{2j-1} \gamma_{2j-1} + \psi_{2j} \gamma_{2j}), \quad (\text{B.5})$$

with ψ_{2j-1} and ψ_{2j} being the wave functions associated with the respective Majorana fermion. Using the fermionized expressions of the Floquet operator in Eq. (B.2), we find its action onto each Majorana operator,

$$\begin{aligned} U_g^\dagger \gamma_{2i-1} U_g &= \cos(\pi g) \gamma_{2i-1} - \sin(\pi g) \gamma_{2i} \\ U_g^\dagger \gamma_{2i} U_g &= \cos(\pi g) \gamma_{2i} + \sin(\pi g) \gamma_{2i-1} \\ U_J^\dagger \gamma_{2i} U_J &= \cos(\pi J) \gamma_{2i} - \sin(\pi J) \gamma_{2i+1} \\ U_J^\dagger \gamma_{2i+1} U_J &= \cos(\pi J) \gamma_{2i+1} + \sin(\pi J) \gamma_{2i}. \end{aligned} \quad (\text{B.6})$$

Applying the Floquet operator U_F to d_α then yields

$$\begin{aligned} U_F^\dagger d_\alpha U_F &= e^{-i\epsilon} d_\alpha = \sum_{j=0} [\psi_{2j-1} \sin(\pi g) \sin(\pi J) - \psi_{2j} \cos(\pi g) \sin(\pi J) \\ &+ \psi_{2j+1} \cos(\pi g) \cos(\pi J) + \psi_{2j+2} \sin(\pi g) \cos(\pi J)] \gamma_{2j+1} + [-\psi_{2j-1} \sin(\pi g) \cos(\pi J) \\ &+ \psi_{2j} \cos(\pi g) \cos(\pi J) + \psi_{2j+1} \cos(\pi g) \sin(\pi J) + \psi_{2j+2} \sin(\pi g) \sin(\pi J)] \gamma_{2j}. \end{aligned} \quad (\text{B.7})$$

The next step is to compare the coefficients of γ_{2j} and γ_{2j+1} on each side. This provides two equations that we may reorder in the following fashion,

$$\begin{pmatrix} \psi_{2j+1} \\ \psi_{2j+2} \end{pmatrix} = T_\epsilon \begin{pmatrix} \psi_{2j-1} \\ \psi_{2j} \end{pmatrix} \quad (\text{B.8})$$

with

$$T_\epsilon = \frac{1}{\sin(\pi J)} \begin{pmatrix} \sin(\pi g) e^{i\epsilon} & \cos(\pi J) - \cos(\pi g) e^{i\epsilon} \\ \cos(\pi J) - \cos(\pi g) e^{i\epsilon} & \frac{e^{-i\epsilon}}{\sin(\pi g)} - 2 \cot(\pi g) \cos(\pi J) + \cos(\pi g) \cot(\pi g) e^{i\epsilon} \end{pmatrix} \quad (\text{B.9})$$

being the transfer matrix, satisfying $\det T_\epsilon = 1$. We first calculate the bulk spectrum of the Floquet model. We make the Bloch wave ansatz $(\psi_{2j-1}, \psi_{2j}) = e^{ikj}(a, b)$ with wavevector k and complex numbers a and b . Making this ansatz transforms the transfer-matrix equation in Eq. (B.8) into a eigenvalue equation, where e^{ik} is the eigenvalue of the transfer matrix T_ϵ . As the determinant of T_ϵ is normalized, the other eigenvalue is e^{-ik} . We may now calculate the

B.1 Single-particle spectrum and eigenstates of the Floquet quantum Ising model

energy of the Bloch waves by tracing over the transfer matrix. As the trace yields the sum of the eigenvalues, we find

$$e^{ik} + e^{-ik} = \frac{1}{\sin(\pi J)} \left[\sin(\pi g) e^{i\epsilon} + \frac{e^{-i\epsilon}}{\sin(\pi g)} - 2 \cot(\pi g) \cos(\pi J) + \cos(\pi g) \cot(\pi g) e^{i\epsilon} \right]. \quad (\text{B.10})$$

Solving for $\cos \epsilon$, we find the bulk mode spectrum as follows,

$$\cos \epsilon = \cos(\pi g) \cos(\pi J) + \sin(\pi g) \sin(\pi J) \cos(k). \quad (\text{B.11})$$

Next, we turn to the calculation of edge modes. We expect that for $\epsilon = 0$ and $\epsilon = \pi$, the system hosts edge modes under the condition that g is close to either 0 or 1. If d_α is associated with an edge mode, the absolute value of the eigenvalues of the transfer-matrix necessarily differs from one, while their product is fixed to one due to the normalization of the determinant. The edge mode localization length is then determined by the smaller eigenvalue ($|\lambda_\epsilon| < 1$). We trace the transfer matrix for quasienergies $\epsilon = 0$ or π , which yields

$$\lambda_{0,\pi} + \lambda_{0,\pi}^{-1} = \frac{2}{\sin(\pi g) \sin(\pi J)} [\pm 1 - \cos(\pi J) \cos(\pi g)]. \quad (\text{B.12})$$

First, we solve for $\epsilon = 0$. The quadratic equation then yields two solutions,

$$\lambda_0 = \frac{1 - \cos(\pi g) \cos(\pi J) \pm [\cos(\pi g) - \cos(\pi J)]}{\sin(\pi g) \sin(\pi J)}, \quad (\text{B.13})$$

of which the smaller one may be simplified to

$$\lambda_0 = \tan\left(\frac{\pi g}{2}\right) \tan\left(\frac{\pi J}{2}\right)^{-1}. \quad (\text{B.14})$$

An analogous calculation for $\epsilon = \pi$ yields the following smaller eigenvalue,

$$\lambda_\pi = -\tan\left(\frac{\pi g}{2}\right)^{-1} \tan\left(\frac{\pi J}{2}\right)^{-1}. \quad (\text{B.15})$$

We note that λ_0 and λ_π are related via the transformation $g \leftrightarrow 1 - g$, indicating a symmetry between zero- and π -modes. Using the eigenvalues, we determine the localization lengths defined via $\psi_j \sim e^{-j/\xi_{0,\pi}}$ to be

$$\begin{aligned} \xi_0 &= \frac{1}{\log(|\lambda_0|^{-1})} = \left\{ \log \left[\tan\left(\frac{\pi J}{2}\right) \right] - \log \left[\tan\left(\frac{\pi g}{2}\right) \right] \right\}^{-1}, \\ \xi_\pi &= \left\{ \log \left[\tan\left(\frac{\pi(1-g)}{2}\right) \right] - \log \left[\tan\left(\frac{\pi J}{2}\right) \right] \right\}^{-1}. \end{aligned} \quad (\text{B.16})$$

We find that the localization length of the Majorana zero modes diverges at $J = g$ whereas for the π -modes, it diverges at $J = 1 - g$. This explains the phase diagram in Fig. 6.1.

B.2 STROBOSCOPIC PERTURBATION THEORY

We consider a general, periodically driven system. The drive here is a combination of 'kick' operators, such that the time evolution operator U_F after one period T may be written as

$$U_F = e^{-iH_0t_0} e^{-iH_1t_1} e^{-iH_2t_2} \dots = e^{-iH_F T}. \quad (\text{B.17})$$

The H_i are arbitrary hermitian operators on the Hilbert space and the t_i arbitrary time intervals. In the following, we will set the period to $T = 1$ for simplicity. We are interested in the corrections to quasienergies and Floquet states when the drive is subject to a kick perturbation, i.e.

$$U_F = e^{-i\lambda V} e^{-iH_F}, \quad (\text{B.18})$$

with V being the perturbation operator and λ a parameter controlling the strength of the perturbation. We expand the Floquet states and quasienergies in powers of the control parameter,

$$\epsilon_n = \epsilon_n^{(0)} + \lambda \epsilon_n^{(1)} + \lambda^2 \epsilon_n^{(2)} + \mathcal{O}(\lambda^3), \quad |\psi_n\rangle = |\psi_n^{(0)}\rangle + \lambda |\psi_n^{(1)}\rangle + \lambda^2 |\psi_n^{(2)}\rangle + \mathcal{O}(\lambda^3). \quad (\text{B.19})$$

Plugging this into the eigenstate equation for the Floquet operator, we find

$$U_F |\psi_n\rangle = e^{-i\epsilon_n} |\psi_n\rangle, \\ e^{-i\lambda V} e^{-iH_F} (|\psi_n^{(0)}\rangle + \lambda |\psi_n^{(1)}\rangle + \dots) = e^{-i(\epsilon_n^{(0)} + \lambda \epsilon_n^{(1)} + \dots)} (|\psi_n^{(0)}\rangle + \lambda |\psi_n^{(1)}\rangle + \dots). \quad (\text{B.20})$$

To calculate the corrections, we compare Eq. (B.20) order by order. We use the following expansion for the energy exponential,

$$e^{-i(\epsilon_n^{(0)} + \lambda \epsilon_n^{(1)} + \lambda^2 \epsilon_n^{(2)} + \dots)} = e^{-i\epsilon_n^{(0)}} e^{-i(\lambda \epsilon_n^{(1)} + \lambda^2 \epsilon_n^{(2)} + \dots)} \\ = e^{-i\epsilon_n^{(0)}} \left(1 - i\lambda \epsilon_n^{(1)} - \lambda^2 \left(i\epsilon_n^{(2)} + \frac{[\epsilon_n^{(1)}]^2}{2} \right) + \mathcal{O}(\lambda^3) \right). \quad (\text{B.21})$$

In zeroth order, we recover the eigenstate equation for the unperturbed problem,

$$e^{-iH_F} |\psi_n^{(0)}\rangle = e^{-i\epsilon_n^{(0)}} |\psi_n^{(0)}\rangle. \quad (\text{B.22})$$

Comparing all first order terms in λ gives the following equation,

$$e^{-iH_F} |\psi_n^{(1)}\rangle - iV e^{-iH_F} |\psi_n^{(0)}\rangle = e^{-i\epsilon_n^{(0)}} (|\psi_n^{(1)}\rangle - i\epsilon_n^{(1)} |\psi_n^{(0)}\rangle). \quad (\text{B.23})$$

To proceed, we project this equation onto the state $\langle \psi_n^{(0)} |$. Since it is an eigenstate of H_F , we may replace the operator by its eigenvalue. We further use that $\langle \psi_n^{(0)} | \psi_n^{(1)} \rangle = 0$, which is due to the normalization condition on $|\psi_n\rangle$. We then find for the first order energy correction,

$$\epsilon_n^{(1)} = \langle \psi_n^{(0)} | V | \psi_n^{(0)} \rangle, \quad (\text{B.24})$$

a result which is reminiscent of its counterpart in Schrödinger time-independent perturbation theory. We may use this result to further calculate the first order correction to the eigenstates of U_F . First, we reorder the terms in Eq. (B.23),

$$(e^{-iH_F} - e^{-i\epsilon_n^{(0)}}) |\psi^{(1)}\rangle = ie^{-i\epsilon_n^{(0)}} (V - \epsilon_n^{(1)}) |\psi_n^{(0)}\rangle. \quad (\text{B.25})$$

We then use the completeness relation of the Floquet states and introduce a unit matrix on the right hand side of Eq. (B.25). The first order energy correction cancels the n -summand,

$$(e^{-iH_F} - e^{-i\epsilon_n^{(0)}}) |\psi^{(1)}\rangle = ie^{-i\epsilon_n^{(0)}} \sum_{m \neq n} \langle \psi_m^{(0)} | V | \psi_n^{(0)} \rangle |\psi_m^{(0)}\rangle, \quad (\text{B.26})$$

and after further inverting the matrix $e^{-iH_F} - e^{-i\epsilon_n^{(0)}}$, we find the first order correction of the Floquet states,

$$|\psi_n^{(1)}\rangle = ie^{-i\epsilon_n^{(0)}} \sum_{m \neq n} \frac{\langle \psi_m^{(0)} | V | \psi_n^{(0)} \rangle}{e^{-i\epsilon_m^{(0)}} - e^{-i\epsilon_n^{(0)}}} |\psi_m^{(0)}\rangle. \quad (\text{B.27})$$

Next, we calculate the second order correction to the quasienergies. For that, we compare the λ^2 terms in Eq. (B.20),

$$-\frac{V^2}{2} e^{-i\epsilon_n^{(0)}} |\psi_n^{(0)}\rangle - iV e^{-iH_F} |\psi_n^{(1)}\rangle + e^{-iH_F} |\psi_n^{(2)}\rangle = -e^{-i\epsilon_n^{(0)}} \left[\left(i\epsilon_n^{(2)} + \frac{[\epsilon_n^{(1)}]^2}{2} \right) |\psi_n^{(0)}\rangle + i\epsilon_n^{(1)} |\psi_n^{(1)}\rangle - |\psi_n^{(2)}\rangle \right]. \quad (\text{B.28})$$

As for the first order, we simplify the expression by projecting onto the zeroth order term of $\langle \psi_n |$. This gives

$$\frac{-e^{-i\epsilon_n^{(0)}}}{2} \langle \psi_n^{(0)} | V^2 | \psi_n^{(0)} \rangle - i \langle \psi_n^{(0)} | V e^{-iH_F} | \psi_n^{(1)} \rangle = -e^{-i\epsilon_n^{(0)}} \left(i\epsilon_n^{(2)} + \frac{[\epsilon_n^{(1)}]^2}{2} \right). \quad (\text{B.29})$$

We solve the equation for the second order correction $\epsilon_n^{(2)}$,

$$\epsilon_n^{(2)} = -\frac{i}{2} \langle \psi_n^{(0)} | V^2 - [\epsilon_n^{(1)}]^2 | \psi_n^{(0)} \rangle + e^{i\epsilon_n^{(0)}} \langle \psi_n^{(0)} | V e^{-iH_F} | \psi_n^{(1)} \rangle. \quad (\text{B.30})$$

After plugging in the first order corrections from Eqs. (B.24) and (B.27) as well as introducing a unit matrix into the first term, we find

$$\epsilon_n^{(2)} = -\frac{i}{2} \sum_{m \neq n} |\langle \psi_m^{(0)} | V | \psi_n^{(0)} \rangle|^2 + i \sum_{m \neq n} \frac{|\langle \psi_m^{(0)} | V | \psi_n^{(0)} \rangle|^2 e^{-i\epsilon_m^{(0)}}}{e^{-i\epsilon_m^{(0)}} - e^{-i\epsilon_n^{(0)}}}. \quad (\text{B.31})$$

Finally, we combine the two terms on the right hand side to obtain

$$\begin{aligned} \epsilon_n^{(2)} &= \frac{i}{2} \sum_{m \neq n} |\langle \psi_m^{(0)} | V | \psi_n^{(0)} \rangle|^2 \frac{2e^{-i\epsilon_m^{(0)}} - (e^{-i\epsilon_m^{(0)}} - e^{-i\epsilon_n^{(0)}})}{e^{-i\epsilon_m^{(0)}} - e^{-i\epsilon_n^{(0)}}} \\ &= \frac{i}{2} \sum_{m \neq n} |\langle \psi_m^{(0)} | V | \psi_n^{(0)} \rangle|^2 \frac{e^{-i\epsilon_m^{(0)}} + e^{-i\epsilon_n^{(0)}}}{e^{-i\epsilon_m^{(0)}} - e^{-i\epsilon_n^{(0)}}} \\ &= \frac{1}{2} \sum_{m \neq n} \frac{|\langle \psi_m^{(0)} | V | \psi_n^{(0)} \rangle|^2}{\tan\left(\frac{\epsilon_n^{(0)} - \epsilon_m^{(0)}}{2}\right)}. \end{aligned} \quad (\text{B.32})$$

B.3 PERTURBATION THEORY FOR SPLITTING DISTRIBUTIONS

In chapter 6, we found that applying a disordered longitudinal field to the periodically driven Ising chain leads to different results, depending on the phase of the system. We saw that the MZM splitting received a dramatic increase even for marginal longitudinal fields while the MPM splitting was surprisingly reduced. To understand these effects and derive analytic expressions for the distribution functions, we want to make use of stroboscopic perturbation theory. Before we begin the calculation, we want to introduce some notation. We consider states that only differ in the occupation of the edge mode partner states. We label these states $|n^{e,o}\rangle$ where the superscript indicates the occupation of the Majorana edge state and n describing the occupation of the bulk states. These states are then related via $|n^e\rangle = \gamma_{L,R}|n^o\rangle$ with $\gamma_{L,R}$ being the Majorana operator localized at the left (right) end of the chain.

In the following, we will consider the disordered longitudinal field as a perturbation V ,

$$V = \frac{\pi}{2} \sum_{i=1}^N h_i Z_i. \quad (\text{B.33})$$

B.3.1 MZM SPLITTING DISTRIBUTION

We want to derive an analytic expression for the splitting distribution of MZMs in the presence of random longitudinal fields. For this, we assume that the fields are smaller than the many-body mean level spacing of 2^{-N} . Then, the perturbation may only couple the partner states

$|n^e\rangle$ and $|n^o\rangle$, reducing the problem to that of a two-level system. The energy splitting that is induced by the longitudinal field is thus determined by the matrix element $\langle n^e|V|n^o\rangle$. This can be simplified by noting that the only relevant contributions may come from the boundary operators $Z_1 = \psi\gamma_L + \dots$ and $Z_N = \psi\gamma_R P + \dots$ with ψ being the amplitude of the Majoranas at the boundaries and P the parity operator. The other Z_i only have a marginal overlap with the boundary Majorana operators that vanishes completely in the limit of $g \rightarrow 0$. We thus find for the matrix elements,

$$v = \langle n^e|V|n^o\rangle \simeq \frac{\pi h_1}{2} \langle n^e|Z_1|n^o\rangle + \frac{\pi h_N}{2} \langle n^e|Z_N|n^o\rangle = \frac{\pi\psi(h_1 + h_N)}{2}. \quad (\text{B.34})$$

Using that the h_i are random variables drawn from a box distribution, $h_i \in [-h, h]$, we find the following probability distribution for the matrix elements,

$$\begin{aligned} p(v) &= \int_{-h}^h dh_1 dh_N \delta\left(v - \frac{\pi\psi(h_1 + h_N)}{2}\right) \\ &= \frac{1}{v_0} \left(1 - \frac{|v|}{v_0}\right) \theta(v_0 - |v|), \end{aligned} \quad (\text{B.35})$$

with $v_0 = \pi\psi h$ being the maximal value attainable for the matrix element. We now assume that the even and odd states $|n^{e,o}\rangle$ lie at energies $\pm\delta_0/2$. Adding the perturbation will then lead to the following correction for the splitting between the states,

$$\delta'_0 = \sqrt{\delta_0^2 + 4v^2}. \quad (\text{B.36})$$

Thus, the splittings are exclusively enhanced by the longitudinal fields. Using our previous result for the distribution function of the matrix elements, we find the following expression for the distribution of the corrected splittings δ'_0 ,

$$p(\delta'_0) = \frac{|\delta'_0|}{2v_0} \left(\frac{1}{\sqrt{\delta_0'^2 - \delta_0^2}} - \frac{1}{2v_0} \right) \theta(|\delta'_0| - \delta_0) \theta\left(\sqrt{\delta_0^2 + 4v_0^2} - |\delta'_0|\right). \quad (\text{B.37})$$

B.3.2 MPM SPLITTING DISTRIBUTION

Since the Majorana modes do not induce degeneracies in the MPM phase, random longitudinal fields will only affect the spectrum in second-order perturbation theory. We may write the energy difference of states with different Majorana occupation as

$$E_n^o = E_n^e + \pi - \delta_n. \quad (\text{B.38})$$

Appendix B

The longitudinal fields shift the splittings δ_n away from the unperturbed splitting δ_π by an amount $\Delta\delta_n$,

$$\delta_n = \delta_\pi + \Delta\delta_n. \quad (\text{B.39})$$

Using the general expressions given in Eq. (6.5), we may write the splitting shift as

$$\Delta\delta_n = \sum_m \left[\frac{|v_{nm}^{eo}|^2}{2 \tan \frac{E_n^e - E_m^o}{2}} - \frac{|v_{nm}^{oe}|^2}{2 \tan \frac{E_n^o - E_m^e}{2}} \right] + \sum_{m \neq n} \left[\frac{|v_{nm}^{ee}|^2}{2 \tan \frac{E_n^e - E_m^e}{2}} - \frac{|v_{nm}^{oo}|^2}{2 \tan \frac{E_n^o - E_m^o}{2}} \right] \quad (\text{B.40})$$

with matrix elements

$$v_{nm}^{ab} = \langle n^a | V | m^b \rangle, \quad a, b \in \{e, o\}. \quad (\text{B.41})$$

The first term in Eq. (B.40) involves processes changing the Majorana parity $-i\gamma_L\gamma_R$ as well as the global fermion parity P . Thus, the bulk parity, defined as $Q = (-i\gamma_L\gamma_R)P$ stays invariant. On the other hand, the second term contains processes that do not change the Majorana parity and thus necessarily change the bulk parity Q .

In the MPM phase, contributions due to coupling within pairs is negligible as the corresponding quasienergy denominator is close to π . Therefore, the effect of the perturbation is determined through coupling between different pairs. As there are many such couplings with comparable magnitude, it is plausible that this effect may be captured within a self-consistent approximation. Hence, we replaced the unperturbed quasienergies in Eq. B.40 with the exact quasienergies $E_n^{e/o}$ in the denominators, in analogy with the self-consistent Born approximation.

Since δ_n is small, we may expand Eq. (B.40) to linear order in δ_n , which yields

$$\delta_n - \delta_\pi = - \sum_m \Sigma_{nm} \delta_m + \Lambda_n, \quad (\text{B.42})$$

with

$$\begin{aligned} \Sigma_{nm} = & \left(\sum_l \frac{|v_{nl}^{eo}|^2}{4 \cos^2 \frac{E_n^e - E_l^e}{2}} + \sum_{l \neq n} \frac{|v_{nl}^{oo}|^2}{4 \sin^2 \frac{E_n^e - E_l^e}{2}} \right) \delta_{nm} \\ & + \frac{|v_{nm}^{eo}|^2}{4 \cos^2 \frac{E_n^e - E_m^e}{2}} - \frac{|v_{nm}^{oo}|^2 (1 - \delta_{nm})}{4 \sin^2 \frac{E_n^e - E_m^e}{2}}, \end{aligned} \quad (\text{B.43})$$

and

$$\Lambda_n = \sum_{m \neq n} \frac{|v_{nm}^{ee}|^2 - |v_{nm}^{oo}|^2}{2 \tan \frac{E_n^e - E_m^e}{2}}. \quad (\text{B.44})$$

Importantly, the energy denominators in the expressions of Σ_{nm} and Λ_n consist of the unperturbed quasienergies.

The form in Eq. (B.42) allows us to write the perturbation theory in concise matrix notation,

$$\delta'_\pi = \frac{1}{1 + \Sigma} (\delta_\pi + \Lambda) \quad (\text{B.45})$$

where δ'_π is the vector of perturbed splittings and δ_π a vector with all entries being the unperturbed splitting.

To derive these expressions, it is useful to split the matrix elements into symmetric and anti-symmetric matrix contributions,

$$\Delta \delta_n = \Delta \delta_n^{eo/oe} + \Delta \delta_n^{ee/oo} \quad (\text{B.46})$$

with

$$\begin{aligned} \Delta \delta_n^{eo/oe} = & \sum_m \frac{|v_{nm}^{eo}|^2 + |v_{nm}^{oe}|^2}{2} \left[\frac{1}{2 \tan \frac{E_n^e - E_m^o}{2}} - \frac{1}{2 \tan \frac{E_n^o - E_m^e}{2}} \right] \\ & + \sum_m \frac{|v_{nm}^{eo}|^2 - |v_{nm}^{oe}|^2}{2} \left[\frac{1}{2 \tan \frac{E_n^e - E_m^o}{2}} + \frac{1}{2 \tan \frac{E_n^o - E_m^e}{2}} \right] \end{aligned} \quad (\text{B.47})$$

and

$$\begin{aligned} \Delta \delta_n^{ee/oo} = & \sum_{m \neq n} \frac{|v_{nm}^{ee}|^2 + |v_{nm}^{oo}|^2}{2} \left[\frac{1}{2 \tan \frac{E_n^e - E_m^e}{2}} - \frac{1}{2 \tan \frac{E_n^o - E_m^o}{2}} \right] \\ & + \sum_{m \neq n} \frac{|v_{nm}^{ee}|^2 - |v_{nm}^{oo}|^2}{2} \left[\frac{1}{2 \tan \frac{E_n^e - E_m^e}{2}} + \frac{1}{2 \tan \frac{E_n^o - E_m^o}{2}} \right]. \end{aligned} \quad (\text{B.48})$$

The quasienergy differences in the denominators may be written as

$$E_n^o - E_m^o = E_n^e - E_m^e - \delta_n + \delta_m, \quad E_n^e - E_m^o = E_n^e - E_m^e - \pi + \delta_m. \quad (\text{B.49})$$

By using the expansions

$$\frac{1}{\tan\left(\frac{x-\pi+\delta_m}{2}\right)} - \frac{1}{\tan\left(\frac{x+\pi-\delta_n}{2}\right)} \simeq -\frac{(\delta_n + \delta_m)}{2 \cos^2\left(\frac{x}{2}\right)}, \quad (\text{B.50})$$

$$\frac{1}{\tan\left(\frac{x-\pi+\delta_m}{2}\right)} + \frac{1}{\tan\left(\frac{x+\pi-\delta_n}{2}\right)} \simeq \frac{2}{\tan\left(\frac{x-\pi}{2}\right)} - \frac{(\delta_n - \delta_m)}{2 \cos^2\left(\frac{x}{2}\right)} \quad (\text{B.51})$$

we find for the symmetric and antisymmetric matrix contributions,

$$\begin{aligned} \Delta\delta_n^{\delta_{eo/oe}} &= \sum_m \frac{|v_{nm}^{eo}|^2 - |v_{nm}^{oe}|^2}{2 \tan \frac{E_n^e - E_m^e - \pi}{2}} - \sum_m \frac{(\delta_n + \delta_m)(|v_{nm}^{eo}|^2 + |v_{nm}^{oe}|^2)}{8 \cos^2 \frac{E_n^e - E_m^e}{2}} \\ &\quad - \sum_m \frac{(\delta_n - \delta_m)(|v_{nm}^{eo}|^2 - |v_{nm}^{oe}|^2)}{8 \cos^2 \frac{E_n^e - E_m^e}{2}} \end{aligned} \quad (\text{B.52})$$

and

$$\begin{aligned} \Delta\delta_n^{\delta_{ee/oo}} &= \sum_{m \neq n} \frac{|v_{nm}^{ee}|^2 - |v_{nm}^{oo}|^2}{2 \tan \frac{E_n^e - E_m^e}{2}} - \sum_{m \neq n} \frac{(\delta_n - \delta_m)(|v_{nm}^{ee}|^2 + |v_{nm}^{oo}|^2)}{8 \sin^2 \frac{E_n^e - E_m^e}{2}} \\ &\quad + \sum_{m \neq n} \frac{(\delta_n - \delta_m)(|v_{nm}^{ee}|^2 - |v_{nm}^{oo}|^2)}{8 \sin^2 \frac{E_n^e - E_m^e}{2}}. \end{aligned} \quad (\text{B.53})$$

Contrary to the MZM case, the splittings in the MPM phase vary over the Floquet spectrum, so that terms involving $\delta_n - \delta_m$ do not vanish. Collecting terms and using $|v_{nm}^{eo}| = |v_{nm}^{oe}|$, we find

$$\delta_n - \delta_\pi = - \sum_m \frac{(\delta_n + \delta_m)|v_{nm}^{eo}|^2}{4 \cos^2 \frac{E_n^e - E_m^e}{2}} - \sum_{m \neq n} \frac{(\delta_n - \delta_m)|v_{nm}^{oo}|^2}{4 \sin^2 \frac{E_n^e - E_m^e}{2}} + \sum_{m \neq n} \frac{|v_{nm}^{ee}|^2 - |v_{nm}^{oo}|^2}{2 \tan \frac{E_n^e - E_m^e}{2}} \quad (\text{B.54})$$

and thus Eqs. (B.42), (B.43) and (B.44).

B.4 CUMULANTS AND CORRELATIONS OF THE SINGLE-PARTICLE SPLITTING DISTRIBUTION

In chapter 7, we related the splittings Δ_n away from π -pairing in the spectrum of the Floquet operator to characteristic time scales of spin correlation functions. In the integrable case ($dh = 0$), these splittings can be decomposed into linear combinations of single-particle splittings δ_n .

B.4 Cumulants and correlations of the single-particle splitting distribution

We here want to explicitly derive expressions for the cumulants of their distribution functions as well as calculate correlation functions.

We start calculating the first cumulant by taking the absolute value of Eq. (7.20) and taking the logarithm,

$$\ln |\delta(\epsilon)| \simeq \sum_i \ln \left| \frac{\delta g/2}{\epsilon' - \delta J_i} \right|, \quad (\text{B.55})$$

with $\epsilon' = \epsilon/\pi - J$. As the $\delta J_i \in [-dJ, dJ]$ are statistically independent, taking the disorder average yields

$$\overline{\ln |\delta(\epsilon)|} \simeq (N-1) \left[\ln \left(\frac{\delta g}{2} \right) - \overline{\ln |\epsilon' - \delta J_i|} \right]. \quad (\text{B.56})$$

The disordered Ising coupling are distributed uniformly,

$$\overline{\ln |\epsilon' - \delta J_i|} = \int_{-dJ}^{dJ} \frac{dx}{2dJ} \ln |\epsilon' - x|. \quad (\text{B.57})$$

The integral can be solved by splitting it at $x = \epsilon'$, which then leads to

$$\overline{\ln |\epsilon' - \delta J_i|} = \frac{1}{2dJ} [(dJ + \epsilon') \ln(dJ + \epsilon') + (dJ - \epsilon') \ln(dJ - \epsilon') - 2dJ] \quad (\text{B.58})$$

Expanding this for small ϵ' and taking the large-chain limit, $N-1 \approx N$, we find for the average of the splitting distribution,

$$\overline{\ln |\delta(\epsilon)|} \simeq -N \left[\ln \left(\frac{2dJ}{\delta g} \right) - 1 + \frac{(\epsilon')^2}{2(dJ)^2} \right]. \quad (\text{B.59})$$

Reintroducing ϵ leads to the expression given in Eq. (7.22).

Next, we calculate the variance of the single-particle splitting distribution. Using the same starting point as before, we find that we can write the variance as follows,

$$\text{var} \ln |\delta(\epsilon)| = \sum_i \overline{\ln^2 \left| \frac{\delta g}{2(\epsilon' - \delta J_i)} \right|} - \overline{\ln \left| \frac{\delta g}{2(\epsilon' - \delta J_i)} \right|}^2, \quad (\text{B.60})$$

as the disordered couplings are statistically independent, $\overline{\delta J_i \delta J_j} = \overline{\delta J_i} \cdot \overline{\delta J_j}$ for $i \neq j$. Due to the logarithm, the prefactor $\delta g/2$ cancels from the variance, so that

$$\text{var} \ln |\delta(\epsilon)| = (N-1) \text{var} \ln |\epsilon' - \delta J_i|. \quad (\text{B.61})$$

Appendix B

We calculate the variance of $\ln |\epsilon' - \delta J_i|$ by evaluating the integral for the second moment of the distribution,

$$\overline{\ln^2 |\epsilon' - \delta J_i|} = \int_{-dJ}^{dJ} \frac{dx}{2dJ} \ln^2 |\epsilon' - x| = \frac{1}{2dJ} \left\{ dJ + \epsilon' [\ln(dJ + \epsilon') - 1]^2 + (dJ - \epsilon') [\ln(dJ - \epsilon') - 1]^2 + 2dJ \right\}. \quad (\text{B.62})$$

Here we used that $\int dx \ln^2 x = x(\ln x - 1)^2 + x$. Using Eq. (B.58), we then find for the variance,

$$\text{var} \ln |\epsilon - \delta J_i| \simeq 1 - \frac{(\epsilon')^2}{2dJ^2}, \quad (\text{B.63})$$

in the limit of small ϵ' . Thus, we find for the variance of the splitting distribution,

$$\text{var} \ln |\delta(\epsilon)| = N \left(1 - \frac{(\epsilon')^2}{2dJ^2} \right) \quad (\text{B.64})$$

which leads to the expression in Eq. (7.22) after reintroducing ϵ .

Finally, we also calculate correlations between different single-particle splittings, measured via

$$\overline{\ln |\delta(\epsilon_1)| \ln |\delta(\epsilon_2)|}^{(c)} = \overline{\ln |\delta(\epsilon_1)| \ln |\delta(\epsilon_2)|} - \overline{\ln |\delta(\epsilon_1)|} \cdot \overline{\ln |\delta(\epsilon_2)|}. \quad (\text{B.65})$$

We again use that the disordered Ising couplings are uncorrelated, yielding

$$\overline{\ln |\delta(\epsilon_1)| \ln |\delta(\epsilon_2)|}^{(c)} = \sum_i \overline{\ln |\epsilon'_1 - \delta J_i| \ln |\epsilon'_2 - \delta J_i|}^{(c)}. \quad (\text{B.66})$$

To evaluate the integral in Eq. (B.66) explicitly, we focus on the case of $\epsilon'_1 = 0$ (band center) and ϵ'_2 being small. We expand to linear order in ϵ'_2 ,

$$\begin{aligned} \overline{\ln |\delta J_i| \ln |\epsilon'_2 - \delta J_i|} - \overline{\ln \delta J_i} \cdot \overline{\ln |\epsilon'_2 - \delta J_i|} &= 1 - |\epsilon'_2| \int_{-dJ}^{dJ} \frac{dx}{2dJ} \frac{\ln |x|}{|x|} \\ &= 1 - |\epsilon'_2| \frac{\ln^2 dJ}{2dJ}. \end{aligned} \quad (\text{B.67})$$

Thus, we find for the splitting correlations,

$$\overline{\ln |\delta(\epsilon_1)| \ln |\delta(\epsilon_2)|}^{(c)} \simeq N \left(1 - \frac{|\epsilon_1 - \epsilon_2| \ln^2 dJ}{2dJ} \right), \quad (\text{B.68})$$

which is the expression given in Eq. (7.23).

B.5 DUAL TRANSFORMATION

In chapter 7, we applied a dual transformation in Eq. (7.13), which relates the fermionic degrees of freedom to domain walls. In 5.2.1, we used the same transformation in Eq. (5.15) to diagonalize the Kitaev chain model. We here briefly want to outline the differences in the case of periodic boundary conditions and finite transverse fields.

First, we find that the transverse field operator in terms of the domain wall fermions is given by

$$\sum_{i=1}^N (1 - 2c_i^\dagger c_i) = - \sum_{i=1}^N (d_j + d_j^\dagger)(d_{j-1} - d_{j-1}^\dagger), \quad (\text{B.69})$$

which is readily checked for terms $i > 1$ by inserting the definition in Eq. (7.13). The sign change of the transverse field was omitted in the main text, as it does not affect the results. For the $i = 1$ term, we further have to take the parity operator P into account. For the Jordan-Wigner fermions, we used the convention $c_{N+1} = -Pc_1$, which translates to

$$d_N = \frac{1}{2}[c_N + c_N^\dagger - P(c_1 - c_1^\dagger)]. \quad (\text{B.70})$$

for the domain wall operators. Using the convention $d_0 = -Pd_N$ thus gives the correct Hamiltonian.

APPENDIX C

C.1 AVERAGE VELOCITY

We here show the calculation for the average velocity of the active quantum particle in the intermediate steady state, i.e. for times $t_s \ll t \ll t_m$. First, we extract the evolution equations of the spin and momentum distributions \mathbf{r}_k and $r_{o,k}$ from Eq. (9.5) via multiplying the equation by a unit matrix or the pauli matrix vector $\boldsymbol{\tau}_k$ and taking the trace, yielding

$$\begin{aligned}
 \partial_t r_{o,k} &= 0, \\
 \partial_t r_{x,k} &= -2\Delta_k r_{y,k} - \frac{1}{2} \sum_{\ell=\pm} \sum_{\alpha=h,c} \Gamma_{\alpha,k}^{(\ell)} r_{x,k}, \\
 \partial_t r_{y,k} &= 2\Delta_k r_{x,k} - \frac{1}{2} \sum_{\ell=\pm} \sum_{\alpha=h,c} \Gamma_{\alpha,k}^{(\ell)} r_{y,k}, \\
 \partial_t r_{z,k} &= \sum_{\alpha=h,c} (\Gamma_{\alpha,k}^- - \Gamma_{\alpha,k}^+) - \sum_{\ell=\pm} \sum_{\alpha=h,c} \Gamma_{\alpha,k}^{(\ell)} r_{z,k}. \tag{C.1}
 \end{aligned}$$

We point out that the coupling to the heat reservoirs leaves the momentum distribution $r_{o,k}$ invariant. Moreover, the time evolution of the spin distribution \mathbf{r}_k is decoupled from $r_{o,k}$.

By setting the time derivatives in Eq. (C.1) to zero, we can estimate the steady state of the evolution equation as

$$r_{o,k} = \frac{1}{\mathcal{Z}} e^{-\beta \epsilon_k} \cosh(\beta \Delta_k), \quad r_{z,k} = \sum_{\alpha=h,c} \xi_{\alpha,k} \left[\sum_{\alpha=h,c} \xi_{\alpha,k} \{n(2\Delta_k, T_\alpha) + 1\} \right]^{-1}, \tag{C.2}$$

and $r_{x,k} = r_{y,k} = 0$. The steady state of the momentum distribution follows from the assumption that the system is initially in thermal equilibrium, as discussed in chapter 9. We may further expand the expression of $r_{z,k}$ to linear order in ΔT , which yields,

$$r_{z,k} = \tanh(\beta \Delta_k) - \Delta T \frac{\Delta_k}{2T^2} \frac{\xi_{h,k} - \xi_{c,k}}{\xi_{h,k} + \xi_{c,k}} \frac{1}{\cosh^2(\beta \Delta_k)} + \mathcal{O}(\Delta T^2). \tag{C.3}$$

Appendix C

The equilibrium contribution to the average velocity vanishes. To linear order in ΔT , we find

$$\langle \hat{v} \rangle = \frac{1}{\mathcal{Z}} \sum_k \frac{\xi_{h,k} - \xi_{c,k}}{\xi_{h,k} + \xi_{c,k}} e^{-\beta \epsilon_k} \frac{\Delta_k \cdot \partial_k \Delta_k}{\cosh(\beta \Delta_k)} \frac{\Delta T}{T^2} + \mathcal{O}(\Delta T^2). \quad (\text{C.4})$$

Beyond linear order, the average velocity is given by

$$\langle \hat{v} \rangle = \sum_k r_{o,k} [\partial_k \epsilon_k - 2r_{z,k} \hat{\Delta}_k \cdot \partial_k \mathbf{d}_k]. \quad (\text{C.5})$$

No active motion is observed, if any of the parameters w_o , \mathbf{d} or \mathbf{B} vanish. This is seen explicitly in Eq. (C.4) for $\mathbf{d} = 0$. For vanishing Zeeman field \mathbf{B} , we find that the $\xi_{\alpha,k}$ become independent of k with the rest of the integrand being odd in k . For $w_o = 0$, the integral takes the form $\sum_k f(\sin k) \cos k$ and consequently vanishes.

We may further evaluate the expression for the average velocity in a few temperature limits. Here we assume that the band width w_o is much larger than the Zeeman and spin-orbit fields. For low temperatures, $T \ll \Delta_k \ll w_o$, the sum in Eq. (C.4) is dominated by the $k = 0$ summand. We find

$$\langle \hat{v} \rangle \simeq \frac{\xi_{h,0} - \xi_{c,0}}{\xi_{h,0} + \xi_{c,0}} \frac{\Delta_0 \cdot \partial_k \mathbf{d}_k|_{k=0}}{\cosh^2(\beta \Delta_0)} \frac{\Delta T}{T^2} = \frac{\xi_{h,0} - \xi_{c,0}}{\xi_{h,0} + \xi_{c,0}} 4\mathbf{B} \cdot \mathbf{d} e^{-2\beta B} \frac{\Delta T}{T^2}. \quad (\text{C.6})$$

At intermediate temperatures, $T, \Delta_k \ll w_o$, the sum is still dominated by its $k = 0$ values, which gives,

$$\langle v \rangle \simeq \frac{\xi_{h,0} - \xi_{c,0}}{\xi_{h,0} + \xi_{c,0}} \frac{\mathbf{B} \cdot \mathbf{d}}{\cosh^2(\beta B)} \frac{\Delta T}{T^2}. \quad (\text{C.7})$$

From this temperature regime, we may extract the optimal temperature T_{opt} maximizing the average velocity. We differentiate Eq. (C.7) with respect to T , which yields the condition,

$$T_{\text{opt}} = B \tanh\left(\frac{B}{T_{\text{opt}}}\right). \quad (\text{C.8})$$

This is solved by $T_{\text{opt}} \simeq 0.83B$.

Lastly, we consider the high-temperature limit of $\Delta_k \ll w_o \ll T$. Here we can expand $e^{-\beta \epsilon_k}$ in powers of β . The zeroth order term of the average velocity vanishes, as it is of the form $\sum_k f(\mathbf{d}_k) \partial_k \mathbf{d}_k$ with \mathbf{d}_k being a periodic function with zero mean. The linear order term of the expansion yields

$$\langle v \rangle \simeq \frac{2}{\mathcal{Z}} \sum_k \frac{\xi_{h,k} - \xi_{c,k}}{\xi_{h,k} + \xi_{c,k}} w_o \cos k \Delta_k \cdot \partial_k \mathbf{d}_k \frac{\Delta T}{T^3}. \quad (\text{C.9})$$

In the simple case of $\mathbf{B} \parallel \mathbf{d}$, the factors $\xi_{\alpha,k}$ do not depend on k anymore, and the sum may be explicitly evaluated, yielding

$$\langle v \rangle \simeq \frac{\xi_h - \xi_c}{\xi_h + \xi_c} w_o \mathbf{B} \cdot \mathbf{d} \frac{\Delta T}{T^3}. \quad (\text{C.10})$$

The here derived temperature dependencies of the average velocity in different regimes are consistent with the discussion in chapter 9.

C.2 MOMENTUM RELAXATION

Using the coupling to the phonon bath defined in Eq. (9.11), we estimate the dissipator \mathcal{D}_m mediating momentum relaxation processes of the density matrix ρ as follows,

$$\begin{aligned} \mathcal{D}_m[\rho] = & \sum_{k,q,\tau,\tau'} \frac{\lambda_q}{N} \nu_{\perp}(\Omega_{\tau,\tau'}^{k,q}, q) |\langle \tau_k | \tau'_{k+q} \rangle|^2 |\mathfrak{n}(\Omega_{\tau,\tau'}^{k,q}, T)| \\ & \times \left(|k+q, \tau'_{k+q}\rangle \langle k, \tau_k | \rho | k, \tau_k \rangle \langle k+q, \tau'_{k+q}| - \frac{1}{2} \{ |k, \tau_k\rangle \langle k, \tau_k |, \rho \} \right), \end{aligned} \quad (\text{C.11})$$

with τ_k labeling the eigenstates of $\tau_{z,k}$ and $\Omega_{\tau,\tau'}^{k,q} = \epsilon_{\tau',k+q} - \epsilon_{\tau,k}$. Furthermore, we defined

$$\nu_{\perp}(\Omega, q) = 2\pi \sum_{\mathbf{q}_{\perp}} \delta(|\Omega| - \omega_{\mathbf{q}}) \quad (\text{C.12})$$

where $\omega_{\mathbf{q}}$ is the dispersion of the phonon bath. Using that $\omega \sim q$ and $\nu(\omega) = |\omega|^p$, one finds $\nu_{\perp}(\omega) \sim |\omega|^{p-1}$ for acoustic phonons. Here, the prefactor in $\nu_{\perp}(\omega)$ is independent of k under the condition that typical group velocities $\partial_k \epsilon_{\tau,k}$ are much larger than the phonon velocity c . An explicit calculation yields $\nu_{\perp}(\omega) = A|\omega|^{p-1}/c^p$ with A being a numerical prefactor.

We extract the evolution equation for the momentum distribution $r_{o,k}$ by tracing $\partial_t \rho = \mathcal{D}_m[\rho]$ over spin space (here we suppress the spin dissipator \mathcal{D}_s as it does not contribute to the evolution equation of $r_{o,k}$, see Eq. (C.1)) and project onto momentum k ,

$$\partial_t r_{o,k} = \sum_{k,q,\tau,\tau'} \frac{\lambda_q}{N} \nu_{\perp}(\Omega_{\tau,\tau'}^{k,q}, q) |\langle \tau_k | \tau'_{k+q} \rangle|^2 (|\mathfrak{n}(\Omega_{\tau,\tau'}^{k,q}, T) + 1| r_{o,k+q,\tau} - |\mathfrak{n}(\Omega_{\tau,\tau'}^{k,q}, T)| r_{o,k,\tau}), \quad (\text{C.13})$$

with $r_{o,k,\tau}$ being the momentum distribution for spin τ , given by

$$r_{o,k,\uparrow} = r_{o,k}(1 + r_{z,k})/2, \quad r_{o,k,\downarrow} = r_{o,k}(1 - r_{z,k})/2. \quad (\text{C.14})$$

Appendix C

By taking the continuum limit, the evolution equation of the momentum distribution transforms into a drift-diffusion equation,

$$\partial_t r_{o,k} = \partial_k [v_D(k) r_{o,k} + D(k) \partial_k r_{o,k}]. \quad (\text{C.15})$$

Keeping only lowest order terms in q_0 , we find for the drift velocity $v_D(k)$,

$$v_D(k) = \frac{A}{c^p} \left[\int_0^\infty \frac{dq}{2\pi} \lambda_q q^p \right] [(1 + r_{z,k})(\partial_k \epsilon_{\uparrow,k})^{p-1} \text{sgn}(\partial_k \epsilon_{\uparrow,k})^p + (1 - r_{z,k})(\partial_k \epsilon_{\downarrow,k})^{p-1} \text{sgn}(\partial_k \epsilon_{\downarrow,k})^p + T \partial_k r_{z,k} (|\partial_k \epsilon_{\uparrow,k}|^{p-2} - |\partial_k \epsilon_{\downarrow,k}|^{p-2})], \quad (\text{C.16})$$

and for the diffusion constant $D(k)$,

$$D(k) = \frac{AT}{c^p} \left[\int_0^\infty \frac{dq}{2\pi} \lambda_q q^p \right] [(1 + r_{z,k}) |\partial_k \epsilon_{\uparrow,k}|^{p-2} + (1 - r_{z,k}) |\partial_k \epsilon_{\downarrow,k}|^{p-2}]. \quad (\text{C.17})$$

In these expressions we also neglected spin-flip processes, which is justified under the condition that $p < 4$ (see discussion in 9.4). We find that both $v_D(k)$ and $D(k)$ involve the spin distribution $r_{z,k}$. Further, we note that momentum relaxation also contributes to the time evolution of $r_{z,k}$, either via the sub-dominant spin-flip processes or through the difference between the spin-conserving scattering rates for the spin-up and spin-down components. However, the imposed time scale hierarchy $t_s \ll t_m$ ensures that momentum relaxation processes act much slower than the processes due to the heat reservoirs. Thus, we can take $r_{z,k}$ to be time-independent here, which further implies time-independent $v_D(k)$ and $D(k)$.

From the drift-diffusion equation, we can readily read off the steady state of the momentum distribution as

$$r_{o,k} = \frac{1}{\mathcal{Z}} \exp \left\{ - \int_0^k dk' \frac{v_D(k')}{D(k')} \right\}. \quad (\text{C.18})$$

In the case of $p = 2$, the distribution may further be written as

$$r_{o,k} = \frac{1}{\mathcal{Z}} \exp \left\{ - \frac{\beta}{2} \int_0^k dk' \text{Tr}_s (\hat{v}_{k'} (\mathbb{1}_s + r_{z,k'} \hat{\Delta}_{k'} \cdot \boldsymbol{\sigma})) \right\}. \quad (\text{C.19})$$

This form directly explains the vanishing average velocity in the steady state (see Fig. 9.4), since it can be written as

$$\langle \hat{v} \rangle = \sum_k r_{o,k} \text{Tr}_s \hat{v}_k (\mathbb{1}_s + r_{z,k} \hat{\Delta}_k \cdot \boldsymbol{\sigma}) = \sum_k \partial_k r_{o,k}. \quad (\text{C.20})$$

This result however is specific to $p = 2$ and does not translate to other powers. For $p = 3$ for example, we find a finite average velocity in the steady state.

Since the momentum relaxation distribution evolves according to a drift-diffusion equation, we can estimate the momentum relaxation time t_m as the time it takes to diffuse across the relevant part of the Brillouin zone with significant occupation probability.

C.3 VELOCITY-VELOCITY CORRELATION FUNCTION

We compute the velocity-velocity correlation function $\langle \hat{v}(t)\hat{v}(t+\bar{t}) \rangle$ via the quantum regression theorem derived in 8.3,

$$\langle \hat{v}(t)\hat{v}(t+\bar{t}) \rangle = \sum_k \text{Tr}_s(\hat{v}_k e^{\mathcal{L}\bar{t}}[\hat{v}_k \rho_k(t)]). \quad (\text{C.21})$$

Here, the density matrix $\rho_k(t)$ is assumed to be the steady state with or without momentum relaxation. For $\bar{t} \ll t_m$, the Liouvillian \mathcal{L} only involves processes due to the spin dissipator \mathcal{D}_s . Using the evolution equations in Eq. (C.1) and considering vectorized density matrices of the form $\rho_k = (r_{o,k,\uparrow}, r_{o,k,\downarrow}, r_{x,k}, r_{y,k})^T$, we can write the Liouvillian in the following matrix form,

$$\mathcal{L} = \begin{pmatrix} A & 0 \\ 0 & B \end{pmatrix}, \quad A = \sum_{\alpha=h,c} \begin{pmatrix} -\Gamma_{\alpha,k}^+ & \Gamma_{\alpha,k}^- \\ \Gamma_{\alpha,k}^+ & -\Gamma_{\alpha,k}^- \end{pmatrix}, \quad B = \begin{pmatrix} -\Gamma_k/2 & -2\Delta_k \\ 2\Delta_k & -\Gamma_k/2 \end{pmatrix}, \quad (\text{C.22})$$

with $\Gamma_k = \sum_{\ell,\alpha} \Gamma_{\alpha,k}^{(\ell)}$. The calculation of the exponential Liouvillian in Eq. (C.21) hence reduces to a calculation of the exponentiated 2×2 matrices A and B . For a general 2×2 matrix $M = m_0 + \mathbf{m} \cdot \boldsymbol{\sigma}$, one readily calculates its exponential as $e^{M\bar{t}} = e^{m_0\bar{t}}(\cosh(m\bar{t}) + \mathbf{m} \cdot \boldsymbol{\sigma} \sinh(m\bar{t})/m)$ with $m = \sqrt{\mathbf{m} \cdot \mathbf{m}}$. Since

$$\sum_{\alpha} \Gamma_{\alpha,k}^{\pm} = \sum_{\alpha} \frac{\Gamma_{\alpha,k}^{\pm} + \Gamma_{\alpha,k}^{\mp} + \Gamma_{\alpha,k}^{\pm} - \Gamma_{\alpha,k}^{\mp}}{2} = \frac{\Gamma_k}{2}(1 \mp r_{z,k}), \quad (\text{C.23})$$

with $r_{z,k}$ corresponding to the steady state, we can write $A = \Gamma_k(1 + (1, ir_{z,k}, r_{z,k})^T \cdot \boldsymbol{\sigma})/2$. Using this form, we find for the exponentials of A and B ,

$$e^{A\bar{t}} = \frac{1}{2} \left[\begin{pmatrix} 1 + r_{z,k} & 1 + r_{z,k} \\ 1 - r_{z,k} & 1 - r_{z,k} \end{pmatrix} + e^{-\Gamma_k \bar{t}} \begin{pmatrix} 1 - r_{z,k} & -(1 + r_{z,k}) \\ -(1 - r_{z,k}) & 1 + r_{z,k} \end{pmatrix} \right], \quad (\text{C.24})$$

$$e^{B\bar{t}} = e^{-\Gamma_k \bar{t}/2} (\cos(2\Delta_k \bar{t}) - i\sigma_y \sin(2\Delta_k \bar{t})). \quad (\text{C.25})$$

Next, we consider the initial state $\hat{v}_k \rho_k(t)$. In matrix form, it is given by

$$\hat{v}_k \rho_k(t) = r_{o,k} \left[w_o \sin(k) - r_{z,k} \hat{\Delta}_k \cdot \partial_k \mathbf{d}_k + (r_{z,k} w_o \sin(k) \hat{\Delta}_k - \partial_k \tilde{\mathbf{d}}_k) \cdot \boldsymbol{\tau}_k \right], \quad (\text{C.26})$$

Appendix C

with $\tilde{\mathbf{d}}$ defined via $\partial_k \mathbf{d}_k \cdot \boldsymbol{\sigma} = \partial_k \tilde{\mathbf{d}}_k \cdot \boldsymbol{\tau}_k$. The matrix form in Eq. (C.26) translates to the following vectorized form,

$$\begin{aligned} \hat{v}_k \rho_k(t) &= r_{o,k} \left((1 + r_{z,k}) \left(w_o \sin(k) - \hat{\Delta}_k \cdot \partial_k \mathbf{d}_k \right), \right. \\ &\quad \left. (1 - r_{z,k}) \left(w_o \sin(k) + \hat{\Delta}_k \cdot \partial_k \mathbf{d}_k \right), -\partial_k \tilde{d}_{x,k}, -\partial_k \tilde{d}_{y,k} \right)^T \\ &= r_{o,k} \left((1 + r_{z,k}) \partial_k \epsilon_{\uparrow,k}, (1 - r_{z,k}) \partial_k \epsilon_{\downarrow,k}, -\partial_k \tilde{d}_{x,k}, -\partial_k \tilde{d}_{y,k} \right) = (\boldsymbol{\rho}_{\text{diag}}, \boldsymbol{\rho}_{\text{off}}) \end{aligned} \quad (\text{C.27})$$

In this notation, we can apply the exponential Liouvillian to the initial state, which yields

$$\begin{aligned} e^{A\bar{t}} \boldsymbol{\rho}_{\text{diag}} &= r_{o,k} \left[\frac{(1 + r_{z,k}) \partial_k \epsilon_{\uparrow,k} + (1 - r_{z,k}) \partial_k \epsilon_{\downarrow,k}}{2} \cdot \begin{pmatrix} 1 + r_{z,k} \\ 1 - r_{z,k} \end{pmatrix} \right. \\ &\quad \left. + e^{-\Gamma_k \bar{t}} \frac{(1 - r_{z,k}^2) (\partial_k \epsilon_{\uparrow,k} - \partial_k \epsilon_{\downarrow,k})}{2} \begin{pmatrix} 1 \\ -1 \end{pmatrix} \right], \end{aligned} \quad (\text{C.28})$$

and

$$e^{B\bar{t}} \boldsymbol{\rho}_{\text{off}} = -e^{-\Gamma_k \bar{t}/2} r_{o,k} \begin{pmatrix} \cos(2\Delta_k \bar{t}) \partial_k \tilde{d}_{x,k} - \sin(2\Delta_k \bar{t}) \partial_k \tilde{d}_{y,k} \\ \sin(2\Delta_k \bar{t}) \partial_k \tilde{d}_{x,k} + \cos(2\Delta_k \bar{t}) \partial_k \tilde{d}_{y,k} \end{pmatrix}. \quad (\text{C.29})$$

In order to calculate the trace in Eq. (C.21), we revert to matrix notation,

$$\begin{aligned} e^{\mathcal{L}\bar{t}} [\hat{v}_k \hat{\rho}(t)] &= r_{o,k} \left\{ \frac{(1 + r_{z,k}) \partial_k \epsilon_{\uparrow,k} + (1 - r_{z,k}) \partial_k \epsilon_{\downarrow,k}}{2} \mathbb{1}_s \right. \\ &\quad - e^{-\Gamma_k \bar{t}/2} [\cos(2\Delta_k \bar{t}) \partial_k \tilde{d}_{x,k} - \sin(2\Delta_k \bar{t}) \partial_k \tilde{d}_{y,k}] \tau_{x,k} \\ &\quad - e^{-\Gamma_k \bar{t}/2} [\sin(2\Delta_k \bar{t}) \partial_k \tilde{d}_{x,k} + \cos(2\Delta_k \bar{t}) \partial_k \tilde{d}_{y,k}] \tau_{y,k} \\ &\quad \left. + \left[\frac{(1 + r_{z,k}) \partial_k \epsilon_{\uparrow,k} + (1 - r_{z,k}) \partial_k \epsilon_{\downarrow,k}}{2} r_{z,k} - e^{-\Gamma_k \bar{t}} (1 - r_{z,k}^2) \hat{\Delta}_k \cdot \partial_k \mathbf{d}_k \right] \tau_{z,k} \right\}. \end{aligned} \quad (\text{C.30})$$

Finally, we find for the correlation function,

$$\begin{aligned} \langle \hat{v}(t) \hat{v}(t + \bar{t}) \rangle &= \sum_k r_{o,k} \left[\text{Tr}_s (\hat{v}_k (1 + r_{z,k} \hat{\Delta} \cdot \boldsymbol{\sigma}))^2 + e^{-\Gamma_k \bar{t}/2} \cos(2\Delta_k \bar{t}) (\hat{\Delta}_k \times \partial_k \mathbf{d}_k)^2 \right. \\ &\quad \left. + e^{-\Gamma_k \bar{t}} (1 - r_{z,k}^2) (\hat{\Delta}_k \cdot \partial_k \mathbf{d}_k)^2 \right]. \end{aligned} \quad (\text{C.31})$$

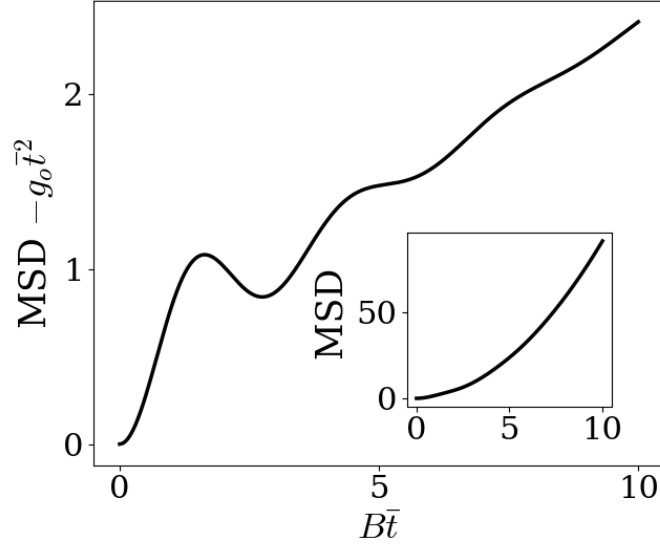


Figure C.1: Mean-square displacement (MSD) calculated from Eq. (C.38). Main Plot shows the MSD with ballistic term $g_0 \bar{t}^2$ subtracted to emphasize on the quantum oscillations. Inset Plot: Full MSD. Parameters: (a),(b) Same as in Fig. 9.4, (b) $T = 0.5B$.

By noting that

$$1 - r_{z,k}^2 = 4 \sum_{\alpha, \alpha'} \frac{\Gamma_{\alpha,k}^+ \Gamma_{\alpha',k}^-}{\Gamma_k^2}, \quad (\text{C.32})$$

we find the form of the correlation function given in chapter 9. From Eq. (C.31), we can read off the constant g_0 in Eq. (9.18) as

$$g_0 = \sum_k r_{o,k} \text{Tr}_s (\hat{v}_k (1 + r_{z,k} \hat{\Delta} \cdot \boldsymbol{\sigma}))^2 - \langle \hat{v}(t) \rangle \langle \hat{v}(\infty) \rangle. \quad (\text{C.33})$$

Analogously to the average velocity, we want to consider the limit $T, \Delta_k \ll w_o$. Then the sum in Eq. (C.31) is dominated by the $k = 0$ term. Consequently, the oscillation period of the correlation function is given by the Zeeman field B . Furthermore, the decay rate of the correlation function is given by $\Gamma_{k=0} = \sum_{\alpha} \xi_{\alpha,0} \coth(B/2T)$, which defines the spin relaxation time t_s in this limit.

C.4 MEAN-SQUARE DISPLACEMENT

In the study of active particles, it is interesting to compute the mean-square displacement (MSD) over a given time interval t , see e.g. Ref. [17]. The position operator \hat{x} starting at an initial time t evolves according to,

$$\hat{x}(t + \bar{t}) = \hat{x}(t) + \int_t^{t+\bar{t}} dt' \hat{v}(t'), \quad (\text{C.34})$$

so that the average location of the active particle after a time \bar{t} is given by

$$\langle \hat{x}(t + \bar{t}) \rangle = \langle \hat{x}(t_0) \rangle + \int_{t_0}^{t_0+\bar{t}} dt' \langle \hat{v}(t') \rangle. \quad (\text{C.35})$$

Here we want to focus on an initial time t in the range $t_s \ll t \ll t_m$ or $t \gg t_m$, so that the average velocity can be taken to be constant (see plateaus in Fig. 9.4), which yields

$$\langle \hat{x}(t + \bar{t}) \rangle = \langle \hat{x}(t) \rangle + \langle \hat{v} \rangle \bar{t}. \quad (\text{C.36})$$

We define the MSD as the fluctuations around the average position of the particle,

$$\text{MSD} = \langle [\hat{x}(t + \bar{t}) - \langle \hat{x}(t + \bar{t}) \rangle]^2 \rangle. \quad (\text{C.37})$$

Using Eq. (C.34) and (C.36), we can express the MSD in terms of the velocity-velocity correlation function as follows,

$$\text{MSD} = \int_t^{t+\bar{t}} dt_1 \int_t^{t+\bar{t}} dt_2 g(t_1 - t_2). \quad (\text{C.38})$$

The correlation function $g(\bar{t})$ is given explicitly in Eq. (9.18). In Fig. C.1, we show that the MSD grows like \bar{t}^2 with superimposed oscillations. The latter are a clear quantum signature of the motion, originating from the Bloch oscillations of the internal degrees of freedom of the active quantum particle.

C.5 DETAILS OF THE SIMULATION

Here we provide details on the simulations underlying the results given in chapter 9. We numerically solve the full Lindblad equation, given by

$$\partial_t \rho = -i[H_p, \rho] + \mathcal{D}_s[\rho] + \mathcal{D}_m[\rho] = \mathcal{L}\rho, \quad (\text{C.39})$$

with \mathcal{D}_s and \mathcal{D}_m being defined in Eq. (9.5) and (C.11). The velocity expectation value that is shown in Fig. 9.4 is calculated via

$$\langle \hat{v}(t) \rangle = \text{Tr}(\hat{v} e^{\mathcal{L}t} \rho^{\text{th}}). \quad (\text{C.40})$$

BIBLIOGRAPHY

1. A.-G. Penner, K. Flensberg, L. I. Glazman, and F. von Oppen, “Resistivity tensor of vortex-lattice states in josephson junction arrays”, *Physical Review Letters* **131**:20, 206001 (2023).
2. S. Reinhardt, A. G. Penner, J. Berger, C. Baumgartner, S. Gronin, G. C. Gardner, T. Lindemann, M. J. Manfra, L. I. Glazman, F. von Oppen, N. Paradiso, and C. Strunk, “Spontaneous supercurrents and vortex depinning in two-dimensional arrays of φ_0 josephson junctions”, *Phys. Rev. B* **112**, 224503 (2025).
3. H. Schmid, A.-G. Penner, K. Yang, L. Glazman, and F. von Oppen, “Robust spectral π pairing in the random-field floquet quantum ising model”, *Phys. Rev. Lett.* **132**, 210401 (2024).
4. A.-G. Penner, H. Schmid, L. I. Glazman, and F. von Oppen, “Subharmonic spin correlations and spectral pairing in floquet time crystals”, *Physical Review B* **111**:18, 184308 (2025).
5. A.-G. Penner, L. Viotti, R. Fazio, L. Arrachea, and F. von Oppen, “Heat-to-motion conversion for quantum active matter”, *Physical Review B* **112**:18, L180303 (2025).
6. A.-G. Penner, F. von Oppen, G. Zaránd, and M. R. Zirnbauer, “Hilbert space geometry of random matrix eigenstates”, *Physical Review Letters* **126**:20, 200604 (2021).
7. I. I. Rabi, S. Millman, P. Kusch, and J. R. Zacharias, “The molecular beam resonance method for measuring nuclear magnetic moments. the magnetic moments of li 6 3, li 7 3 and f 19 9”, *Physical review* **55**:6, 526 (1939).
8. C. Roos, T. Zeiger, H. Rohde, H. Nägerl, J. Eschner, D. Leibfried, F. Schmidt-Kaler, and R. Blatt, “Quantum state engineering on an optical transition and decoherence in a paul trap”, *Physical Review Letters* **83**:23, 4713 (1999).
9. M. Bastrakova, N. Klenov, and A. Satanin, “One-and two-qubit gates: rabi technique and single unipolar pulses”, *Physics of the Solid State* **61**:9, 1515–1522 (2019).
10. Y. Kanamori and S.-M. Yoo, “Quantum computing: principles and applications”, *Journal of International Technology and Information Management* **29**:2, 43–71 (2020).
11. M. S. Rudner and N. H. Lindner, “Floquet topological insulators: band structure engineering to non-equilibrium phenomena”, *arXiv preprint arXiv:1909.02008* (2019).
12. R. Roy and F. Harper, “Periodic table for floquet topological insulators”, *Phys. Rev. B* **96**, 155118 (2017).
13. A. G. Grushin, Á. Gómez-León, and T. Neupert, “Floquet fractional chern insulators”, *Physical Review Letters* **112**:15, 156801 (2014).

Bibliography

14. F. Wilczek, “Quantum Time Crystals”, *Phys. Rev. Lett.* **109**, 160401 (2012).
15. M. te Vrugt and R. Wittkowski, “Metareview: a survey of active matter reviews”, *Eur. Phys. J. E* **48**, 12 (2025).
16. M. Yamagishi, N. Hatano, and H. Obuse, “Proposal of a quantum version of active particles via a nonunitary quantum walk”, *Sci. Rep.* **14**, 28648 (2024).
17. Y. Zheng, B. Liebchen, and H. Löwen, *Mimicking quantum self-propulsion creates a generic route to quantum active matter*, 2024.
18. T. Nadolny, C. Bruder, and M. Brunelli, “Nonreciprocal synchronization of active quantum spins”, *Phys. Rev. X* **15**, 011010 (2025).
19. J. Bardeen, L. N. Cooper, and J. R. Schrieffer, “Theory of superconductivity”, *Physical review* **108**:5, 1175 (1957).
20. M. Tinkham, *Introduction to superconductivity*, Courier Corporation, 2004.
21. B. D. Josephson, “Possible new effects in superconductive tunnelling”, *Physics letters* **1**:7, 251–253 (1962).
22. V. Ambegaokar and A. Baratoff, “Tunneling between superconductors”, *Physical review letters* **10**:11, 486 (1963).
23. A. Silver and J. Zimmerman, “Quantum states and transitions in weakly connected superconducting rings”, *Physical Review* **157**:2, 317 (1967).
24. J. Koch, T. M. Yu, J. Gambetta, A. A. Houck, D. I. Schuster, J. Majer, A. Blais, M. H. Devoret, S. M. Girvin, and R. J. Schoelkopf, “Charge-insensitive qubit design derived from the cooper pair box”, *Physical Review A—Atomic, Molecular, and Optical Physics* **76**:4, 042319 (2007).
25. R. Fazio and H. Van Der Zant, “Quantum phase transitions and vortex dynamics in superconducting networks”, *Physics Reports* **355**:4, 235–334 (2001).
26. L. B. Ioffe, M. V. Feigel’man, A. Ioselevich, D. Ivanov, M. Troyer, and G. Blatter, “Topologically protected quantum bits using josephson junction arrays”, *Nature* **415**:6871, 503–506 (2002).
27. J. M. Kosterlitz, “The critical properties of the two-dimensional xy model”, *Journal of Physics C: Solid State Physics* **7**:6, 1046 (1974).
28. M. Lankhorst, A. Brinkman, H. Hilgenkamp, N. Poccia, and A. Golubov, “Annealed low energy states in frustrated large square josephson junction arrays”, *Condensed Matter* **3**:2, 19 (2018).
29. J. Villain, “Theory of one-and two-dimensional magnets with an easy magnetization plane. ii. the planar, classical, two-dimensional magnet”, *Journal de Physique* **36**:6, 581–590 (1975).
30. P. Gupta, S. Teitel, and M. J. P. Gingras, “Glassiness versus order in densely frustrated josephson arrays”, *Phys. Rev. Lett.* **80**, 105–108 (1998).
31. W. Stewart, “Current-voltage characteristics of josephson junctions”, *Applied physics letters* **12**:8, 277–280 (1968).

32. D. McCumber, “Effect of ac impedance on dc voltage-current characteristics of superconductor weak-link junctions”, *Journal of Applied Physics* **39**:7, 3113–3118 (1968).
33. W. Xia and P. Leath, “Defects, vortices, and critical current in josephson-junction arrays”, *Physical review letters* **63**:13, 1428 (1989).
34. C. Lobb, D. W. Abraham, and M. Tinkham, “Theoretical interpretation of resistive transition data from arrays of superconducting weak links”, *Physical Review B* **27**:1, 150 (1983).
35. <https://zenodo.org/records/17501497>.
36. J. C. Ciria and C. Giovannella, “Vortex dynamics in classical josephson junction arrays: models and recent experimental developments”, *J. Phys.: Cond. Matt.* **10**:7, 1453–1485 (1998).
37. R. Fazio and H. S. J. van der Zant, “Quantum phase transitions and vortex dynamics in superconducting networks”, *Phys. Rep.* **355**:4, 235–334 (2001).
38. B. Pannetier, J. Chaussy, R. Rammal, and J. C. Villegier, “Experimental fine tuning of frustration: two-dimensional superconducting network in a magnetic field”, *Phys. Rev. Lett.* **53**, 1845–1848 (1984).
39. B. J. van Wees, H. S. J. van der Zant, and J. E. Mooij, “Phase transitions of josephson-tunnel-junction arrays at zero and full frustration”, *Phys. Rev. B* **35**, 7291–7294 (1987).
40. L. N. Vu, M. S. Wistrom, and D. J. Van Harlingen, “Imaging of magnetic vortices in superconducting networks and clusters by scanning squid microscopy”, *Appl. Phys. Lett.* **63**:12, 1693–1695 (1993).
41. H. D. Hallen, R. Seshadri, A. M. Chang, R. E. Miller, L. N. Pfeiffer, K. W. West, C. A. Murray, and H. F. Hess, “Direct spatial imaging of vortices in a superconducting wire network”, *Phys. Rev. Lett.* **71**, 3007–3010 (1993).
42. S. Teitel and C. Jayaprakash, “Josephson-junction arrays in transverse magnetic fields”, *Phys. Rev. Lett.* **51**, 1999–2002 (1983).
43. T. C. Halsey, “Josephson-junction arrays in transverse magnetic fields: ground states and critical currents”, *Phys. Rev. B* **31**, 5728–5745 (1985).
44. M. Lankhorst, A. Brinkman, H. Hilgenkamp, N. Poccia, and A. Golubov, “Annealed low energy states in frustrated large square josephson junction arrays”, *Condensed Matter* **3**:2 (2018).
45. M. R. Kollahchi and J. P. Straley, “Ground state of the uniformly frustrated two-dimensional xy model near $f=1/2$ ”, *Phys. Rev. B* **43**, 7651–7654 (1991).
46. A. Vallat and H. Beck, “Classical frustrated xy model: continuity of the ground-state energy as a function of the frustration”, *Phys. Rev. Lett.* **68**, 3096–3099 (1992).
47. J. P. Straley and G. M. Barnett, “Phase diagram for a josephson network in a magnetic field”, *Phys. Rev. B* **48**, 3309–3315 (1993).
48. M. Franz and S. Teitel, “Vortex-lattice melting in two-dimensional superconducting networks and films”, *Phys. Rev. B* **51**, 6551–6574 (1995).

Bibliography

49. C. Denniston and C. Tang, “Incommensurability in the frustrated two-dimensional XY model”, *Phys. Rev. B* **60**, 3163–3168 (1999).
50. S. J. Lee, J.-R. Lee, and B. Kim, “Patterns of striped order in the classical lattice coulomb gas”, *Phys. Rev. Lett.* **88**, 025701 (2001).
51. F. Falo, A. R. Bishop, and P. S. Lomdahl, “I-v characteristics in two-dimensional frustrated josephson-junction arrays”, *Phys. Rev. B* **41**, 10983–10993 (1990).
52. A. van Otterlo, K.-H. Wagenblast, R. Fazio, and G. Schön, “Response of josephson-junction arrays near the quantum phase transition”, *Phys. Rev. B* **48**, 3316–3326 (1993).
53. L. Balents and D. R. Nelson, “Quantum smectic and supersolid order in helium films and vortex arrays”, *Phys. Rev. B* **52**, 12951–12968 (1995).
54. P. Martinoli, R. Theron, J.-B. Simond, R. Meyer, Y. Jaccard, and C. Leemann, “Superconducting vortices in triangular and square josephson junction arrays”, *Physica Scripta* **1993**:T49A, 176 (1993).
55. *C. M. Marcus, private communication.*
56. J. Shabani, M. Kjaergaard, H. J. Suominen, Y. Kim, F. Nichele, K. Pakrouski, T. Stankevic, R. M. Lutchyn, P. Krogstrup, R. Feidenhans’l, S. Kraemer, C. Nayak, M. Troyer, C. M. Marcus, and C. J. Palmstrøm, “Two-dimensional epitaxial superconductor-semiconductor heterostructures: a platform for topological superconducting networks”, *Phys. Rev. B* **93**, 155402 (2016).
57. C. G. L. Böttcher, F. Nichele, M. Kjaergaard, H. J. Suominen, J. Shabani, C. J. Palmstrøm, and C. M. Marcus, “Superconducting, insulating and anomalous metallic regimes in a gated two-dimensional semiconductor–superconductor array”, *Nat. Phys.* **14**:11, 1138–1144 (2018).
58. C. G. L. Böttcher, F. Nichele, J. Shabani, C. J. Palmstrøm, and C. M. Marcus, *The Berezinskii-Kosterlitz-Thouless Transition and Anomalous Metallic Phase in a Hybrid Josephson Junction Array*, 2022.
59. C. G. L. Böttcher, F. Nichele, J. Shabani, C. J. Palmstrøm, and C. M. Marcus, *Dynamical vortex transitions in a gate-tunable Josephson junction array*, 2022.
60. E. Wigner, “On the interaction of electrons in metals”, *Phys. Rev.* **46**, 1002–1011 (1934).
61. J. V. José, L. P. Kadanoff, S. Kirkpatrick, and D. R. Nelson, “Renormalization, vortices, and symmetry-breaking perturbations in the two-dimensional planar model”, *Phys. Rev. B* **16**, 1217–1241 (1977).
62. S. Teitel, “The two-dimensional fully frustrated xy model”, in *40 years of berezinskii–kosterlitz–thouless theory*, World Scientific, 2013, pp. 201–235.
63. W. Ren and E. Vanden-Eijnden, “A climbing string method for saddle point search”, *J. Chem. Phys.* **138**:13, 134105 (2013).
64. B. I. Halperin and D. R. Nelson, “Resistive transition in superconducting films”, *J. Low Temp. Phys.* **36**:5-6, 599–616 (1979).

65. J. D. Sau and S. Tewari, *Non-zero, symmetric, off-diagonal resistance from rotational symmetry breaking in a moire system*, 2023.
66. S. Reinhardt, “Magnetochiral effects in josephson junctions and two-dimensional josephson arrays”, PhD thesis (Universität Regensburg, 2025).
67. F. Ando, Y. Miyasaka, T. Li, J. Ishizuka, T. Arakawa, Y. Shiota, T. Moriyama, Y. Yanase, and T. Ono, “Observation of superconducting diode effect”, *Nature* **584**:7821, 373–376 (2020).
68. C. Baumgartner, L. Fuchs, A. Costa, S. Reinhardt, S. Gronin, G. C. Gardner, T. Lindemann, M. J. Manfra, P. E. Faria Junior, D. Kochan, et al., “Supercurrent rectification and magnetochiral effects in symmetric josephson junctions”, *Nature nanotechnology* **17**:1, 39–44 (2022).
69. B. Pal, A. Chakraborty, P. K. Sivakumar, M. Davydova, A. K. Gopi, A. K. Pandeya, J. A. Krieger, Y. Zhang, M. Date, S. Ju, et al., “Josephson diode effect from cooper pair momentum in a topological semimetal”, *Nature physics* **18**:10, 1228–1233 (2022).
70. K.-R. Jeon, J.-K. Kim, J. Yoon, J.-C. Jeon, H. Han, A. Cottet, T. Kontos, and S. S. Parkin, “Zero-field polarity-reversible josephson supercurrent diodes enabled by a proximity-magnetized pt barrier”, *Nature Materials* **21**:9, 1008–1013 (2022).
71. B. Turini, S. Salimian, M. Carrega, A. Iorio, E. Strambini, F. Giazotto, V. Zannier, L. Sorba, and S. Heun, “Josephson diode effect in high-mobility insb nanoflags”, *Nano Letters* **22**:21, 8502–8508 (2022).
72. S. Ghosh, V. Patil, A. Basu, Kuldeep, A. Dutta, D. A. Jangade, R. Kulkarni, A. Thamizhavel, J. F. Steiner, F. von Oppen, et al., “High-temperature josephson diode”, *Nature Materials* **23**:5, 612–618 (2024).
73. A. Costa, C. Baumgartner, S. Reinhardt, J. Berger, S. Gronin, G. Gardner, T. Lindemann, M. Manfra, J. Fabian, D. Kochan, et al., “Sign reversal of the josephson inductance magnetochiral anisotropy and $0-\pi$ -like transitions in supercurrent diodes”, *Nature Nanotechnology* **18**:11, 1266–1272 (2023).
74. N. Lotfizadeh, W. F. Schiela, B. Pekerten, P. Yu, B. H. Elfeky, W. M. Strickland, A. Matos-Abiague, and J. Shabani, “Superconducting diode effect sign change in epitaxial al-inas josephson junctions”, *Communications Physics* **7**:1, 120 (2024).
75. A. Banerjee, M. Geier, M. A. Rahman, C. Thomas, T. Wang, M. J. Manfra, K. Flensberg, and C. M. Marcus, “Phase asymmetry of andreev spectra from cooper-pair momentum”, *Physical Review Letters* **131**:19, 196301 (2023).
76. A. Buzdin, “Direct coupling between magnetism and superconducting current in the josephson φ 0 junction”, *Physical review letters* **101**:10, 107005 (2008).
77. S. Reinhardt, T. Ascherl, A. Costa, J. Berger, S. Gronin, G. C. Gardner, T. Lindemann, M. J. Manfra, J. Fabian, D. Kochan, et al., “Link between supercurrent diode and anomalous josephson effect revealed by gate-controlled interferometry”, *Nature Communications* **15**:1, 4413 (2024).
78. A. F. Andreev, “The thermal conductivity of the intermediate state in superconductors”, **46**:5, 1823–1828 (1964).

Bibliography

79. F. Dolcini, “Andreev reflection”, Lecture Notes for XXIII Physics GradDays **5**, 9 (2009).
80. C. Beenakker, “Universal limit of critical-current fluctuations in mesoscopic josephson junctions”, Physical review letters **67**:27, 3836 (1991).
81. A. Reynoso, G. Usaj, C. Balseiro, D. Feinberg, and M. Avignon, “Anomalous josephson current in junctions with spin polarizing quantum point contacts”, Physical review letters **101**:10, 107001 (2008).
82. T. Yokoyama, M. Eto, and Y. V. Nazarov, “Anomalous josephson effect induced by spin-orbit interaction and zeeman effect in semiconductor nanowires”, *Phys. Rev. B* **89**, 195407 (2014).
83. M. Rzchowski, S. Benz, M. Tinkham, and C. Lobb, “Vortex pinning in josephson-junction arrays”, Physical Review B **42**:4, 2041 (1990).
84. J. F. Steiner, L. Melischek, M. Trahms, K. J. Franke, and F. von Oppen, “Diode effects in current-biased josephson junctions”, Physical Review Letters **130**:17, 177002 (2023).
85. D. E. Shalóm and H. Pastoriza, “Vortex motion rectification in josephson junction arrays with a ratchet potential”, *Phys. Rev. Lett.* **94**, 177001 (2005).
86. W. Gillijns, A. V. Silhanek, V. V. Moshchalkov, C. J. O. Reichhardt, and C. Reichhardt, “Origin of reversed vortex ratchet motion”, *Phys. Rev. Lett.* **99**, 247002 (2007).
87. P. Pfeuty, “The one-dimensional ising model with a transverse field”, *Ann. Phys.* **57**:1, 79–90 (1970).
88. S. Sachdev, *Quantum phase transitions*, Second, Cambridge University Press, Cambridge, 2011.
89. A. Y. Kitaev, “Unpaired Majorana fermions in quantum wires”, *Physics-Uspeski* **44**:10S, 131–136 (2001).
90. V. Khemani, A. Lazarides, R. Moessner, and S. L. Sondhi, “Phase Structure of Driven Quantum Systems”, *Phys. Rev. Lett.* **116**, 250401 (2016).
91. D. V. Else, B. Bauer, and C. Nayak, “Floquet time crystals”, *Phys. Rev. Lett.* **117**, 090402 (2016).
92. P. Jordan and E. Wigner, “Über das paulische äquivalenzverbot”, *Zeitschrift für Physik* **47**:9, 631–651 (1928).
93. A. Y. Kitaev, “Unpaired majorana fermions in quantumwires”, *Physics-uspekhi* **44**:10S, 131 (2001).
94. A. Lerose, M. Sonner, and D. A. Abanin, “Scaling of temporal entanglement in proximity to integrability”, Physical Review B **104**:3, 035137 (2021).
95. K. A. Matveev, “Coulomb blockade at almost perfect transmission”, *Phys. Rev. B* **51**, 1743–1751 (1995).
96. J. J. Sakurai and J. Napolitano, *Modern quantum mechanics*, Cambridge University Press, 2020.
97. K. Viebahn, “Introduction to floquet theory”, Institute for Quantum Electronics, ETH Zurich **8093** (2020).
98. H. Schmid, “Interacting quantum spins with periodic, quasiperiodic and direct-current drives”, PhD thesis (2025).

99. X. Mi, M. Sonner, M. Y. Niu, K. W. Lee, B. Foxen, R. Acharya, I. Aleiner, T. I. Andersen, F. Arute, K. Arya, et al., “Noise-resilient edge modes on a chain of superconducting qubits”, *Science* **378**:6621, 785–790 (2022).
100. M. Thakurathi, A. A. Patel, D. Sen, and A. Dutta, “Floquet generation of Majorana end modes and topological invariants”, *Phys. Rev. B* **88**, 155133 (2013).
101. B. Bauer, T. Pereg-Barnea, T. Karzig, M.-T. Rieder, G. Refael, E. Berg, and Y. Oreg, “Topologically protected braiding in a single wire using Floquet Majorana modes”, *Phys. Rev. B* **100**:4, 041102 (2019).
102. L. Jiang, T. Kitagawa, J. Alicea, A. R. Akhmerov, D. Pekker, G. Refael, J. I. Cirac, E. Demler, M. D. Lukin, and P. Zoller, “Majorana fermions in equilibrium and in driven cold-atom quantum wires”, *Phys. Rev. Lett.* **106**, 220402 (2011).
103. P. Fendley, “Strong zero modes and eigenstate phase transitions in the xyz/interacting majorana chain”, *J. Phys. A* **49**:30, 30LT01 (2016).
104. D. V. Else, P. Fendley, J. Kemp, and C. Nayak, “Prethermal strong zero modes and topological qubits”, *Phys. Rev. X* **7**, 041062 (2017).
105. J. Kemp, N. Y. Yao, C. R. Laumann, and P. Fendley, “Long coherence times for edge spins”, *J. Stat. Mech.* **2017**:6, 063105 (2017).
106. D. J. Yates, F. H. L. Essler, and A. Mitra, “Almost strong $(0, \pi)$ edge modes in clean interacting one-dimensional Floquet systems”, *Phys. Rev. B* **99**, 205419 (2019).
107. H.-C. Yeh, A. Rosch, and A. Mitra, *Decay rates of almost strong modes in Floquet spin chains beyond Fermi’s Golden Rule*, 2023.
108. J.-P. Bouchaud and A. Georges, “Anomalous diffusion in disordered media: Statistical mechanisms, models and physical applications”, *Phys. Rep.* **195**:4-5, 127–293 (1990).
109. P. W. Brouwer, M. Duckheim, A. Romito, and F. von Oppen, “Probability Distribution of Majorana End-State Energies in Disordered Wires”, *Phys. Rev. Lett.* **107**, 196804 (2011).
110. D. A. Abanin, W. De Roeck, W. W. Ho, and F. ç. Huveneers, “Effective hamiltonians, prethermalization, and slow energy absorption in periodically driven many-body systems”, *Phys. Rev. B* **95**, 014112 (2017).
111. C. Bruder, R. Fazio, and G. Schön, “Superconductor–mott-insulator transition in bose systems with finite-range interactions”, *Phys. Rev. B* **47**, 342–347 (1993).
112. L. S. Levitov, T. P. Orlando, J. B. Majer, and J. E. Mooij, *Quantum spin chains and Majorana states in arrays of coupled qubits*, 2001.
113. J. Q. You, Z. D. Wang, W. Zhang, and F. Nori, “Encoding a qubit with Majorana modes in superconducting circuits”, *Scientific Rep.* **4**, 5535, 5535 (2014).
114. S. Plugge, A. Rasmussen, R. Egger, and K. Flensberg, “Majorana box qubits”, *New J. Phys.* **19**:1, 012001 (2017).

Bibliography

115. T. Karzig, C. Knapp, R. M. Lutchyn, P. Bonderson, M. B. Hastings, C. Nayak, J. Alicea, K. Flensberg, S. Plugge, Y. Oreg, C. M. Marcus, and M. H. Freedman, “Scalable designs for quasiparticle-poisoning-protected topological quantum computation with majorana zero modes”, *Phys. Rev. B* **95**, 235305 (2017).
116. Y. Oreg and F. von Oppen, “Majorana Zero Modes in Networks of Cooper-Pair Boxes: Topologically Ordered States and Topological Quantum Computation”, *Ann. Rev. Cond. Mat. Phys.* **11**, 397–420 (2020).
117. M. P. Zaletel, M. Lukin, C. Monroe, C. Nayak, F. Wilczek, and N. Y. Yao, “Colloquium: Quantum and classical discrete time crystals”, *Rev. Mod. Phys.* **95**, 031001 (2023).
118. K. Sacha and J. Zakrzewski, “Time crystals: a review”, *Rep. Prog. Phys.* **81**:1, 016401 (2017).
119. V. Khemani, R. Moessner, and S. L. Sondhi, *A brief history of time crystals*, 2019.
120. S. Choi *et al.*, “Observation of discrete time-crystalline order in a disordered dipolar many-body system”, *Nature* **543**:7644, 221–225 (2017).
121. J. Zhang *et al.*, “Observation of a discrete time crystal”, *Nature* **543**:7644, 217–220 (2017).
122. J. Randall, C. E. Bradley, F. V. van der Gronden, A. Galicia, M. H. Abobeih, M. Markham, D. J. Twitchen, F. Machado, N. Y. Yao, and T. H. Taminiau, “Many-body-localized discrete time crystal with a programmable spin-based quantum simulator”, *Science* **374**:6574, 1474–1478 (2021).
123. X. Mi *et al.*, “Time-crystalline eigenstate order on a quantum processor”, *Nature* **601**:7894, 531–536 (2022).
124. P. Frey and S. Rachel, “Realization of a discrete time crystal on 57 qubits of a quantum computer”, *Science Advances* **8**:9, eabm7652 (2022).
125. D. V. Else, C. Monroe, C. Nayak, and N. Y. Yao, “Discrete Time Crystals”, *Annu. Rev. Condens. Matter Phys.* **11**:1, 467–499 (2020).
126. C. W. von Keyserlingk, V. Khemani, and S. L. Sondhi, “Absolute stability and spatiotemporal long-range order in floquet systems”, *Phys. Rev. B* **94**, 085112 (2016).
127. F. M. Surace, A. Russomanno, M. Dalmonte, A. Silva, R. Fazio, and F. Iemini, “Floquet time crystals in clock models”, *Phys. Rev. B* **99**, 104303 (2019).
128. A. Lazarides, A. Das, and R. Moessner, “Fate of Many-Body Localization Under Periodic Driving”, *Phys. Rev. Lett.* **115**, 030402 (2015).
129. N. Y. Yao, A. C. Potter, I.-D. Potirniche, and A. Vishwanath, “Discrete time crystals: rigidity, criticality, and realizations”, *Phys. Rev. Lett.* **118**, 030401 (2017).
130. P. Ponte, Z. Papić, F. ç. Huveneers, and D. A. Abanin, “Many-Body Localization in Periodically Driven Systems”, *Phys. Rev. Lett.* **114**, 140401 (2015).
131. E. Bairey, G. Refael, and N. H. Lindner, “Driving induced many-body localization”, *Phys. Rev. B* **96**, 020201 (2017).

132. M. Sonner, M. Serbyn, Z. Papić, and D. A. Abanin, “Thouless energy across the many-body localization transition in Floquet systems”, *Phys. Rev. B* **104**, L081112 (2021).
133. P. Sierant, M. Lewenstein, A. Scardicchio, and J. Zakrzewski, “Stability of many-body localization in Floquet systems”, *Phys. Rev. B* **107**, 115132 (2023).
134. E. Lieb, T. Schultz, and D. Mattis, “Two soluble models of an antiferromagnetic chain”, *Ann. Phys.* **16**:3, 407–466 (1961).
135. P. Pfeuty, “An exact result for the 1D random Ising model in a transverse field”, *Phys. Lett. A* **72**:3, 245–246 (1979).
136. Y. Imry, “Active transmission channels and universal conductance fluctuations”, *Europhys. Lett.* **1**:5, 249 (1986).
137. M. Titov, D. Braun, and Y. V. Fyodorov, “Log - normal distribution of level curvatures in the localized regime: analytical verification”, *J. Phys. A: Math. and Gen.* **30**:10, L339 (1997).
138. S. Asmussen, J. L. Jensen, and L. Rojas-Nandayapa, “On the Laplace transform of the lognormal distribution”, *Methodol. Comput. Appl. Probab.* **18**, 441–458 (2016).
139. D. J. Thouless, “Maximum metallic resistance in thin wires”, *Phys. Rev. Lett.* **39**, 1167–1169 (1977).
140. V. I. Oseledec, “A multiplicative ergodic theorem, lyapunov characteristic numbers for dynamical systems”, *Trans. Moscow Math. Soc.* **19**, 197–231 (1968).
141. D. J. Thouless, “A relation between the density of states and range of localization for one dimensional random systems”, *J. Phys. C: Sol. St. Phys.* **5**:1, 77 (1972).
142. D. J. Thouless, “Percolation and localization”, in *Ill-condensed Matter*, edited by R. Balian, R. Maynard, and G. Toulouse, Ecole d’ete de physique theoretique Les Houches, North-Holland Publishing Company, 1979.
143. H. Sahu and F. Iemini, *Information scrambling and entanglement dynamics in floquet time crystals*, 2024.
144. A. Pizzi, J. Knolle, and A. Nunnenkamp, “Period- n Discrete Time Crystals and Quasicrystals with Ultracold Bosons”, *Phys. Rev. Lett.* **123**, 150601 (2019).
145. A. Pizzi, J. Knolle, and A. Nunnenkamp, “Higher-order and fractional discrete time crystals in clean long-range interacting systems”, *Nat Comm* **12**:1, 2341 (2021).
146. G. Giachetti, A. Solfanelli, L. Correale, and N. Defenu, “Fractal nature of high-order time crystal phases”, *Phys. Rev. B* **108**, L140102 (2023).
147. E. van Nieuwenburg, Y. Baum, and G. Refael, “From Bloch oscillations to many-body localization in clean interacting systems”, *Proc. Natl. Acad. Sci.* **116**:19, 9269–9274 (2019).
148. A. Kshetrimayum, J. Eisert, and D. M. Kennes, “Stark time crystals: Symmetry breaking in space and time”, *Phys. Rev. B* **102**, 195116 (2020).
149. S. Liu, S.-X. Zhang, C.-Y. Hsieh, S. Zhang, and H. Yao, “Discrete Time Crystal Enabled by Stark Many-Body Localization”, *Phys. Rev. Lett.* **130**, 120403 (2023).

Bibliography

150. F. Iemini, A. Russomanno, J. Keeling, M. Schirò, M. Dalmonte, and R. Fazio, “Boundary Time Crystals”, *Phys. Rev. Lett.* **121**, 035301 (2018).
151. K. Tucker, B. Zhu, R. J. Lewis-Swan, J. Marino, F. Jimenez, J. G. Restrepo, and A. M. Rey, “Shattered time: can a dissipative time crystal survive many-body correlations?”, *New J. Phys.* **20**:12, 123003 (2018).
152. B. Zhu, J. Marino, N. Y. Yao, M. D. Lukin, and E. A. Demler, “Dicke time crystals in driven-dissipative quantum many-body systems”, *New J. Phys.* **21**:7, 073028 (2019).
153. F. M. Gabbett, F. Carollo, M. Marcuzzi, J. P. Garrahan, and I. Lesanovsky, “Discrete Time Crystals in the Absence of Manifest Symmetries or Disorder in Open Quantum Systems”, *Phys. Rev. Lett.* **122**, 015701 (2019).
154. C. Booker, B. Buča, and D. Jaksch, “Non-stationarity and dissipative time crystals: spectral properties and finite-size effects”, *New J. Phys.* **22**:8, 085007 (2020).
155. M. Krishna, P. Solanki, M. Hajdušek, and S. Vinjanampathy, “Measurement-Induced Continuous Time Crystals”, *Phys. Rev. Lett.* **130**, 150401 (2023).
156. H.-P. Breuer and F. Petruccione, *The theory of open quantum systems*, OUP Oxford, 2002.
157. A. G. Redfield, “On the theory of relaxation processes”, *IBM Journal of Research and Development* **1**:1, 19–31 (1957).
158. L. Mandel and E. Wolf, *Optical coherence and quantum optics*, Cambridge university press, 1995.
159. M. Lax, “Formal theory of quantum fluctuations from a driven state”, *Physical Review* **129**:5, 2342 (1963).
160. M. C. Marchetti, J. F. Joanny, S. Ramaswamy, T. B. Liverpool, J. Prost, M. Rao, and R. A. Simha, “Hydrodynamics of soft active matter”, *Rev. Mod. Phys.* **85**, 1143–1189 (2013).
161. C. Bechinger, R. Di Leonardo, H. Löwen, C. Reichhardt, G. Volpe, and G. Volpe, “Active particles in complex and crowded environments”, *Rev. Mod. Phys.* **88**, 045006 (2016).
162. S. Ramaswamy, “Active matter”, *J. Stat. Mech.: Theory Exp.* **2017**:5, 054002 (2017).
163. J. Toner, *The physics of flocking: birth, death, and flight in active matter*, Cambridge University Press, 2024.
164. K. Sone, K. Yokomizo, K. Kawaguchi, and Y. Ashida, “Hermitian and non-hermitian topology in active matter”, arXiv preprint arXiv:2407.16143 (2024).
165. K. Adachi, K. Takasan, and K. Kawaguchi, “Activity-induced phase transition in a quantum many-body system”, *Phys. Rev. Res.* **4**, 013194 (2022).
166. R. Khasseh, S. Wald, R. Moessner, C. A. Weber, and M. Heyl, *Active quantum flocks*, 2023.
167. H. Yuan, L. X. Cui, L. T. Chen, and C. P. Sun, *Quantum vicsek model for active matter*, 2024.
168. K. Takasan, K. Adachi, and K. Kawaguchi, “Activity-induced ferromagnetism in one-dimensional quantum many-body systems”, *Phys. Rev. Res.* **6**:2, 023096 (2024).

169. P. Hänggi and F. Marchesoni, “Artificial brownian motors: controlling transport on the nanoscale”, *Rev. Mod. Phys.* **81**, 387–442 (2009).
170. X.-L. Qi and S.-C. Zhang, “Field-induced gap and quantized charge pumping in a nanoscale helical wire”, *Phys. Rev. B* **79**, 235442 (2009).
171. T. Kudernac, N. Ruangsapichat, M. Parschau, B. Maciá, N. Katsonis, S. R. Harutyunyan, K.-H. Ernst, and B. L. Feringa, “Electrically driven directional motion of a four-wheeled molecule on a metal surface”, *479*:7372, 208–211 (2011).
172. R. Bustos-Marín, G. Refael, and F. von Oppen, “Adiabatic quantum motors”, *Phys. Rev. Lett.* **111**, 060802 (2013).
173. Q. Meng, S. Vishveshwara, and T. L. Hughes, “Spin-transfer torque and electric current in helical edge states in quantum spin hall devices”, *Phys. Rev. B* **90**, 205403 (2014).
174. L. Arrachea and F. von Oppen, “Nanomagnet coupled to quantum spin hall edge: an adiabatic quantum motor”, *Physica E* **74**, 596–602 (2015).
175. A. Bruch, S. V. Kusminskiy, G. Refael, and F. von Oppen, “Interacting adiabatic quantum motor”, *Phys. Rev. B* **97**, 195411 (2018).
176. D. von Lindenfels, O. Gräß, C. T. Schmiegelow, V. Kaushal, J. Schulz, M. T. Mitchison, J. Goold, F. Schmidt-Kaler, and U. G. Poschinger, “Spin Heat Engine Coupled to a Harmonic-Oscillator Flywheel”, *Phys. Rev. Lett.* **123**:8, 080602 (2019).
177. R. Kosloff and A. Levy, “Quantum heat engines and refrigerators: continuous devices”, *Ann. Rev. Phys. Chem.* **65**:1, 365–393 (2014).
178. L. M. Cangemi, C. Bhadra, and A. Levy, *Quantum engines and refrigerators*, 2023.
179. G. Benenti, G. Casati, K. Saito, and R. S. Whitney, “Fundamental aspects of steady-state conversion of heat to work at the nanoscale”, *Phys. Rep.* **694**, 1–124 (2017).
180. L. Arrachea, “Energy dynamics, heat production and heat–work conversion with qubits: toward the development of quantum machines”, *Rep. Prog. Phys.* **86**:3, 036501 (2023).
181. S. Vinjanampathy and J. Anders, “Quantum thermodynamics”, *Contemporary Physics* **57**:4, 545–579 (2016).
182. J. Goold, M. Huber, A. Riera, L. d. Rio, and P. Skrzypczyk, “The role of quantum information in thermodynamics—a topical review”, *Journal of Physics A: Mathematical and Theoretical* **49**:14, 143001 (2016).
183. B. Loewe, A. Souslov, and P. Goldbart, “Flocking from a quantum analogy: spin–orbit coupling in an active fluid”, *New J. Phys.* **20**, 013020 (2018).
184. A. Ambainis, E. Bach, A. Nayak, A. Vishwanath, and J. Watrous, “One-dimensional quantum walks”, in *ACM Conferences*, Association for Computing Machinery, New York, NY, USA, 2001, pp. 37–49.
185. W. Dür, R. Raussendorf, V. M. Kendon, and H.-J. Briegel, “Quantum walks in optical lattices”, *Phys. Rev. A* **66**:5, 052319 (2002).

Bibliography

186. A. Peruzzo, M. Lobino, J. C. Matthews, N. Matsuda, A. Politi, K. Poulios, X.-Q. Zhou, Y. Lahini, N. Ismail, K. Wörhoff, et al., “Quantum walks of correlated photons”, *Science* **329**:5998, 1500–1503 (2010).
187. J.-P. Brantut, C. Grenier, J. Meineke, D. Stadler, S. Krinner, C. Kollath, T. Esslinger, and A. Georges, “A thermoelectric heat engine with ultracold atoms”, *Science* **342**:6159, 713–715 (2013).
188. K. Baumann, C. Guerlin, F. Brennecke, and T. Esslinger, “Dicke quantum phase transition with a superfluid gas in an optical cavity”, *Nature* **464**:7293, 1301–1306 (2010).
189. H. Schmid, Y. Peng, G. Refael, and F. von Oppen, “Self-similar phase diagram of the fibonacci-driven quantum ising model”, *Phys. Rev. Lett.* **134**, 240404 (2025).
190. L. Bennett, B. Melchers, and B. Proppe, *Curta: A General-purpose High-Performance Computer at ZEDAT, Freie Universität Berlin*, 2020.
191. W. Ren and E. Vanden-Eijnden, “A climbing string method for saddle point search”, *The Journal of chemical physics* **138**:13 (2013).